



Politecnico di Bari

Repository Istituzionale dei Prodotti della Ricerca del Politecnico di Bari

Thermography for defect detection and structural integrity analysis: comparison of new and established methods and novel procedures for a robust quantitative assessment

This is a PhD Thesis

Original Citation:

Availability:

This version is available at <http://hdl.handle.net/11589/189177> since: 2020-01-14

Published version

Politecnico di Bari
DOI: 10.60576/poliba/iris/d-accardi-ester_phd2020

Terms of use:

Altro tipo di accesso

(Article begins on next page)



Politecnico
di Bari

LIBERATORIA PER L'ARCHIVIAZIONE DELLA TESI DI DOTTORATO

Al Magnifico Rettore
del Politecnico di Bari

La sottoscritta Ester D'Accardi nata a Taranto (TA) il 11/04/1991

residente a Taranto in via Lupoli n°2 e-mail ester.daccardi@poliba.it

iscritta al 3° anno di Corso di Dottorato di Ricerca in Ingegneria Meccanica e Gestionale ciclo XXXII

ed essendo stata ammessa a sostenere l'esame finale con la prevista discussione della tesi dal titolo: "Thermography for defect detection and structural integrity analysis: comparison of new and established methods and novel procedures for a robust quantitative assessment"

DICHIARA

- 1) di essere consapevole che, ai sensi del D.P.R. n. 445 del 28.12.2000, le dichiarazioni mendaci, la falsità negli atti e l'uso di atti falsi sono puniti ai sensi del codice penale e delle Leggi speciali in materia, e che nel caso ricorressero dette ipotesi, decade fin dall'inizio e senza necessità di nessuna formalità dai benefici conseguenti al provvedimento emanato sulla base di tali dichiarazioni;
- 2) di essere iscritto al Corso di Dottorato di ricerca Ingegneria Meccanica e Gestionale ciclo XXXII, corso attivato ai sensi del "Regolamento dei Corsi di Dottorato di ricerca del Politecnico di Bari", emanato con D.R. n.286 del 01.07.2013;
- 3) di essere pienamente a conoscenza delle disposizioni contenute nel predetto Regolamento in merito alla procedura di deposito, pubblicazione e autoarchiviazione della tesi di dottorato nell'Archivio Istituzionale ad accesso aperto alla letteratura scientifica;
- 4) di essere consapevole che attraverso l'autoarchiviazione delle tesi nell'Archivio Istituzionale ad accesso aperto alla letteratura scientifica del Politecnico di Bari (IRIS-POLIBA), l'Ateneo archiverà e renderà consultabile in rete (nel rispetto della Policy di Ateneo di cui al D.R. 642 del 13.11.2015) il testo completo della tesi di dottorato, fatta salva la possibilità di sottoscrizione di apposite licenze per le relative condizioni di utilizzo (di cui al sito <http://www.creativecommons.it/Licenze>), e fatte salve, altresì, le eventuali esigenze di "embargo", legate a strette considerazioni sulla tutelabilità e sfruttamento industriale/commerciale dei contenuti della tesi, da rappresentarsi mediante compilazione e sottoscrizione del modulo in calce (Richiesta di embargo);
- 5) che la tesi da depositare in IRIS-POLIBA, in formato digitale (PDF/A) sarà del tutto identica a quelle **consegnate**/inviate/da inviarsi ai componenti della commissione per l'esame finale e a qualsiasi altra copia depositata presso gli Uffici del Politecnico di Bari in forma cartacea o digitale, ovvero a quella da discutere in sede di esame finale, a quella da depositare, a cura dell'Ateneo, presso le Biblioteche Nazionali Centrali di Roma e Firenze e presso tutti gli Uffici competenti per legge al momento del deposito stesso, e che di conseguenza va esclusa qualsiasi responsabilità del Politecnico di Bari per quanto riguarda eventuali errori, imprecisioni o omissioni nei contenuti della tesi;
- 6) che il contenuto e l'organizzazione della tesi è opera originale realizzata dal sottoscritto e non compromette in alcun modo i diritti di terzi, ivi compresi quelli relativi alla sicurezza dei dati personali; che pertanto il Politecnico di Bari ed i suoi funzionari sono in ogni caso esenti da responsabilità di qualsivoglia natura: civile, amministrativa e penale e saranno dal sottoscritto tenuti indenni da qualsiasi richiesta o rivendicazione da parte di terzi;
- 7) che il contenuto della tesi non infrange in alcun modo il diritto d'Autore né gli obblighi connessi alla salvaguardia di diritti morali od economici di altri autori o di altri aventi diritto, sia per testi, immagini, foto, tabelle, o altre parti di cui la tesi è composta.

Luogo e data Bari, 18/12/2019

Firma

Ester D'Accardi

La sottoscritta, con l'autoarchiviazione della propria tesi di dottorato nell'Archivio Istituzionale ad accesso aperto del Politecnico di Bari (POLIBA-IRIS), pur mantenendo su di essa tutti i diritti d'autore, morali ed economici, ai sensi della normativa vigente (Legge 633/1941 e ss.mm.ii.),

CONCEDE

- al Politecnico di Bari il permesso di trasferire l'opera su qualsiasi supporto e di convertirla in qualsiasi formato al fine di una corretta conservazione nel tempo. Il Politecnico di Bari garantisce che non verrà effettuata alcuna modifica al contenuto e alla struttura dell'opera.
- al Politecnico di Bari la possibilità di riprodurre l'opera in più di una copia per fini di sicurezza, back-up e conservazione.

Luogo e data Bari, 18/12/2019

Firma

Ester D'Accardi



Department of Mechanics, Mathematics and Management
MECHANICAL AND MANAGEMENT ENGINEERING
Ph.D. Program
SSD: ING-IND/14– MECHANICAL DESIGN AND
MACHINE CONSTRUCTION

Final Dissertation

Thermography for defect detection and
structural integrity analysis:
comparison of new and established
methods and novel procedures for a
robust quantitative assessment

by

Ester D'Accardi

Supervisors:

Prof. Umberto Galietti

Ing. Davide Palumbo

Coordinator of Ph.D. Program:

Prof. Giuseppe Pompeo Demelio

Course n°32, 01/11/2016-31/10/2019



Politecnico
di Bari

Department of Mechanics, Mathematics and Management
MECHANICAL AND MANAGEMENT ENGINEERING

Ph.D. Program

**SSD: ING-IND/14–MECHANICAL DESIGN AND
MACHINE CONSTRUCTION**

Final Dissertation

**Thermography for defect detection and structural
integrity analysis: comparison of new and
established methods and novel procedures for a
robust quantitative assessment**

by

Ester D'Accardi:

Ester D'Accardi

Referees:

Prof. Chiara Colombo

Prof. Riccardo Nobile

Supervisors:

Prof. Umberto Galletti

U. Galletti

Ing. Davide Palumbo

D. Palumbo

Coordinator of Ph.D Program:

Prof. Giuseppe Pompeo Demelio

G. Demelio

*«Fama di loro il mondo esser non lassa;
misericordia e giustizia li sdegna:
non ragioniam di lor, ma guarda e passa.»*

*Inferno, Canto III.
Dante Alighieri*

I hereby declare that this submission is my own work and that, to the best of my knowledge and belief, it contains nor material previously published or written by another person nor material which has been accepted for the award of any other degree or diploma of the university or other institute of higher learning, except where due acknowledgment has been made in the text.

Ester D'Accardi

23/10/2019, Bari

Abstract

Subsurface defects can be detected by pulsed thermography, starting from the evaluation of the temperature response at the surface. However, it is necessary a post-processing of the raw thermal data, in order to provide quantitative information, such as defect depth and size.

In the past, many algorithms have been developed to localize defects with a very good contrast and also to estimate their depths such as Thermal Signal Reconstruction (TSR®) and Pulsed Phase Thermography (PPT). There are also different numerical models, one, two or three dimensional, that describe the thermal behavior after a pulsed test of a certain duration that help to have an estimation about the correct thermographic parameter to perform a quantitative analysis.

Therefore, a lot of very important parameters, such as the acquisition frequency, the power of the heat sources, the truncation window size in terms of analysis window and also the required geometrical resolution change with the used material, the sample geometry and also the type of expected defect (delamination, crack, porosity, flat bottom hole); for this reason the same have to be selected carefully.

Even if many publications have been already dealing with these topics, within this dissertation a new approach is proposed for performing a quantitative and correct analysis after a pulsed test.

In particular, a very critical type of material has been studied, such as the aluminum one, because the major part of the past works regards the composite materials, which are not affected by the problems due to the high diffusivity when a pulsed test is performed.

A very large investigation concern the possibility to detect the defects in an aluminum sample with different flat bottom holes, having also very critical aspect ratio values less than 2, by applying different post-processing algorithms such as Principal Component Thermography (PCT), Pulsed Phase Thermography (PPT), Thermal Signal Reconstruction (TSR®), Slope and Square Correlation Coefficient (R^2).

The influence of the truncation window size, the flash power, and the acquisition frequency has been investigated and also different set-ups, with very different peculiarities, have been used in order to compare the possible achieved results.

The new proposed quantitative approach starts from the evidence that exists a linear correlation between the defect aspect ratios and their relative contrasts, shown after the application of different post-processing algorithms and a suitable truncation window size. This experimental evidence has been also explained by simulating the thermal behavior with different well-established models. In this way, the possibility to have an estimation of defect depth and size is however demonstrated by using a very low-cost set-up with very competitive acquisition parameters.

The limits of PPT and TSR® algorithms are shown when the aim is to have quantitative information in very high diffusivity materials.

An important part of this dissertation regards the application of the pulsed thermography to investigate the thermal

behavior of different materials and typical defects involved within several industrial and research applications. In this part of the dissertation, the results in terms of “how to analyze a thermographic data to characterize a defect and quantify it” obtained within the first part, will be used and further studies to solve and investigate components with real and particular types of defects.

Finally, new procedures very similar to the one proposed in the first part to quantify imposed defects, will be outlined and described, for evaluating the quality of industrial processes of spread interest, that require not only the identification of the defect, but the control of decisive process parameters .

In particular, a lot of pulsed tests, by using different energy sources and IR cameras, and also different thermographic parameters in terms of frame rate and pulse duration have been performed to detect typical defects in a Metal Additive Manufacturing process. This particular type of defects is not simple to detect because they are very small and superficial and also their typical irregular 3D shape involves small air pockets inside the material.

A new and suitable approach has been proposed to control the integrity of a real component by using the thermography as a non-destructive technique. The starting point of this procedure is the comparison between the results reached by using two very different non-destructive techniques, such as the pulsed thermography in terms of Pulsed Phase Thermography and the ultrasonic one in terms of C-scan map with a Phased Array Technology, in the estimation of delamination depth in a composite material. The proposed approach allows for extracting the sound area from the same real component to get information about defect size and depth of a defective part having the same its geometry.

Novel procedures for a robust quantitative assessment have been carried out. The first one regards the application of a very simple transmission set-up in order to perform pulsed tests to control the quality of different RSW (Resistance Spot Welding) joints. Different steel joints were obtained from the RSW process by varying the main process parameters such as current and time. By studying the thermal behavior in correspondence of the nugget of these welded joints, it is possible to find different thermographic “indexes”, capable of assessing the quality of joints.

A further investigation regards the possibility to use a thermographic method for estimating the coating thickness by using a calibration curve, like the approach shown in the case of an aluminum sample with different flat bottom holes. The investigation regards a coating and a basic material in steel with very close thermophysical properties. For this reason, also in this case, the limits that shown the classical methods to do a quantitative analysis in this type of application are shown in detail. However, by using a very low-cost equipment, mainly for the used infrared camera, that is a microbolometer one, it will be shown how these limits can be overcome, by developing a new thermographic procedure capable to provide an estimation of the coating thickness from 1 to 10 mm.

All the investigated applications are related by a main topic: the possibility and also the necessity to use the thermography as a quantitative control in a lot of industrial and research applications. It is worth to underline that, it is necessary to have a standard as reference, such as a sample with different imposed defects, or a sample with quality feature well known, or again another type of non destructive technique, in order to calibrate pre and post-processing thermographic parameters before to move on to the analysis of a real component.

The variety of the treated real problems such as the detection of typical metal additive manufacturing defects, shows once again as thermography is a versatile and competitive type of non destructive control in terms of time and costs and as a more that promising technique to talk about of “integrity analysis” in the field of engineering.

Contents

Abstract	1
Table of Contents	3
List of Figures	6
List of Tables	13
Introduction	15
Motivation	15
Research objectives	16
Thesis contribution	17
1 Active thermography	20
1.1 Heating exchange: thermal radiation	20
1.2 The infrared thermographic system	27
1.3 Infrared thermography in NDT&E scenery	35
1.4 Pulsed Thermography	36
1.4.1 Data acquisition	36
1.4.2 Theoretical remarks	37
1.4.2.1 Flash thermography	37
1.4.2.2 Stepped&long pulse thermography	42
1.4.3 Data processing	44
1.4.3.1 Slope and Square Correlation Coefficient R^2	44
1.4.3.2 Thermal Signal Reconstruction (TSR®)	46
1.4.3.3 Pulsed Phase Thermography (PPT)	49
1.4.3.4 Principal Component Thermography (PCT)	51
1.4.3.5 Apparent thermal effusivity	52
1.5 Lock-in thermography	53
1.5.1 Data acquisition	53
1.5.2 Theoretical remarks	54
1.5.3 Data processing	55

2	Quantitative data analysis with pulsed thermography	57
2.1	Defect Size Estimation	57
2.1.1	Thermal contrast and its definitions	57
2.1.2	Empirical methods for defect size estimation	58
2.2	Defect Depth Estimation	58
2.2.1	Quantitative Depth Estimation in the Time Domain	58
2.2.2	Quantitative Depth Estimation in the Frequency Domain	60
2.2.3	Influence of the selected sound and defective area	62
2.2.4	Influence of the truncation window size	62
2.2.5	Influence of the frame rate	63
2.2.6	Influence of the pulse duration and the evaluation start	64
2.2.7	Influence of the defect size	65
2.3	Final remarks	66
3	Pulsed thermography: evaluation and quantitative analysis	67
3.1	Materials and methods	67
3.2	Data analysis procedure	68
3.2.1	A new procedure for the identification of the sound and the defective material	71
3.2.2	A “new way” to process the thermographic maps: preliminary results	74
3.3	The influence of the truncation window size: first experimental results	78
3.4	The influence of the truncation window size: a further investigation frame by frame	90
3.5	Results and discussion: by comparing different thermographic algorithms in terms of defect detectability	98
4	By using a calibration approach to estimate defect size and depth	104
4.1	A new procedure to quantify the defects in a material with high diffusivity	105
4.1.1	Theoretical and experimental motivations	105
4.1.2	By using two different set-ups and very different thermographic equipment: two different frame rates and pulse durations	112
4.1.3	Experimental results and validation	114
4.2	The limits of PPT and TSR® methods for a correct depth estimation in aluminum material	120
4.2.1	Influence of the pulse duration	120
4.2.2	Influence of the frame rate	121
4.3	Final remarks	125
5	Case studies	127
5.1	By using pulsed thermography to detect typical defects of Metal Additive Manufacturing process	127
5.1.1	Metal Additive Manufacturing: Laser Powder Bed Fusion (L-PBF) process and its typical defects	127
5.1.2	Materials and methods	129
5.1.3	Theoretical remarks and experimental investigations	134
5.1.4	Pulsed thermographic results by using a flash source	136

5.1.5	Pulsed thermographic results by using a laser source	141
5.1.6	By comparing the achieved results: a quantitative approach	147
5.1.7	Final remarks and future steps	151
5.1.8	Activity acknowledgements	153
5.2	Pulsed Phase Thermography Approach for the Characterization of Delaminations in CFRP and Comparison to Phased Array Ultrasonic Testing	153
5.2.1	Materials and methods	153
5.2.1.1	Samples	154
5.2.1.2	Ultrasonic testing equipment	155
5.2.1.3	Thermographic set-up	157
5.2.2	By using Pulsed Phase Thermography to estimate depth delaminations	158
5.2.3	A comparison between the ultrasonic and PPT results in terms of depth estimation	161
5.2.4	Some final considerations	166
5.3	A new thermographic procedure for the non-destructive evaluation of RSW joints	167
5.3.1	Materials and methods	168
5.3.2	The problem of emissivity variation and its influence on thermographic analysis	171
5.3.3	A new procedure to emissivity compensation	172
5.3.4	The proposed thermographic procedure in order to characterize the joint quality by avoiding the emissivity compensation	173
5.3.5	By using thermographic technique and relative thermal indices to control RSW process	176
5.3.6	Some final considerations and future steps	181
5.4	A thermographic procedure for the measurement of the tungsten carbide coating thickness	182
5.4.1	Materials and methods	183
5.4.2	The limits of well-established methods (apparent thermal effusivity and TSR®) for estimating metal coating thickness	186
5.4.3	By using slope algorithm and a calibration procedure to the thickness coating estimation	189
5.4.4	Final remarks	194
6	Conclusions and future developments	196
	Bibliography	198
	Appendix A: IR cameras and energy sources specifications	213
	Appendix B: Matlab® Code	219
	Acknowledgements	223

List of Figures

1.1	The electromagnetic spectrum.	21
1.2	Planck distribution for different representative temperatures.	23
1.3	Emissivity and relative emitted energy for black, gray and real body, a schematization.	24
1.4	Stefan–Boltzmann law: power radiated by a grey body with different emissivities.	25
1.5	Surface effects illumination.	26
1.6	Atmosferic transmission of IR Wavelengths.	28
1.7	The schematization of an IR thermal imaging system.	28
1.8	Basic components of a thermal imaging system.	31
1.9	IR detector technology; type of sensors and wavelength.	33
1.10	Illustration of field of view (FOV) and instantaneous field of view (IFOV).	34
1.11	Experimental configuration in active thermography in reflection and transmission mode.	37
1.12	Thermal behavior after a pulsed test: finite body and diameter influence models.	40
1.13	Temperature trend over time for a pulsed test in transmission mode Eq. 1.24.	41
1.14	Typical trend of rear surface temperature history after a transmission test: Parker method.	42
1.15	Temperature trend in defect and sound area, Stepped approach and Long Pulsed approach	43
1.16	Temperature cooling down after a Dirac pulse: theoretical trends for sound and defect area in a double log scale.	45
1.17	Log–log graph of the cooling phase: R^2 and m values assessed for different defects and relative sound (square wave, modulation period 240 s) [87].	46
1.18	Defect detection by the TSR® method, logarithmic polynomial fitting and derivation [20].	47
1.19	Temperature (a) , (b) 1^{st} , and (c) 2^{nd} time derivatives for a generic defective and sound area, after a flash test [127].	48
1.20	Similarities of the thermograms and logarithmic derivatives in the case of a slab of thickness L submitted to pulse- (a) and step- (b) heating. Same results would be observed for an infinite thermal resistance defect embedded at a depth $z_d = L$ in a semi-infinite medium or in a slab. The graphs show the ‘precession’ 2 of the early detection due to the successive differentiation [76].	48
1.21	Data acquisition and processing by PPT [127].	50
1.22	Thermographic data conversion from a 3D sequence to a 2D A matrix in order to apply SVD and finally conversion of 2D U matrix into a 3D matrix containing the EOFs [20].	52
1.23	Influence of a thickness variation (from 100 μm to 300 μm) and an adhesion defect (50 μm of air under a 300 μm coating) on the apparent effusivity curve [84].	53

1.24	Experimental set-up for lock-in thermography (reflection mode).	54
1.25	Four point methodology for amplitude and phase delay estimation by lock-in thermography.	55
2.1	Contrast curve (blue) and second derivative (orange) of a flat bottom hole in stainless steel (depth 0.12", diameter 1"). The second derivative peak occurs significantly earlier than the peak contrast time [56].	60
2.2	Depth quantification with the phase contrast and blind frequency.	61
2.3	Influence of the size of the truncation window on phase for a 1 mm depth flat-bottomed hole on a Plexiglas® at $f_s=22.55$ Hz, $\Delta t=889$ ms; temperature profile [167].	63
2.4	The influence of the truncation window size on the phase contrast: decreasing $w(t)$ diminishes frequency resolution [167].	63
3.1	Aluminum sample with simulated defects used for thermographic tests; the nominal sizes of the sample and the defects are expressed in mm.	68
3.2	The used set-up for the thermographic pulsed tests.	68
3.3	The effects of the normalization related to the first frame after the flash excitation; (a) before normalization, first and second frames; (b) after normalization, first and second frames.	69
3.4	The effects of the application of a Gaussian filter, contrast related to the 2 nd principal component result, by considering the defect with a diameter of 12 mm and a depth of 1 mm; maps and related trends.	70
3.5	An example of obtained results: the slope signal after only 16 frames of analysis; (a) 2D map, (b) surface map.	71
3.6	An example of "sign change"; second derivative (TSR®), frame 40, 2D maps and relative surfaces; (a) positive sign, (b) negative sign.	72
3.7	An example of the sound individuation by "std method": the trend of standard deviation (2 nd principal component map, defect with diameter 16 mm and depth 1 mm).	73
3.8	An example of the confront between the "standard deviation" method and the "contrast full-width at half-maximum (semi-contrast)" one for evaluating the sound material; the normalized contrast by considering the result related to the 2 nd principal component.	74
3.9	Phase and phase contrast trends by considering a defect and the relative sound as example.	75
3.10	The trend of the phase contrast as a function of the frequency, defects at 1mm depth; an application of the "std-method" when a sequence of maps is considered.	76
3.11	Comparison among the several algorithms in terms of maximum normalized contrast; single trends.	76
3.12	Comparison among the several algorithms in terms of maximum normalized contrast; final maps, (a) PCT, (b) PPT, phase, (c) R^2 , (d) slope, (e) TSR®, polynomial, (f) TSR®, 1 st derivative (g) TSR®, 2 nd derivative (truncation window size: 256 frames, 128 seconds).	77
3.13	Comparison among the several algorithms in terms of depth (a) and size (b) of detected defects.	78
3.14	SBC values for the Slope algorithm and for different truncation window sizes; (a) 16 frames-0.08 s, 32 frames-0.16 s, 64 frames-0.32 s, 128 frames-0.68 s, 256 frames-1.28 s, 512 frames-2.56 s, 1024 frames-5.12 s.	79
3.15	Comparison among the different algorithms in terms of the detected defects number for each analysis interval in a bar plot.	80

3.16 Comparison of different algorithms in terms of maximum SBC.	81
3.17 Comparison of different algorithms in terms of maximum SBC: a particular zoom for the smaller defects.	81
3.18 SBC versus r for TSR® 1 st derivative 1024 frames, error bars and confidence bounds on the found linear model.	83
3.19 SBC versus r for TSR® 2 nd derivative 256 frames, error bands and confidence bounds on the found linear model.	83
3.20 SBC versus r for PPT (phase) 128 frames, error bands and confidence bounds on the found linear model.	84
3.21 SBC versus r for PPT (amplitude) 512 frames, error bands and confidence bounds on the found linear model.	84
3.22 SBC versus r for PCT (2 nd principal component) 1024 frames, error bands and confidence bounds on the found linear model.	85
3.23 SBC versus r for R^2 512 frames, error bands and confidence bounds on the found linear model. . . .	85
3.24 SBC versus r for slope 1024 frames, error bands and confidence bounds on the found linear model. .	86
3.25 Slope contrast vs frames number; (a) diameter 16 mm (b) diameter 12 mm (c) diameter 8 mm (d) diameter 4 mm (fixed depth).	87
3.26 R^2 contrast vs frames number; (a) diameter 16 mm (b) diameter 12 mm (c) diameter 8 mm (d) diameter 4 mm (fixed depth).	88
3.27 Slope contrast vs frames number; (a) depth 1 mm (b) depth 2 mm (c) depth 3 mm (d) depth 4 mm (e) depth 5 mm (fixed diameter).	89
3.28 R^2 contrast vs frames number; (a) depth 1 mm (b) depth 2 mm (c) depth 3 mm (d) depth 4 mm (e) depth 5 mm (fixed diameter).	90
3.29 Slope contrast frame by frame.	91
3.30 R^2 contrast frame by frame.	92
3.31 TSR® 1 st derivative contrast over the time (10 s of analysis).	92
3.32 TSR® 2 nd derivative contrast over the time (10 s of analysis).	93
3.33 PPT phase contrast over the time (10 s of analysis).	93
3.34 Slope contrast frame by frame: a zoom to underline the change of sign with the depth and defect size; (a) depth 3 mm (a_1) zoom depth 3 mm, (b) depth 4 mm (b_1) zoom depth 4 mm.	94
3.35 Slope overview; linear correlation SBC vs. r (R^2 index), detected defect number and weighted SBC, an analysis frame by frame.	95
3.36 R^2 overview; linear correlation SBC vs. r (R^2 index), detected defect number and weighted SBC during the entire observation time, an analysis frame by frame.	96
3.37 1 st derivative (TSR®) overview; linear correlation SBC vs. r (R^2 index), detected defect number and weighted SBC during the entire observation time.	96
3.38 2 nd derivative (TSR®) overview; linear correlation SBC vs. r (R^2 index), detected defect number and weighted SBC during the entire observation time.	97
3.39 Phase overview; linear correlation SBC vs. r (R^2 index), detected defect number and weighted SBC during the entire observation time.	97

3.40	Best maps for each algorithm of analysis by considering the truncation window size for which the greatest number of defects were detected.	99
3.41	A comparison among different post processing algorithms after only 0.14s of analysis.	101
3.42	Thermographic maps related to the first column of the Tab. 3.5: (a) 1 st derivative TSR®, (b) 2 nd derivative TSR®, (c) slope, (d) R^2 , (e) phase (PPT).	102
4.1	Thermal trends (a), Slope trends (b) and the relative slope contrast over the time (c) for a defect and relative sound (diameter 12 mm, depth 2 mm).	106
4.2	Comparison between simulated (a) and experimental slope contrast (b) for different aspect ratios; depth 3 mm.	106
4.3	Correlation between slope contrasts and relative defect aspect ratios for different truncation window sizes, chosen as example (1 second-200 frames (a), 2 seconds-400 frames (b), about 9 seconds-1845 frames (c)).	107
4.4	simulated (a) and experimental linearity (b) between the defect aspect ratios and the relative slope contrasts.	108
4.5	Experimental delta temperature over time (expressed as frames number) related to the sound regions highlighted in red in a thermographic map showed as example (double log-scales).	109
4.6	Thermal defect trends (a) and relative contrasts (b) for a finite body.	110
4.7	Simulated (a, semi-infinite body and b, finite body) and experimental slope contrast (c) for different aspect ratios; depth 3 mm.	111
4.8	Simulated and experimental linear correlation between the defect aspect ratios and the relative slope contrasts: a comparison between Almond 2D model-semi-infinite body, Almond 2D-finite body model and experimental one.	111
4.9	Experimental slope results shown in terms of mean and standard deviation for the considered sound area.	112
4.10	Aluminum sample with simulated defects (nominal sizes and depths) used for thermographic tests.	113
4.11	The used set-up for the comparative thermographic pulsed tests.	114
4.12	Slope results after an analysis interval of 2.15 seconds: linear correlation between defect slope contrasts and relative aspect ratios and corresponding slope map (1 test).	115
4.13	Mean calibration curve (aspect ratio vs. slope contrast) and relative replication results (3 tests).	116
4.14	Calibration curve (aspect ratio vs. slope contrast) with the estimated regression line (linear model), the prediction bounds (external curves) and the 95% confidence bounds.	117
4.15	Defect size estimation by using the semi contrast method (an example of the obtained results by considering the underline defect and the relative sound).	118
4.16	Second derivative trends (defect size 6 mm, depth 2 mm). Set-up showed in Fig. 3.2.	120
4.17	Second derivative trends (defect size 6 mm, depth 2 mm). Set-up showed in Fig. 4.11 (200 Hz).	121
4.18	Second derivative trends (defect size 12 mm, different depth 1-5 mm). Set up showed in Fig. 4.11 (200 Hz).	122
4.19	Defect main parameters vs Time second derivative peak; set up showed in Fig.3 with a low frame rate 200 Hz (a) and 1000 Hz (b).	123
4.20	TSR® second derivative trends for the defects chosen as validation data set (truncation window size 0.5 seconds).	123

4.21	Phase contrast trends; set up showed in Fig. 3.2 (3 kJ).	124
4.22	Phase contrast trends; set up showed in Fig. 4.11 (24 kJ).	125
5.1	Typical defects in Metal Additive Manufacturing process.	128
5.2	SLM Solutions Group AG, Type 280 HL.	129
5.3	Some of the tested samples.	132
5.4	Pulsed thermographic set-up with 4 flash lamps.	133
5.5	Pulsed thermographic set-up with a widened laser beam.	134
5.6	The comparison of numerical simulation with different values of λ , where other parameters are shown in Tab. 1.2 for a steel 316 L, $Q=6400 J/m^2$, $f=1000$ Hz.	135
5.7	Data fitting with a polynomial of 5 degree and analysis of the relative first derivative for different truncation window sizes (time intervals); thermographic maps corresponding to the maximum reached SBC by considering the sound region highlighted in a black square.	137
5.8	A comparison between the sample PK007 (keyhole defects) and PK010 (lack of fusion defects); maps related to the maximum achieved SBC, TSR® algorithm, analysis of the first and second derivative for different time intervals.	138
5.9	A comparison among the samples PK008, PK009 and PK010, lack of fusion defects at different depths; the maximum SBC, analysis of the second derivative sequences.	139
5.10	A comparison among the samples PK001-PK004, with defects at different depths and heights, produced by a gap during the laser illumination.	140
5.11	Raw thermal data by using a laser source, power 550 W, period of 500 ms, PK007.	141
5.12	PK007, 1000 ms, 500 W, stepped and long pulse analysis; slope, intercept and R^2 (linear fitting of 500 frames)	142
5.13	Influence of the laser pulse duration, by analyzing the same parameter at the same laser power (500 W); stepped analysis.	143
5.14	Influence of the laser pulse duration, by analyzing the same parameter at the same laser power (500 W); long pulse analysis.	143
5.15	Influence of the laser power, same laser duration (500ms), long pulse analysis.	144
5.16	A comparison between the sample PK007 (keyhole defects) and PK010 (lack of fusion defects).	145
5.17	A comparison among the samples PK008, PK009 and PK010, lack of fusion defects at different depths; the maximum SBC.	146
5.18	A comparison between the samples PK003 and PK004, with defects at different depths and heights, produced by a gap during the laser illumination.	147
5.19	By comparing the different solution in terms of used set-up, sample PK007, size estimation, (a) flash set-up, (b) laser set-up.	148
5.20	Transmission set-up by using a flash source.	149
5.21	Transmission set-up by using a laser source.	149
5.22	By comparing the different solution in terms of used set-up, sample PK007, depth estimation.	150
5.23	The influence of the truncation window size on the slope and R^2 algorithms, long pulse analysis; (a) slope map, frame 329, 0.658 s, (b) R^2 map, frame 75, 0.15 s (c) R^2 map, frame 1000, 2 s, maps taking in correspondence of the maximum SBC	152

5.24 SBC phase map $f=0.4883$ Hz (positive) , SBC phase map $f=7.8125$ Hz (negative), SBC PCT map, frame 672, 1.34 s, Gaussian filter std=1.	152
5.25 Lateral (a) and top (b) view of analyzed component.	155
5.26 Ultrasonic set up (a) and a particular of the probe and its support (b).	155
5.27 Visualization in the A-Scan, B-Scan, C-Scan mode of the entire stringer (a) and one of its extremities (b).	157
5.28 Set-up used for PPT acquisition (lamp angle 30° , sample-camera 900 mm, sample-flash lamps 150 mm)	158
5.29 Depth and frequency relation (PPT algorithm).	159
5.30 Comparison between ultrasonic and thermographic map at different depths; sound sector 13. a 0.9–1.2 mm/0.3916 Hz; b 0.6–0.9 mm/0.7812 Hz; c 0.3–0.6 mm/1.1718 Hz; d 0–0.3 mm/1.5612 Hz. . .	160
5.31 Comparison between ultrasonic and thermographic map at different depths; defective sector 1. a 0.9–1.2 mm/0.3916 Hz; b 0.6–0.9 mm/0.7812 Hz; c 0.3–0.6 mm/1.1718 Hz; d 0–0.3 mm/1.5612 Hz. .	161
5.32 Phase and phase contrast trends for a defect chosen as an example.	162
5.33 A scheme of the procedure used to get contrast phase maps for a real sample.	163
5.34 Matching thermographic maps-a frequency example (3.906 Hz).	164
5.35 Blind frequencies (BF) and maximum phase contrast (MPC) maps for the defected sectors. (a) sector 1, (b) sector 14	164
5.36 Map scanned along the entire depth-threshold value set at 60% of the peak amplitude, sector 1. . . .	165
5.37 Map scanned along the entire depth-threshold value set at 60% of the peak amplitude, sector 14. . .	165
5.38 Specimens investigated and cross section of the welded area; (a) specimen 2, stick weld, (b) specimen 3, material expulsion, (c) specimen 5, correct parameters.	169
5.39 Experimental transmission set-up adopted for thermographic tests.	170
5.40 Laser set-up adopted for experimental reflection tests (a), with a particular detail (b).	170
5.41 Emissivity compensation: (a) hot frame, (b) cold frame, (c) emissivity map.	172
5.42 The final result of emissivity compensation; long pulse analysis by using slope algorithm, laser excitation of 500 ms.	173
5.43 Temperature trend over time for a pulsed test in transmission mode (Eq. 1.24), steel material. . . .	174
5.44 Comparison among the mean values of temperature over time for the investigated specimens, after the flash test in transmission configuration.	175
5.45 Comparison among the mean value of temperature over time for the specimen 3, after the move mean filter and data fitting.	176
5.46 Results in terms of 2D maps for each index.	177
5.47 Results obtained for the examined specimens, by considering the index t_{min}	178
5.48 Micro graphs in correspondence of the nuggets; in order from upwards to below: specimen 2 (stick weld), specimen 5 (the one taking as reference, with in red circle the weld zone), specimen 3 (material expulsion).	179
5.49 Correlation among the thermographic indexes and the process parameters ($I*t_c$), transmission set-up: (a) coefficient d versus $I*t_c$, (b) t_{min} versus $I*t_c$	180

5.50	Correlation among the thermographic indexes and the process parameters ($I * t_c$), reflection configuration and laser spot source (cooling down-long pulse analysis): (a) slope versus $I * t_c$ before emissivity compensation, (b) t_{min} versus $I * t_c$ after emissivity compensation.	180
5.51	Picture of one of the reference-coated samples.	184
5.52	Pulsed Infrared thermography set-up.	185
5.53	Laser setup to perform “long pulse” tests.	186
5.54	Mean temperature decay trends observed for the first 700 frame of the cooling stage for all the specimens.	187
5.55	Influence of a thickness variation of the coating (from 1,00E-01 mm to 10,10E-01 mm) on the apparent effusivity profiles.	188
5.56	Influence of a thickness variation of the coating (from 1,00E-01 mm to 10,10E-01 mm) on the 1 st derivative (TSR®) trends.	189
5.57	Mean temperature decay by considering the pixel with maximum temperature value and relative error bars on 5 replications; training data set.	190
5.58	Mean temperature decay by considering the pixel with maximum temperature value and relative error bars on 5 replications; validation data set.	191
5.59	Data dispersion plot (thickness vs slope) with the estimated regression line (linear model), the prediction bounds (external curves) and the 95% confidence bounds.	192
5.60	Data dispersion plot (thickness vs slope) with the estimated regression line (second order polynomial model), the prediction bounds (external curves) and the 95% confidence bounds.	192
1	IR camera FLIR X6540 SC	213
2	Layout of Camera Infratec ImageIR.	215
3	Lamp Hensel EH Pro 6000.	215
4	Scheme and components for square wave pulse generation: pulse and function generator.	218
5	FLIR SC655.	219

List of Tables

1.1	Emissivity values for different materials (real surfaces).	27
1.2	Main materials thermal properties database.	30
3.1	Slope algorithm: evaluation of the SBC-r correlation for different analysis intervals and relative defect number.	79
3.2	The weighted SBC value for each algorithm obtained with Eq. 1.56.	82
3.3	Comparison among the different algorithms in terms of the linear correlation between SBC and r. . .	86
3.4	Final comparison among the different algorithms.	99
3.5	Maximum detected defect number and minimum aspect ratio with the relative time interval necessary.	100
3.6	Compromise choice by highlighting the best truncation window size that allows to have the maximum detected defect number with a good weighted contrast and a good linearity.	100
4.1	% errors on the mean value in terms of aspect ratio, size and depth by using the mean calibration curve (3 replications in both cases).	119
4.2	% errors in terms of size and depth by using the calibration curve after only a single measurement. .	119
5.1	PK001-PK004 defects geometry in terms of size and height.	130
5.2	PK005-PK016 defects sizes.	131
5.3	PK001-PK016 defects characteristics in terms of depth, height and energy.	132
5.4	Thermographic parameters and set-up distances for pulsed flash thermography.	133
5.5	Thermographic parameters and set-up distances for pulsed laser thermography.	134
5.6	Influence of the laser power, same laser duration (500ms), long pulse analysis, maximum achieved SBC.	144
5.7	By comparing the different solution in terms of used set-up, sample PK007, maximum SBC	148
5.8	Thermographic parameters and set-up distances for pulsed flash thermography.	149
5.9	Thermographic parameters and set-up distances for pulsed flash thermography.	149
5.10	Process parameters used for obtaining the RSW joints.	169
5.11	Results obtained for each thermal index in terms of mean and standard deviation values.	178
5.12	Thicknesses of WC-Co-Cr coatings.	184
5.13	Thermophysical data properties of WC-Co-Cr coatings and steel substrate [2].	184
5.14	Slope values related to validation samples and 95% confidence bounds on them.	193

5.15	Expected values of the thickness by using the models accompanied by their accuracy and precision with respect to the nominal values.	193
5.16	Expected values of the thickness by using the models accompanied by their accuracy with respect to the nominal values if single measurements are carried out.	194
1	FLIR X6540 SC	213
2	Technical Specification FLIR SC655.	219

Introduction

Motivation

The structural integrity of materials, components and structures has to be assessed for quality control, safety regulations and product specifications. Numerous testing techniques have been developed for maintenance and condition monitoring. These techniques can be categorised into two main classes: destructive testing, based on fracture mechanics, and non-destructive testing, which leaves the inspected component undamaged. The most commonly used NDT methods in industry include visual inspection, liquid penetrant inspection, magnetic particle inspection, eddy current testing, ultrasonic testing, radiography and thermography [1, 2]. Non-destructive testing (NDT) are characterized to be low cost, safe, fast and not dangerous tests to control a lot of applications and final components.

Moreover, the material, the processes, and the new applications are constantly evolving hence the destructive and non-destructive techniques should be adaptable and versatile, as well [3, 4, 5].

Among the several NDT techniques, that are used in all industrial fields nowadays, Infrared Thermography (IT) stands out as a very useful control for non-contact, fast and full-field inspection. It is based on the analysis of a temperature response at the sample surface when an external stimulation source is applied to induce a difference in temperature between a defect and the relative sound zone. This is known as the active approach in IT. An active thermographic inspection requires two basic components: a thermal sensor, typically an infrared thermal camera and an external source to heat the tested component [5].

Mainly, there are two different thermographic techniques [5]: Pulsed Thermography and Lock-in Thermography.

Pulsed Thermography is known as a technique performed in a non-stationary regime by using a flash or a laser source to stimulate the component with a pulse of a certain duration. It is fast and simple (when compared with the Lock-in), but defect characterization in terms of defect depth, size and thermal properties evaluation is complex because, basically, it requires suitable procedures of data processing of raw thermal data [5, 6, 7]. In this regard, several algorithms have been developed to improve the thermal contrast and to develop a quantitative thermographic analysis, such as the Pulsed Phase Thermography (PPT) [8, 9, 10] and the Thermal Signal Reconstruction (TSR®) [11, 12, 13]. The principles of both methods are well known and based on the one-dimensional model of the heat conduction equation from which the information about the defect depth can be obtained. Basically, the TSR® algorithm analyzes the measured thermographic data in the time domain, by an accurate investigation of the first and second derivative of the thermal sequences. A polynomial fitting in a double logarithmic scale allows for improving the quality of data, as proposed for the first time by Shepard [11, 12]. The PPT algorithm, instead, evaluates the cooling thermal behavior in the frequency domain, by means of the Fast Fourier Transformation (FFT) of the acquired signal. These algorithms provide very good results, especially in the evaluation of defects in composite materials [14, 15].

Even if several works talk about the possibility to use these thermographic techniques for defect detection, few of these show a quantitative approach, mainly when materials with high diffusivity are considered.

Indeed, for this type of material, the limits are primarily due to the very high speed of the thermal phenomena that require very high sample rates to acquire data in the first part of the cooling trend. This latter contains very useful information about defects and it is very important for size and depth estimation. Another important issue regards the pulse duration. Flash lamps are characterized by a pulse duration of 3-5 ms that can be considered short for low diffusivity materials such as composite, but it is long for high diffusivity materials. In the latter case, the thermal phenomena can occur during the heating pulse (shallow defects) and then no quantitative information about defects can be retrieved investigating the cooling behavior [16, 17, 18, 19, 20, 21].

Besides, Thermography has a number of approaches differing in terms of experiment set-up, thermographic technique applied and the way in which the collected data are processed. Infrared thermography is highly dependent on the sensor selection and the experimental set-up adopted. Adequate setup and testing procedures are necessary to avoid questionable results in the thermographic investigation. Pre and post-processing parameters have to be selected carefully according to the investigated application, to provide useful quantitative information.

Research objectives

The main objective of this research is to develop new quantitative procedures for defect characterization and, more in general for ensuring quality requirements in different applications, by starting from an accurate analysis of a sample with known imposed defects or a quality standard (such a sample with particular properties, characteristic or geometry) in order to calibrate the same procedure. After a correct calibration with standard samples and references, it is possible to move on the analysis of a real component or case study in order to detect and to quantify the defects, or more in general to provide quantitative information about the studied application.

In order to complete this task, a series of specific features are studied and can be stated as follow:

- Examining the fundamental concepts based on Active Thermography, in terms of physics of thermal radiation and body emissivity (Chapter 1).
- Reviewing the fundamental thermophysical principles behind Pulsed Thermography, with particular attention to the post-processing algorithms and the quantitative analysis (Chapter 1, section 4).
- Assessing the influence of different parameters, such as sound area location, material's thermal properties, oversampling, time and frequency resolution on quantitative results (Chapter 2).
- Studying the influence of the truncation window size when a post-processing analysis involved the raw thermal data (Chapter 3, section 3).
- Showing the defect detectability after a pulsed test by using different post-processing algorithms in an aluminum sample with imposed defects (Chapter 3, section 4).
- Explaining the necessity to use different post-processing algorithms, showing their strengths and weaknesses (Chapter 3, section 4).
- Developing a new procedure to have an estimation of defect depth and size, starting from the experimental and simulated evidence that exists a linear correlation between defects aspect ratio (diameter/depth) (Chapter 4, section 1.1).

- Showing the limits of the classical well-known methods based on one dimensional models such as blind frequency and second derivative peak in the depth estimation when defects inside a material with a very high diffusivity are examined (Chapter 4, section 2).
- Providing an offline and quantitative control of very advanced and nowadays industrial applications such as the Laser-Powder Bed Fusion process (L-PBF) and its typical defects (Chapter 5, section 1)
- Using the ultrasonic technique as standard to estimate the depth of very small delaminations in real component made in composite materials and to make a correlation with the Pulsed Phase Thermographic results expressed in terms of blind frequencies (Chapter 5, section 2).
- Proposing a new thermographic procedure to control the quality of thin welded joints produced by Resistance Spot Welding process (RSW) (Chapter 5, section 3), and for estimating the thickness coating when both the materials are steels with very similar thermophysical properties and to show the limits of the classical methods (Chapter 5, section 4).

Thesis contribution

This thesis is organized into 6 main chapters and sees the contribution of different works and organizations.

In Chapter 1, the place of IT in the NDT&E scenario is firstly described. Some experimental concepts, such as data acquisition, defect detection and the main problems that come from non-uniform heating by using active thermography are discussed, together with the basic theories of the main post-processing algorithms, used in literature to process raw thermal data. The main models of heat transmission, with particular attention to Almond models, are summarized, in order to show the thermophysical phenomena involved within a pulsed test. The theoretical bases to do a quantitative analysis by using Thermography as a non-destructive technique are investigated and described in Chapter 2, together with some methodologies already developed for estimating the depth and size of defects.

Chapter 3 and 4 move on different previous conference and journal publications, that provide a full quantitative analysis of an aluminum sample with different flat bottom holes.

1. D'Accardi, E., Palumbo, D., Tamborrino, R., & Galietti, U. (2018). Quantitative analysis of thermographic data through different algorithms. *Procedia Structural Integrity*, 8, 354-367.
2. D'Accardi, E., Palumbo, D., Tamborrino, R., Cavallo, P., & Galietti, U. (2018). Pulsed Thermography: Evaluation and quantitative analysis of defects through different post-processing algorithms. In *Proceedings of the Conference QIRT*.
3. D'Accardi, E., Palumbo, D., Tamborrino, R., & Galietti, U. (2018). A quantitative comparison among different algorithms for defects detection on aluminum with the pulsed thermography technique. *Metals*, 8(10), 859.
4. D'Accardi, E., Palumbo, D., Tamborrino, R., & Galietti, U. (2019, May). The influence of the truncation window size on the quantitative thermographic results after a pulsed test on an aluminum sample: comparison among different post-processing algorithms. In *Thermosense: Thermal Infrared Applications XLI* (Vol. 11004, p. 110040M). International Society for Optics and Photonics.

5. D'Accardi E., Palumbo D., Galietti U. By quantifying defects in high diffusivity materials: a new procedure and a comparison with well-established models, submitted for publication.

Different case studies are in Chapter 5; the pulsed thermography is used to provide quantitative information in different new and widespread applications.

For the first time, this type of non-destructive technique is used to detect typical defects generated during a Metal Additive Manufacturing Process, known as the Laser-Powder Bed Fusion process (L-PBF) or most commonly as Selective Laser Melting (SLM). Different components in steel AISI 316L are produced with imposed defects, generated during the same process by changing the laser parameters, increasing and decreasing the energy density; in this way, defects in keyhole mode and for lack of fusion are generated. Different pulsed tests are performed in order to study the thermal behavior of this new type of defects, by involving different energy sources (laser and flash lamps) and infrared cameras at different wavelengths. The samples used for these experiments are provided within the BAM project ProMoAM thanks for cooperation of Gunther Mohr and Kai Hilgenberg, instead the thermographic experiments are performed during the abroad visiting research period in the same BAM institute (Bundesanstalt für Materialforschung und -prüfung (BAM), Unter den Eichen 87, 12205 Berlin, Germany), thanks to the contribution of the Division 8.7-Thermographic Methods and the collaboration of Dr. rer. nat. Christiane Maierhofer and Dr. Simon J. Altenburg.

A part of the work done during my visiting Ph.D. student period is included in a conference work:

D'Accardi, E., Altenburg, S., Maierhofer, C., Palumbo, D., & Galietti, U. (2019). Detection of Typical Metal Additive Manufacturing Defects by the Application of Thermographic Techniques. In Multidisciplinary Digital Publishing Institute Proceedings (Vol. 27, No. 1, p. 24).

Another important part of this dissertation regards the capability of PPT algorithm in estimating delamination depths in CFRP components used in aeronautics. The investigated component has a non-uniform geometry and the defects inside have been generated during the production process. The specimen has been investigated through the application of both the ultrasonic technique and the thermographic one. Thermographic phase images elaborated with suitable computational processing have been compared with Ultrasonic C-scan images; the ultrasonic technique has been used to validate the PPT results in terms of defect depth estimation.

This work was supported by the DiTECO project (Defects, damage, and repair techniques in the production processes of large structures in composite - PON3 Axis I Title III) funded by MIUR and the Ultrasonic tests and results were carried out thanks to the contribution of the Italian research center ENEA (ENEA C.R. CASACCIA, Via Anguillarese, 301 - S.Maria di Galeria, Rome, Italy), in particular with the collaboration of Dr. Fania Palano.

Some results are already published within a journal work:

D'Accardi, E., Palano, F., Tamborrino, R., Palumbo, D., Tatì, A., Terzi, R., & Galietti, U. (2019). Pulsed Phase Thermography Approach for the Characterization of Delaminations in CFRP and Comparison to Phased Array Ultrasonic Testing. *Journal of Nondestructive Evaluation*, 38(1), 20.

An important aim of this dissertation is to propose new thermographic procedures for the offline control of components and evaluating their quality in order to optimize manufacturing processes.

In this regard, a new procedure is proposed with the application of the pulsed thermography for the quality control of RSW thin welded joints. The used welded joints were produced within the project “CAMPUS Manufacturing”. Visual inspections by using micrographs were carried out in the lab “Metallography and Microscopy Laboratory” of Polytechnic of Bari, thanks to Prof. Ing. Gianfranco Palumbo and Ing. Pasquale Lino Guglielmi, and show results in agreement with the thermographic one (Chapter 5, section 3).

An important part of the activities done within this project is described in the work:

Palumbo, D., D’Accardi, E., & Galietti, U. (2019, May). A new thermographic procedure for the non-destructive evaluation of RSW joints. In *Thermosense: Thermal Infrared Applications XLI* (Vol. 11004, p. 110040N). International Society for Optics and Photonics.

The aim of the last part within the Chapter 5, section 4, is to propose a calibration procedure, very similar to the one carried out for the flat bottom holes of the aluminum sample (Chapter 4, section 1), to evaluate the thickness of coatings in WC-CoCr. In this way, the versatility of the used approach is again confirmed. In the same section, the limits of the classical algorithms, usually used for this type of application, (second derivative and apparent thermal effusivity) are described, especially in the case of too thin or too thick coatings and for two materials with very close thermophysical properties.

This part contains the following contribution:

Tamborrino, R., D’Accardi, E., Palumbo, D., & Galietti, U. (2019). A thermographic procedure for the measurement of the tungsten carbide coating thickness. *Infrared Physics & Technology*, 98, 114-120.

Chapter 1

Active thermography

1.1 Heating exchange: thermal radiation

The common opinion of the concept of ‘Heat Transfer’ is that shows the energy interaction that occurs solely due to the temperature difference between a system and its surroundings, in the presence or absence of an intervening medium “source”. In general, the term Heat Transfer can refer also to the different modes of energy exchange: conduction, convection and radiation.

Conduction occurs when thermal energy is passed from atom to atom through the inter-atomic forces which tend to maintain the inter atomic spacing [22, 23, 24, 25, 26]. The conduction heat transfer, described by Fourier’s law of heat diffusion, states that the local heat flux $\dot{Q}_{cond}[W/m^2]$ can be related to the local temperature gradient $\nabla T[^\circ C/m]$ with a proportional relation through $k[W/m^\circ C]$ which is the thermal conductivity. The conduction heat transfer equation is:

$$\dot{Q}_{cond} = -k\nabla T \quad (1.1)$$

The minus sign indicates the spontaneous heat transfer occurring between higher to lower temperatures, or down the temperature gradient, according to the Second Law of Thermodynamics. Here, the physical phenomena sees the presence of a medium transfer without any flow of the medium. In particular, in a metal solid, thermal energy is transferred through the vibration and collision of particles, due to the presence of free electrons, and it is also spread through electron diffusion.

Convection heat transfer requires the presence of an intervening physical medium between the investigated system object and its surroundings. In this case, the medium is the fluid that flows between the system being heated/cooled and its surroundings. Mathematically, this phenomena is governed by the following Newton’s law:

$$\dot{Q}_{conv} = h(T_s - T_f) \quad (1.2)$$

Here, the investigated physical concept shows that the heat flux from a surface at $T_s[^\circ C]$ temperature to a surrounding fluid, whose temperature far from the surface is $T_\infty[^\circ C]$, is proportional to temperature difference $T_s - T_f$, where T_f is the fluid temperature and h is the heat transfer coefficient $[W/m^2^\circ C]$ [22, 24].

Theory on Radiation is the result of over 40 years of research contributions from many dedicated scientists

starting with Kirchhoff's enouncement of his law in 1859 and his black body definition in 1860, followed by the work of Stefan (1879) and Boltzmann (1884); and Wien in 1893; among others, and that culminated with the enouncement of Planck's law in 1900. He proposed a mathematical solution to characterize the radiant energy distribution over the entire frequency spectra; in this regard, the radiation can be viewed either as the transportation of tiny particles called photons or quanta, or as the propagation of electromagnetic waves. Then, the radiation is the transfer of thermal energy in the form of electromagnetic waves, and in this case, there is not the aid of a medium: solar energy, X-rays, Cosmic rays are clear examples on how energy propagates by means of radiation. A schematic representation of the electromagnetic spectrum is provided by Fig. 1.1.

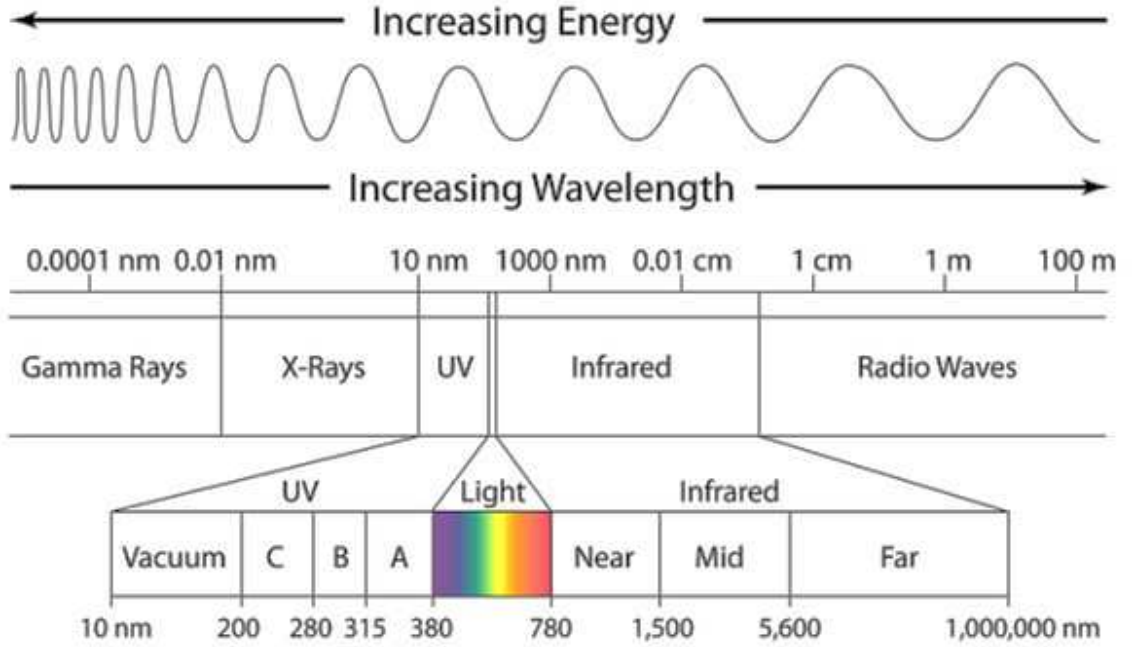


Figure 1.1: The electromagnetic spectrum.

Basically, the amount of radiated energy by a photon E , is correlated to the corresponding wavelength λ , or frequency f , of an electromagnetic wave, through the following equation:

$$E = hf = \frac{hc}{\lambda} \quad (1.3)$$

where h is the Planck's constant ($6.6237 \times 10^{-34} Js$) and c ($2.9979 \times 10^8 m/s$) is the light speed in the medium through which the light is passing. Eq. 1.3 establishes that radiation has dual wave-particle nature, in some cases it is convenient to consider that light propagates as a stream of energy packets (photons), in other cases it is convenient to refer to light as an electromagnetic wave. The dual wave-particle nature of radiation represents, as well, the basis of Einstein's theory of Relativity [25]. From this Eq. 1.3, the relationship between frequency and wavelength can be obtained:

$$f = \frac{c}{\lambda} \quad (1.4)$$

Radiation in the Electromagnetic Spectrum is often categorized by wavelength. Short wavelength radiation is of the highest energy and can be very dangerous - Gamma, X-rays and ultraviolet are examples of short wavelength radiation. Longer wavelength radiation is of lower energy and is usually less harmful - examples include radio, microwaves and infrared. Although infrared radiation is not visible, humans can sense it as heat. The infrared part of the spectrum (0.74 - 1000 μm) can be further subdivided into five parts: Near Infrared (NIR) from 0.74 to 1 μm ; Short Wavelength Infrared (MIR) from 1 to 3 μm ; Medium Wavelength Infrared (MWIR) from 3 to 5 μm ; Long Wavelength Infrared (LWIR) from 8 to 14; and Very long Wavelength Infrared (VLWIR) from 14 to 1000 μm [26].

Every object with a temperature above absolute zero (that corresponds to 0 K, or -273 °C) emits electromagnetic (EM) radiation over virtually all wavelengths. This results from the tiny random motions of particles, atoms and molecules, in the object, which can be described by a thermal energy and thus define the object's temperature.

The amount of radiation emitted at each wavelength depends only on the object's temperature and not on any other property of the object, such as its chemical composition. Scientists usually refer to this as thermal radiation. Alternatively, they also use the term 'black body' radiation, where a black body is a theoretical object that completely absorbs all of the light that it receives and reflects none. A black body also is a perfect emitter of light over all wavelengths, but there is one wavelength at which its emission of radiation has its maximum intensity.

Electromagnetic radiation emitted from a black body ($E_{\lambda,b}$) can be calculated using Planck's law, as in Eq. 1.5, where C_1 and C_2 are constants, λ is the wavelength and T is the temperature [26].

$$E_{\lambda,b}(\lambda, T) = \frac{C_1 \lambda^{-5}}{\exp(C_2/\lambda T - 1)} \quad (1.5)$$

Fig. 1.2 shows the Planck's distribution for different representative temperatures: from the Cosmic Microwave Background (CMB) radiation (8000 K), to the emitted surface temperature of a Blue Star (the most energetic kind of star at about 40000 K). Between these curves in the same graph, the Planck distribution is shown in the case of the Sun's surface temperature (5800 K), a common incandescent light bulb temperature (3000 K), and a black body (273.15 K).

As depicted in Fig. 1.2 the following points emerge:

- $E_{\lambda,b}$ is a continuous function of λ , for every value of λ , there is an unique value for $E_{\lambda,b}$,
- for every temperature there is a peak in terms of $E_{\lambda,b}$;
- for a given λ , $E_{\lambda,b}$ increases with temperature, as stated by second law of thermodynamics;
- the peak of $E_{\lambda,b}$ is shifted to the left for increasing temperatures;
- there is more energy difference per degree at shorter wavelengths.

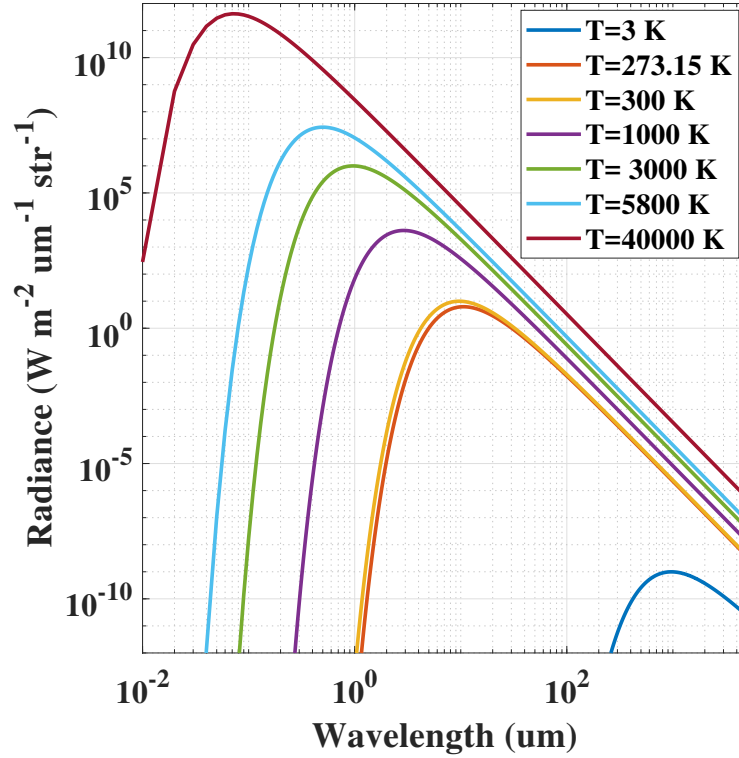


Figure 1.2: Planck distribution for different representative temperatures.

By integrating several times over all frequencies (or wavelengths) the equation Eq. 1.5, and opportunely operating a change of variables, it is possible to obtain the equation known as Stefan-Boltzmann Law, that states as the total radiant emission is proportional to the fourth power of its absolute temperature.

$$E_b = \sigma T^4 \quad (1.6)$$

where $\sigma = 5.6697 \times 10^{-8} \text{ W/m}^2 \text{ K}^4$ is the Stefan-Boltzmann constant.

It is also interesting to know the wavelength at which the black body radiation distribution function shows a peak for a given temperature. Wien's attempted to answer to this question by setting the Wien's displacement law in its more general form:

$$E_{b,\lambda}(\lambda, T) = T^5 f(\lambda, T) \quad (1.7)$$

By dividing the previous equation by T^5 , it is possible to obtain a result that is a function only of the product λT . Wien measured the spectral distributions for a black body at different temperatures. In this way, he found that the peak energy was proportional to their corresponding wavelength by a constant $C_3 = 2897.8 \mu\text{mK}$, that was called the third radiation constant:

$$\lambda_{\max} T = C_3 \quad (1.8)$$

Planck's law is an invaluable tool to estimate spectral distribution for a black body, which corresponds to the theoretical maximum possible emission from any real object [27]. Therefore, for a given wavelength and in a given incident direction, there can be no body which absorbs more radiation than a black body. Any real body has to absorb a radiation which is lower than that of the black body. Besides, of great importance in NDT&E, the energy emitted by a body (real or black body) is a function of his surface temperature, and for a real object it is obviously minus than the one emits by a perfect black body. However, the energy emitted by a real body and detected by an IR detector, depends as well on the real object surface properties, mainly its emissivity, as discussed as follow.

The emissivity of a body is defined formally for a wavelength λ by Eq. 1.9, as the ratio of the radiant energy emitted by the body to the radiation that would be emitted by a black body at the same conditions (temperature, wavelength and direction).

$$\epsilon_{\lambda}(\lambda, T_s) = \frac{E_{\lambda}(T_s)}{E_{\lambda,b}(T_s)} \quad (1.9)$$

as defined by Kirchoff. A real body emits only a fraction of the thermal energy emitted by a black body at the same temperature. If the emissivity is constant and independent of the wavelength, the body is defined a grey body and $\epsilon(\lambda, TS) = \epsilon = \text{constant} < 1$.

The emissivity of real objects is not constant, but it changes with the wavelength; for this reason, they cannot be considered grey bodies (Fig. 1.3). However, it is usually assumed that for short wavelength intervals, the emissivity can be considered as a constant. This assumption is used to treat real objects as grey bodies. In IT, although the emissivity of real objects is wavelength dependent, and, therefore, they cannot be considered true grey bodies, they are treated as such by averaging their emissivity through short intervals, in which the infrared sensor works. This average is also possible because the emissivity is a slow varying function of wavelength for solid objects.

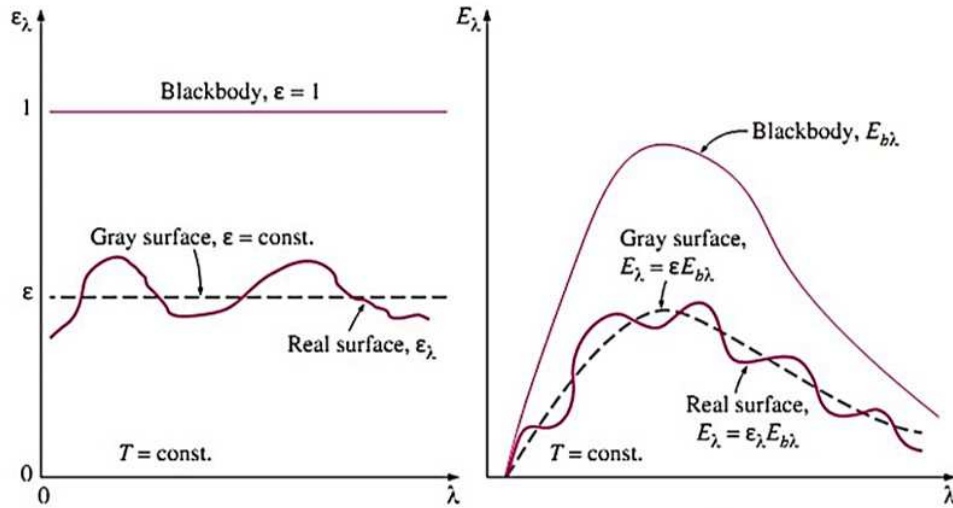


Figure 1.3: Emissivity and relative emitted energy for black, gray and real body, a schematization.

Combining the emissivity expression for a grey body and Eq. 1.6, Eq. 1.10 is obtained. This equation is the Stefan–Boltzmann formula for grey body radiators. Fig. 1.4 shows a graphical representation of this equation for different emissivity values.

$$E = \varepsilon \sigma T^4 \quad (1.10)$$

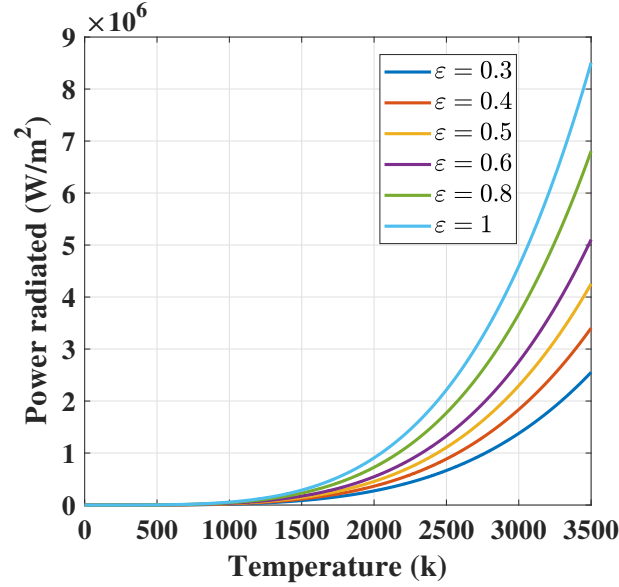


Figure 1.4: Stefan–Boltzmann law: power radiated by a grey body with different emissivities.

If all of the radiation energy falling on an object is absorbed (no transmission or reflection), the absorptivity α is equal to the emissivity, at any specified temperature and wavelength. It is true only for a black body. According to Kirchhoff's law, this can be expressed as:

$$\varepsilon_\lambda = \alpha_\lambda \quad (1.11)$$

In general, the absorptivity is a measure of the fraction of absorbed energy by a surface. For real surfaces, absorptivity range is between 0 and 1.

The part of the radiation energy which is not absorbed by a real body surface is transmitted or reflected. In the same way, not all the incident energy is re-emitted by the surface: one part of the energy is absorbed, one part is transmitted. In active thermography applications, we are interested in capturing the emissions coming from a surface following an external excitation. Part of the energy that is being emitted by a surface is the reflection from several external sources, other than the active thermal excitation, and another part is energy coming from the inside. As a result, surface emission is a complex process resulting from a balance between transmission, absorption, and reflection. Three parameters are used to describe these phenomena: the spectral absorptance α_λ , which is the fraction of the spectral radiant power absorbed by the object, the spectral reflectance ρ_λ , which is the fraction of the spectral radiant power reflected by the object, and the spectral transmittance τ_λ , which is the fraction of the spectral radiant power transmitted by the object. These three parameters are wavelength dependent.

As illustrated in Fig. 1.5, a fraction of the irradiation G is absorbed; another fraction is reflected; and for semi-transparent materials, another fraction is transmitted through the surface. Part of the energy reflected and diffused is detected by an infrared detector.

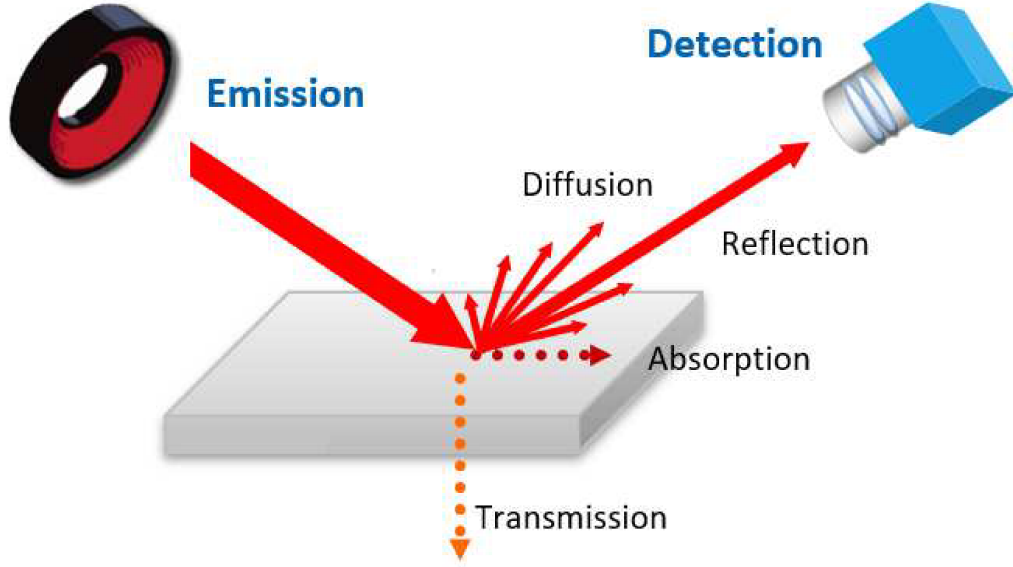


Figure 1.5: Surface effects illumination.

By the energy conservation principle [37]:

$$G = \alpha G + \rho G + \tau G \quad (1.12)$$

by dividing for G :

$$\alpha + \rho + \tau = 1 \quad (1.13)$$

that becomes:

$$\varepsilon = 1 - \rho \quad (1.14)$$

for opaque materials, where $\tau = 0$.

For a black body however at a given temperature $G = Eb$ [28].

For all these reasons, in order to increase emissivity to a value near to 1, it is a common practice to cover the samples if it is possible before to inspection. This procedure helps, at the same time, to diminish emissivity variations on the surface and to eliminate reflections from the environment. Real surfaces of plastics and woods are close to the behavior of a black body (not reflecting) surfaces having $\varepsilon \approx 0.9$, while metals are characterized by much less $\varepsilon \approx 0.1$; in Tab. 1.1 the main emissivity values for different materials are reported.

material	ϵ emissivity
paper	0.93
brick	0.5-0.9
wood	0.8-0.9
water	0.67
paint white	0.9-0.95
aluminum	0.05
stainless steel (polished)	0.22
steel (polished, oxidised)	0.08-0.8

Table 1.1: Emissivity values for different materials (real surfaces).

1.2 The infrared thermographic system

IR Imaging Systems usually has centered mainly on the wavelengths of the two atmospheric windows 3–5 μm [middle wavelength IR (MWIR)] and 8–14 μm (LWIR region; atmospheric transmission is the highest in these bands and the emissivity maximum of the objects at $T \approx 300\text{ K}$ is at the wavelength $\lambda \approx 10\text{ micron}$), though in recent years there has been increasing interest in longer wavelengths stimulated by space applications. There are two reasons that explain why MWIR and LWIR are investigated in IT: the band of peak emissions and the atmospheric transmittance. The first reason is due to the relation between temperature and wavelength. The most effective measurement for a particular temperature should be carried out for the wavelength, at which most intensity is emitted (Fig. 1.1). Measuring at a different wavelength would require a much more sensitive camera to achieve identical results. Thus, for most applications, wavelengths longer than SWIR are required. The second reason is related to the atmospheric transmittance. Infrared radiation spreads through air, being absorbed by various air particles, mostly by CO_2 and H_2O (Fig. 1.6) [29]. The degree to which air absorbs infrared radiation depends on the wavelength. In the MWIR and LWIR bands, this absorption is low, allowing more radiation to reach the sensor of the camera. Therefore, the MWIR band is preferred when inspecting high temperature objects and the LWIR band when working with near room temperature objects.

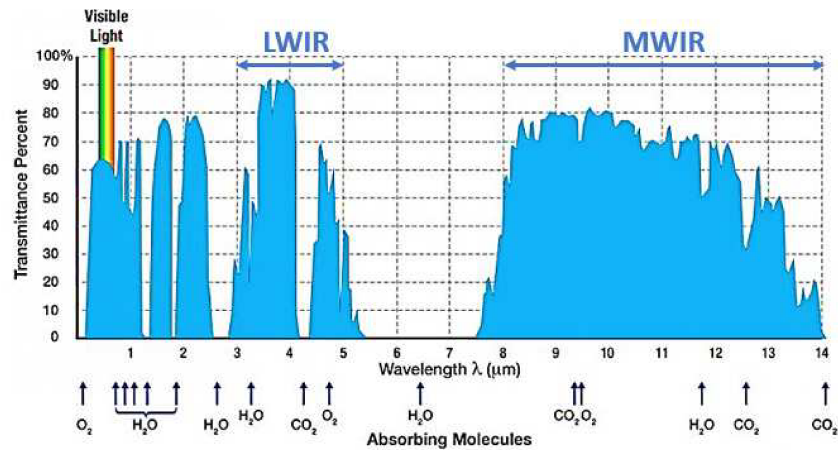


Figure 1.6: Atmospheric transmission of IR Wavelengths.

Fig. 1.7 shows the basic elements of an Infrared System: (1) a thermal excitation source; (2) a sample; (3) a detector (IR camera); (4) a signal and image analysis post-processing system (PC); and (5) the results (in terms of single map or sequence of thermograms).

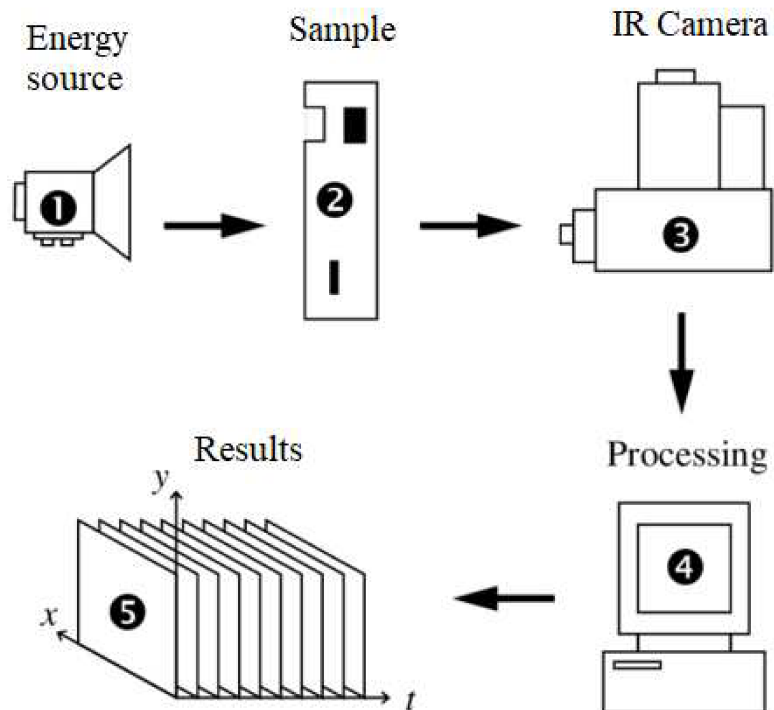


Figure 1.7: The schematization of an IR thermal imaging system.

When the object of interest is in equilibrium with the rest of the environment, it is possible to create a thermal

contrast on the surface by using a thermal source; this approach is known as active one in IT. Instead, when a thermal gradient between the environment and the object of interest exist, the object can be inspected using a passive approach.

The excitation source (1) is crucial for the thermographic measuring chain. Its performance has a decisive effect on the results. Active IT employs different types of external excitation sources as optical radiation (e.g., halogen heat lamps and laser), electromagnetic stimulation (induced eddy currents and microwaves), mechanical ultrasonic waves and material enabled features in composites, in order to generate heat in the component under inspection. Optical sources include lasers, LEDs, Xenon flash tubes, halogen lamps, and common (incandescent) electrical bulbs. Such heaters are well controlled and may deliver a considerable amount of energy onto the surface of a test object. The most powerful heat sources are high power CO_2 and diode lasers [30]. The drawbacks of optical heaters are the presence of reflected radiation during heating/cooling, which may be significantly reduced in the case of lasers and LEDs, and a need for high material absorbance in the spectral range of their output. The optical heaters typically used in active thermography are Xenon flash tubes, which provide up to $0.5 \text{ million } Wm^2$ for flash lamps and to 30 kWm^2 for halogen lamps [31].

A tested material (2) can be described by a few specific thermophysical properties: density, specific heat, conductivity, effusivity, diffusivity and emissivity. Other properties that characterize a material are emissivity, reflectivity and transmissivity, described already in the previous paragraph.

Density $\rho \text{ (kg/m}^3\text{)}$, is a measure of mass per unit volume. Specific heat $c_p \text{ (J/kgK)}$, is the thermodynamic property, which states the amount of heat required for a single unit of mass of a substance to be raised by one degree of temperature. When the product (ρc_p) is combined, it provides an indication of the ability of the material to store thermal energy, i.e. their heat capacity [32].

Thermal conductivity $k \text{ (W/mK)}$ is a thermophysical property of matter defined as:

Conductivity gives an indication of the energy diffusion rate by conduction for a particular material. The defining equation for thermal conductivity is:

$$q = -k \nabla T \quad (1.15)$$

where q is the heat flux, k is the thermal conductivity, and ∇T is the temperature gradient. This is known as Fourier's Law for heat conduction. For the same thermal gradient, heat flux will increase with k . In general, $k_{solids} > k_{liquids} > k_{gas}$.

Thermal diffusivity $\alpha \text{ (mm}^2/\text{s)}$ is the thermal conductivity divided by density and specific heat capacity at constant pressure. It measures the material's ability to conduct heat in relation to its capacity to store it [33].

$$\alpha = \frac{k}{\rho c_p} \quad (1.16)$$

In a substance with high thermal diffusivity, heat moves rapidly through it because the substance conducts heat quickly relative to its volumetric heat capacity or thermal bulk. The thermal diffusivity is a measure of the thermal energy diffusion rate through the material. The diffusion rate will increase with the ability to conduct heat and decrease with the amount of thermal energy needed to increase the temperature. Large values of diffusivity mean that objects respond fast to changes of the thermal conditions. Therefore, this quantity governs the timescale of heat transfer into materials. If a material has voids or pores in its structure, then both the thermal conductivity and density decrease, so the thermal diffusivity changes. This implies a variation of the heat transfer within the material

is affected, leading to observable changes of surface temperatures in the vicinity of the defects.

Effusivity e ($W\sqrt{s}/m^2 \cdot K$), is a thermophysical property relevant to transient surface heating processes [32], which is present in all materials (solids, liquids, pastes, powders, and gases). Effusivity measures the material ability to exchange heat with its surroundings and is defined as:

$$e = \sqrt{k\rho c_p} \quad (1.17)$$

This quantity will govern how much the temperature of an object changes if it is invested with thermal energy.

In Tab. 1.2 thermophysical properties of common NDT&E materials are reported.

<i>Material</i>	<i>Thermal Conductivity</i> k (W/mK)	<i>Density</i> ρ (kg/m ³)	<i>Specific Heat</i> c_p (J/kgK)	<i>Thermal Diffusivity</i> α (mm ² /s)	<i>Thermal Effusivity</i> e ($W\sqrt{s}/m^2 K$)
Air	0.025	1.29	1004	19.4	6
Aluminum (pure)	225.94	2698	921	91	23688
Aluminum 6061	167	2007	896	64	17329
Aluminum 7079	121.34	2740	795	55.7	16258
Steel 304	14.644	7920	502	3.68	7631
Steel 316	13.53	8230	470	3.598	7230
Lucite Plexiglas	0.152	1200	1297	0.1	486
Teflon	0.251	2170	1004	0.12	740
Graphite Sheet 70 Um(In-Plane)	800	1100	850	855	27350
Epoxy/Carbon Fiber Composite	78.8	1400	1130	49.81	11165
E-Glass Fiber Composite	1.30	2600	810	0.617	1654

Table 1.2: Main materials thermal properties database.

An IR camera (3) captures the (weak and noisy) thermal signatures coming from the target (sample+environment). The principal components of a radiometer are: the optical receiver, the detector or detector matrix, and in some cases a cooling system. Here again, every element of the radiometer contributes to further degrade the signal, i.e. optical, electronic and electromagnetic noise.

The essential elements of an original form of infrared imager are illustrated as a block diagram in Fig. 1.8. They are:

- An optical system that can form an image of an external scene using radiation in the infrared wavelength range.
- One or more detector elements that can convert this radiation into electrical signals proportional to the radiation falling onto them.
- Some systems require a scanning mechanism that scans the infrared image in a regular pattern across the detector element(s), although most modern imagers do not require this, since they use large detector arrays

that completely cover the field of view of the imager (the detectors are arranged in a matrix of columns and rows: focal plane arrays (FPA)).

- An electronic processor that processes the detector outputs and converts them into a video signal.
- A display unit that generates a visual image from the video signal [33].

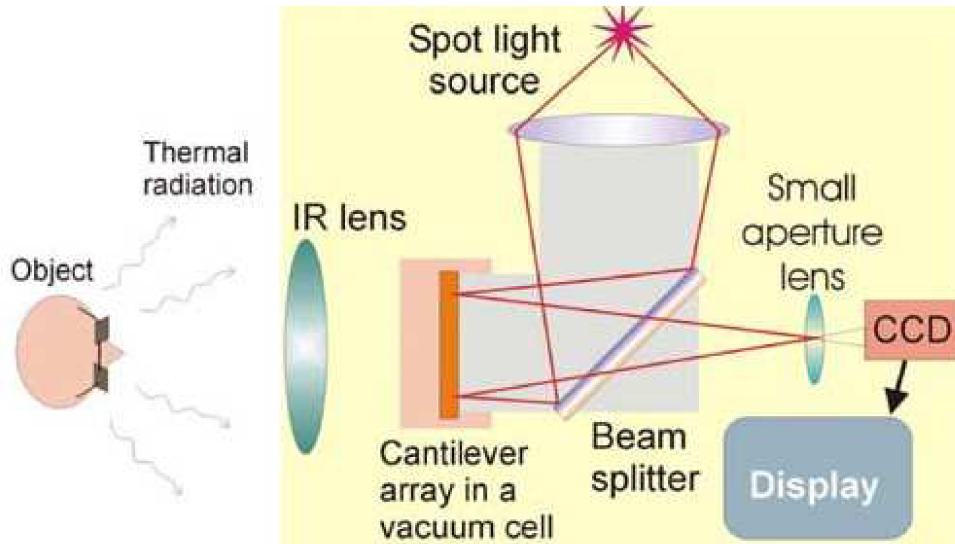


Figure 1.8: Basic components of a thermal imaging system.

The optical systems used in thermal imagers are designed and function in the same way as optical systems for visible wavelengths. The main difference is that most of the materials used for thermal wavelengths are different from those used for visible wavelengths; besides, there are also some differences between optical materials used in the 3–5 μm band and those used in the 8–14 μm band. An important aspect of some of the lens materials is their relatively high refractive index compared with those of the glasses used for visible wavelength optics. This has an important effect: uncoated surfaces have a high reflectivity. The high reflectivity means that these materials must be used with an anti reflection coating, in order to reduce the radiation caused by multiple reflections between optical surfaces. The main effect of unwanted reflections is that within the thermal image a cooled detector element virtually sees a part of itself. This usually results in a dark or bright halo in the center of the image. Developing efficient coatings for some of these materials has been an important aspect of thermal imaging. In many applications it is possible to find a plane-parallel-sided window between the thermal imager and the external scene, in order to protect the imager from the external environment.

The most important part of a thermal imager is the detector or detector array. Infrared detectors are classified into thermal types and photonic (quantum) types. Thermal detectors use the infrared energy as heat and their photo sensitivity is independent of wavelength. Thermal detectors do not require cooling, but have disadvantages that response time is slow and detection capability is low. In contrast, photonic detectors offer higher detection performance and a faster response speed, although their photo sensitivity is dependent on wavelength. In general, quantum detectors must be cooled for accurate measurement, except for detectors used in the near infrared region. Types of

thermal detectors include thermocouples, bolometers, pneumatic detectors, pyroelectric detectors and liquid crystals. Photonic detectors are subdivided in photoemissive detectors, based on the emission of carriers from a metal to a semiconductor material through absorption of radiation; and quantum detectors, which can be photoconductors (the electrical conductivity increases with temperature) or photovoltaic (or photodiode) detectors (a current proportional to incident radiation flows through the diode junction of the semiconductor).

An example of detector that belong to the family of thermal detectors is the bolometer/microbolometer. The microbolometer technology is based on the resistance change with temperature of a resistor element and is the mostly employed in handheld IR systems. Basically, a microbolometer consists of two platinum strips, covered with lampblack; one strip is shielded from the radiation and the other one is exposed to it. Microbolometer detectors are mostly based on pyroelectric and ferroelectric materials or microbolometer technology. The material are used to form pixels with highly temperature-dependent properties, which are thermally insulated from the environment and read electronically. Microbolometers are characterized by relatively low sensitivities/detectivities, broad/flat spectral response curves, and slow response times of about 10 ms [34].

Cooled detectors are typically contained in a vacuum-sealed case or Dewar and cryogenically cooled. The cooling is necessary for the operation of the semiconductor materials used. Typical operating temperatures range from 4 K to just below room temperature, depending on the detector technology. Most modern cooled detectors operate in the 60 K to 100 K range, depending on type and performance level. The camera may need several minutes to cool down before it can begin working. The most commonly used cooling systems are rotary Stirling engine cryocoolers. Although the cooling apparatus is comparatively bulky and expensive, cooled infrared cameras provide superior image quality compared to uncooled ones. Materials used for cooled infrared detection include photodetectors based on a wide range of narrow gap semiconductors including indium antimonide (3-5 μm), indium arsenide, mercury cadmium telluride (MCT) (1-2 μm , 3-5 μm , 8-12 μm), lead sulfide, and lead selenide.

Thermal imaging cameras with a cooled detector offer some advantages over thermal imaging cameras with an uncooled detector. However, they are more expensive.

In selecting the type of detector to use in a thermal imager there are several main performance parameters to consider:

- The wavelength band in which it operates
- The thermal sensitivity and spatial resolution that can be achieved
- The integration time
- The frequency response
- Cooling requirements and the associated complexity, cost, and possible inconveniences
- Reliability and cost

Unfortunately, microbolometers camera do not offer the possibility to fix the integration time. Rather, the integration time is given by their thermal time constant. The frame rate of these cameras cannot be changed by the user. For all these reason, their use is is limited to a few and particular applications.

Follow a brief description of the previously mentioned performance parameters for an infrared camera.

As already specified, the infrared spectrum is divided into near-IR, shortwave (SWIR), medium wave (MWIR) and long wave (LWIR). To detect radiation at these wavelengths, a number of different detector technologies are used. While shortwave IR sensors are typically composed of Indium Gallium Arsenide (InGaAs), MWIR sensors typically rely on Indium Antimonide (InSb). SWIR and MWIR detectors can be actively cooled, increasing sensitivity and at the same time adds to the cost of cameras based around them.

In the LWIR range, Mercury Cadmium Telluride (MCT) and Strained Layer Superlattice (SLS) detectors provide a high-level of temperature precision. However, both technologies require active cooling, which increases cost. A lower cost, albeit less sensitive option in the LWIR, is the microbolometer, typically found in less expensive handheld cameras. For many applications, microbolometer-based cameras provide an affordable alternative to those that are actively-cooled. The wavelength ranges of all these detectors is illustrated in Fig. 1.9.

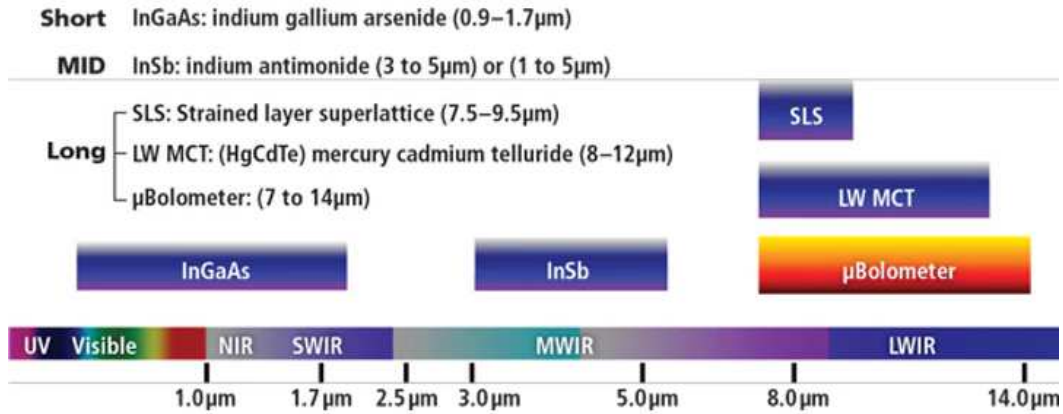


Figure 1.9: IR detector technology; type of sensors and wavelength.

Sensitivity expresses the ability of an infrared camera to display a very good image even if the thermal contrast in a scene is low. Put another way, a camera with good sensitivity can distinguish objects in a scene that have very little temperature difference between them. Sensitivity is most often measured by a parameter called Noise Equivalent Temperature Difference or NETD. NETD is defined as the amount of infrared radiation required to produce an output signal equal to the system's own noise. This is a noise rating of the system and should be as low as possible. NETD is typically expressed in mill-Kelvin (mK). Typical values for uncooled, microbolometer detector thermal cameras are on the order of 45 mK. Scientific cameras with photon-based and cryogenically cooled detectors can achieve NETD values of about 18 mK. The noise measurement value should be specified at a particular object temperature, as this impacts the measurement. Example: NETD @ 30°C : 60 mK. In order to measure the noise equivalent temperature difference of a detector, the camera must be pointed at a temperature-controlled black body. The black body needs to stabilize before starting the measurement. The noise equivalent temperature difference is then being measured at a specific temperature. It is not a single snapshot measurement, but rather a temporal measurement of noise. The temperature of a technical black body T_{ob} measurement area is usually equal to 30 °C, with a background temperature T_o of 22 °C, and the difference $T_{ob} - T_o$ should be within 5–10 K. A greater value of NETD indicates a lower sensitivity of the camera. For this reason, in the technical data of IR cameras, the NETD parameter is called 'thermal sensitivity' or 'temperature resolution' [35].

FOV, or Field of View, is the largest area that your imager can see at a set distance. In other words, the FOV is the angular extent of the observable object field. Sometimes the FOV is also given as the area seen by the camera. It

is typically described in horizontal degrees by vertical degrees—for example, $23^\circ \times 17^\circ$. IFOV, or Instantaneous Field of View (otherwise known as Spatial Resolution), is the smallest detail within the FOV that can be detected or seen at a set distance. It means that at certain distance, you may not be able to see certain small details if your Spatial Resolution is not good enough. IFOV measurement, or Instantaneous Field of View Measurement (otherwise known as Measurement Resolution), is the smallest detail that you can get an accurate temperature measurement upon at a set distance. These are a measure of the spatial resolution of an IR camera. The FOV depends on both the camera lens and the FPA dimensions. Focal Plane Arrays (FPAs) are today's most common IR imaging configuration. An FPA is made up of rows and columns of individual IR detectors. The fill factor is an important parameter in selecting FPAs, it provides the IR-sensitive material to total surface (including the signal transmission paths) ratio. The higher the fill factor, the higher the sensitivity, the cooling efficiency and the overall image quality of the system. From the FOV, IFOV can be determined by dividing the FOV by the number of FPA pixels in a line (horizontal or HIFOV) or in a column (Fig. 1.10) [35].

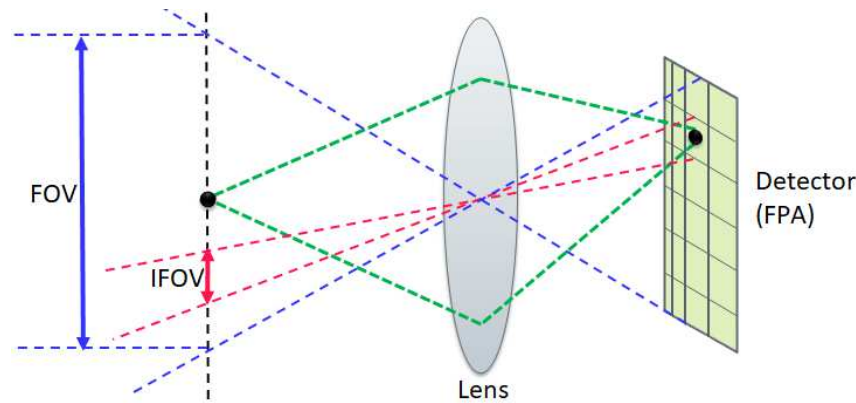


Figure 1.10: Illustration of field of view (FOV) and instantaneous field of view (IFOV).

Another important parameter is the specification of accuracy (or, more precisely, inaccuracy), that gives the absolute value of the temperature measurement error for black body temperature measurements. For most thermocameras, the absolute temperature accuracy is specified to be ± 2 K or $\pm 2\%$ of the temperature measured.

The accurate analysis of transient thermal processes requires a sufficient time resolution of thermal imaging compared to the characteristic thermal time constant of the process to be investigated. Most practitioners use bolometer cameras that do not offer the possibility of a select-able integration or exposure time (that, for definition, is the time it takes a pixel to produce a useful conversion) in contrast to photon detector. In data sheets of imaging systems equipped with bolometer focal plane arrays, the time resolution is usually just characterized by the frame rate as the relevant camera parameter. Mostly this value is assumed to be related to the time resolution for the imaging analysis [34]. A detector with a high integration time responds more slowly to temperature changes; as a consequence, the maximum signal is much lower than the correct 100% signal. If the detector time constants are much lower (nanoseconds to microseconds), these detectors respond much faster and the temperature of an object can be correctly determined. In cooled detector, it is possible to select the integration time and also the frame rate (the speed) of the camera; usually, when the frame rate of the camera increases, there is a windowing of the detectable object, so the spatial resolution decreases with the investigable area.

These are the main performance parameters that characterize an IR camera; however the choice of which camera

to use, uncooled or cooled, or a particular type of both, depends on the application and the sustainable costs.

IR cameras without an analysis software (4) would just provide qualitative false color images of objects. However, whenever quantitative results are needed like temperatures, line plots, or reports, software tools are indispensable. All manufacturers of thermal imaging systems provide a variety of software tools ranging from general-purpose software packages including, for example, thermal image analysis and generation of infrared inspection reports. The general-purpose software mostly contains the following key features: level and span adjustment; selectable color palette and isotherms; definition of spot analysis, lines, and areas with temperature measurements for maximum, minimum, and average temperatures; adjustment of object parameters (emissivity) and measurement parameters (e.g., humidity, object distance, ambient temperature); creation of reports with flexible design and layout. For a very detailed analysis of static or transient thermal processes sophisticated software is available. Sophisticated software usually includes more complex data storage, analysis, and camera operation tools: a remote control of the camera from the PC together with high-speed IR data acquisition, analysis, and storage; raw data acquisition and analysis, radiometric calculations; different data format export, automatic conversion to, for example, JPEG, BMP, AVI, or MATLAB® format.

Traditional and new IR image processing techniques are reviewed in references [35, 36]. These techniques are intended to reduce noise at pre and post processing stages, to enhance image contrast and to retrieve useful information from the images. Finally, the resulting processed data must provide qualitative or quantitative outputs allowing to assess the conditions of the target (5).

1.3 Infrared thermography in NDT&E scenery

Infrared Thermography in the NDT&E scene Non Destructive Testing and Evaluation (NDT&E) involves all inspecting techniques used to examine a part or material or system without impairing its usefulness [36]. The objective of a NDT&E technique is to provide information about (at least one of) the following parameters [36]: discontinuities and separations; structure; defects, porosity and delaminations; dimensions and metrology; physical and mechanical properties; composition and chemical analysis; stress and dynamic response; signature analysis; and abnormal source of heat.

There exist several NDT&E techniques, none of which is able to reveal all the required information.

The National Materials Advisory Board (NMAB) Ad Hoc Committee on Nondestructive Evaluation adopted a classification system of 6 major categories [36]:

1. Mechanical-optical (Visual Testing);
2. Penetrating radiation (Radio graphic Testing);
3. Electromagnetic-electronic (Eddy Current Testing, Magnetic Particle Testing);
4. Sonic-ultrasonic (Ultrasonic Testing);
5. Thermal and Infrared (Infrared Thermography);
6. Chemical-analytical (Liquid Penetrant Testing).

The appropriate technique depends on the thickness and nature of the material being inspected, as well as in the type of discontinuity that must be detected, especially its depth. Infrared and Thermal testing involves temperature and heat flow measurements to predict or diagnose failure. IT is a nondestructive, non-contact and non-intrusive mapping of thermal patterns on the surface of the objects.

For the studies conducted in this research work, active thermography has been used. There are, basically, 3 techniques widely used in NDT&E: Pulsed Thermography (PT), Lock-in Thermography (LT) and Vibrothermography [98].

However in the literature, there is some confusion when the different authors talk about of thermographic techniques, intended as way to acquire thermal data, instead of post-processing algorithms or ways to analyze the raw thermal data. For this reason in this work, we talk about two main techniques: Pulsed Thermography and Lock-in thermography.

Stepped and long pulse thermography are types of analysis and as ideas and data acquisition come from the pulsed thermographic technique. In the same way, when we talk about Pulsed Phase Thermography (PPT) and Thermal Signal Reconstruction (TSR®), these will be algorithms useful to provide a post-processing of the raw thermal data that come from a pulsed test, and not techniques.

In terms of theoretical remarks and models which can be useful to explain and simulate the thermophysical principles, there are some differences between pulsed and stepped/long pulse thermography, explained mainly from a different pulse duration.

In the following sections, the thermophysical principles, together with theoretical remarks, data acquisition and processing of pulsed and lock-in thermography will be shown, so creating order in the literature.

1.4 Pulsed Thermography

1.4.1 Data acquisition

In the last years, pulsed thermography has been established as a non destructive technique for detection of sub-surface defects in many different materials, from metals to composite one. Hence, for this type of approach to be effectively applied, a condition must be added: the thermophysical properties of the internal defect (e.g. voids, inclusions, delamination etc.) have to be different from those of the specimen's material. Without this condition, no defect detection is possible.

In PT, data acquisition is carried out as shown in Fig. 1.11 and can be summarized as follows. First, energy sources (xenon flash tubes) are used to heat the specimen surface. The pulse duration may vary from a few ms (~3-15 ms using flash lamps) to several seconds (using halogen lamps or a laser source), depending on the thermophysical properties of both, the specimen and the defects. There are two different modes for carrying out the raw thermal data: reflection mode, when the IR camera and the heating source are in the same side, and transmission one, when the latest are in the opposite side. A reflection configuration is used when the inspecting defects are closer to the heated surface, instead transmission is preferred for deeper defects or in order to provide some information about the thermophysical properties of the examined sample. The thermal changes are recorded with an infrared camera. A synchronization unit is needed to control the time between the launch of the thermal pulse and the recording with the IR camera. Data is stored as a 3D matrix. Defective zones will appear at higher or lower temperature with respect to non defective areas, depending on the thermal properties of both the material and the defect. Although heat diffusion

is a complex problem, the relationship between defect depth and time has been exploited by many researchers to obtain qualitative and quantitative results. The thermogram 3D matrix can be processed by using post processing algorithms described below.

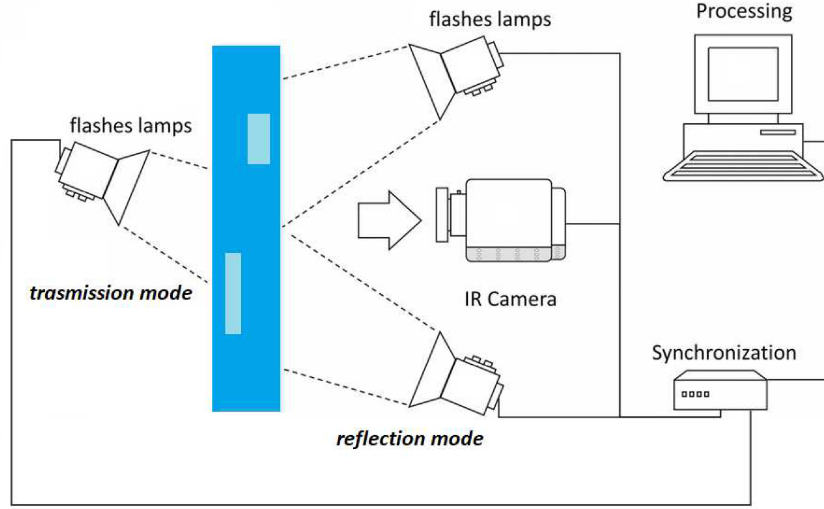


Figure 1.11: Experimental configuration in active thermography in reflection and transmission mode.

1.4.2 Theoretical remarks

1.4.2.1 Flash thermography

Basically, flash thermography consists of heating the sample with an infinitesimal impulse and recording the surface temperature decay curve with an IR camera. Abnormal behavior of this temperature decay curve shows subsurface defects. Qualitatively, the phenomenon can be described in this way: during the cooling down, the temperature of the material changes lapidary after the initial thermal perturbation; it is due to the thermal front propagation for diffusion and also to the radiation and convection losses. The presence of a defect reduces the diffusion rate so when the cooling down is observed, the defects show a different temperature respect of the relative sound area and also the temperature decay evolves differently. Consequently, deeper defects will be observe later and show a minor contrast. For the first time, Cielo et al. [37] showed that there is a relation between the observation time t and the defect depth, and in particular this function is a radical square. In the same way, Allport et al. [38] demonstrated that the loss of contrast c is inversely proportional to the cube of the depth.

$$t \sim \frac{z^2}{\alpha} c \sim \frac{1}{z^3}$$

with α that indicates the material thermal diffusivity. The detection phenomena is shown in Fig. 1.12, by using the models described below.

Mathematically, after an infinitesimal short heating pulse, or after a so-called Dirac delta pulse, the surface temperature of a semi-infinite body, over the time t and depth z , is described by the well-known equation [39]:

$$T(z, t) = T_0 + \frac{Q}{e\sqrt{\pi t}} \exp\left(-\frac{z^2}{4\alpha t}\right) \quad (1.18)$$

where T_0 is the starting temperature, e is the effusivity, α is the thermal diffusivity and Q is the absorbed energy density. Here, the purely one-dimensional case, neglecting finite pulse duration and heat losses for radiation and convection is considered. This equation is only valid in the case of homogeneous and isotropic materials and it can be considered as the one-dimensional solution of the Fourier Equation for a Dirac delta function.

If we consider the temperature trend on the surface of the body, the Eq. 1.18 is simplified in the equation Eq. 1.19 [39]:

$$T(z=0, t) = T_0 + \frac{Q}{e\sqrt{\pi t}} \quad (1.19)$$

with a theoretical slope equal to -0.5 in a double logarithmic scale.

In the case of a finite body with a thickness L , by considering a one-dimensional model [39], the thermal wave is reflected theoretical infinite times from the back and front sizes of the tested sample. The equation that describes this thermal behavior is (Eq. 1.20):

$$T(t) = \frac{Q}{e\sqrt{\pi t}} \left[1 + 2 \sum_{n=1}^{\infty} R^n e^{-\frac{(nL)^2}{\alpha t}} \right] \quad (1.20)$$

where R is the thermal reflection coefficient of the solid-air interface $R = \frac{e-e_b}{e+e_b}$ (where e indicates the solid thermal effusivity and e_b the air-basic material surface), that can be considered equal to 1 and n is the number of reflections. Eq. 1.20 was obtained from the inverse Laplace function of the convolution of the thermal response function of a sample thickness L , with a Dirac delta function impulse of magnitude Q .

As a first approximation, a region containing a delamination-like defect can be treated as a layer of thickness d , the depth of the defect below the surface, and the expression is the same of the Eq. 1.20, by replacing the sample thickness L with the thickness layer d [40].

The equations described above are analytical expressions obtained assuming uniform heating across the surface and subsequent uniform, one-dimensional, thermal conduction into the heated sample.

Real defects are finite in their dimensions and the heat flows around the same cannot be considered one-dimensional, so it is necessary to consider the real defect size and the lateral conduction. For a circular defect of diameter D and by considering the defect aspect ratio $P = \frac{D}{d}$, the Eq. 1.20 can be re-written as Eq. 1.21 [40]:

$$T(t) = \frac{Q}{e\sqrt{\pi t}} \left[1 + 2 \left(\sum_{n=1}^{\infty} R^n e^{-\frac{(nd)^2}{\alpha t}} \right) \left(1 - e^{-\frac{(Pd)^2}{16\alpha t}} \right) \right] \quad (1.21)$$

Layered carbon or glass fiber composites are important types of material that are inspected using flash thermography. For these, in-plane and through thickness (z direction) thermal properties are different. Typically, in-plane thermal diffusivity is several times larger than through thickness thermal diffusivity. If the ratio of in-plane to z direction thermal diffusivity is indicated as m , Eq. 1.21 becomes [40]:

$$T(t) = \frac{Q}{e\sqrt{\pi t}} \left[1 + 2 \left(\sum_{n=1}^{\infty} R^n e^{-\frac{(nd)^2}{\alpha t}} \right) \left(1 - e^{-\frac{(Pd)^2}{16m\alpha t}} \right) \right] \quad (1.22)$$

By using the models described with Eq. 1.20 and the Eq. 1.21, it is therefore possible to explain the experimental behaviors after a pulsed test of an infinitesimal duration.

In order to evaluate the influence of the real sample thickness on the defect thermal behavior, it is necessary to

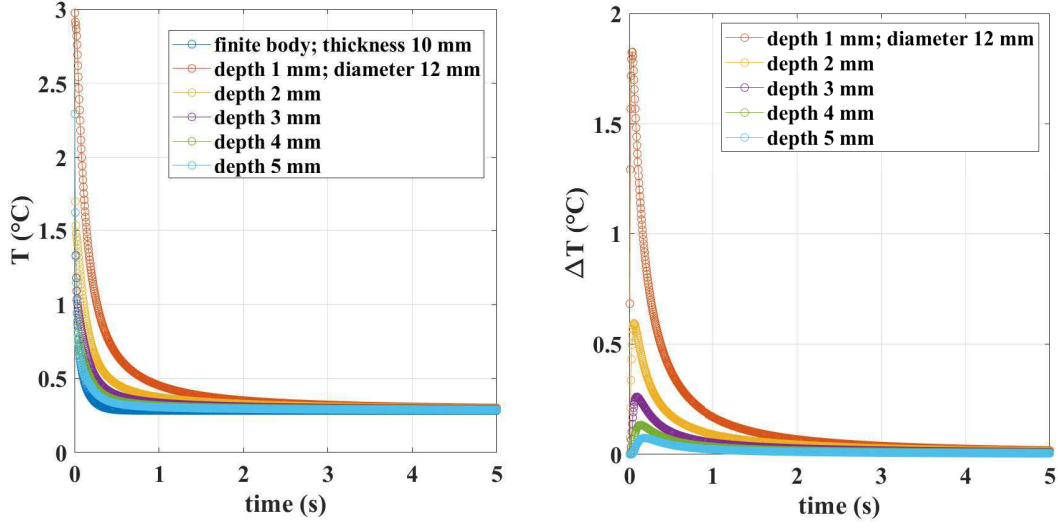
modify the Eq. 1.22 [38]; in this way, the thermal contrast is re-defined by considering as sound the temperature over a plate of specified thickness L , by using the Eq. 1.23.

In this way, to obtain the defect thermal behavior in terms of temperature, it is necessary to simulate the thermal sound behavior by using the Eq. 1.20 for a finite L thickness and the expression of the thermal contrast by using Eq. 1.23 for the different defects aspect ratios.

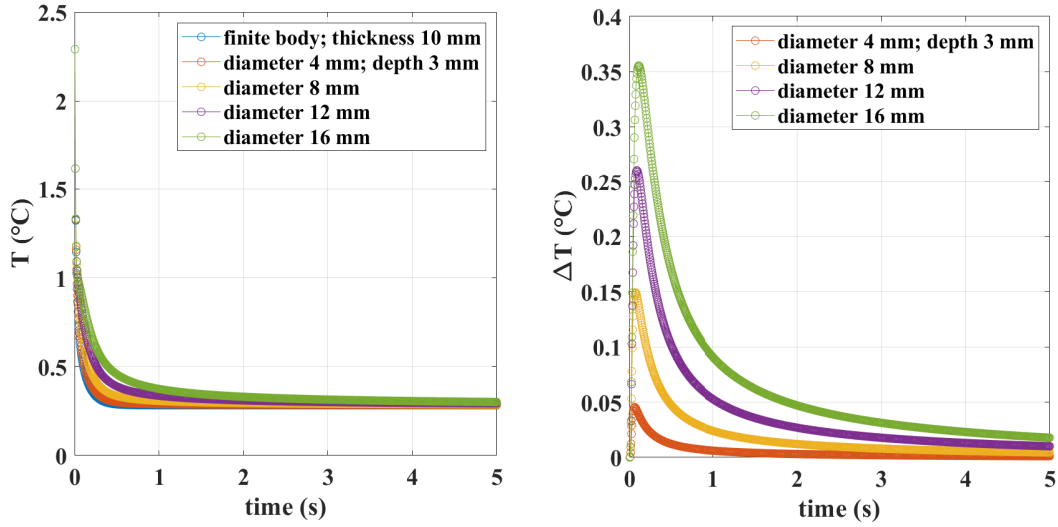
$$\Delta T(t) = 2 \frac{Q}{e\sqrt{\pi t}} \left(\sum_{n=1}^{\infty} R^n e^{-\frac{(nd)^2}{\alpha t}} - \sum_{n=1}^{\infty} R^n e^{-\frac{(nL)^2}{\alpha t}} \right) \left(1 - e^{-\frac{(Pd)^2}{16\alpha t}} \right) \quad (1.23)$$

These equations (Eq. 1.21, Eq. 1.22, Eq. 1.23) are mathematical models that describe the thermal behavior after a pulsed test of an infinitesimal duration in reflection configuration; the theoretical results that can be obtained by using these different thermographic models for different materials are already shown in several works [39, 41, 42, 45, 49, 50, 51, 52], but the authorship of these models is from D. P. Almond [39, 40, 41, 42, 43, 44, 45, 46, 47, 48]. However, there are other works and authors that developed numerical, mathematical and also finite element models in order to study this typical cooling thermal behavior [53, 54, 55, 56, 57, 58, 6, 7].

Here (Fig. 1.12), the temperature decay curve is depicted by analyzing the case of an aluminum sample, together with the relative thermal contrasts by considering different simulated circular defects (flat bottom holes). The used material for these simulations is an aluminum one, with these thermophysical properties: $\rho = 2700 \text{ (kg/m}^3\text{)}$, $k = 190 \text{ (W/mK)}$, $cp = 880 \text{ (J/kgK)}$. For the acquisition parameters, the energy density Q is setted equal to 6400 J/m^2 and the acquisition frequency is 200 Hz . The influences of defect depth and defect size are shown in Fig. 1.12, together with the geometrical characteristics in terms of defect depth and size, and entire thickness sample.



(a) Influence of defect depth.



(b) Influence of defect diameter.

Figure 1.12: Thermal behavior after a pulsed test: finite body and diameter influence models.

If the material parameters are known, these equations are well suited for estimating maximum surface temperatures and temporal temperature changes and thus for selecting optimum measurement parameters like temperature range, temperature resolution and frame rate of the IR camera as well as the required measurement duration. The other way around, if experimental data have been already recorded, a fit of the experimental temperature evolution using the previous equations enables estimation of the absorbed energy and of material parameters and their changes due to defects.

Flash thermography can be well described by 1D analytical models [50, 59, 60] also in the case of transmission configuration. Here, the temperature T as a function of time t at the backside ($x = L$, transmission) of a plate having a thickness L , a diffusivity α , a density ρ and a specific heat capacity c_p is given by:

$$T(t) = \frac{Q}{L\rho c_p} \left[1 + 2 \sum_{n=1}^{\infty} (-R)^n e^{-\frac{n^2 \pi^2}{L^2} \alpha t} \right] \quad (1.24)$$

Eq. 1.24 shows as the temperature rise depends on the material properties and the thickness of the specimen. In particular, the time in which the maximum temperature is reached depends on thickness of plate, it decreases as the thickness decreases. In Fig. 1.13, the temperature trend is reported as a function of the thickness by considering the same thermophysical aluminum material properties used to show the previous models, $f = 200 \text{ Hz}$, $Q = 2400 \text{ J/m}^2$.

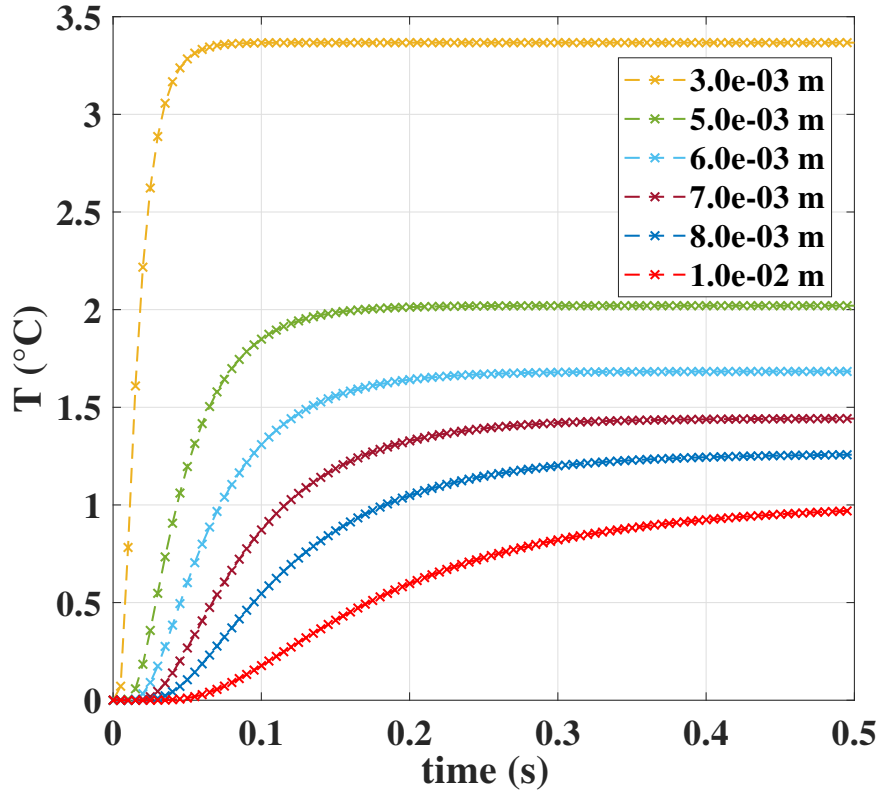


Figure 1.13: Temperature trend over time for a pulsed test in transmission mode Eq. 1.24.

In case of no heat loss, the rear surface temperature of the sample will attain a peak maximum and stay therefore an indefinite time period as depicted in Fig. 1.13, in fact by using an 1D model.

From this model, a well-known flash method of determining the material thermal diffusivity α descends: the Parker method [61, 62, 63, 64, 65, 66]. This method assumes that the sample is adiabatic and isotropic; the thermal diffusivity is calculated from $t_{0.5}$, the time taken for the thermogram to reach half of the maximum rise in temperature and L , the thickness of the sample material (Fig. 1.14):

$$\alpha = 0.1388 \frac{L^2}{t_{0.5}} \quad (1.25)$$

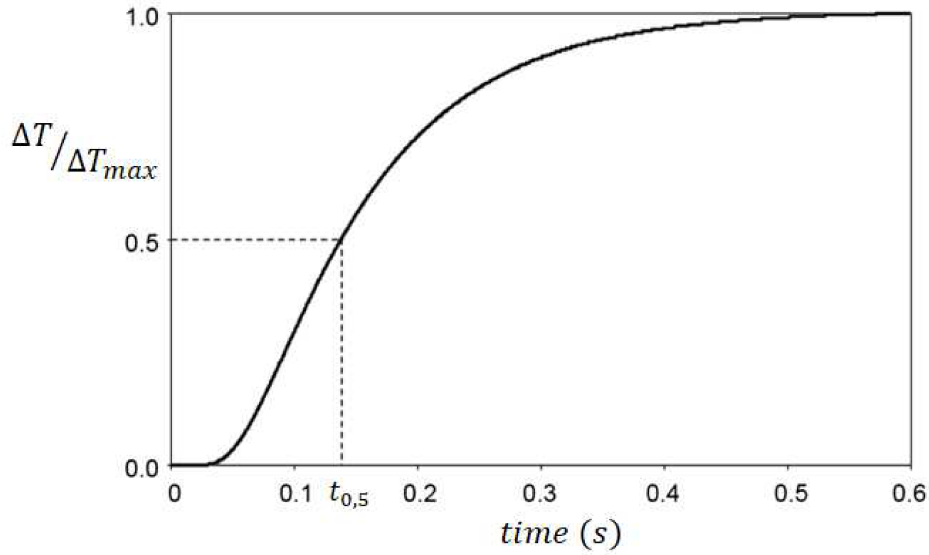


Figure 1.14: Typical trend of rear surface temperature history after a transmission test: Parker method.

The applicability of this method is limited as it assumes ideal sample conditions. To render it more suitable for practical experimental conditions, other methods which factor in finite pulse duration, heat losses, non-homogeneous materials and non-uniform heating have been developed over the past few years [67, 68, 69, 70, 71, 72].

1.4.2.2 Stepped&long pulse thermography

Compared to flash heating approach, relatively less previous research has been conducted for stepped and long pulse ones. Basically, we talk about of stepped and long pulsed thermography in order to indicate, respectively, the analysis of the raw pulsed data during the heating phase and during the cooling one, after a pulsed test of a certain duration. In these cases inexpensive lamps can be used, but halogen lamps or lasers such that to excite the tested component for a few seconds (the time depends from the material and its thermophysical properties); typically, they have to be driven by power amplifiers and specialized processing of the thermal images is required. Many workers in the field are aware that this long pulse excitation technique can be effective for some favorable applications. However, there appears to have been little detailed study of the capabilities of thermographic NDE employing this “long pulse” mode of thermal stimulation. In fact, much of the work has focused on examining thin coatings.

Here, we must distinguish between long pulsed thermography and step heating thermography. In long pulsed thermography, heating is applied for a selected period of time, eg. 5 s, and then thermal images are collected as the test piece cools down. In step heating thermography, thermal images are collected whilst the test piece is heated up.

Unlike the pulsed approach, during the step heating, very often the thermal wave reaches the defect during the heating phase [41, 73, 74, 75, 76, 77, 78, 79, 80, 81, 82, 83]. If the sound area is more thermally diffusive than the defect, at the end of heating, the surface above the defect is warmer than the sound material, and exchanges heat by conduction and convection more quickly than the sound material. Similar to the pulsed approach, the difference in temperature reached during the heating and the following cooling behavior will depend on the different thermophysical properties between defective and sound material as well as on the depth and type of defect Fig. 1.15.

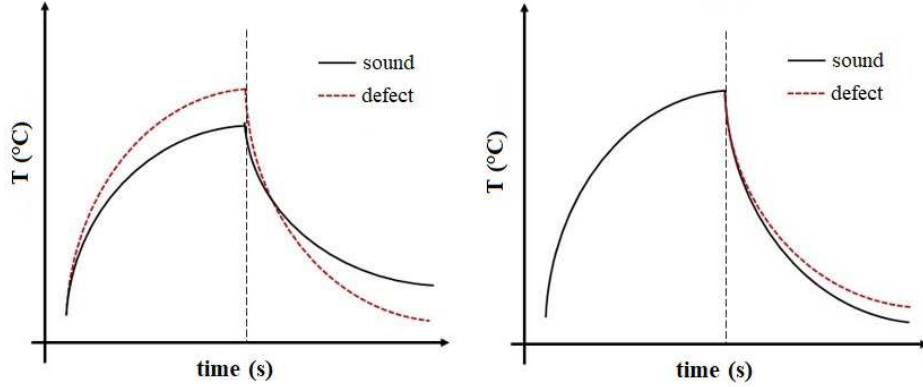


Figure 1.15: Temperature trend in defect and sound area, Stepped approach and Long Pulsed approach

Follow a brief description of the models useful to describe these types of analysis.

The temperature increase during a step heating analysis for a semi-infinite body (or a thermally thick slab) follows the equation:

$$\Delta T = \frac{2q\sqrt{t}}{e\sqrt{\pi}} \quad (1.26)$$

where q is the heat flux density, e is the thermal effusivity and t is the time [76, 77]. In the case of a slab of finite thickness L , the surface temperature increase is given by the equation:

$$T(t) = \frac{2q\sqrt{t}}{e\sqrt{\pi}} \left[1 + \sqrt{\pi} \sum_{n=1}^{\infty} 2xierfc \left(\frac{nL}{\sqrt{kt}} \right) \right] \quad (1.27)$$

where k indicates the thermal diffusivity.

If a slab with defect of infinite thermal resistance is considered, the equation that describes this thermal behavior is obtained by replacing the slab thickness L with the defect depth z .

$$T(t) = \frac{2q\sqrt{t}}{e\sqrt{\pi}} \left[1 + \sqrt{\pi} \sum_{n=1}^{\infty} 2ierfc \left(\frac{nz}{\sqrt{kt}} \right) \right] \quad (1.28)$$

By using the analytical solution proposed by Balages et al. (1986) [83] or the quadrupole method [69, 70, 71, 72, 73], it is possible to obtain a solution that considers a slab with a large-extent defect, but with the thermal losses due to the material thermal resistance. The long pulse excitation response can be obtained by representing it as being a sequence of impulse responses, starting from the equation valid for an infinitesimal pulse duration. The defect image thermal contrast, $T_c(t)$, may be obtained by integration of the impulse response function [41]:

$$T_c(t) = \int_{\tau=0}^{t_p} \frac{2W}{e\sqrt{\pi(t+\tau)}} \left[\sum_{n=1}^{\infty} e^{-\frac{(nd)^2}{\alpha(t+\tau)}} - \sum_{n=1}^{\infty} e^{-\frac{(nL)^2}{\alpha(t+\tau)}} \right] \left(1 - e^{-\frac{(D/2)^2}{4\alpha(t+\tau)}} \right) d\tau \quad (1.29)$$

In Eq. 1.29, W is power density or heat flux (W/m^2) created at the surface by the absorption of optical energy from an energy source (laser, halogen lamps) applied for a duration of t_p . Here, only the case that considers both the influence of the finite thickness L and the diameter D is reported, because the other minor cases can be demonstrated

in the same way.

1.4.3 Data processing

In order to provide quantitative information from the raw thermal data, a post-processing is necessary. Several algorithms have been developed in the past to satisfy this aim, to detect and localize defects and also to estimate their depth and size.

Here, the physical principles of the main algorithms will be described. In general, these tools can be useful in order to analyze data that come from a pulsed test, of an infinitesimal duration but also in the case of stepped/long pulse analysis; however, the contrast created by the defect occurs right after reaching the semi-infinite medium regime for pulse-heating, but much later for the step-heating. This will have no influence for the detection of the defect, but will perhaps make the quantitative characterization (depth identification) more difficult [76, 77].

Besides, when the PPT algorithm is applied, the thermal signal is evaluated in the frequency domain: in order to get the data in this domain, Fourier transformation, especially FFT is used to calculate the phase shift for different frequencies. The usage of FFT assumes a periodic signal or a temporal however limited in time. Unfortunately, this is not the case for the temperature signal after a short pulse heating and more during and after a stepped/long pulse analysis, for this reason the transformation to the frequency domain generates some errors, especially when the aim is to provide quantitative information [6, 7].

1.4.3.1 Slope and Square Correlation Coefficient R^2

In a double logarithmic scale, the equation Eq. 1.18 can be rewritten as follow:

$$\ln(\Delta T) = \ln\left(\frac{Q}{e}\right) - \frac{1}{2}\pi t \quad (1.30)$$

and so, in the case of a semi-infinite body, Dirac pulse and adiabatic conditions, a theoretical sound material shows a slope equal to -0.5 (Fig. 1.16) [98].

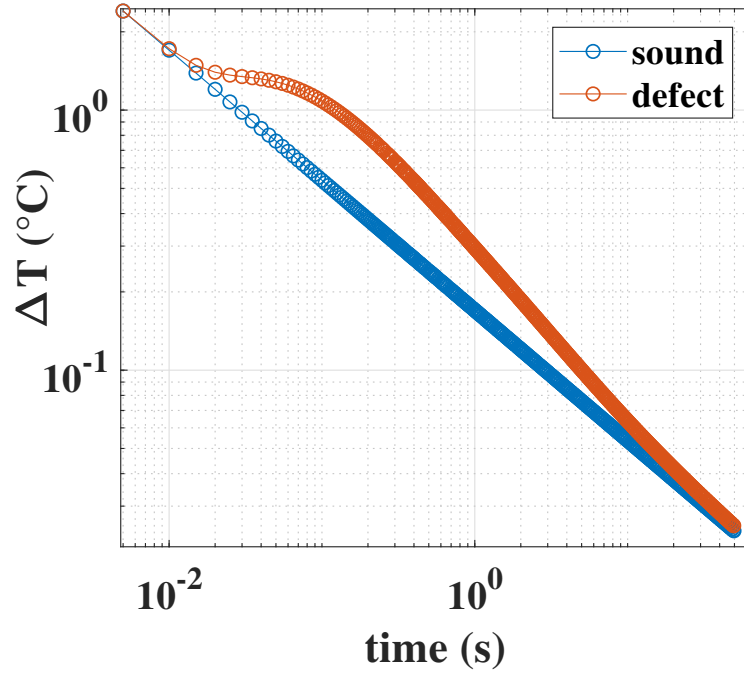


Figure 1.16: Temperature cooling down after a Dirac pulse: theoretical trends for sound and defect area in a double log scale.

In Fig. 1.16, the surface temperature evolution following a theoretical application of a Dirac pulse is plotted for a thin homogeneous plate (blue curve) and for the same plate when a typical defect (air layer) is present under the surface (orange curve). The presence of the defect determines a modification of thermal profile during cooling with a typical non-linear behavior.

Galietti et al. in [87] proposed two parameters (algorithms) that can be useful to analyze thermal data during the cooling phase: the slope (m) and the linearity R^2 of data.

As shown in Fig. 1.17 the cooling trend in the presence of a defect deflects from the theoretical sound one: a measure of this deviation is the slope value (m), that looks different from -0.5 . Another index of this deviation is R^2 value. In [87] the R^2 is defined as $R^2 = 1 - (SS_{res}/SS_{tot})$, where SS_{res} is the residual sum of squares and SS_{tot} is the total sum of squares. In the case of a simple linear regression, R^2 equals the square of the Pearson correlation coefficient between the observed and predicted data values of the dependent variable. The value of this coefficient is between 0 and 1 where: 1 indicates that the regressors well predict the value of the dependent variable in the sample, while 0 indicates that this doesn't happen; for a sound material we will therefore expect values of R^2 close to 1, and under the hypothesis of a Dirac pulse just the same to 1, instead for a defect area this value is less than 1.

Examples of values R^2 and slope m are reported in Fig. 1.17 in the analysis of a composite sample with imposed defects (flat bottom holes). The higher values of the two parameters were obtained for a shallow defect (defect 2), while the deeper defect (defect 7) showed lower values. This particular behavior could be used for discerning defect depth with respect to the sound material [87].

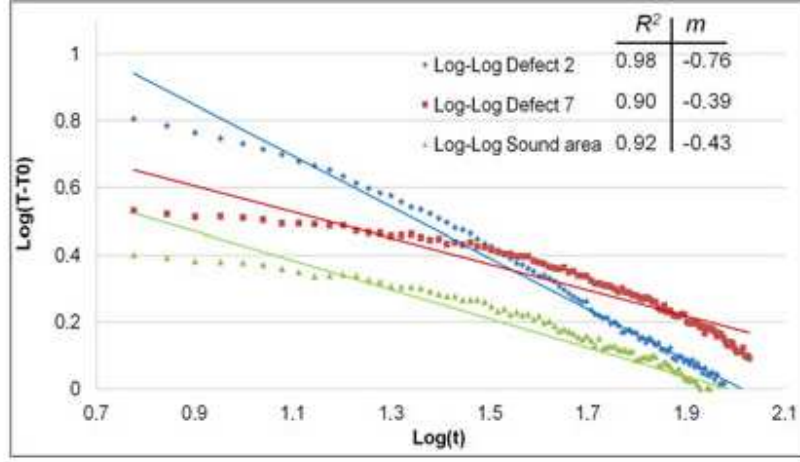


Figure 1.17: Log-log graph of the cooling phase: R^2 and m values assessed for different defects and relative sound (square wave, modulation period 240 s) [87].

In [74, 76, 77], the analogies between the slope and the R^2 in a pulse and step-heating are theoretical explained, in order to demonstrate the possibility to apply these algorithms in both cases.

Several works show the effectiveness of these post processing algorithms [19, 20, 21, 74, 85, 86, 87] for the defect detection, localization and characterization.

1.4.3.2 Thermal Signal Reconstruction (TSR®)

Thermographic Signal Reconstruction (TSR®) [71] is an attractive post processing algorithm that allows to increase spatial and temporal resolution of a sequence, reducing the amount of data to be manipulated at the same time. TSR® is based on the assumption that, non-defective pixels temperature profiles should follow the decay curve given by the one-dimensional solution of the Fourier Eq. 1.19 at the surface for a semi-infinite body stimulated by a Dirac delta function, i.e. Eq. 1.30, that can be rewritten as taking the natural logarithm of both sides.

Shepard [71] proposes to use a low order (n degree) polynomial function to fit the experimental data:

$$\ln(\Delta T) = a_0 + a_1 \ln(t) + a_2 \ln^2(t) + \dots + a_n \ln^n(t) \quad (1.31)$$

Typically, n is set to 4 or 5 to avoid “ringing” and insure a good correspondence between fitting accuracy and signal de-noising for different NDT&E applications [11, 12, 13]. MatLab® provides a direct polynomial fitting function `polyfit()`, in this thesis widely used to provide several results, though the patent version offers some differences of the author knowledge [71].

As a result, the TSR® method Fig. 1.18 provides a significant degree of data compression; in fact, there is a replacement of the sequence of temperature maps in the time, by a series of $(n+1)$ images that correspond to the polynomial coefficient: $a_0(i, j), \dots, a_n(i, j)$. From this series of $(n+1)$ maps it is possible to reconstruct a full thermographic sequence, in addition to obtain a drastic reduction of the data amount [49, 73].

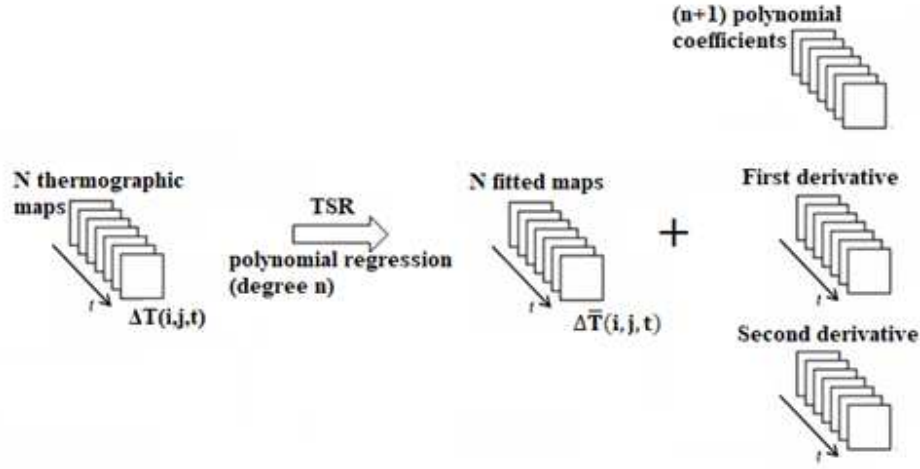


Figure 1.18: Defect detection by the TSR® method, logarithmic polynomial fitting and derivation [20].

It is also convenient to analyse the 1st and the 2nd logarithmic derivatives of the polynomial fitted thermographic sequence [11, 12, 19, 20, 21]. With this fitting operation, there is a significative reduction of the original temporal noise and the transition to the derivative analysis increases the contrast between the defective and the relative sound area. For each pixel, the time sequence can be differentiated using these expressions:

$$\frac{d \ln(\Delta T)}{d \ln(\Delta t)} = \sum_{n=1}^n n a_n \ln^{n-1} t \quad (1.32)$$

$$\frac{d^2 \ln(\Delta T)}{d [\ln(\Delta t)]^2} = \sum_{n=2}^n n a_n \ln^{n-2} t \quad (1.33)$$

First time derivatives indicate the rate of cooling while second time derivatives refer to the rate of change in the rate of cooling. Therefore, time derivatives should be more sensitive to temperature changes than raw thermal images [105].

Fig. 1.19 corresponds to a typical temperature decay for a defective (dotted line) and a non-defective (plain line) area. The first and the second time derivative as calculated with Eq. 1.32 and Eq. 1.33, and the typical trends are shown in Fig. 1.19.

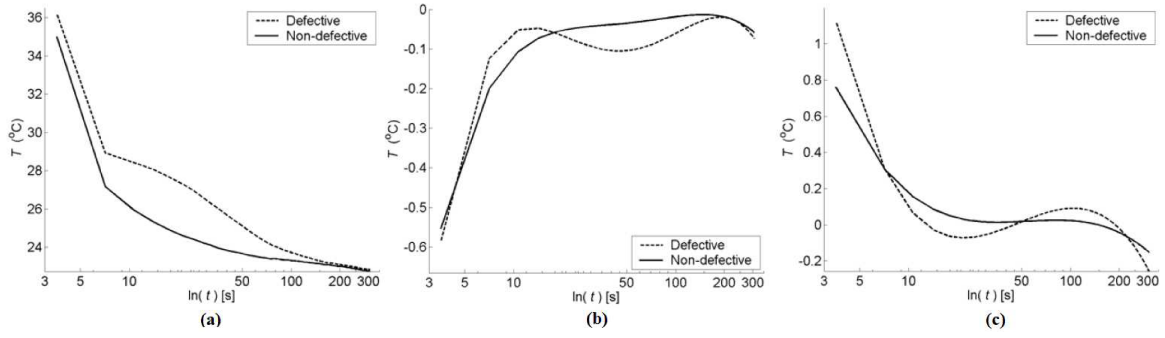


Figure 1.19: Temperature (a) , (b) 1^{st} , and (c) 2^{nd} time derivatives for a generic defective and sound area, after a flash test [127].

The selection of experimental parameters is quite intuitive: for high conductivity materials and shallow defects is necessary to choose high sampling frequency and short acquisition time because the time evolution of the surface temperature changes rapidly; for low conductivity materials and deep defects it is better to choose low sampling frequency and long acquisition time since the time evolution of the surface temperature changes slowly.

The possibility to apply the TSR® algorithm to step-heating thermography is theoretically established in the work of Balageas [76], by analyzing the case of a slab without defect or with a defect of infinite thermal resistance.

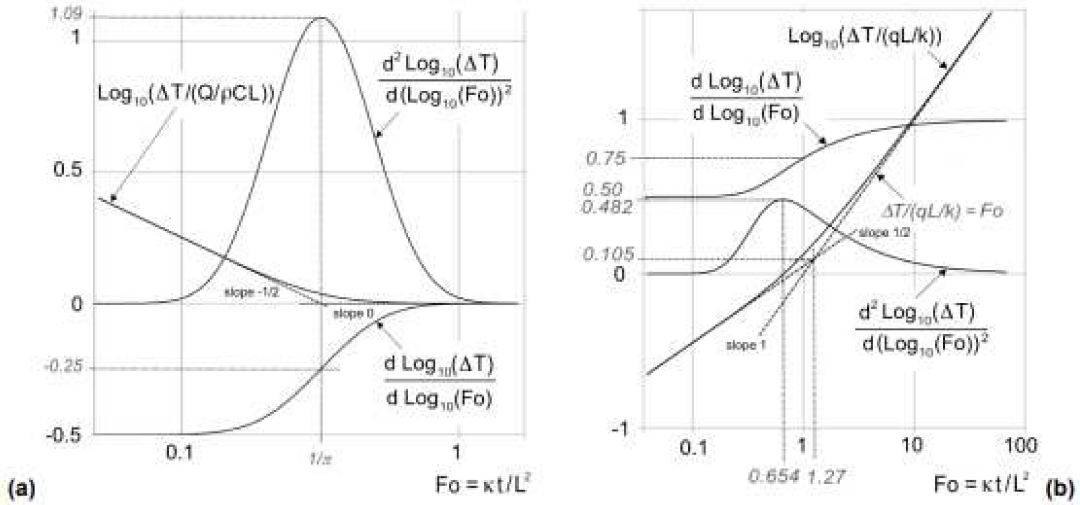


Figure 1.20: Similarities of the thermograms and logarithmic derivatives in the case of a slab of thickness L submitted to pulse- (a) and step- (b) heating. Same results would be observed for an infinite thermal resistance defect embedded at a depth $z_d = L$ in a semi-infinite medium or in a slab. The graphs show the ‘precession’ 2 of the early detection due to the successive differentiation [76].

where $F_0 = \frac{\kappa t}{L^2}$ is the Fourier number. Fig. 1.20 illustrates the typical normalized thermograms for both heat deposition types: as expected, two asymptotes are found for pulse-heating ($-1/2$ slope for short times and null-slope for late times), as well as for step heating ($+1/2$ slope for short times and $+1$ slope for late times). Pulse- and step-heating curves are similar, at least at the beginning of the transition period when an early detection can be

achieved. In a similar way, in [76] the step-heating derivative curves are computed and are shifted along the y-scale, in order to point out the similarities with pulse-heating trends. In [77] the possibility to experimentally apply those processing tools to the relaxation phase occurring once the heating is off (squared-shape or long pulse-heating) have been showed for detection and imaging of realistic delamination-like defects in a composite material.

1.4.3.3 Pulsed Phase Thermography (PPT)

Pulsed phase thermography (PPT) [2, 5, 6, 7, 8, 9, 10, 17, 19, 20] is a technique that transforms thermographic data from the time domain into the frequency domain using Fast Fourier Transform (FFT). Any wave form, periodic or not, can be approximated by the sum of purely harmonic waves oscillating at different frequencies. The Continuous Fourier Transform (CFT) can be expressed as:

$$F(w) = \int_{-\infty}^{+\infty} f(t) \exp^{-j\omega t} dt = A(w) \exp^{i\phi(w)} \quad (1.34)$$

where $w = 2\pi f$. For the PPT, the Discrete Fourier Transform (DFT) is usually preferred because we are working with sampled signals for the actual implementation of the solution.

$$F_n = t \sum_{k=0}^{N-1} T(k\Delta t) \exp^{-j2\pi nk/N} = Re_n + Im_n \quad (1.35)$$

where Re and Im are respectively the real part and imaginary part of the transformed data, the subscript n is the increasing frequency, Δt is the sampling interval and N is the total number of thermograms (infrared images). The phase and amplitude maps are finally obtained using the following relation:

$$A_n = \sqrt{Re_n^2 + Im_n^2} \quad \varphi_n = \tan^{-1} \left(\frac{Im_n}{Re_n} \right) \quad (1.36)$$

Amplitude and phase maps (Fig. 1.21) are obtained by repeating this process for all pixels (x, y) of the field of view. With N time increments available (with N corresponds also to the thermograms in the sequence), N/2 frequency values are available (due to the symmetry of the Fourier transforms) [2, 5, 6, 35, 36].

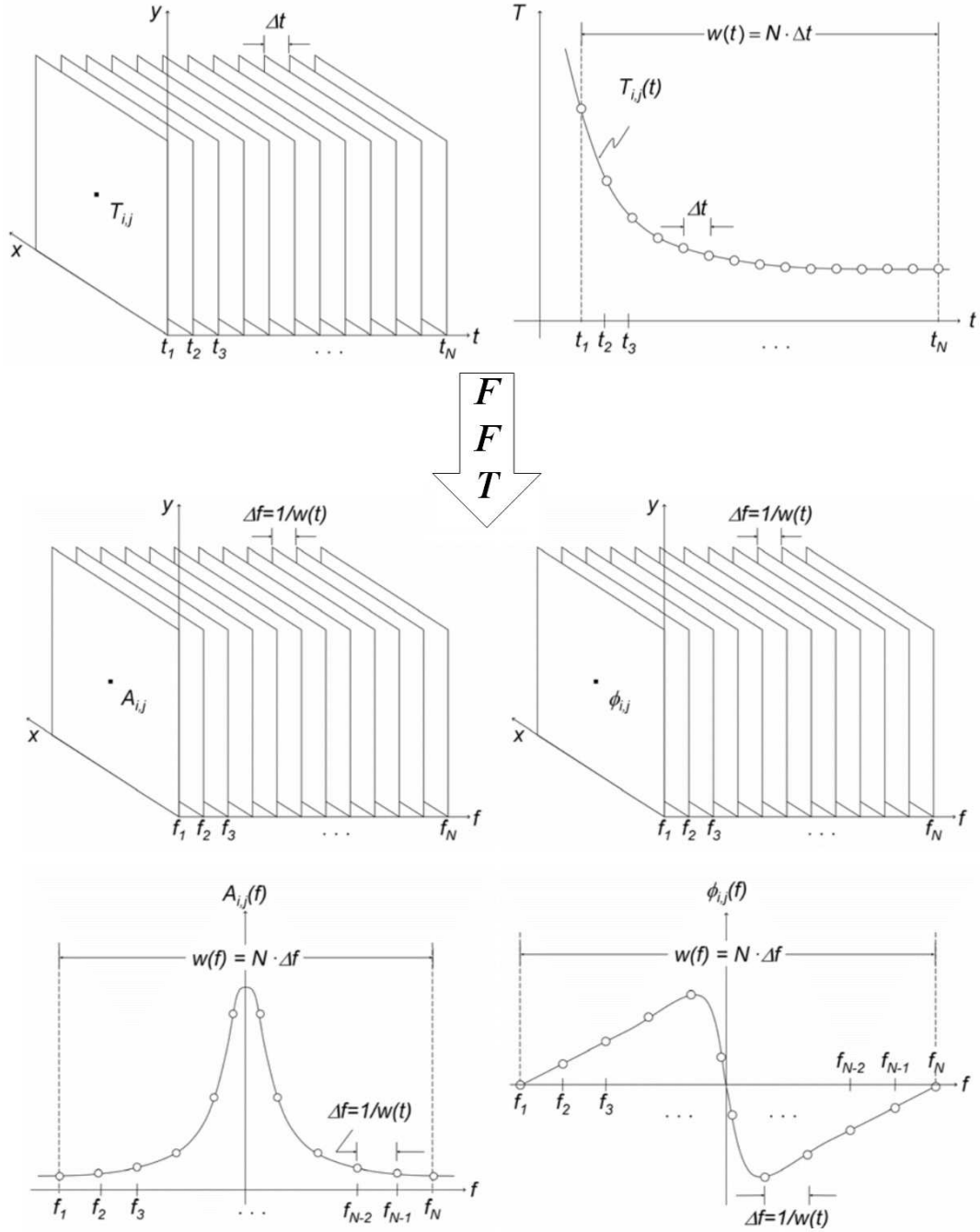


Figure 1.21: Data acquisition and processing by PPT [127].

The quality of the results depends on two important parameters, the sampling rate f_s , and the acquisition time (t_{acq}), i.e. the maximum truncation window $w(t)$. Theoretically, the sampling rate should be high enough to increase the available frequency ($f_{max} = f_s/2$) and capture early thermal changes. The truncation window $w(t)$ should be as

large as possible to increase frequency resolution and to be able to characterize a wide range of depths, especially deep defects that are detectable only at very low frequencies. The material thermal properties are critical in choosing of Δt and $w(t)$. In fact, the much higher time resolution requirement on high conductivity materials is compensated in part by the need of a smaller truncation window. More frames had to be included for aluminum to incorporate more data especially at the beginning of the sequence, where thermal changes are critical. The number of frames N could be further reduced without loss of pertinent information using a higher sampling rate with a shorter $w(t)$ [2, 5, 6, 35, 36]. Other details about the testing parameters for the PPT technique can be found in references [2, 5, 6]. The Fast Fourier Transform (FFT) algorithm, available in software packages such as MatLab®, greatly reduces the computation time and is therefore privileged. It should also be pointed out that the direct implementation of the DFT, as shown in Eq. 1.35 above, requires approximately n^2 complex operations. However, computationally efficient algorithms can require as little as $n \log_2(n)$ operations [19, 20, 86].

1.4.3.4 Principal Component Thermography (PCT)

The Principal Component Thermography (PCT) is a thermographic algorithm based on the Principal Component Analysis (PCA) to extract features and reduce the noise by converting the thermal response data into a system of orthogonal components [88, 89, 90, 91, 92, 93]. In general, the PCA is a linear projection technique for converting a matrix A to a matrix of the lower dimension, by projecting A into a new set of principal axes. One simple approach to the PCA is to use Singular Value Decomposition (SVD), already implemented in the software Matlab® as a function. In general, a matrix A of the dimension $M \times N$ ($M > N$) can be decomposed as:

$$A = URV^T \quad (1.37)$$

where U is the eigenvector matrix of the dimension $M \times N$, R is an $N \times N$ diagonal matrix with positive or zero elements representing the singular values of matrix A , V^T is the transpose of an $N \times N$ matrix. To apply the SVD to thermographic data, the 3D thermogram matrix representing time and spatial variations has to be converted in a 2D $M \times N$ matrix A [88, 89, 90]. This can be done by converted the thermograms for every time as columns in A , as illustrated in Fig. 1.22. Under this configuration, the columns of U represent a set of orthogonal statistical modes known as Empirical Orthogonal Functions (EOFs) that describe the data spatial variations. Besides, the Principal Components (PCs), which represent time variations, are arranged in matrix V^T . The resulting U matrix that provide spatial information can be reconverted into a 3D sequence as illustrated in Fig. 1.22 [20].

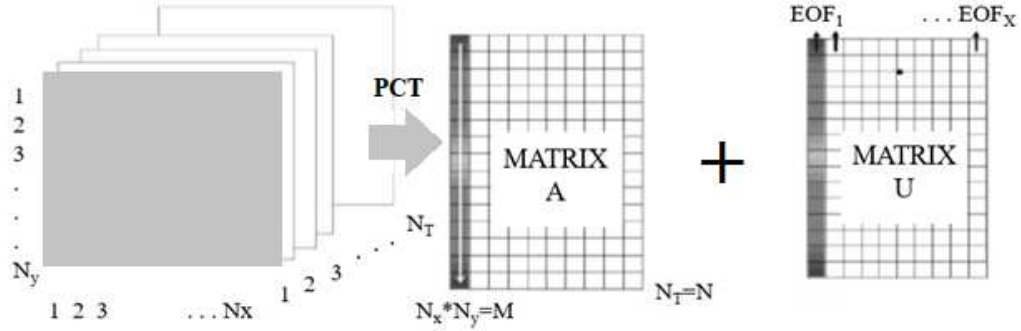


Figure 1.22: Thermographic data conversion from a 3D sequence to a 2D A matrix in order to apply SVD and finally conversion of 2D U matrix into a 3D matrix containing the EOFs [20].

The uncorrelated variables are linear combinations of the original variables, and the first component contain the data with higher variance, while the consecutive components are with decreasing variances, so they are the symbol of noise. Therefore, only few components, in particular often the second principal one, need to be examined in the thermography data analysis to detect defects.

1.4.3.5 Apparent thermal effusivity

The surface temperature of a homogeneous sample decays as $1/\sqrt{t}$ after the energy deposition, as curve blue in Fig. 1.16 illustrates in logarithmic graphical form. From any point of this curve, it is possible to identify the single-valued of the so-called apparent thermal effusivity [42, 62, 78, 83, 84, 94, 95]:

$$e_{app}(L, t) = \frac{Q}{T(L, t)\sqrt{\pi t}} \quad (1.38)$$

where L is the sample thickness or, alternately, the coating thickness (m), t the time (s), $T(L, t)$ is the surface temperature of a coating layer of thickness L deposited onto a semi-infinite body, heated by a Dirac pulse and not subjected to heat exchange with the environment and Q the absorbed energy density (J/m^2). Eq. 1.39 shows how a thickness variation ΔL results in a dilation or compression of the time axis according to a scale factor $a = \frac{1}{(1 + \frac{\Delta L}{L})^2}$.

$$e_{app}(L + \Delta L, t) = e_{app}(L, at) \quad (1.39)$$

If the log-log representation is adopted, the (Eq. (4)) describes the effect of ΔL in a simple translation along the $\log(t)$ axis.

$$\log(e_{app}(L + \Delta L, \log(t))) = \log(e_{app}(L, \log(a) + \log(t))) \quad (1.40)$$

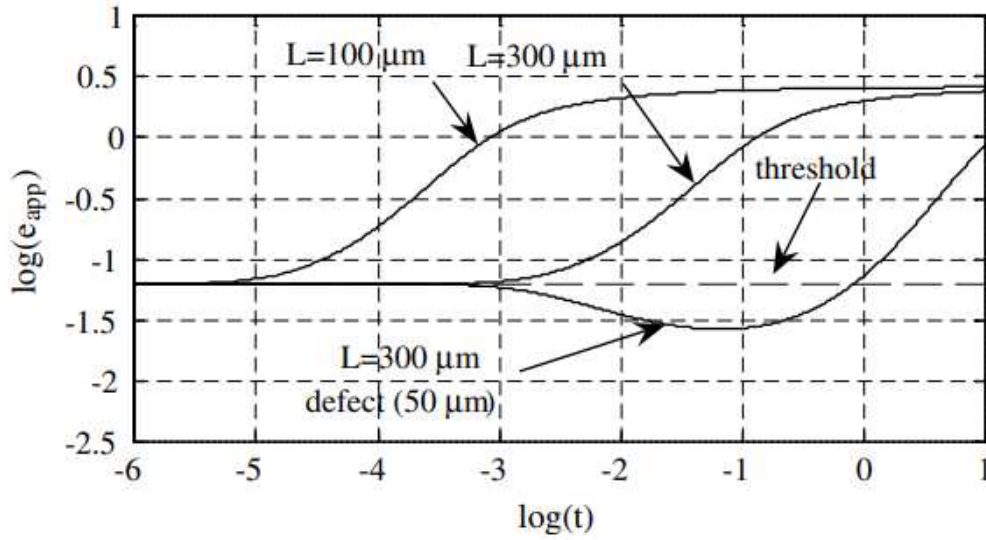


Figure 1.23: Influence of a thickness variation (from $100\ \mu\text{m}$ to $300\ \mu\text{m}$) and an adhesion defect ($50\ \mu\text{m}$ of air under a $300\ \mu\text{m}$ coating) on the apparent effusivity curve [84].

In literature [78, 83, 84, 94, 95], the ΔL translation in a double log scale, together with an apparent change of the thermal effusivity e_{app} , is used to discern the thickness coating variations.

Besides, the presence of a defect causes the appearance of a minimum and therefore a distortion of the e_{app} curve, as shown in Fig. 1.23. This value could be assumed as the discriminating threshold that allows distinguishing adhesion defect from coating variations. Unfortunately, this simple procedure can not be used in practice, because the actual testing conditions distort the e_{app} curve. The threshold value, which corresponds to the value of first sample after the end of heating, is in fact strongly dependent on hardly controllable parameters: the heating pulse duration and the synchronization between the heating source and the acquisition device.

1.5 Lock-in thermography

1.5.1 Data acquisition

In Lock-in Thermography (LT), energy is delivered to the specimen's surface in the form of periodic thermal waves, several experiences must be performed to cover the entire specimen thickness. A high frequency is chosen for the first test (covering shallow defects) and then, frequency is progressively decreased until the entire thickness is included or the minimum available frequency of the equipment is set [97, 98, 99, 100, 101]. In addition, for an adequate measurement of the phase delay angle recorded at the surface, a permanent regime, in which no transient effect is present, needs to be attained each time, slowing-down the process even further. Furthermore, the maximum depth that can be detected is limited by the equipment's range of select-able frequencies.

Fig. 1.24 depicts a lock-in thermography set-up (reflection mode).

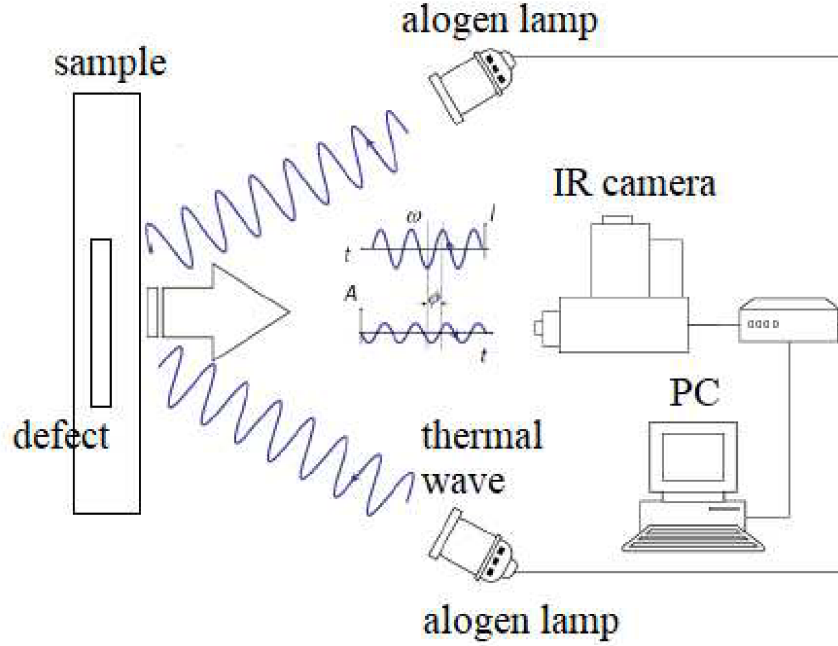


Figure 1.24: Experimental set-up for lock-in thermography (reflection mode).

Two lamps are shown although it is possible to use several lamps mounted on a frame to reduce the non-uniform heating and/or to increase the amount of energy delivered to the surface. It is also possible to use different optical sources, such as halogen lamps, laser. The lamps send periodic waves (e.g. sinusoids) at a given modulation frequency ω , for at least one cycle, ideally until a steady state is achieved, which depends on the specimen's thermal properties and the defect depth. Furthermore, the energy required to perform an LT experiment is generally less than in other active techniques, which might be interesting if a low power source is to be used or if special care has to be given to the inspected part [102, 103, 104, 105, 106, 107, 108].

1.5.2 Theoretical remarks

The Fourier's Law one-dimensional solution for a periodic thermal wave propagating through a semi-infinite homogeneous material may be expressed as [101]:

$$T(z, t) = T_0 \exp\left(-\frac{z}{\mu}\right) \cos\left(\frac{2\pi z}{\lambda} - \omega t\right) \quad (1.41)$$

where T_0 [°C] is the initial change in temperature produced by the heat source, ω [rad/s] is the modulation frequency ($\omega = 2\pi f$, with f being the frequency in Hz), λ [m] is the wavelength; and μ [m] is the diffusion length given by [101]:

$$\mu = \sqrt{\frac{2\alpha}{\omega}} = \sqrt{\frac{\alpha}{\pi f}} \quad (1.42)$$

where k is the thermal conductivity, ρ is the density, c_p is the specific heat at constant pressure, ω is the mod-

ulation frequency and α is the thermal diffusivity. Eq. 1.42 refers to homogeneous materials [101, 102, 103], but qualitative considerations can also be extended to composite laminates. This equation indicates that higher modulation frequencies restrict the analysis in a near-surface region, while low-frequency thermal waves propagate deeper but very slowly [101, 102, 103]. The main drawback of the technique is that, for depth evaluation, the operator has to change and to perform different test, each time changing the frequency of thermal excitation.

1.5.3 Data processing

Contrary to PT for which a great variety of processing techniques are available, as described previously, only a few signal processing techniques are commonly used for LT data.

A four-point methodology for sinusoidal stimulation is frequently cited [104, 105] as a tool to retrieve amplitude and phase. The four point methodology for sinusoidal stimulation is illustrated in Fig. 1.25.

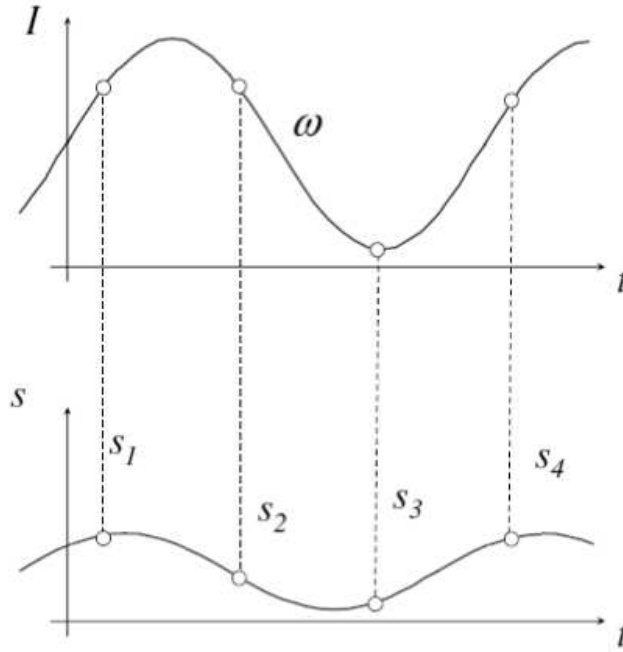


Figure 1.25: Four point methodology for amplitude and phase delay estimation by lock-in thermography.

The sinusoidal input signal I is represented on the top of Fig. 1.25, while the response signal S is depicted at the bottom. Input and output signals have the same shape when sinusoids are used, there is only a change in amplitude A and phase ϕ that can be calculated as follows:

$$A = \sqrt{(S_1 - S_3)^2 + (S_2 - S_4)^2} \quad \phi = \arctan\left(\frac{S_1 - S_3}{S_2 - S_4}\right) \quad (1.43)$$

The 4-point method is fast but it is valid only for sinusoidal stimulation and is affected by noise. The signal can be de-noised in part by averaging of several points and/or by increasing the number of cycles. Furthermore, in order to obtain information about the full depth of a component, different tests have to be performed at different modulated frequencies, and consequently, in the case of a large structure, the application of LT technique can involve elevated

testing time.

Another possibility is to fit the experimental data using least squares regression, and to use this synthetic data to calculate the amplitude and the phase [100].

Alternatively, as for the case of PT, the discrete Fourier transform (DFT) can be used to extract amplitude and phase information from LT data [108], like the PPT approach previously illustrated.

Palumbo and Galietti, in [87], propose the use of a modulated square wave as a heat source in order to reduce the testing time. In fact, in this case, as demonstrated in other works [109, 110, 111], the thermal response of material contains information about high-order frequencies proportional to the main frequency. By decomposing the thermal response in time domain as the sum of a singular sinusoidal wave, the equation is obtained:

$$T_m(t) = a + bt + \sum_{n=1}^{\infty} \Delta T_n \sin(n\omega t + \varphi_n) \quad n = 1, 3, 5, 7, \dots \quad (1.44)$$

where t is the time, a and b are two constants (that can be obtained by applying a last-square fit method) used to model the average temperature growth of the material, ω is the modulated frequency of the main harmonic (first Fourier component), and ΔT_n and φ_n are the amplitude and the phase of n th Fourier component. By considering the terms up to $n = 5$, it is possible to write:

$$T_m(t) = a + bt + \Delta T_1 \sin(\omega t + \varphi_1) + \Delta T_3 \sin(3\omega t + \varphi_3) + \Delta T_5 \sin(5\omega t + \varphi_5) \quad (1.45)$$

Eq. 1.45 allows to obtain information about the amplitude and phase signal of high-order excitation frequencies with respect to the main by a single lock-in test. On the other hand, the signal energy information is distributed on all harmonics, and then the higher harmonics are characterized by a lower signal to noise ratio. This could affect the quality of results. For this reason, it is convenient to fix n equal to 3 or 5. Another advantage of the square wave excitation is that the first cycle of a lock-in test can be used as step heating thermography. More precisely, the cooling phase of the first cycle can be used to evaluate defects [87, 96]. Once again, two parameters can be used to analyze thermal data during the cooling phase: the slope (m) and the linearity R^2 of data.

Chapter 2

Quantitative data analysis with pulsed thermography

2.1 Defect Size Estimation

2.1.1 Thermal contrast and its definitions

PT is probably the most extensively investigated approach because of its ease of deployment [112]. Raw PT data however, is difficult to handle and analyze. There are a great variety of processing algorithms that have being developed to get quantitative suitable information [35, 113, 114]. These data processing algorithms are useful for defect characterization, i.e. determination of the size, depth and thermal resistance of a defect [115, 116], or for the evaluation of surface coatings [42, 117]. Most of these techniques is based and, basically, starts by the thermal contrast evaluation. Various thermal contrast definitions exist [5], but they all share the need to specify a sound area S_a and a defective one. For instance, the absolute thermal contrast $\Delta T(t)$ is defined as [5]:

$$\Delta T(t) = \Delta T_{defect} - \Delta T_{sound} \quad (2.1)$$

with $T(t)$ being the temperature at time t , $T_{defect}(t)$ the temperature of a defective pixel or the average value of a group of pixels (very often a group of 3x3 pixels is considered), and $T_{sound}(t)$ the temperature at time t for the a sound region. This definition can be used in the case of the simple raw thermal data, but also after a post processing parameter computation, in order to obtain a contrast in terms of slope, phase, amplitude and so on. Other thermal contrast definitions have been proposed to estimate the thermal contrast such as the Running Contrast, the Normalized Contrast and the Standard Contrast [167]. In this work, the definition of the normalized contrast or signal background contrast will be often used in order to compare the different post processing results in the same scale:

$$SBC = \frac{MS_D - MS_S}{SD_S} \quad (2.2)$$

where MS_D is the signal due to the defect, MS_S is the mean value of the sound and SD_S is the standard deviation of the sound (background). The used definition is very similar to the signal noise ratio SNR.

Thermal contrast or more in general the contrast for a precise post processing parameter, provide a good indi-

cation of defect characteristics (qualitative and quantitative) when working with relatively shallow defect in homogeneous materials and when a size estimation is required. This simple operation is the departing point for more elaborated analysis. For instance, by locating the time and temperature values for which a generic contrast is maximum for a pixel, it is possible to reconstruct Maximum Contrast (or Peak Contrast) time grams and thermograms. It is also possible to use half the time of maximum contrast [115], the peak slope contrast [116] or the early-time contrast [117], i.e. the time at which thermal contrast begins, in order to reduce the influence of thermal diffusion and to get information about the defect size. However, as explained in next paragraph, the main drawback of classical thermal contrast is establishing and defining a sound area, especially if automated analysis is needed. Even when a “sound” definition is straightforward, considerable variations on the results are observed when changing the location of the “sound” as is well-known [116].

2.1.2 Empirical methods for defect size estimation

The size of defects may be measured directly from the thermograms by knowing the spatial resolution of the employed optics. However, this procedure can be applied successfully only for particular cases (defects of great size and at low depths). Otherwise, the low thermal contrast does not allow for precise measurements. In some cases, specific treatments of images as filtering and restoration may improve defect visualization.

For the PT technique, Giorleo and Meola [127], Giorleo and Meola propose the method of the middle height relating to the temperature profile along the line through the defect centre and by assuming a temperature difference $\Delta T > 0.2^\circ\text{C}$ for the defect detectability. This criterion can be expressed in dimensionless form in terms of the ratio

$$T^* = \frac{T_m - T}{T_m - T_c} \geq 0.5 \quad (2.3)$$

where T_m is the average temperature in the undamaged zone around the defect, T is the local temperature in the damaged zone, T_c is the temperature in the centre of the defect. If a post processing algorithm is used to improve the quality of the raw thermal data, it is possible to substitute the temperature with the examined parameter, such as the phase one, for example, and obtaining similar relations to the previous one.

Another possibility is the estimation of the defect size by investigating the distribution of the time derivative of the temperature over the surface of the sample. First step is to find the maximum contrast between the defect area and the reference area. As second step the tangents on both sides of the temperature profiles at the half of the maximum contrast are set. The defect size is defined as the distance between the intersections of these two tangents with the base line over the reference area.

As a third method, the position of the maximal slope of the temperature profile can be used to define the defect size. With these characteristic points it is possible to determine the size analogous to the method of the tangents and look for the intersections, or use the points of the maximum slope directly.

Since many methods for depth determination require the knowledge of the defect size, there are only a few publications dealing with the quantitative determination of the defect size after applying contrast enhancing pre processing methods.

2.2 Defect Depth Estimation

2.2.1 Quantitative Depth Estimation in the Time Domain

For quantitative depth prediction in the time domain, the main and common idea of the different developed

methods is based on the fact that, when studying the heat diffusion into the investigated material after the application of a thermal pulse, the time taken for the thermal wave to be reflected back to the surface is inversely proportional to the thermal diffusivity of the material and directly proportional to the square of its depth, as already specified in Chapter 1 [118]. The first proposed and the most commonly used method utilizes the time point when the maximum thermal contrast between a defective and a pre selected reference point occurs, known as Peak Contrast Time [119]. Even though this informative parameter can produce quantitative depth information, one of its major limitations is the fact that the peak contrast appears relatively late, when the 3D heat diffusion around the defect has a great influence on the acquired results, or stated otherwise it strongly depends from the defect size.

Consequently, different methods have also been proposed investigating the use of earlier temporal points, targeting to the produced accuracy enhancement [120]. One of the earliest time points on a temperature–time evolution curve, which is used for defect depth estimations, is the moment when the behavior of the studied temperature signal above the defect diverges from the one of the reference sound signal [121]. Usually, as raw thermal data contain noise, the not simple and unique choice of a threshold level is required to identify this point on the temperature–time curve [115]. Besides, the determination of this value requires an acquisition frequency high enough to accurately capture this precise time during a cooling down, impeding the providing of accurate results in the case of shallow defects characterization [122] and for very high diffusive materials.

Another method used to estimate the defect depth is the moment when the thermal contrast curve shows its peak slope [123, 124]. This point can be easily found as it corresponds to the peak of the 1st derivative of the thermal contrast and is commonly referred as Peak Slope Time method. The exact relationship between depth and peak slope time can be determined by solving, for this specific time value, the one-dimensional equation that describe the cooling behavior after a flash test:

$$t_{peak} = 3.64 \frac{z^2}{\pi^2 \alpha} \quad (2.4)$$

where t_{peak} is the time at which the peak in the slope contrast occurs, z is the defect depth in a sample of thickness L and α the thermal diffusivity of the tested material and where the proportionality coefficient equal to 3.64 was found to be valid regardless the type of the material when $\frac{z}{L} \leq 0.5$ [124].

Finally, with the TSR® technique [11, 12, 13, 19, 71, 73], as already specified in Chapter 1, the temperature time function is plotted in double logarithmic scale by a polynomial fitting and then its first and second derivatives can be calculated, by starting from the one dimensional equation valid for a finite body, after a Dirac pulse. The first derivative shows the in-flexion point at a time indicated with t_w , therefore the second derivative has its maximum at this time.

$$t_w = \frac{L^2}{\pi \alpha} \quad (2.5)$$

Shepard et al. in [56] illustrate several benefits of the TSR® derivative method. “The derivative signal is free of temporal noise, rises earlier and reaches its maximum as the contrast signal is just emerging from the noise. The earlier detection capability of TSR® is highly advantageous, as it is less susceptible to convection, 2-dimensional cooling as heat “leaks” out of the trap created by a discrete flaw, and noise that becomes prevalent later in the sequence as the temperature falls. Unlike contrast, TSR® derivatives remain invariant with respect to excitation energy (within the limits of camera dynamic range and temperature sensitivity). Additionally, the TSR® derivatives remove apparent temperature variations due to emissivity or excitation non-uniformity”.

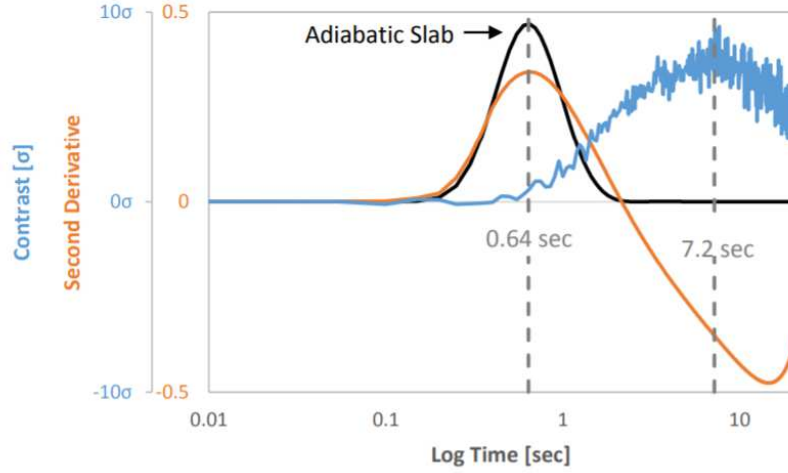


Figure 2.1: Contrast curve (blue) and second derivative (orange) of a flat bottom hole in stainless steel (depth 0.12", diameter 1"). The second derivative peak occurs significantly earlier than the peak contrast time [56].

However, as already demonstrated in some works, there are some problems when this method is used to have a depth estimation, especially when a material with high diffusivity is investigated. In particular, this time is dependent from the acquisition frequency, the pulse duration, the chosen truncation window size, and the polynomial degree. It was also demonstrated that this time is strongly dependent from the defect size. In this work there is a discussion about the results obtainable by applying this feature, and in particular a panoramic of the main parameters that influence this estimation. A comparison among other methods will be also discussed, by analyzing also different materials with high diffusivity.

It is necessary once again to point out that in this work a generic Matlab® routine is used to perform polynomial fitting. However, TSR® is a patented method [71] that is only available in software programs sold by its developers, using optimized, proprietary algorithms. While the generic approach is adequate for the purposes of the comparison performed in this thesis, it is not the authorized, commercial version.

2.2.2 Quantitative Depth Estimation in the Frequency Domain

Frequency domain analysis using quantitative Pulsed Phase Thermography (PPT) and phase data to have a depth prediction approach similar to the early detection in time domain analysis [2, 6, 7, 112]. This approach consists of identifying the depth of the defect from the frequency for which the phase contrast between a defective and a sound area crosses the zero-contrast line. Recalling from the previous section 2.1.1, the absolute thermal contrast is defined as the surface temperature difference between a defective zone ΔT_{defect} , and a non-defective region or sound area ΔT_{sound} Eq. 2.1. In a similar way, a definition for the absolute phase contrast $\Delta\phi$, can be found in literature [125]:

$$\Delta\phi = \phi_{defect} - \phi_{sound} \quad (2.6)$$

where ϕ_{defect} is the phase for a defective area, and ϕ_{sound} is the phase value for a defined sound area. This phase contrast definition, is used in combination with the so-called blind frequency concept f_b , to solve inverse problems by LT and by PPT.

This technique relies on the thermal diffusion length, i.e., $\mu = \sqrt{(\alpha/\pi f)}$ as the depth of the defect can be

estimated from a relationship of the form [126]:

$$z = C_1 \mu = C_1 \sqrt{\frac{\alpha}{\pi f_b}} \quad (2.7)$$

where C_1 is a correlation constant and f_b (Hz) is the blind frequency, defined as the limiting frequency at which the feature of interest presents enough phase contrast for its detection in the frequency spectrum.

The above described procedure for quantitative analysis requires the determination of the blind frequency and of the correlation coefficient C_1 , when the material's thermal properties are known, and so a sample with imposed defects is necessary. Conventional experimental C_1 value when using the phase in experiments is set in a range from 1.5 to 2 [167], with $C_1 = 1.8$ frequently adopted [167].

Fig. 2.2 shows the phase and phase contrast profiles for the case of thick defects (flat-bottomed holes) at two different depths.

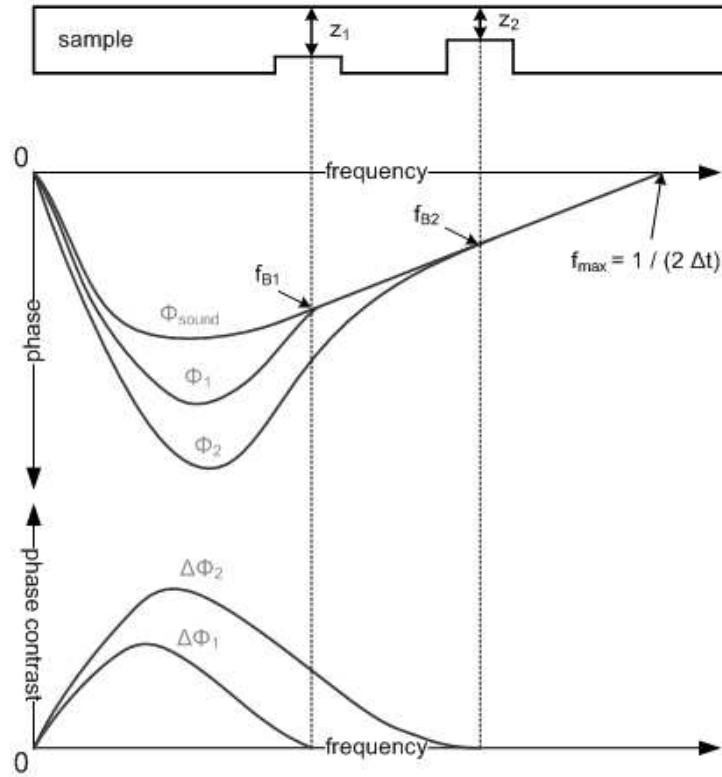


Figure 2.2: Depth quantification with the phase contrast and blind frequency.

As shown, defects are visible from '0' to a given frequency, i.e. the blind frequency (f_{b,z_1} and f_{b,z_2}) which is lower for deeper defects ($f_{b,z_1} > f_{b,z_2}$). As reported within Ibarra dissertation [167], no depth discrimination can be made at frequencies higher than f_b , since profiles merge with the sound area phase profile into a straight line for $f > f_b$. Consequently, shallow defects have a larger frequency range of visibility than deeper one. This analysis suggests that there exists an "optimal" sampling rate to retrieve all the important spectral information for a flaw at a particular depth, which will correspond to the blind frequency at that particular depth f_b .

2.2.3 Influence of the selected sound and defective area

An inappropriate selection of a sound area and a defective one may affect the calculations for depth and size estimation, making this decision a crucial parameter when these estimations have to be performed. As is well known for the thermal case [112], (temperature) contrast depends on the selected sound area. This is primarily due to non-uniform heating and emissivity variations on the surface. Contrast calculations using the phase greatly increase the accuracy of the results, since phase is less affected by these two problems as pointed out above. Still, phase shows some variability on non-defective zones that contribute to the uncertainty of the results [2, 5, 6].

In literature [2, 56, 73, 77], different procedures were followed for the respective depth measurements in both the time and frequency domain analyses, and the influence of this choice is shown. Besides, a new procedure has been introduced in the work of D'Accardi et al. [86] and then resumed in the work of Palumbo et al. [74] in order to make a semi automatic detection of the sound and defective area, independent of the sign of the analyzed post processing parameter. This procedure will be discussed after in the results.

2.2.4 Influence of the truncation window size

Considering the time domain, acquisition should ideally last until thermal changes in the specimen are negligible, e.g. when surface temperature is in equilibrium with its surroundings. However, it could take long time before reaching these conditions, especially for low conductivity materials. In practice, acquisition is truncated when surface temperature shows no thermal contrast with respect to a (contiguous) non-defective area. Once data is acquired, it would be desirable to use all the available information. However, it is sometimes useful to sacrifice time resolution (reducing N in consequence) to increase the area to be simultaneously processed and, after during the post processing, to reduce the computation time. As known, the maximum time resolution corresponds to $\Delta t = 1/f_s$, and the maximum window size is $w(t) = t_{acq}$, where t_{acq} is the duration time in terms of acquisition, within the test. In Fig. 2.3, the concept of the truncation window size is shown by analyzing the simple temperature profile over the time, and by considering an example used by Ibarra Castanedo in [167]. The width of the truncation window $w(t)$, is given by [128]:

$$w(t) = N\Delta t \quad (2.8)$$

where $w(t)$ indicates the size of the truncation window, the total number of points that are going to be sampled N , and the spacing between them Δt .

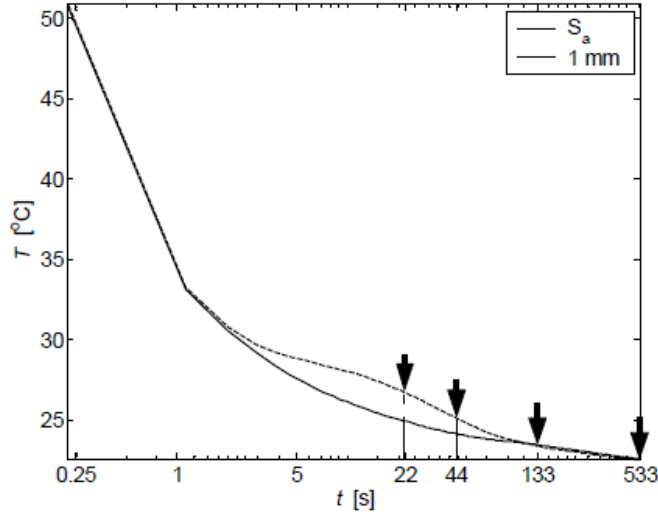


Figure 2.3: Influence of the size of the truncation window on phase for a 1 mm depth flat-bottomed hole on a Plexiglas® at $f_s=22.55$ Hz, $\Delta t=889$ ms; temperature profile [167].

In [167], Ibarra Castanedo has demonstrated the great influence of the $w(t)$ size on the resulting phase spectra; in general, a decreasing in terms of $w(t)$ diminishes the frequency resolution.

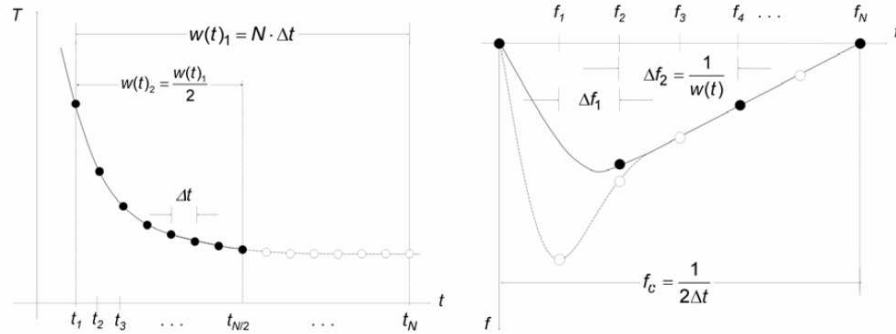


Figure 2.4: The influence of the truncation window size on the phase contrast: decreasing $w(t)$ diminishes frequency resolution [167].

Oswald Tranta, in [6, 7], summarized the effects of the importance of this parameter in the depth estimation by using PPT and TSR® methods and by adopting a FEM simulation model.

However, the choice of this parameter changes based on the used post processing algorithm, and obviously, the correct choice changes and depends on the material and the defect characteristics.

In this final work, an important study is carried out by analyzing the importance of this choice on the quantitative results that are possible to reach by the application of different post processing algorithms, after a pulsed test.

2.2.5 Influence of the frame rate

The definition of the sampling rate is given by [128]:

$$f_s = N\Delta f = \frac{1}{\Delta t} \quad (2.9)$$

As shown in different works [2, 92, 93, 112], the spectrum obtained by FFT, and so if a PPT analysis is performed, the sampling frequency defines the maximal frequency available. Therefore, N points should also be used to compute the transformation, since more points would introduce redundancy, and fewer points would not take advantage of all the available information [128]. However, as stated before, only half the spectra needs to be conserved, reducing the total number of frequency components to $N/2$. Moreover, because of the periodicity requirements for the CFT-DFT equivalency, calculations must be confined to cover only one period of the frequency spectra. In such a case, we should evenly spread the $N/2$ point over one cycle centered upon the origin. The $N/2$ frequency components are separated Δf from each other, where [128]:

$$\Delta f = \frac{1}{N\Delta t} = \frac{1}{w(t)} \quad (2.10)$$

From Eq. 2.10, frequency domain sample spacing Δf , is inversely related to the width of the time domain truncation window $w(t)$. Therefore, to estimate finely spaced frequency components (small Δf), we need to use a large $w(t)$, so these parameters, and therefore these choices are closely linked. In different works of Ibarra Castanedo [2, 92, 93, 112], the influence of this parameter on the results in terms of depth estimation, by using the PPT algorithm and in particular the phase parameter are shown. In particular, it is clear that this choice has a stronger effect especially when a shallow defect is examined; in fact, if the defect depth is less, which means the zero crossing frequency is higher and so, for a good depth estimation and also simple detection of shallow defects high sampling frequency is necessary.

Instead, if a material with a very high diffusivity is analyzed, like the aluminum one, the choice of these two parameters is even more important and, in general, higher frequencies and shorter time are required for a correct defect characterization. Even if there are different works that analyzed the influence of the acquisition frequency on the possible achieved results when composite and polymer materials are investigated, few works took care about the quantitative evaluation of this parameter when the examination regards, instead, an aluminum material.

In this work, there will be an investigation of this choice, also by using different set ups and different cameras that allow to reach different results when a quantitative analysis on an aluminum material is performed.

2.2.6 Influence of the pulse duration and the evaluation start

The derivations, that in the previous sections are shown in order to describe the pulse phenomena, have assumed a Dirac delta heating. Real measurements cannot have infinitesimal short pulse, and it is well known [6, 7] that shortening of the heating pulse is decisive, especially for shallow defects and materials with high diffusivity, where the temperature changes occur shortly after the excitation. Normal flash lamps allow pulse duration of about 3-5 ms and, based on the defect depth and the material diffusivity, a pulse test performed with these typical excitation values can be also as a step heating; this influences the depth estimation both for PPT and TSR® methods. In fact, it will be demonstrated as a pulse flash heating of 5 ms doesn't allow to see the second derivative peak time when an aluminum material is investigated; besides, the temperature deviation that is possible to underline in the presence of a shallow defect respect of the relative sound one occurs already during the heating and in this sense, the thermal diffusivity becomes decisive. That way, the heating pulse duration can have a different importance based on the material and the defect depth.

Instead, when a step heating is performed, longer input pulses can provide several measurement benefits [129].

For example, a longer pulse allows a larger energy input into the system without having to change the power source or lamp. Higher energy dramatically increases the temperature change which reduces the sensitivity to measurement noise. For example, with a 4 kW power source, the energy input is 50 times larger with a 100ms pulse than would be a 2 ms pulse, producing approximately a 50 times larger surface temperature contrast for the same material. For materials with large thermal diffusivity or shallow defects this may not be as critical as the temperature signal is large enough to overcome thermal noise. However, for materials with small thermal diffusivity and when analyzing deeper defects, the ability to simply adjust the pulse time to increase the energy allowing for a larger temperature signal is quite appealing. Additionally, longer pulses can be achieved with standard halogen or LED lighting without the expense of a high-power pulsed voltage source. This ability to use a longer pulse is especially attractive in non-traditional applications to low thermal diffusivity materials such as polymers and powders. These applications are of particular interest in the additive manufacturing (AM) of metal components via powder processes. As shown by Masamune and Smith [130], thermal conductivity of powder beds is significantly smaller than the thermal conductivity of their bulk material counterpart. Thus, the thermal diffusivity are significantly smaller as well and modified testing parameters/equipment would be required for studying powder bed and green components produced by processes such as binder jetting [131]. These techniques would also be appropriate for studying other green powder parts produced by traditional metal and ceramic powder techniques and for polymer AM components. The longer pulse would be helpful for defect detection and improved accuracy. Previous studies have already begun to look at the use of longer pulses up to essentially continuous heating for defect detection. Kim et al. [132] showed that active thermography with a heating duration of 150 s could detect wall thinning in nuclear pipe components though no effort was made to quantify thickness changes. Recently Almond et al. [41] studied a new method of analytical quantification of defect depths using pulse lengths of 5 s. Based on the estimated heat flux applied to the surface above a defective region, they could compare the experimental temperature contrast to predicted contrast and correlate that to a prescribed defect depth. Recently, Pierce and Crane [133] testing a low thermal diffusivity polymer, found that the pulsed thermography quantification method derived by Ringermacher et al. could also be used with longer pulses when the starting point for the peak slope time was taken as the midpoint of the pulse.

In this work, the results achieved by using a long pulse duration, instead a flash excitation, will be shown for the detection of typical defects within a Metal Additive Manufacturing process, when a laser source provide pulse durations of different lengths.

On the other hand, if the heating is not a Dirac delta pulse, the temperature cooling down in a double log scale does not start with a slope equal to -0.5, especially for high diffusivity materials [6, 7]. In the case of a pulse heating with a finite duration the temperature decay deviates rapidly from this theoretical sound behavior.

2.2.7 Influence of the defect size

As already shown by several authors [2, 5, 6, 7, 40, 56] and as very easy to understand, if you have two different defect with a different size, but same depth, the thermal contrast is higher in the case of larger defect; besides, it can be easily demonstrated by applying one of the models that describes the pulse thermal behavior by considering the size influence, the peak times in the case of thermal contrast and log first derivative methods decrease as the defect size decreases. Same considerations are valid in the case of defects with same size, but different depths. The defect detection capability of a pulse test is often demonstrated by simulated the defects as Flat-Bottom Holes (FBH). For large diameter to depth (aspect) ratios, the FBH is typically indicated by the emergence of a localized hot spot in the IR image sequence. The FBH initially behaves identically to an extended adiabatic interface, allowing the centre-point depth to be determined using a one-dimensional model, before three-dimensional effects become

dominant. However, for FBH with smaller aspect ratios, three-dimensional effects become dominant increasingly early. The dependence of these three-dimensional effects on aspect ratio is evident in the first and second logarithmic derivatives obtained through Thermographic Signal Reconstruction® (TSR®) [56], but also in the case of phase contrast by Pulsed Phase Thermography (PPT). If the defect is small, the maximum of the 2nd derivative is shifted to shorter times, although the depth of the defect is the same; the zero crossing frequency depends also on the defect size: small defects see higher zero-crossing [6, 7]. This causes a not correct depth estimation, as also within this work will be emphasized and demonstrated.

2.3 Final remarks

It is not simple to use the thermographic techniques as a quantitative control because there are no standard procedures, but the final results changes based on the application and to certain variables, linked to the set-up and to the thermographic input parameters that can be used and chosen. As already investigated in literature, even if the works that address the subject in question are still few, different limitations and dependencies affected the normal thermographic methods used to do a quantitative analysis of the raw thermal data. Another problem that is often encountered and that the proposed procedures are not explained step by step and that the performed tests and post processing analyzes are often not repeatable.

Within this chapter has been given an idea of the problems that can be encountered when one wants to make a quantitative analysis of the thermographic data, and some indications about the mistakes that can be made. However, the research in this area is not yet complete, the dependencies in terms of defect depth and size, frame rate, pulse length, time of acquisition and analysis have been studied only for some post processing algorithms, often only by simulating the problem with mathematical equations and FEM models. There is something of experimental analysis, but, as shown previously, it concerns composite materials and is mainly applied to samples with imposed defects.

As already specified, the most widely used methods, Thermographic Signal Reconstruction (TSR®), Pulse Phase Thermography (PPT), Slope and Principal Component Analysis (PCA) have all been demonstrated to outperform unprocessed results. However, the methods are quite different in their underlying mathematical approaches and in how results are presented to, and must be interpreted by the end-user. In the past few years, numerous studies have attempted to provide comparative analysis of some, or all of these techniques.

In the next sections, we will evaluate several different results that can be obtained by using these types of post processing analyzes in different ways and for different materials, type of defects and applications, and compare their specific objectives, evaluation criteria, procedure, intermediate results, analyzes and possible conclusions, and identify strengths and pitfalls specific to thermography that should be considered for comparative studies.

A careful analysis of the limits and dependencies on the parameters highlighted in this chapter will be further investigated. Through a careful analysis of the different post processing algorithms, the study of different applications will be evaluated and their advantages and disadvantages shown each time.

The following study in chapters 3 and 4, which concerns an aluminum sample test, is propaedeutic to understand an analysis of this type, to propose a new quantitative procedure and to use the results found to study applications concerning real components and particular defects.

Chapter 3

Pulsed thermography: evaluation and quantitative analysis

Pulsed thermography is commonly used as non-destructive technique for evaluating defects within materials and components. However, raw thermal imaging data are usually not suitable for quantitative evaluation of defects. As already specified and explained before, it was necessary to process the raw thermal data acquired to obtain a series of satisfactory results for a correct and quantitative material evaluation. In the last years, many data processing algorithms have been developed and each of them provide enhanced detection and sizing of flaws.

In this part of dissertation, starting from the same brief pulsed thermographic test carried out on an aluminum specimen with twenty flat bottom holes of known nominal size (diameter and depth), different algorithms have been compared. The algorithms used have been: Pulsed Phase Thermography (PPT) [5, 6, 7, 8, 9, 10], Slope and Square Correlation Coefficient (R^2) [19, 20, 21, 74, 85, 86, 87], Thermal Signal Reconstruction (TSR®) [11, 12, 13], Principal Component Analysis (PCT) [88, 89, 90]. The physical and mathematical theoretical bases of these algorithms are already explained in Chapter 1. By analyzing the results obtained using different approaches, it was possible to focus on the advantages, disadvantages and sensitivity of the various thermographic algorithms implemented.

3.1 Materials and methods

An aluminum sample, shown in Fig. 3.1, with several flat bottom holes of different diameters and depths, has been used for thermographic pulsed tests. The defect nominal sizes in terms of diameter and depth are reported in the same figure.

The thermographic tests have been performed using the IR camera FLIR X6540 SC with the thermal sensitivity (NETD) < 25 mK and with on a cooled detector with a full frame window of 640x512 pixels. A sample rate of 200 Hz has been adopted by assuming a frame window of 464x328 pixels.

The used set up is shown in Fig. 3.2. In particular, two flash lamps with a total energy of 3000 J and a pulse duration of 5 ms have been positioned very close to the specimen (10 cm) and at the same side of the IR camera. This latter has been placed at about 1 m from the specimen, to obtain a geometrical resolution of 0.25 mm/pixel. The two lamps are synchronized using the same power generator. Moreover, three replicates of the same test were carried out, maintaining unaltered set-ups and test parameters. The acquisition time has been fixed at 15 s.

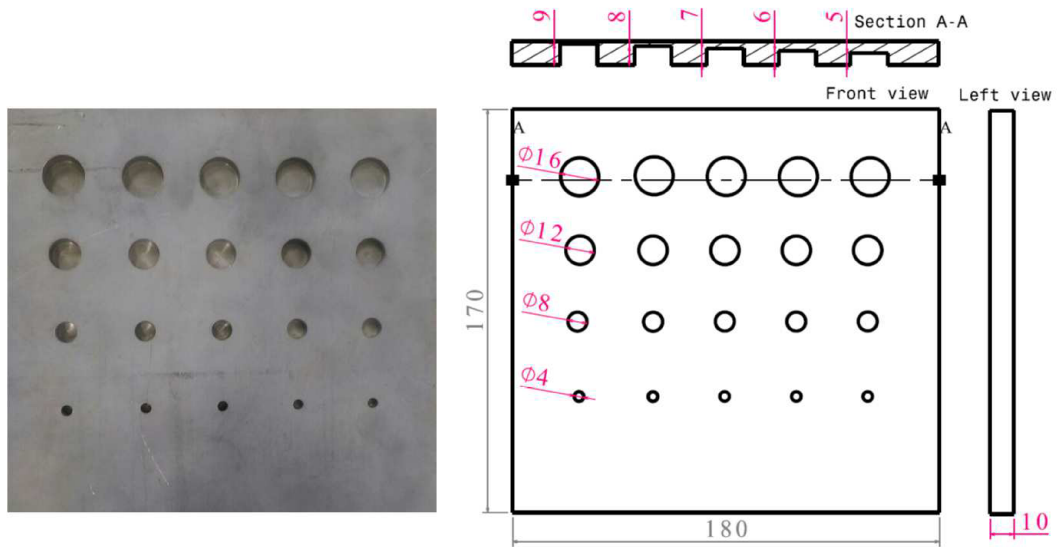


Figure 3.1: Aluminum sample with simulated defects used for thermographic tests; the nominal sizes of the sample and the defects are expressed in mm.



Figure 3.2: The used set-up for the thermographic pulsed tests.

3.2 Data analysis procedure

The application of the different post processing algorithms has required a further elaboration of acquired data to obtain better results. For instance, a pre processing procedure was implemented before the application of each algorithm. The steps of this procedure can be summarized as follows:

- Importing of the thermographic sequence (3D matrix);
- Subtracting of the average of the first ten cold frames to the whole sequence to obtain the ΔT sequence over time;

- Normalizing the local temperature values at any time by dividing them to the value evaluated at time t' sufficiently near to the pulse occurrence (the time t' corresponds to the instant in which the maximum ΔT is reached) [56]. This pixel-wise operation gives to each pixel, at time t' , the value equal to 1 to the normalized temperature rise. The advantage of this step is to reduce the effects of non-perfect heating of the sample and the variability of the optical properties of the surface, such as absorptivity and emissivity [19]. The effects of the normalization are summarized and shown in Fig. 3.3.
- The 3D final sequence, obtained in this way, has been processed by using the proposed post processing algorithms.
- A Gaussian filter has been applied ($\sigma = 1$), in all cases, on each thermographic map, in order to decrease the noise. The effects of the application of this filter are shown for an example of thermographic result reported in Fig. 3.4.

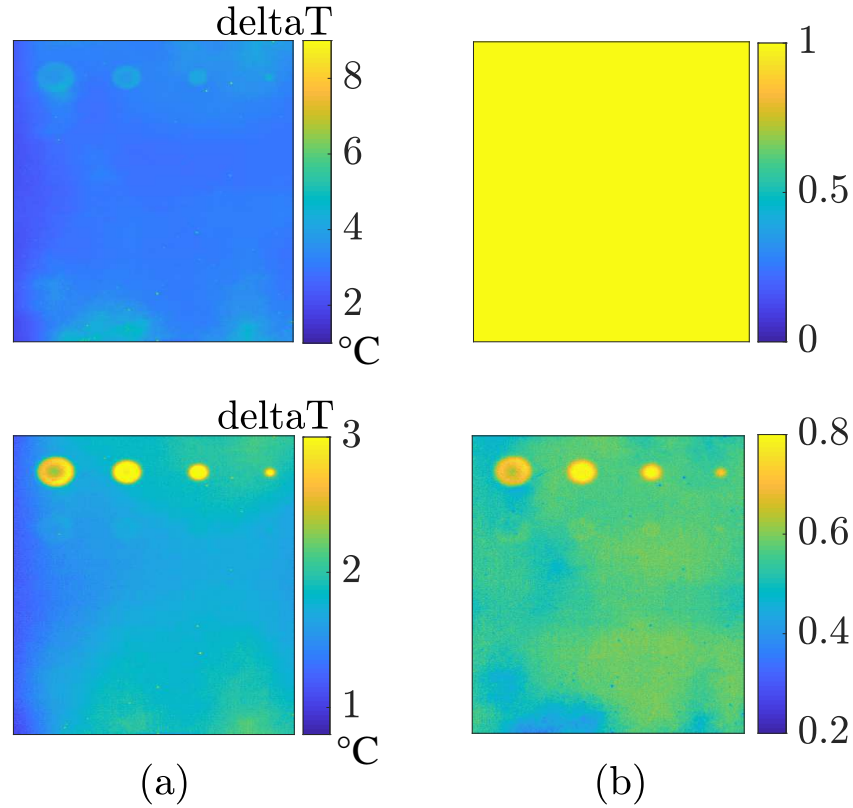


Figure 3.3: The effects of the normalization related to the first frame after the flash excitation; (a) before normalization, first and second frames; (b) after normalization, first and second frames.

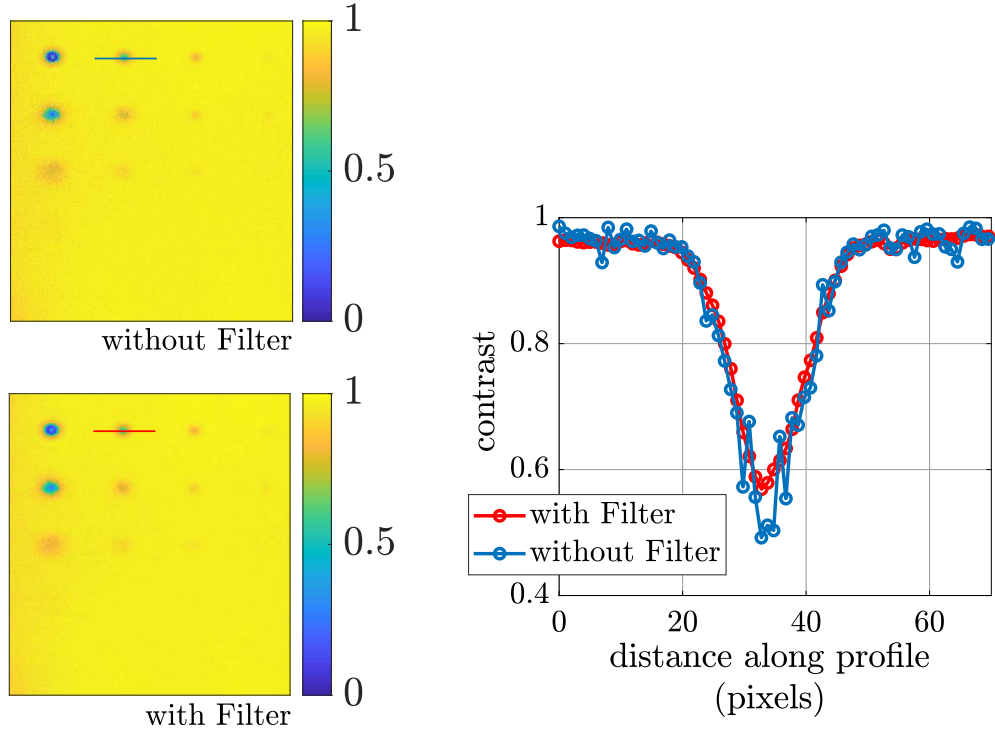


Figure 3.4: The effects of the application of a Gaussian filter, contrast related to the 2nd principal component result, by considering the defect with a diameter of 12 mm and a depth of 1 mm; maps and related trends.

Each algorithm was implemented by using the various functions already present in the Matlab® library.

More precisely:

- The *fft* function for the PPT algorithm and the functions “angle” and “abs” in order to obtain the phase and the amplitude maps, respectively;
- The *svd* (Singular Value Decomposition) function for the PCT algorithm;
- The *polyfit*, *polyval* and *polyder* functions for the TSR®, Slope and R^2 algorithms.

In particular, by using the *fft* function already implemented in Matlab® environment, the discrete Fourier transform (DFT) of the signal is computed, pixel by pixel, using a fast Fourier transform (FFT) algorithm, already written in Matlab®. In this way, the signal is obtained for each pixel along the frequency spectrum and, using the angle and abs functions, the amplitude and the phase maps are computed for each analyzed frequency. Obviously, the obtained results in terms of phase and amplitude depend on the truncation window size (analysis interval) and on the acquisition frequency.

For the PCT algorithm, the *svd* function in Matlab® returns numeric unitary matrices U and V with the columns containing the singular vectors, and a diagonal matrix S containing the singular values. The matrices satisfy the condition $A = U \times S \times V'$, where A is the initial matrix with the normalized delta-temperature, pixel by pixel, and where V' is the Hermitian transpose (the complex conjugate of the transpose) of V . The singular vector computation uses variable-precision arithmetic. In this case, the economical SVD version has been chosen because it is faster: if A is an m -by- n matrix with $m > n$, then SVD computes only the first n columns of U . In particular, the matrix U

contains the principal components, used to achieve the shown results. For applying the PCT analysis, it has been necessary to subtract from each data array the average of the same and to normalize respect to standard deviation, as indicated in the literature, Rajic N. (2002).

The evaluation of slope, R^2 and 1^{st} and 2^{nd} derivatives after a polynomial fitting (TSR® algorithm) has been obtained by processing the thermal sequences using the Matlab® commands `polyfit`, `polyval` and `polyder` for a polynomial fit of the data of first degree in the case of slope and R^2 and fifth for the polynomial fitting and related 1^{st} and 2^{nd} derivatives. In order to evaluate the polynomial coefficients of the chosen fitting, the already implemented Matlab® functions perform an ordinary least squares calculation.

All algorithms have returned several types of thermographic maps, like the one reported as example in Fig. 3.5.

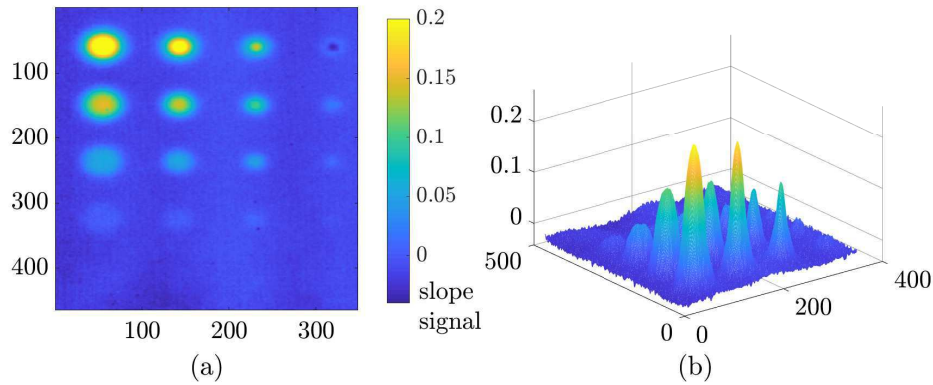


Figure 3.5: An example of obtained results: the slope signal after only 16 frames of analysis; (a) 2D map, (b) surface map.

3.2.1 A new procedure for the identification of the sound and the defective material

To characterize every flaw, it has been necessary to identify a sound zone to be taken as a reference. A common problem to all implemented methods is the definition of the sound zone. In literature, as already cited, there is not a specific procedure to identify this zone, unequivocally. For a pulsed thermographic test, several ways have been tested to define the sound reference: i) from a prior knowledge a part of an image is taken as the sound reference; ii) a test sample is identical to the one analyzed and within defects; iii) in the single pixel analysis, the soundness is determined locally, for each pixel, considering the thermogram evolution at any time. In the work of Giorleo G. et al. (2002) [127], the method of the “contrast full-width at half-maximum” has been proposed to discern defect and sound. However, this method is unattainable, because it is dependent on the nature of the physical and thermographic parameters that are being analyzed, and, hence, from the sign change between the defect and the sound zone Fig. 3.6. This dependence from the sign makes non-automatic the procedure, and then make it rather slow if there are many thermographic maps to analyze (as in the case of this work) or if there are any defects in the tested specimens.

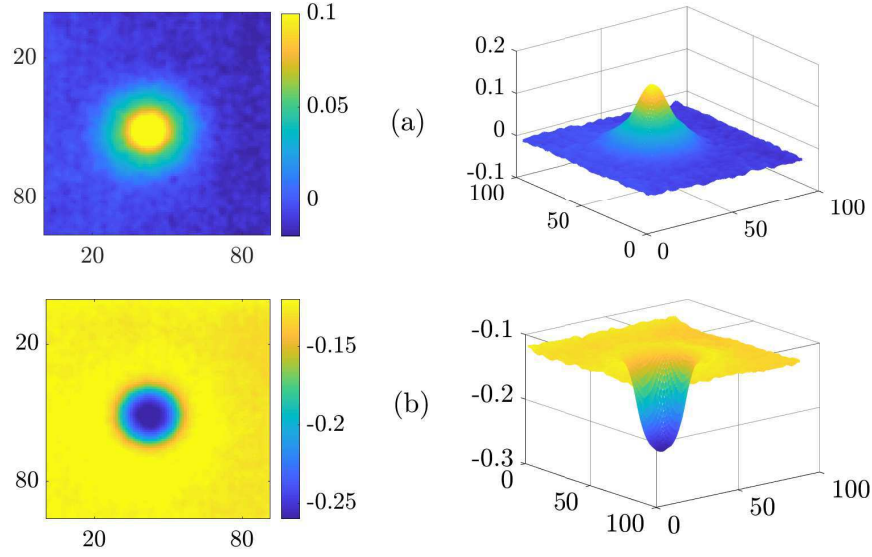


Figure 3.6: An example of "sign change"; second derivative (TSR®), frame 40, 2D maps and relative surfaces; (a) positive sign, (b) negative sign.

Then, it has been used a new method to detect the sound and defect zone by analyzing the trend of the standard deviation (std) of the acquired data. This new method, which for brevity will be indicated by the acronym "std method", is described below in detail and applied to the specific case study for each obtained map and for each used algorithm.

For each defect, it has been chosen an area so as to consider the sound and the defect zone and to have the same number of pixels for each defect/area. In this way, a matrix has been obtained for each defect and relative sound and so it has been calculated the trend of the standard deviation for row and for column, getting results similar to the following (example). As well known and obvious, the standard deviation trend is always positive, regardless of the parameter sign. As you can see from Fig. 3.7 and as might be expected, the trend of standard deviation shows a peak where the defect is present. It has been chosen a threshold of 0.5 on the trend of standard deviation (which is the same in all algorithms) to discriminate the sound area from the defect area, Fig. 3.7. In particular, to define this threshold, a delta has been calculated on the trend of standard deviation with reference to 98° percentile and 2° percentile; as highlighted in Fig. 3.7, the sound area is that under the 0.5 threshold, while for the defect, after locating the peak of this trend, it has been chosen the pixels with value greater than the 98% of the peak value.

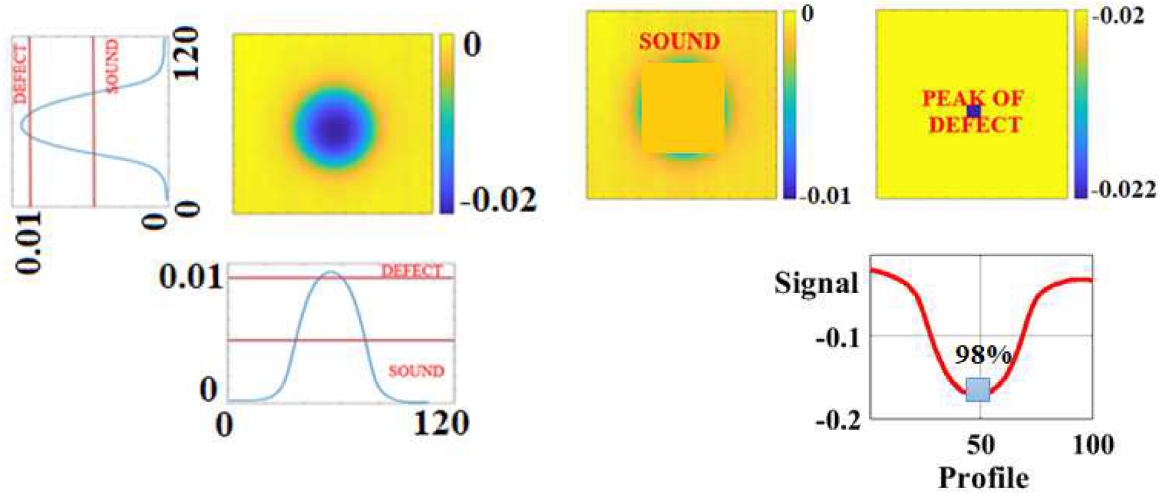


Figure 3.7: An example of the sound individuation by “std method”: the trend of standard deviation (2^{nd} principal component map, defect with diameter 16 mm and depth 1 mm).

This logic, used to detect the presence of the defect, has been maintained for each algorithm. To make automatic the research of the defects, the same threshold value has been maintained. In particular, the value of 0.5 referred to the standard deviation has been chosen for avoiding the overlapping of the defect zones which occurred in the maps extracted by using PPT algorithm. In these maps Fig. 3.7, because of the mutual influence among defects, another threshold value would have led to few defective pixels for evaluating the sound zone. However, as shown in Fig. 3.7, for some algorithms, this choice has not been advantageous, because, when evaluating the sound area, there is also a presence of some defective pixels. So the normalized contrast is lower and the obtained result is more conservative.

Then, the normalized contrast (SBC) from Eq. 2.2, for each defect and for each physical and thermographic parameter obtained as final result has been calculated. The results obtained using the developed “standard deviation” method are in agreement with those obtained using the “contrast full-width at half-maximum (semi-contrast)” method, as it is shown in the following plot, selected as example. The blue areas are the ones taking in consideration as sound material to calculate the “semi-contrast” for each defect; instead, the defective signal is the one obtained by considering the mean of a matrix 3×3 in the center of the thermal signature of the defect. For the individuation of the defective and sound areas with the “std-method” the semi-automatic procedure described above has been adopted.

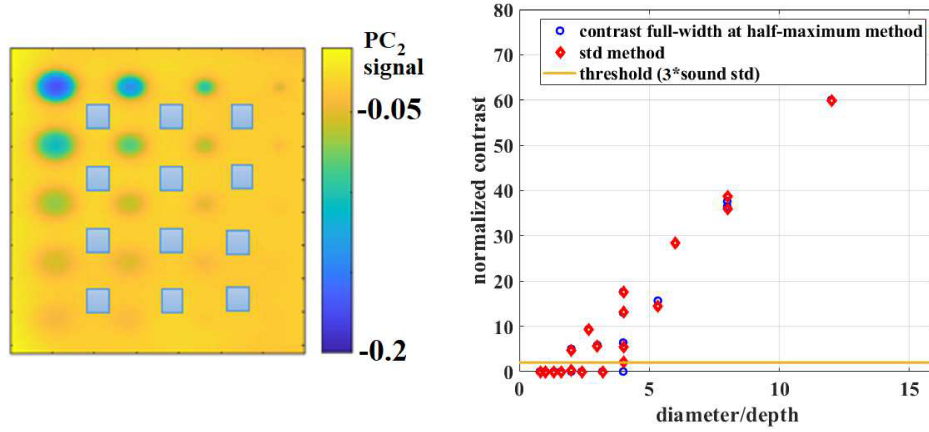


Figure 3.8: An example of the confront between the "standard deviation" method and the "contrast full-width at half-maximum (semi-contrast)" one for evaluating the sound material; the normalized contrast by considering the result related to the 2^{nd} principal component.

The plot in Fig. 3.8 shows the trend of the normalized contrast (SBC) versus the depth-diameter ratio (r) for each defect. Very similar graphs have been obtained from the other developed algorithms. The defect detection has been assessed by imposing a threshold value equal to 3 times the sound standard deviation SD_S , for each algorithm and for each performed analysis. In this way, defects are detected if:

$$MS_D - MS_S > 3xSD_S \quad (3.1)$$

In the literature, a similar criterion has been used for the quantitative analysis of defects [127]. It is important to underline as the threshold value depends on several factors such as, the material, kind of defects, adopted heat sources, surface condition, etc. In our case, as shown in Fig. 3.8, the chosen threshold seems to give a good response about the detectability of defects. In fact, the threshold value allows for detecting at least the defects above the aspect ratio of two, which represents the limit for the PT technique [5, 6, 7, 8, 9, 10, 11] and discards the false positives. Moreover, the proposed approach follows the probabilistic criterion according to which, if a phenomenon is distributed as a Gaussian normal distribution, the 95% of the values falls in the range between $\mu \pm 3\sigma$. It follows that the probability of finding a single defected pixel with a contrast below $3\sigma + MS_S$ is equal to 0.

In order to compare the reached results and in order to have the same scale for each analysis carried out, it is necessary to choose a single standard deviation value with reference to the sound area. In Fig. 3.8 the sound areas chosen to assess the MS_S and SD_S values are shown. For each defect, the same sound area has been considered as the sum of the sound areas indicated in red in Fig. 3.8.

3.2.2 A "new way" to process the thermographic maps: preliminary results

In the first instance, for all implemented algorithms, it has been chosen to analyze 256 frames of the decay curve corresponding to 1.28 s because, in this time interval, the thermal phenomena can be considered terminated and because when a Fast Fourier Transform (FFT) analysis is performed, it is best to have a number of data equal to a power of two.

The described procedure in terms of sound and defect identification has been applied for each algorithm and for each obtained map/sequence of maps. In the case of algorithms that return a single map (slope and R^2) or for which

the fundamental analysis can be limited to a single result (PCT-2nd principal component), the analysis of the final result is more simple: the algorithm for automatic defect search is applied, the automatic procedure is repeated for each defect and the normalized contrast relative to the analyzed map is calculated. Different is, instead, the case of a sequence of maps to analyze (phase PPT and TSR® in terms of polynomial, 1st and 2nd derivative). The same type of analysis has been adopted for phase (PPT) and TSR® results. For brevity, the phase PPT case will be described, but similar considerations can be made and so shown in the case of TSR® results. By applying the FFT analysis on the thermographic sequence, a phase map has been obtained for each extracted frequency. In order to compact the results, a defect is chosen to be analyzed at a time. In fact, as known, for each considered pixel, the phase trend is a function in the frequency domain; the difference between a defective pixel and the relative sound one is the phase contrast over the frequency.

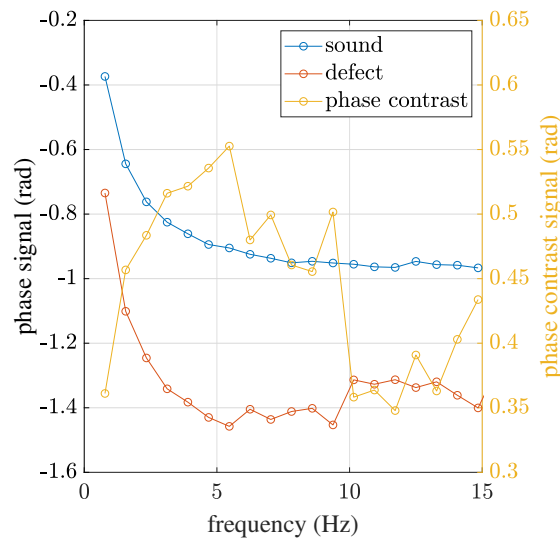


Figure 3.9: Phase and phase contrast trends by considering a defect and the relative sound as example.

In particular, the difference of this trend between the defect and the relative sound area shows a peak at a precise frequency value which depends from the depth and the size of the defect. At this frequency, the contrast between the defect and the sound area is maximum. In Fig. 3.10, an example of this trend is reported; the defective and the relative sound zones, to calculate these trends, have been identified with the “std method”. The values that are equal to 0 don’t exceed the chosen threshold.

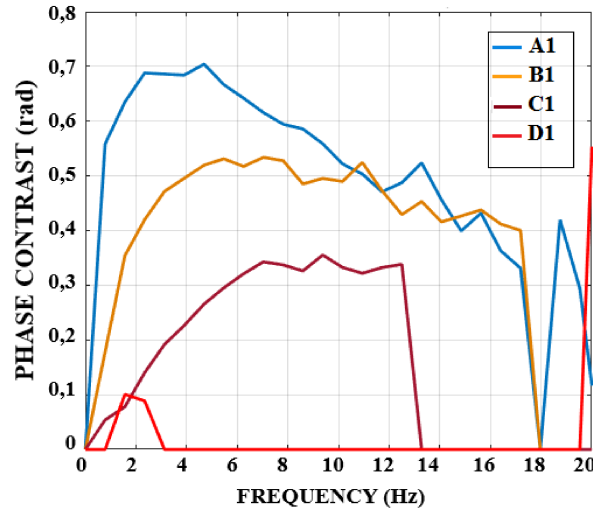


Figure 3.10: The trend of the phase contrast as a function of the frequency, defects at 1mm depth; an application of the “std-method” when a sequence of maps is considered. .

The automatic procedure is repeated for each defect and the frequency corresponding to the maximum contrast for each of them is identified: this frequency depends on the size and depth of the same defects. In this way, the results are compacted into a single 2D matrix and the maximum normalized contrast is calculated for each defect thus identified. In this way also the results related to the TSR® algorithm are carried out.

For brevity, the graphs related to the normalized contrast and the final maps are reported as final comparison in two different figures (Fig. 3.11-Fig. 3.12).

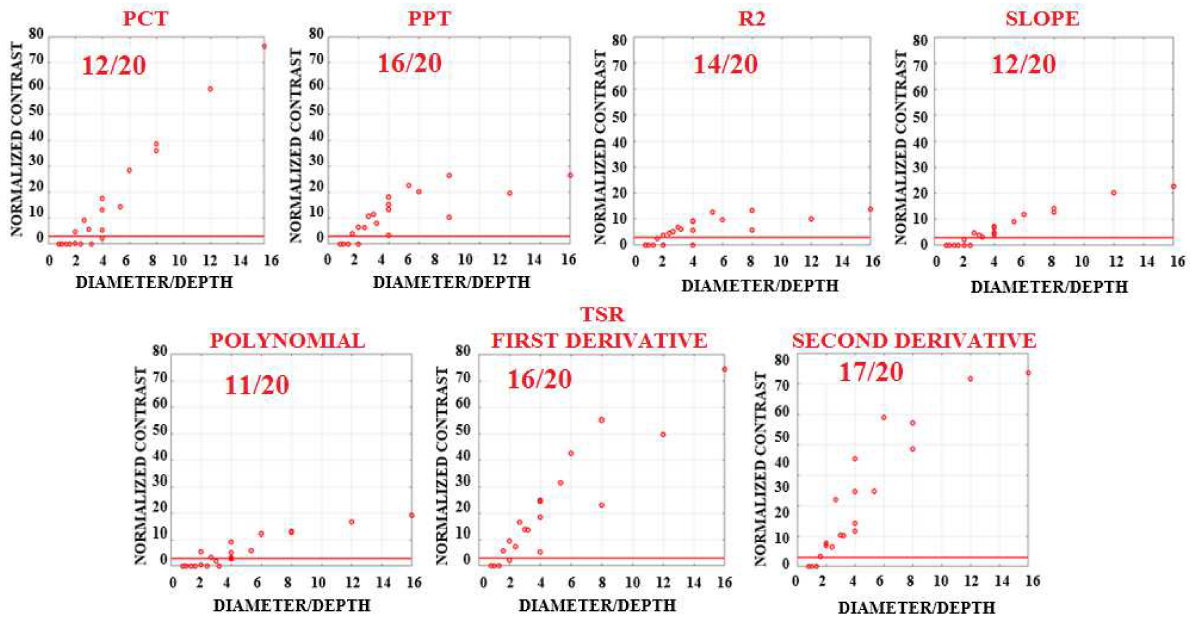


Figure 3.11: Comparison among the several algorithms in terms of maximum normalized contrast; single trends.

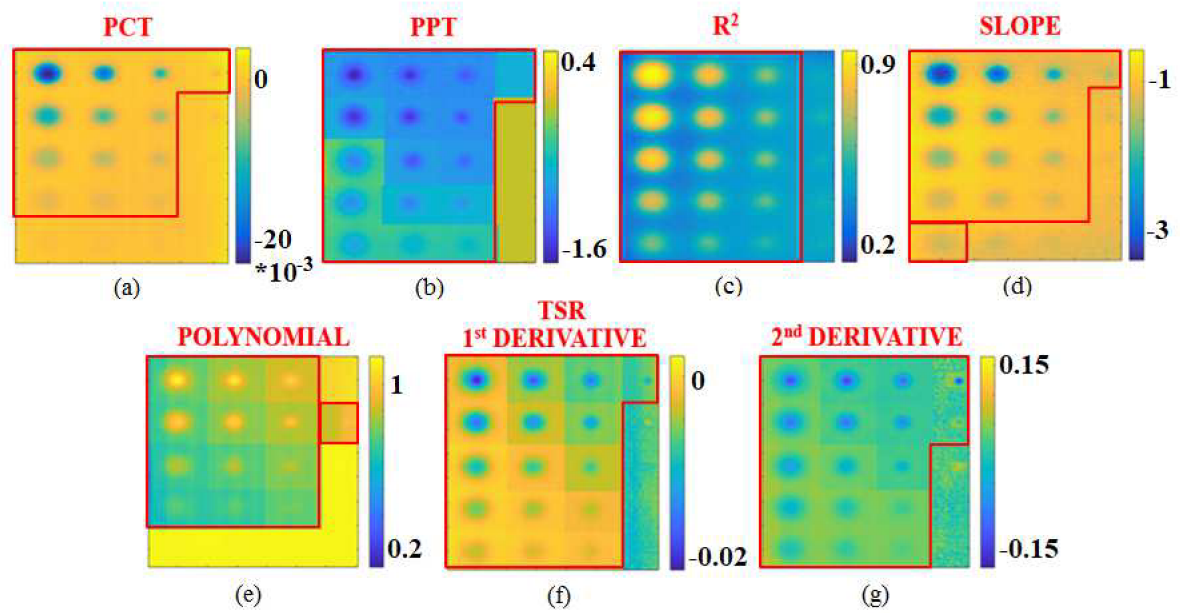


Figure 3.12: Comparison among the several algorithms in terms of maximum normalized contrast; final maps, (a) PCT, (b) PPT, phase, (c) R^2 , (d) slope, (e) TSR®, polynomial, (f) TSR®, 1st derivative (g) TSR®, 2nd derivative (truncation window size: 256 frames, 128 seconds).

The results obtained for each algorithm have been compared in order to show the differences among the several algorithms implemented. The several algorithms have been compared in terms of:

- number of detected defects (columns in blue in Fig. 3.13);
- number of detected defects with a specific depth (Fig. 3.13a);
- number of detected defects with a specific diameter (Fig. 3.13b);
- maximum normalized contrast (already shown Fig. 3.11).

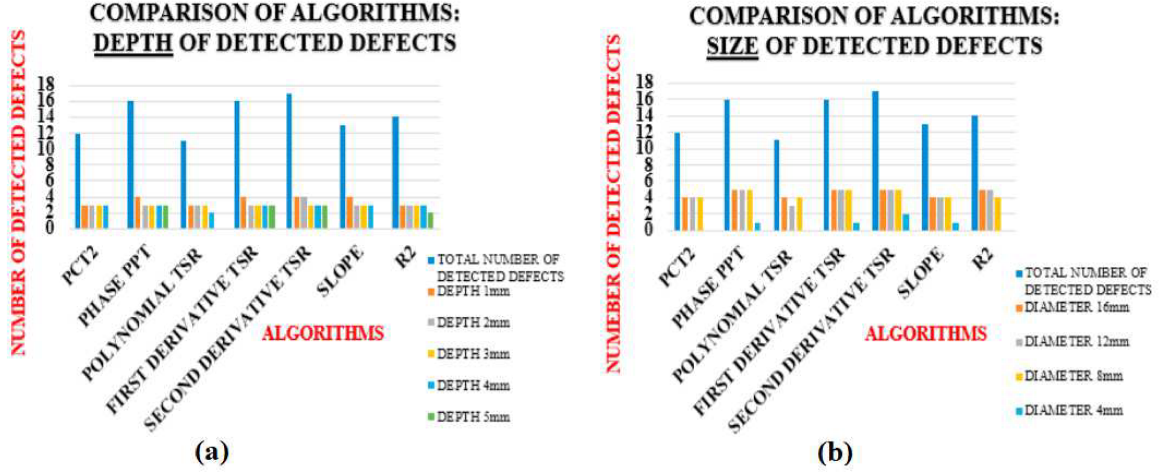


Figure 3.13: Comparison among the several algorithms in terms of depth (a) and size (b) of detected defects.

The TSR® algorithm, in particular, the second derivative of the polynomial, seems to return the best results: 17/20 defects have been detected at the calculator, with an elevate normalized contrast. The PPT algorithm shows a good sensitivity to detect the analyzed defects, with a number of 16/20 defects detected. However, the normalized contrast results obtained using PPT algorithm are much lower than the obtained TSR® results. The PCT algorithm returns good results in terms of maximum normalized contrast, however doesn't show a great sensitivity in detecting both small and deep defects, for a total of 12/20 detectable defects. The algorithms of the R^2 and the slope do not show great results, in particular it seems that the R^2 is more influenced by the size of the defect (0/5 defects of 4mm diameter-Fig. 3.13b) instead of the depth (2/4 defects of 5mm depth-Fig. 3.13a), while for the slope algorithm the opposite occurs. These last algorithms show also fairly low contrast (Fig. 3.11).

The analysis thus conducted shows how the application of different calculation algorithms leads to obtaining complementary results among them; besides, it is clear that the chosen analysis window influences the results obtained, mainly in terms of maximum normalized contrast and number of detected defects, and that the same influences in a different way the obtained results based on the used algorithm.

For this reason, it is necessary a further analytical and experimental investigation concerning the influence and the influences of the truncation window size on the chosen analysis and then on the obtained results.

3.3 The influence of the truncation window size: first experimental results

In particular, seven different sets of frames and then seven intervals of the cooling curve were chosen for analysis: 16, 32, 64, 128, 256, 245 512, 1024 frames. The power of 2 for each interval has been chosen to perform a fast post processing analysis with the PPT algorithm (Fast Fourier Transform). The last interval corresponds to 5.12 seconds. As example, in Fig. 3.14, the several trends for each analyzed interval are shown in the case of the slope algorithm computation.

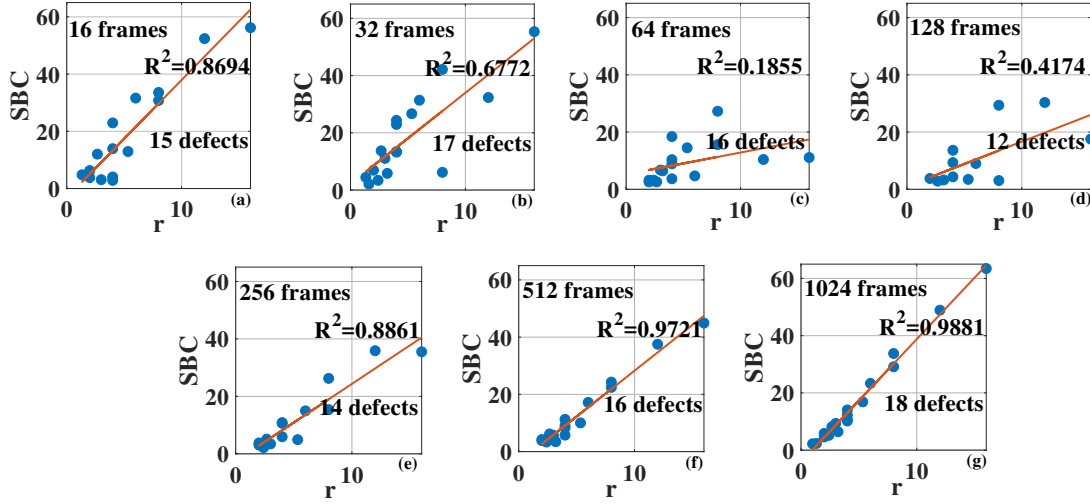


Figure 3.14: SBC values for the Slope algorithm and for different truncation window sizes; (a) 16 frames-0.08 s, 32 frames-0.16 s, 64 frames-0.32 s, 128 frames-0.68 s, 256 frames-1.28 s, 512 frames-2.56 s, 1024 frames-5.12 s.

For completeness of information, in the Fig. 3.14, is reported another parameter of comparison: the goodness of a linear fit expressed in terms of Square Correlation Coefficient R^2 and which indicates how linearly the data are correlated in terms of SBC and respective defect aspect ratio (r). In Tab. 3.1, the obtained results for each interval and for the chosen post processing algorithm (slope) are summarized and this value is indicated together with the number of detected defects, because, of course, these parameters are closely connected: we can only speak of a good linear approximation only if, however, there is a high number of detected defects within the same considered analysis interval.

truncation window size	goodness of approximation	number of detected defects
16 frames, 0.08 s	0.87	15
32 frames, 0.16 s	0.68	17
64 frames, 0.32 s	0.19	16
128 frames, 0.64 s	0.42	12
256 frames, 1.28 s	0.89	14
512 frames, 2.56 s	0.97	16
1024 frames, 5.12 s	0.99	18

Table 3.1: Slope algorithm: evaluation of the SBC- r correlation for different analysis intervals and relative defect number.

In this case, for this algorithm, the better results, in terms of both the linearity and the number of detected defects, are obtained for a number of frames equal to 1024. This is not always true in the case of the other algorithms and not always a good correlation between SBC and r is obtained.

Therefore, a way to compare the different algorithms consists on the analysis of the number of the detected defects for each interval. The obtained results are presented in a bar plot by reporting in x-axis the different chosen intervals and in y-axis the number of the detected defects for each algorithm Fig. 3.15. In this analysis, the amplitude algorithm obtained after the application of a PPT analysis has been added by applying the same procedure described

before; the results obtained in the case of the application of TSR® algorithm are and will be summarized only in terms of 1st and 2nd derivative, as they are better than those achieved by the simple analysis of the polynomial fitting in temperature, and therefore redundant.

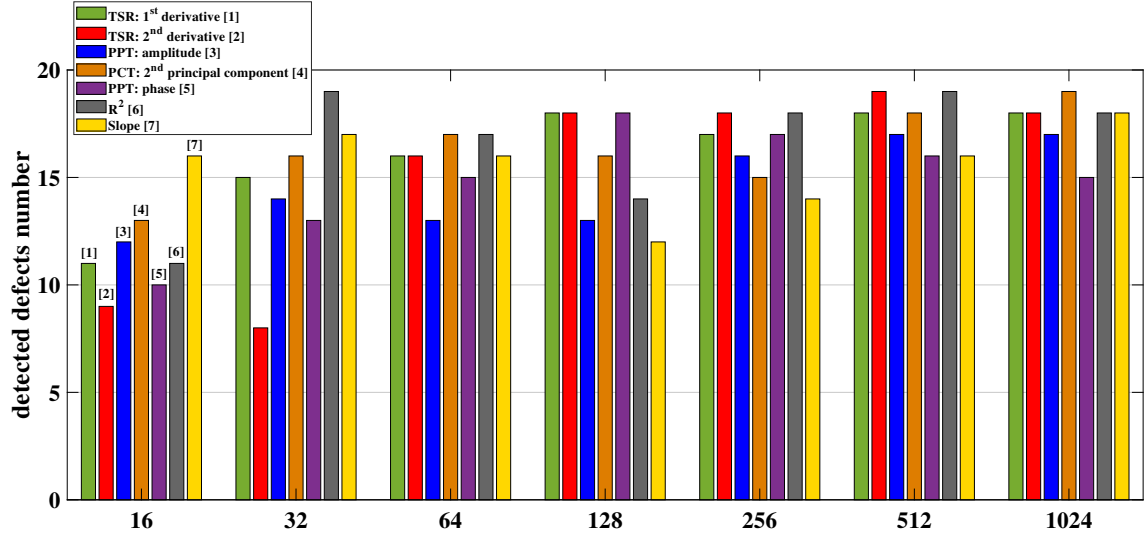


Figure 3.15: Comparison among the different algorithms in terms of the detected defects number for each analysis interval in a bar plot.

Fig. 3.15 is a summary that gives an indication about the number of defects that can be detected in a certain time interval and for a specific analysis algorithm. However, an indication is also needed about “how” a particular defect is detected, so a quantitative information in terms of depth and size.

Certainly, a parameter that gives an indication about “how” a defect is diagnosed and can be characterize is the contrast. As the previous results already shown, the parameter of the maximum contrast, expressed in terms of normalized contrast (SBC), changes with the chosen algorithm, the analysis interval and, obviously, the examined defect in terms of depth and size. Fig. 3.16 shows the trend of the maximum SBC versus the aspect ratio r for each algorithm independently by the truncation window size at which this is achieved.

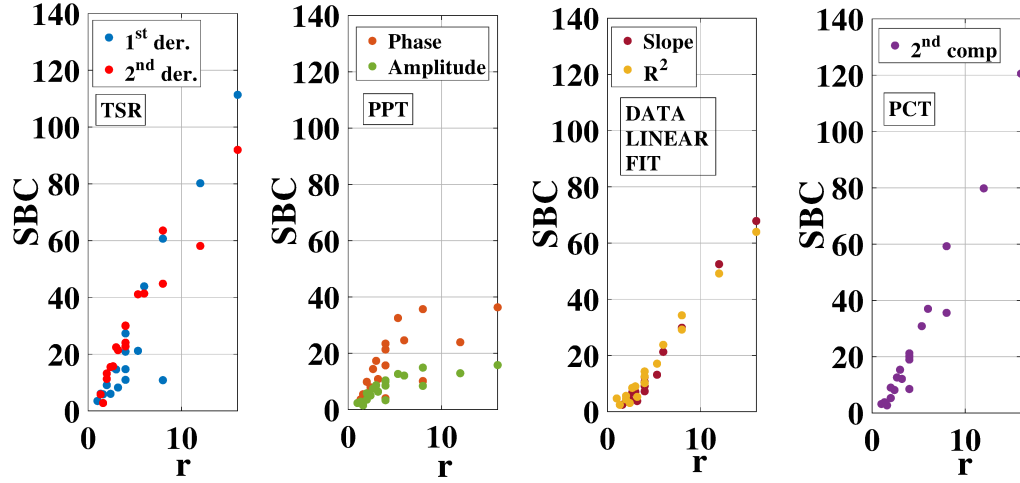


Figure 3.16: Comparison of different algorithms in terms of maximum SBC.

As expected, the SBC is influenced by the aspect ratio r and in this regard, it is not simple to discern the best algorithm by considering only the maximum value of the SBC. In fact, for the defects with a small aspect ratio $r < 4$, the TSR® analysis returns a 2^{nd} derivative that seems to get the better results Fig. 3.17; the PCT algorithm in terms of 2^{nd} derivative and the 1^{st} derivative (TSR®) show a higher SBC with respect to the 2^{nd} derivative (TSR®) for the larger and superficial defects. The PPT algorithm, both for the amplitude and the phase analysis output, seems to show the lower SBC value for most of the detected defects. Finally, the R^2 algorithm seems to be “in the middle” of the achieved results.

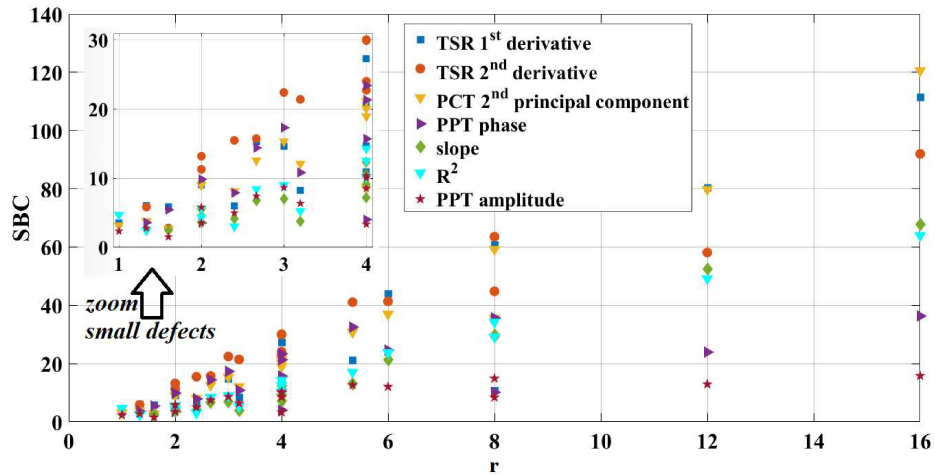


Figure 3.17: Comparison of different algorithms in terms of maximum SBC: a particular zoom for the smaller defects.

To obtain a parameter able to quantify the goodness of each algorithm in terms of a single maximum SBC value, it has been chosen the weighted average, calculated as follows:

$$\bar{x} = \frac{\sum_{i=1}^n x_i p_i}{\sum_{i=1}^n p_i} \quad (3.2)$$

when x_i indicates the SBC value for each defect and p_i is the relative weight, represented by the aspect ratio r ; the defects below the threshold value were considered with SBC equal to 0.

Algorithm	Weighted SBC
PCT (2 nd principal component)	49.11
TSR® 2 nd derivative	46.06
TSR® 1 st derivative	45.47
R^2	28.96
Slope	28.74
PPT (phase)	21.89
PPT (amplitude)	10.62

Table 3.2: The weighted SBC value for each algorithm obtained with Eq. 1.56.

The results reported in the Tab. 3.2 confirm the comments emerged from the previous graphical comparison; it seems that the PCT returns the better results if this analysis feature is chosen.

However, the “contrast”, meant as one, is not the only parameter that can indicate how a defect has been diagnosed; it is certainly a quantitative evaluation, but it must be accompanied by an estimation of the “size” of the defect. As shown before, by analyzing the summarized results in Fig. 3.14 and in Tab. 3.2, in the case of application of the slope algorithm, an indication of this quantitative measure is the possible linear correlation between the SBC and the relative defect aspect ratio, and “how linear” this is, when there are a good number of defects detected. An adequate index to judge the goodness of the linear fitting is certainly the R^2 .

For brevity, in the following figures (Fig. 3.18-Fig. 3.24), the better results in terms of linear correlation between the SBC and the aspect ratio r for each algorithm are shown, regardless the number of the analyses frames. As will be seen, the best truncation window size to reach this aim changes a lot according to the chosen algorithm. For completeness of information, in the following figures (Fig. 3.20-Fig. 3.25), the error bar has been reported for each detected defect and so for each aspect ratio. The error bar has to be considered as the standard deviation of the single data from the average of three replications. Besides, for each found linear model the confidence bounds at 95% are reported.

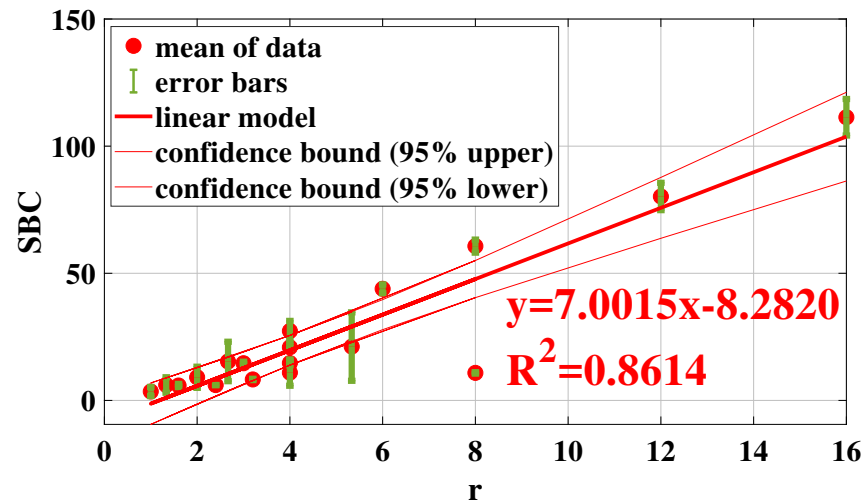


Figure 3.18: SBC versus r for TSR® 1st derivative 1024 frames, error bars and confidence bounds on the found linear model.

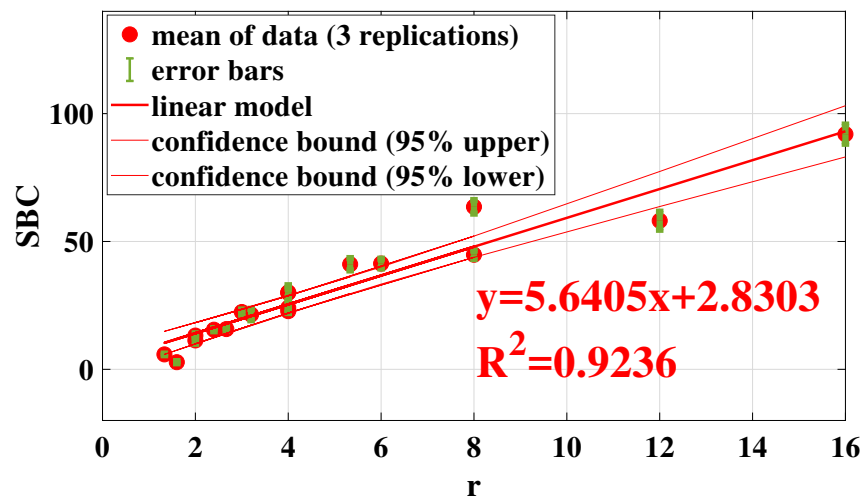


Figure 3.19: SBC versus r for TSR® 2nd derivative 256 frames, error bands and confidence bounds on the found linear model.

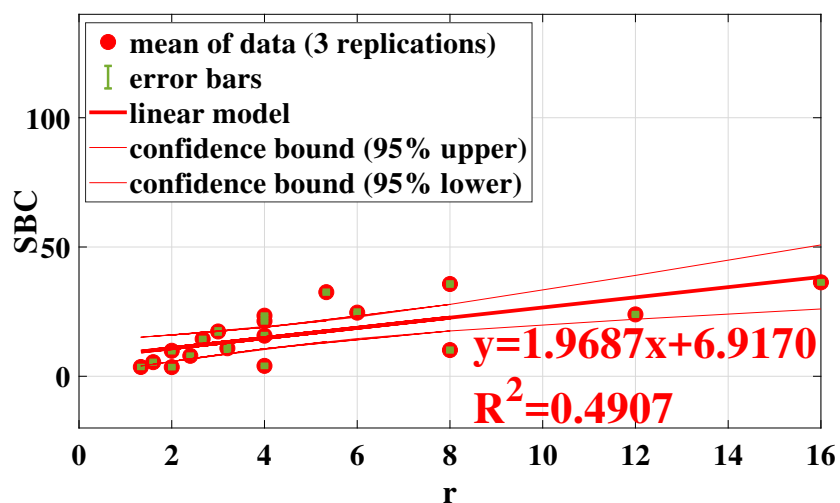


Figure 3.20: SBC versus r for PPT (phase) 128 frames, error bands and confidence bounds on the found linear model.

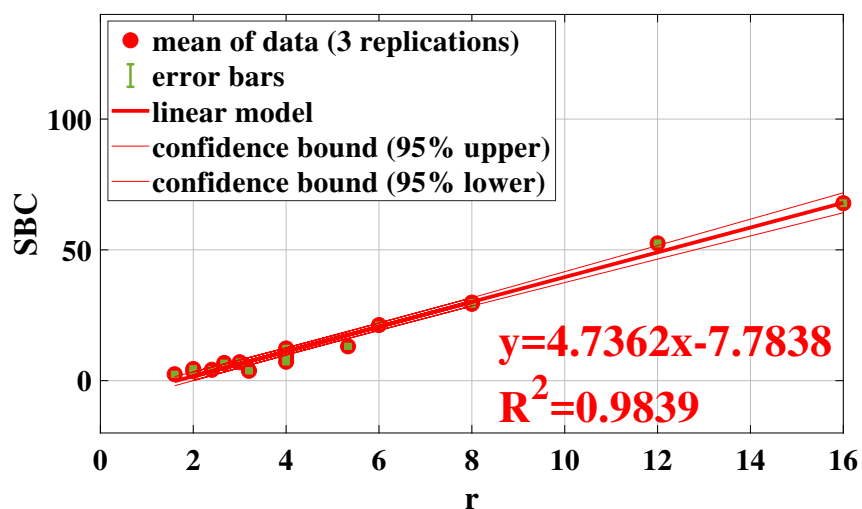


Figure 3.21: SBC versus r for PPT (amplitude) 512 frames, error bands and confidence bounds on the found linear model.

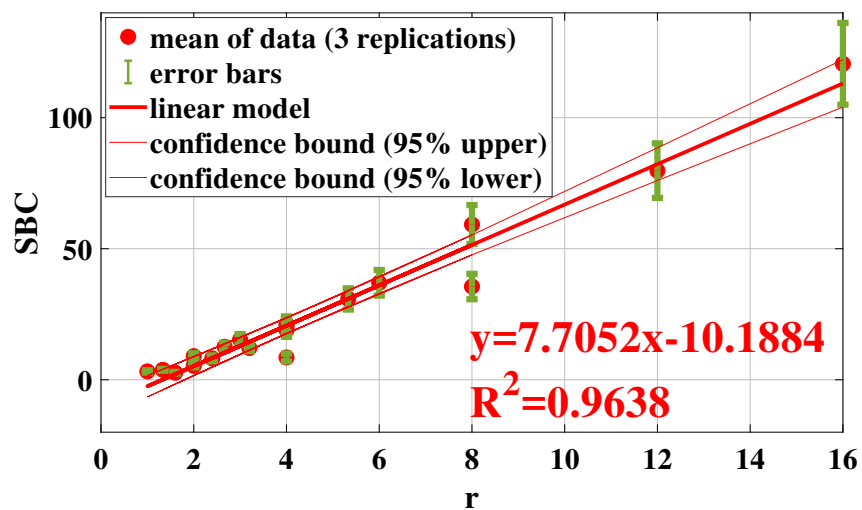


Figure 3.22: SBC versus r for PCT (2nd principal component) 1024 frames, error bands and confidence bounds on the found linear model.

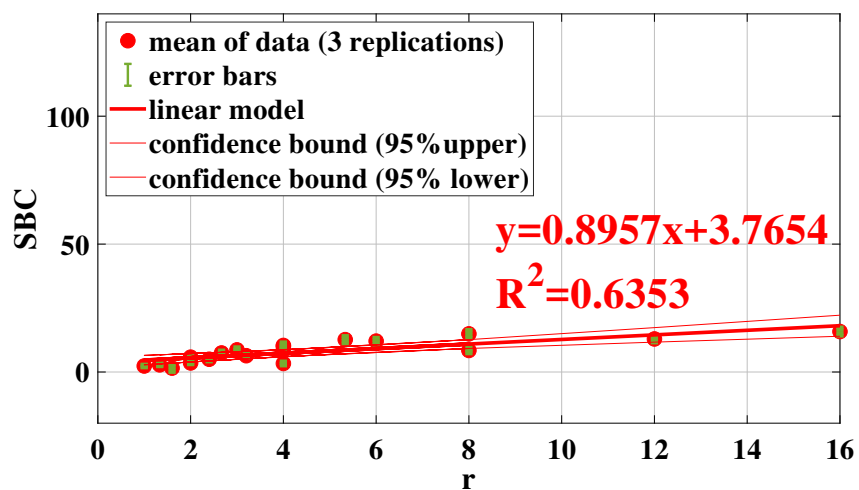


Figure 3.23: SBC versus r for R^2 512 frames, error bands and confidence bounds on the found linear model.

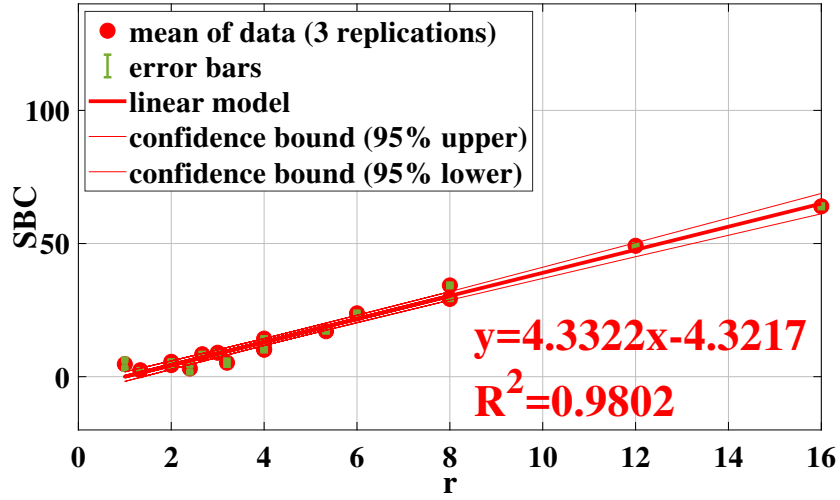


Figure 3.24: SBC versus r for slope 1024 frames, error bands and confidence bounds on the found linear model.

In Tab. 3.3, the obtained results for each algorithm, shown in the previous figures (Fig. 3.20-Fig. 3.25), are summarized:

Algorithm	Truncation window size	Linear Correlation Index (R^2)
TSR@ 1 st derivative	1024 frames	0.86
TSR@ 2 nd derivative	256 frames	0.92
PPT (phase)	128 frames	0.49
PPT (amplitude)	512 frames	0.98
PCT (2 nd principal component)	1024 frames	0.96
R^2	512 frames	0.64
Slope	1024 frames	0.98

Table 3.3: Comparison among the different algorithms in terms of the linear correlation between SBC and r .

From Tab. 3.3, emerges that the algorithms of the PPT amplitude and the slope, return the better results, with a value of square correlation coefficient of about 0.98. On the contrary, it seems that the worst algorithm is the PPT phase, because for this algorithm the SBC is less influenced by the value of the aspect ratio r (Fig. 3.21); same consideration can be made in the case of R^2 algorithm: in particular the shallow defects (depth 1mm) influence a lot this type of analysis, by showing a contrast much lower than expected and so useful to delineate a more linear trend. In this regard, the motivation is already explained and it is due to the pulse heating duration of the flash test, however too long for this depth and for this type of material.

Besides, from the analysis of the statistics parameters in terms of error bars and confidence bounds, different results emerge; in particular, from the analysis of the error bars, the PCT algorithm seems to return very different contrast values, and so the results of the application of this algorithm seem to be non-repeatable. It is noteworthy, that the reported error is not a measurement error, but an error on the obtained results in terms of contrast. Instead, for the linear model and the relative confidence bounds at 95%, the algorithms of the R^2 , slope and amplitude return the better results, because the width of the confidence interval is very narrow, and so the data are distributed very well around the chosen model.

However, the analysis carried out leads, in any case, to a precise and unique conclusion: the parameter of the truncation window size have a great influence on the obtained results.

In particular, for some algorithms as the slope and the square correlation coefficient R^2 , where the result is unique for each analysis interval, the choice made can lead to completely opposite results.

The graph, shown below, summarizes what has been said: the non-normalized contrast trend over the time (expressed in number of frames) is reported considering the selected analysis intervals. The different trends are reported by considering different depths and fixed the size in terms of diameter Fig. 3.25.

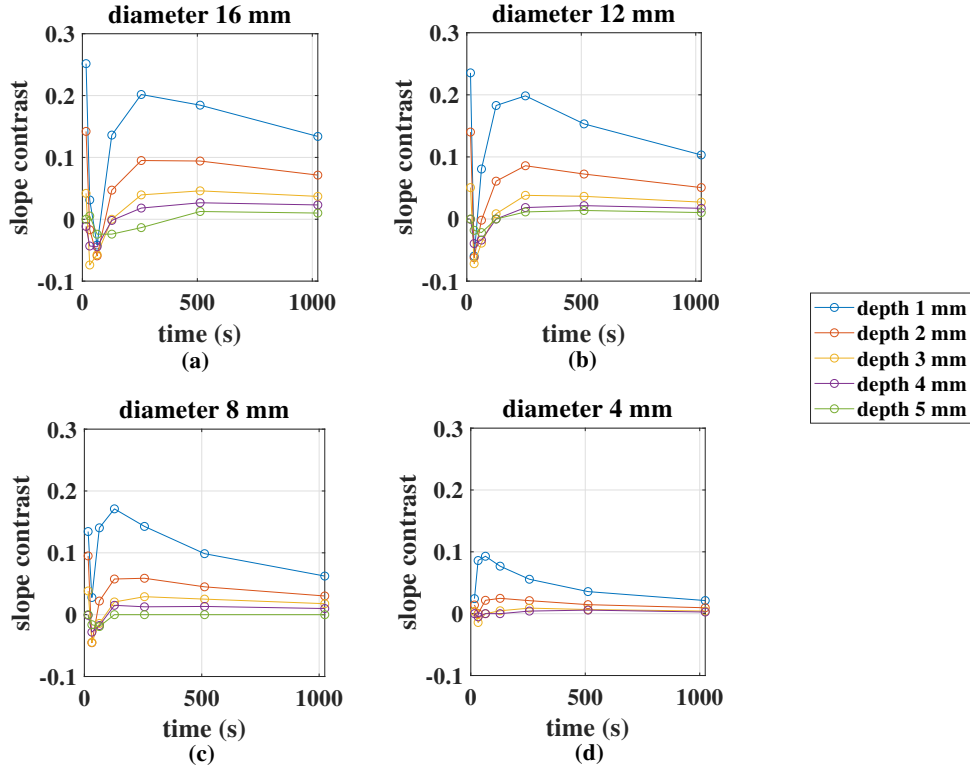


Figure 3.25: Slope contrast vs frames number; (a) diameter 16 mm (b) diameter 12 mm (c) diameter 8 mm (d) diameter 4 mm (fixed depth).

Fig. 3.25 shows that the trends of the signal contrast for this slope algorithm seem fairly regular. Defects of 16 and 12 mm sizes show a change in sign for a fixed number of frames equal to about 128. This “blind value” for the signal slope contrast seems to depend also on the defect depth. However, it is necessary to thicken the analysis interval between 64 and 256 frames to evaluate a possible dependence on the defect depth. Bigger defects (16 and 12 mm sizes) reach a maximum contrast for 256 frames that moving to 128 frames for smaller defects. Finally, the signal contrast decreases until to reach a plateau value in correspondence of 512 and 1024 frames (longer analyzes). As expected, the number of frames has a great influence on the thermographic results. As it can be seen from the analysis of the previous graphics, a different behavior of the thermal contrast as the number of frames increases is observed for the superficial defects. In fact, the defects placed to 1 mm and 2 mm from the surface shows the higher signal contrast within a time interval of 0.08 s. This behavior is possible because the thermal waves reach these

defects already during the heating phase. In this regard, the thermographic technique can be considered as a stepped test rather than a pulsed one. The deeper defects show a maximum value of the signal contrast in correspondence of a suitable value of the frames number. In particular, this value changes as function of the depth and size of defects. In other words, each defect owns an optimal truncation window of thermal data, as well as each analysis algorithm.

Similar graphs can be obtained by analyzing the R^2 results (Fig. 3.26).

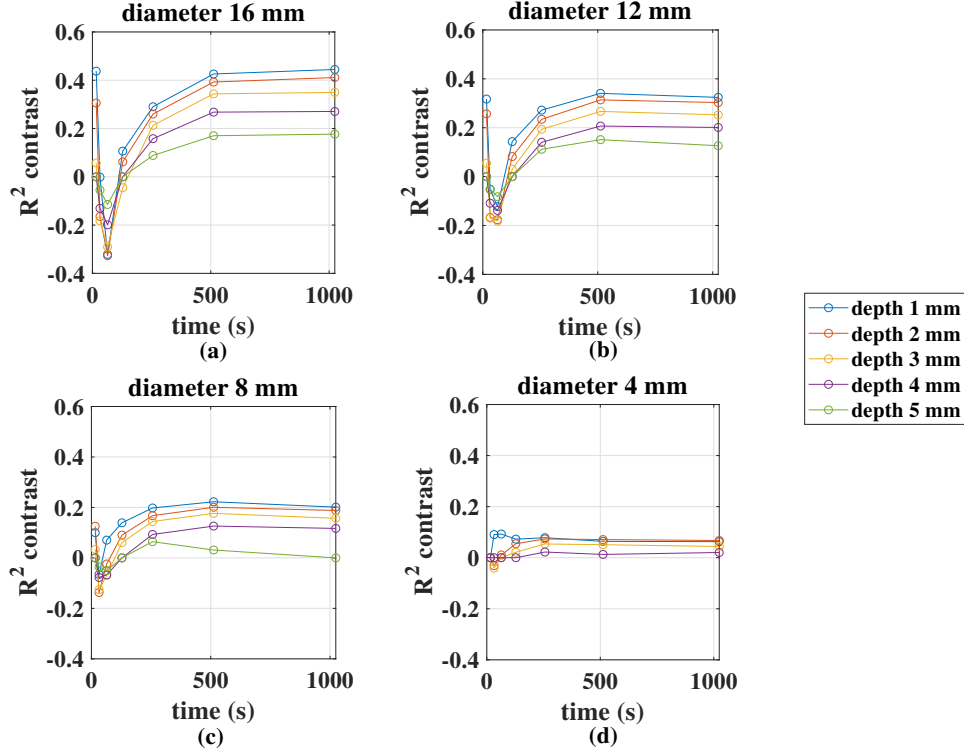


Figure 3.26: R^2 contrast vs frames number; (a) diameter 16 mm (b) diameter 12 mm (c) diameter 8 mm (d) diameter 4 mm (fixed depth).

Similar comments to the previous one, made in the case of slope contrast, can be done by analyzing the R^2 signal contrast trends. In the analysis of these latest results, it should also be emphasized that the maximum contrast for all defects is placed around to 512 frames (about 2.5 seconds of analysis); in fact, above 512 frames of analysis, the signal contrast does not change significantly and then, in this specific regard, if the aim is to reach the maximum contrast, a further data analysis seems superfluous, because the computed times increases, and the contrast remains however the same.

For completeness, also the same graphs, as a function of the diameter per depth set, are shown for both algorithms.

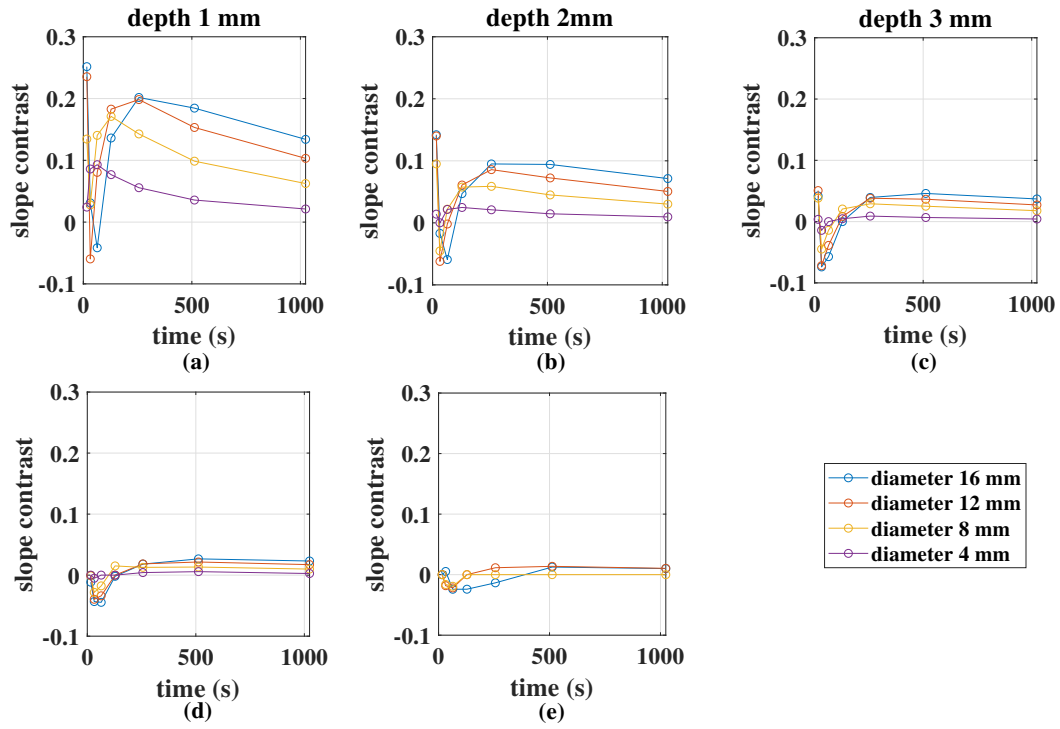


Figure 3.27: Slope contrast vs frames number; (a) depth 1 mm (b) depth 2 mm (c) depth 3 mm (d) depth 4 mm (e) depth 5 mm (fixed diameter).

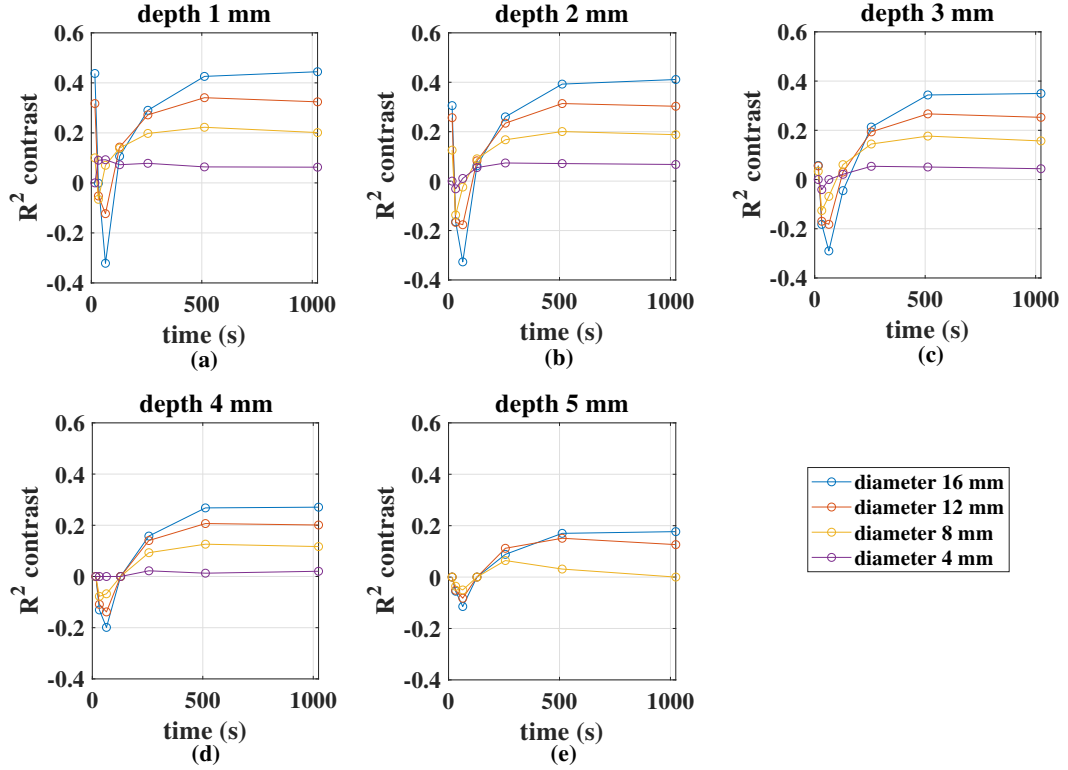


Figure 3.28: R^2 contrast vs frames number; (a) depth 1 mm (b) depth 2 mm (c) depth 3 mm (d) depth 4 mm (e) depth 5 mm (fixed diameter).

However, it is necessary to underline, that these graphs, in both cases, have been obtained by considering the simple contrast and not the normalized one (SBC), and so the chosen threshold value taken on the sound standard deviation was not taken into account. In this regard, it will be necessary a further investigation by considering more analysis intervals and the threshold std trend over the time, mainly because in both cases exists an analysis window within which the investigated defects are not detected; in this sense, it might seem that the chosen algorithm does not provide any results or that, in any case, it is not being exploited to the best of its ability. Within the next section (Section 3.4), further results will be shown, by analyzing the slope and the R^2 behaviors over the time, frame by frame, and compare the same with the well established one in order to underline advantages and disadvantages of each in the defect detectability and characterization.

3.4 The influence of the truncation window size: a further investigation frame by frame

The obtained results for the first chosen intervals have shown a strong dependence by this choice for all investigated points of view, such as number of detected defects, maximum SBC and correlation between SBC and aspect ratio; from this derives the idea of treating the slope and R^2 data by analyzing their behavior frame by frame and comparing it with that obtained by applying well-known algorithms such as PPT in terms of phase and TSR® in terms of 1st and 2nd derivative. The latest one allowing the analysis in the time domain or equivalently in the fre-

quency one, starting from a complete analysis which concerns the entire sequence and that gives as output a sequence of images of the same length (or half in the case of PPT) than the starting one, and therefore not just a single map. Therefore, the slope and R^2 results will be analyzed frame by frame and compared with the one obtained by applying TSR® and PPT as usually shown in the literature or analyzing the entire sequence. In fact, for mathematical reasons such as the approximation of the data with a polynomial fitting, the choice to analyze a very low number of data can lead to the application of the algorithm not to the best of its abilities and, therefore, to partially incorrect or, in any case, not excellent results. In the following figures (Fig. 3.30-Fig. 3.34), the chosen threshold to define if a defect is detected or not in a semi-automatic way by the calculator is shown as an area bar in green. This threshold is fixed equal 2 times the sound standard deviation and the SBC, for each defect, is computed as already explained in detail in the previous sections. However, it is necessary to underline that in the results that will be shown below, only one replication of the test was considered and the final Gaussian filter was not applied.

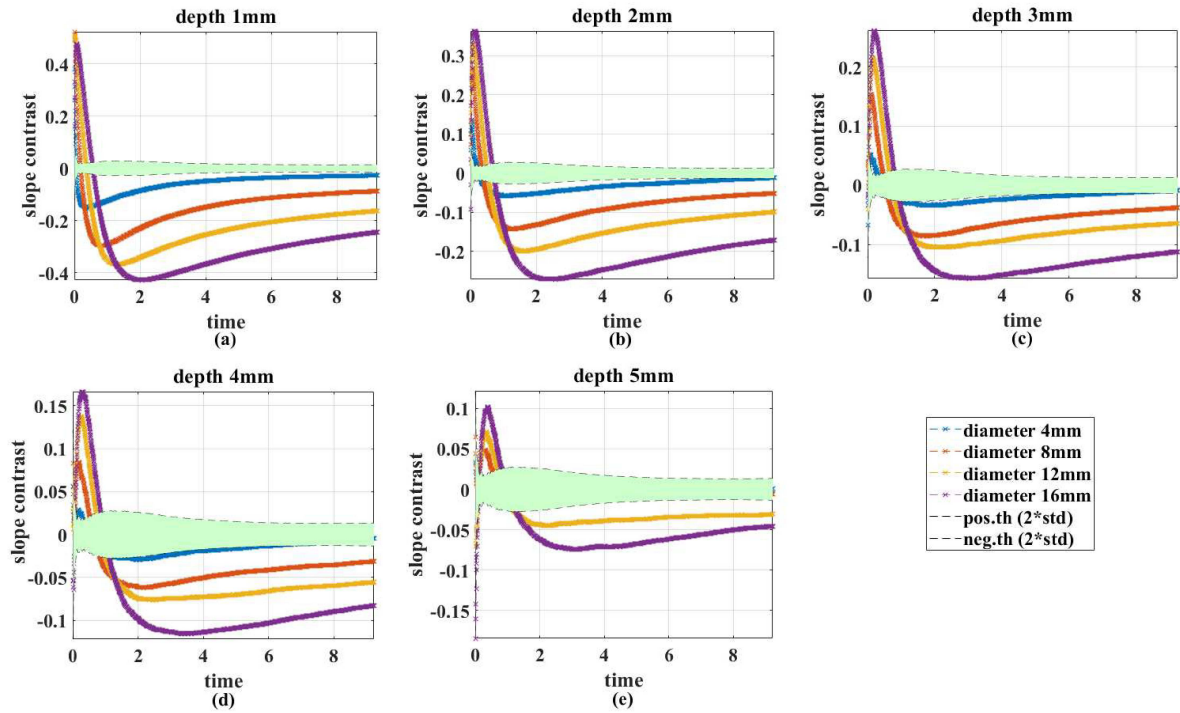
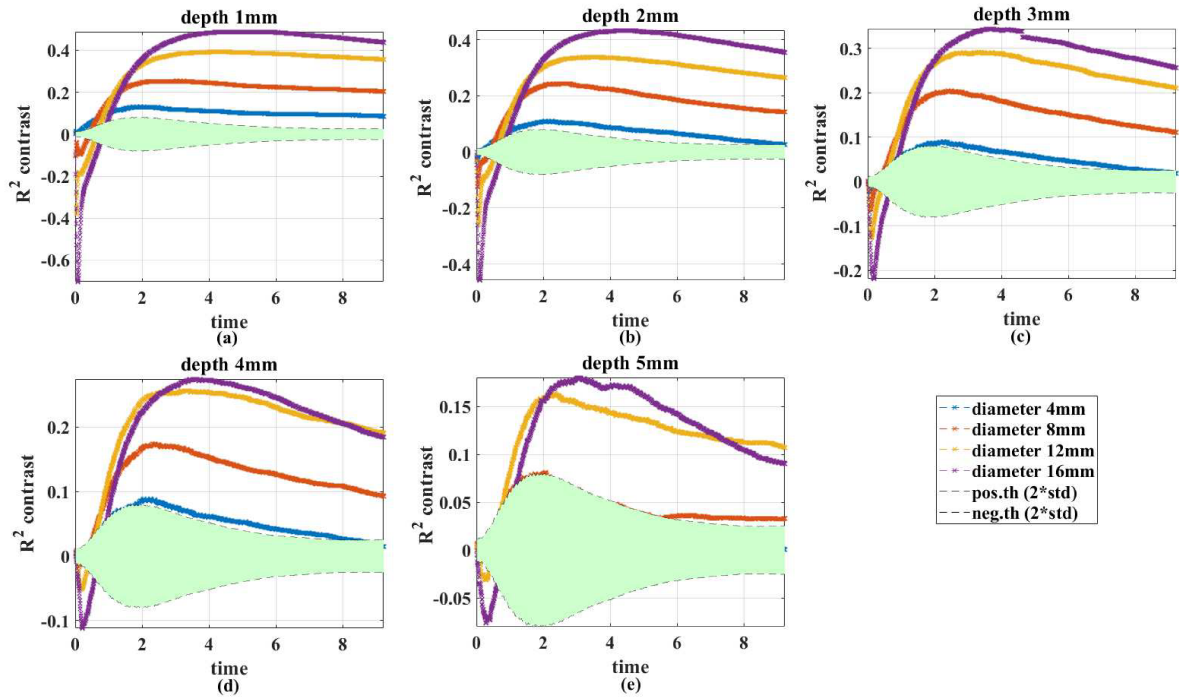
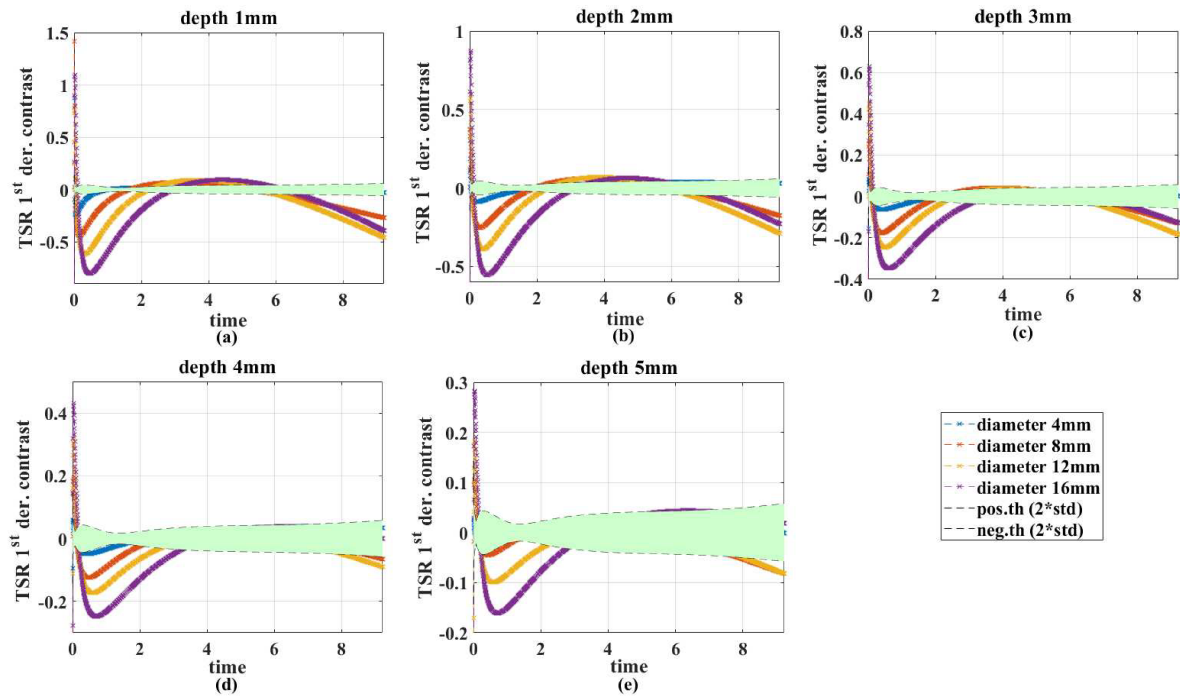


Figure 3.29: Slope contrast frame by frame.

Figure 3.30: R^2 contrast frame by frame.Figure 3.31: TSR 1st derivative contrast over the time (10 s of analysis).

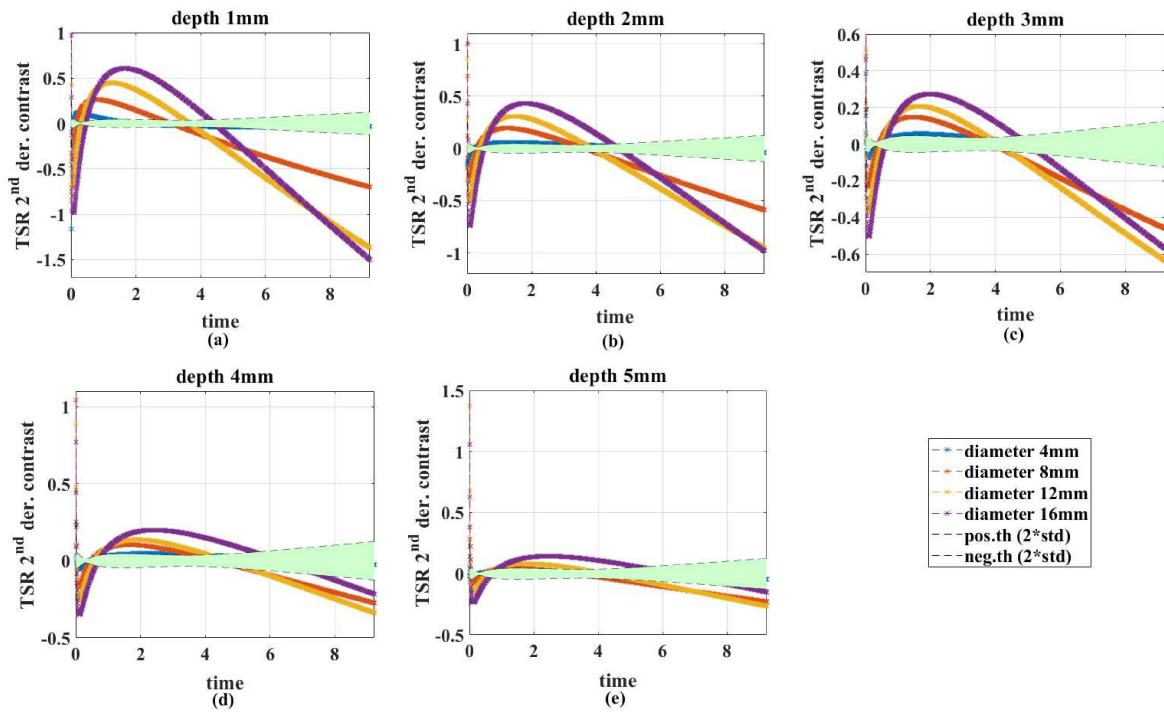
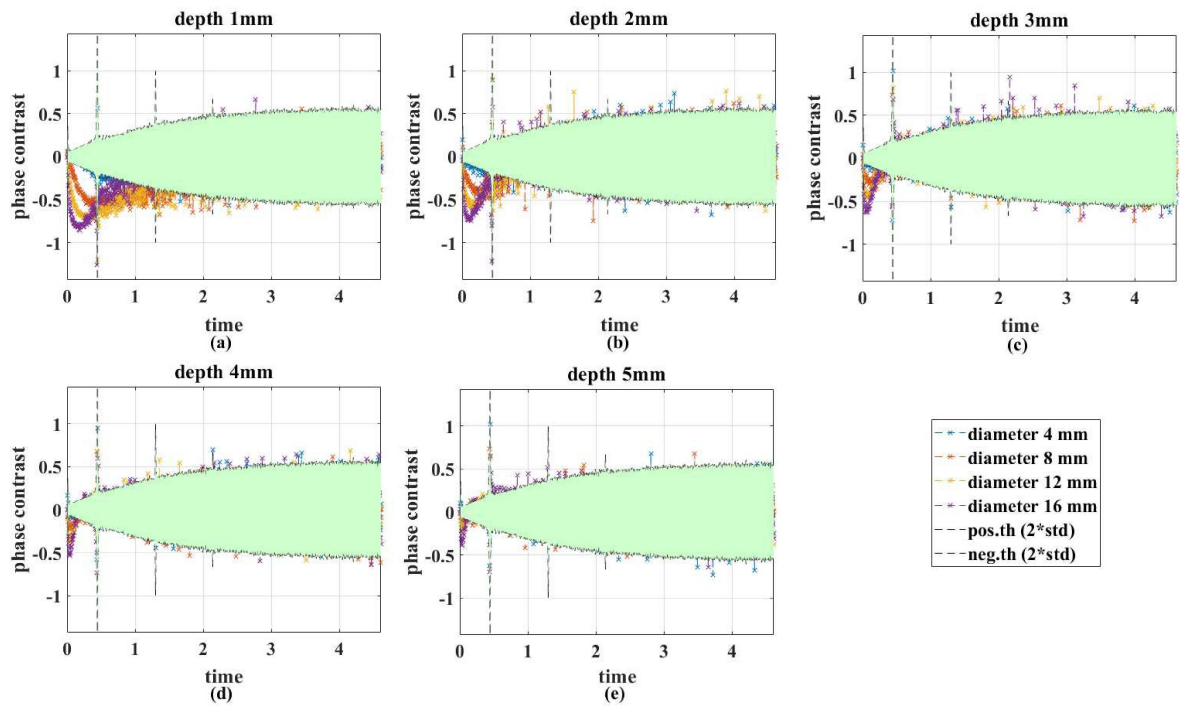
Figure 3.32: TSR® 2^{nd} derivative contrast over the time (10 s of analysis).

Figure 3.33: PPT phase contrast over the time (10 s of analysis).

The obtained results can be summarized as follows. i) Obviously, the areas in which the plots for each defect are visible can be used for the analyses because the contrast exceeds the set threshold and so it indicates the actual presence of a defect and it can not be confused with the noise. ii) It is also possible to note that for each plot it is chosen to show the data set when there is a change of the size and the depth is fixed (one depth and different size for plot), in order to show that there is a shift of the maximum and also a shift in the time when the defect changes the sign. For all algorithms and for the used frequency (not too much high for a material with a high diffusivity), it is not possible to identify the defect depth in a precise way with the individuation of a precise frame or time when there is a “change” (maximum, minimum, change of sign) because this depends also from the defect size and not only from the relative depth (Fig. 3.34). iii) It should also be noted that the standard deviation shows a decreasing trend in the case of slope and R^2 because, as time increases, the number of frames analyzed increases also (flattens the average value), unlike what happens for the TSR® and PPT where instead the noise increases because the window is fixed and as time increases the analyzed maps are more noisy.

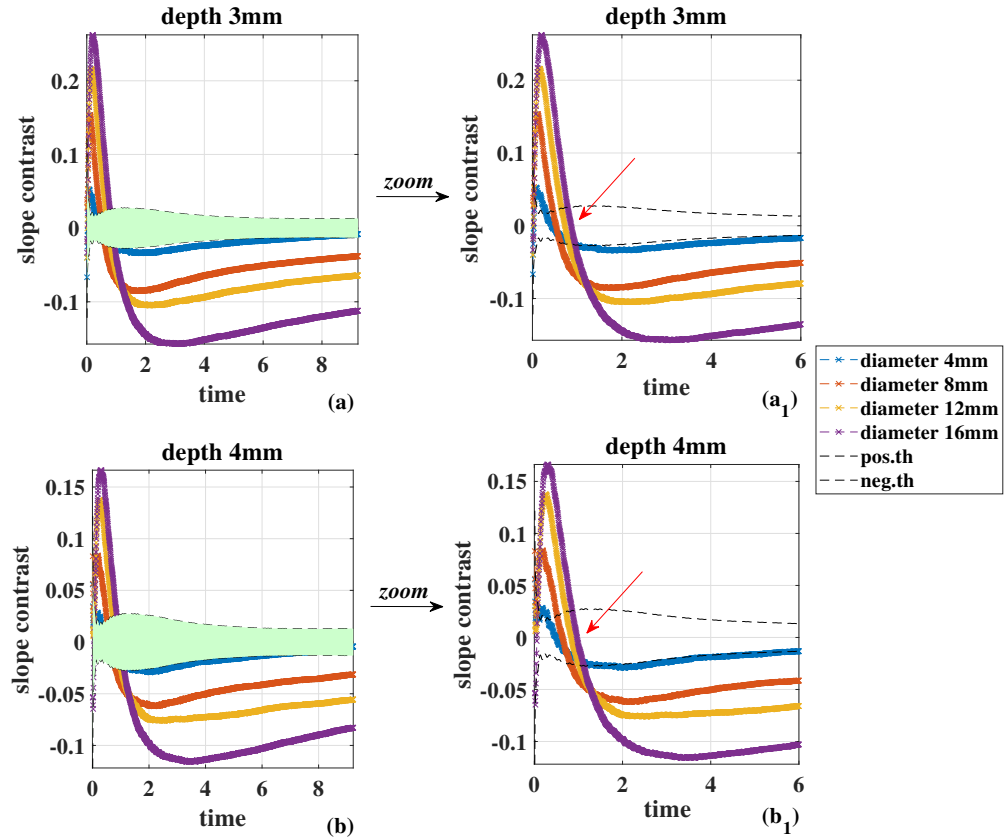


Figure 3.34: Slope contrast frame by frame: a zoom to underline the change of sign with the depth and defect size; (a) depth 3 mm (a_1) zoom depth 3 mm, (b) depth 4 mm (b_1) zoom depth 4 mm.

However, it is not very simple to summarize all the results that are shown in the previous figures (Fig. 3.29-Fig. 3.33); in order to choose the more useful window size for each algorithm and in order to summarize the obtained results, it is necessary to fix an aim or better a point of view for which to have a comparison among these different

types of post-processing analyses. In fact, only to observe the previous plots, it is possible to note that the most good interval changes based on what is observed.

In the following figures (Fig. 3.35-Fig. 3.39), for TSR®, 1st and 2nd derivatives, PPT in terms of phase and for slope and R^2 , the obtained results are summarized focusing to the same aims analyses until now: i) number of detected defects (blue trends), ii) goodness expressed in terms of R^2 of the correlation between SBC and defect aspect ratio r , when a linear calibration is investigated (green trends), iii) weighted SBC. All plots have the same y-scale in order to show better the various comparisons. It is worth emphasizing that the chosen threshold is always fixed to 2 times the standard deviation for plotting all these trends: from this derives the broken and non-continuous trend for the 3 investigated and compared aims; as already specified, in order to have a right evaluation of the weighted SBC and the goodness of the linear fitting/correlation, it is necessary to look first the number of detected defects because their correct evaluation is closely to that of the first parameter: a high weighted SBC or a good linear correlation has meaning only if there is a considerable number of diagnosed defects.

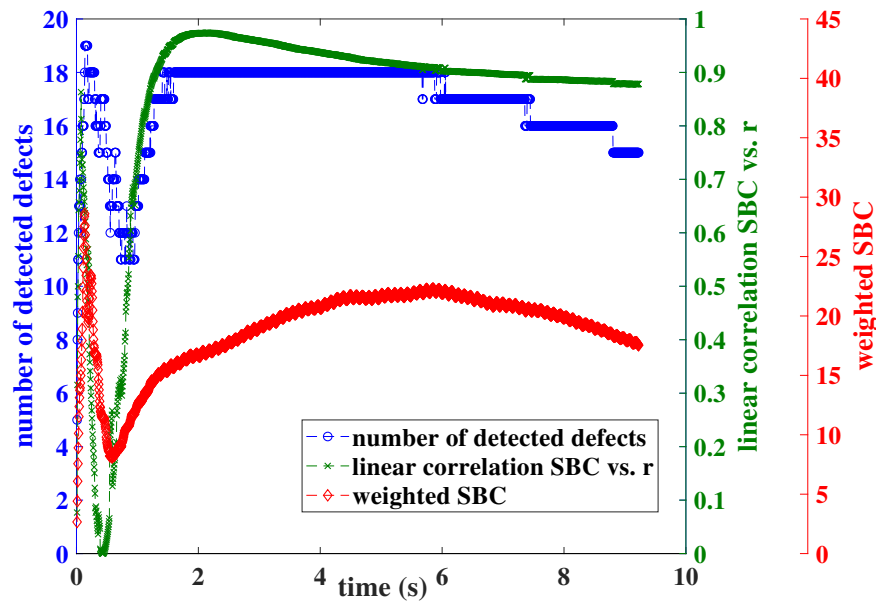


Figure 3.35: Slope overview; linear correlation SBC vs. r (R^2 index), detected defect number and weighted SBC, an analysis frame by frame.

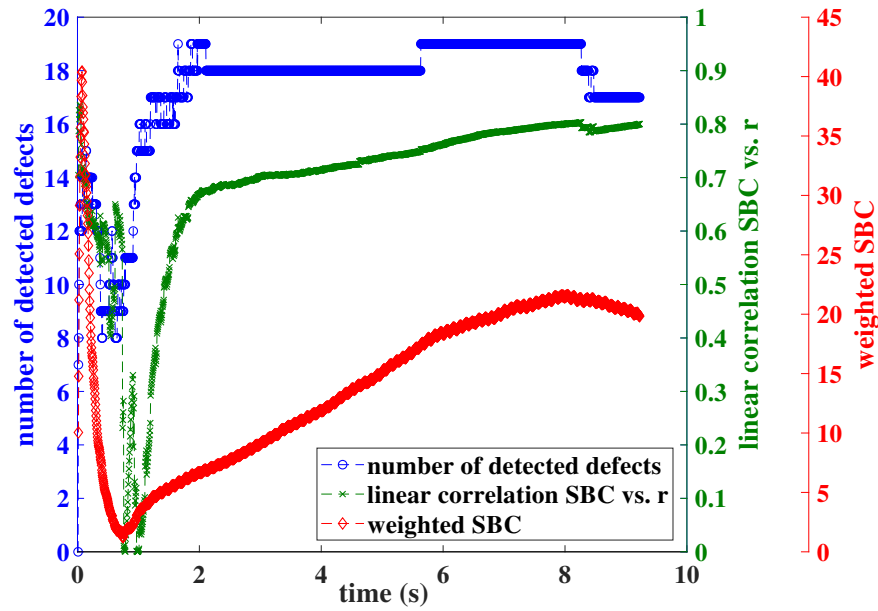


Figure 3.36: R^2 overview; linear correlation SBC vs. r (R^2 index), detected defect number and weighted SBC during the entire observation time, an analysis frame by frame.

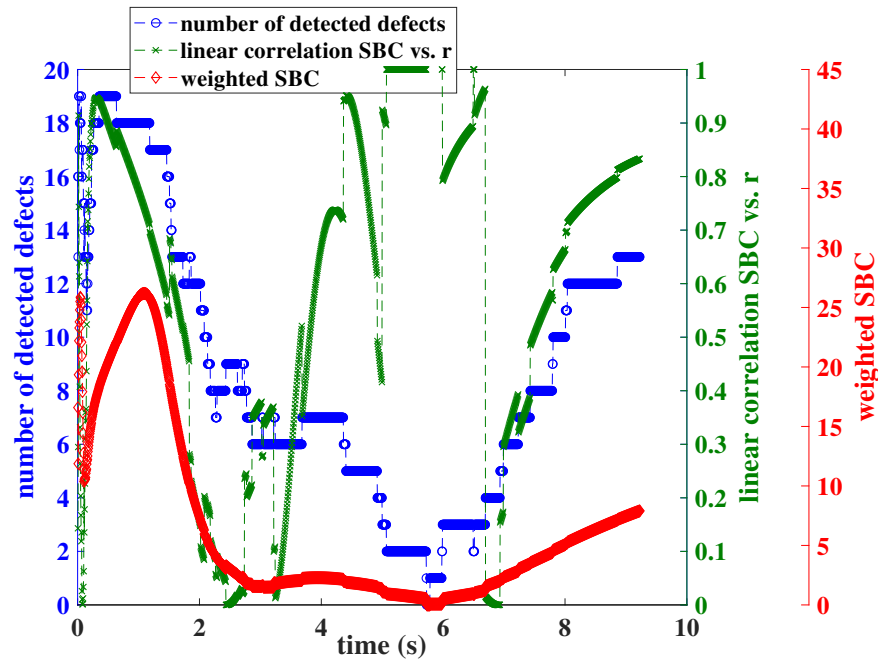


Figure 3.37: 1^{st} derivative (TSR®) overview; linear correlation SBC vs. r (R^2 index), detected defect number and weighted SBC during the entire observation time.

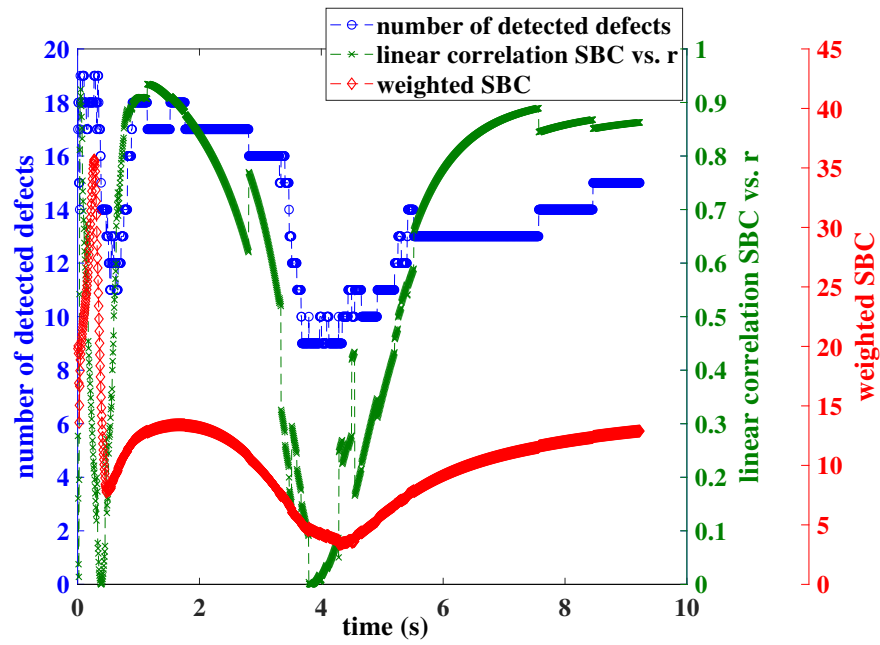


Figure 3.38: 2^{nd} derivative (TSR®) overview; linear correlation SBC vs. r (R^2 index), detected defect number and weighted SBC during the entire observation time.

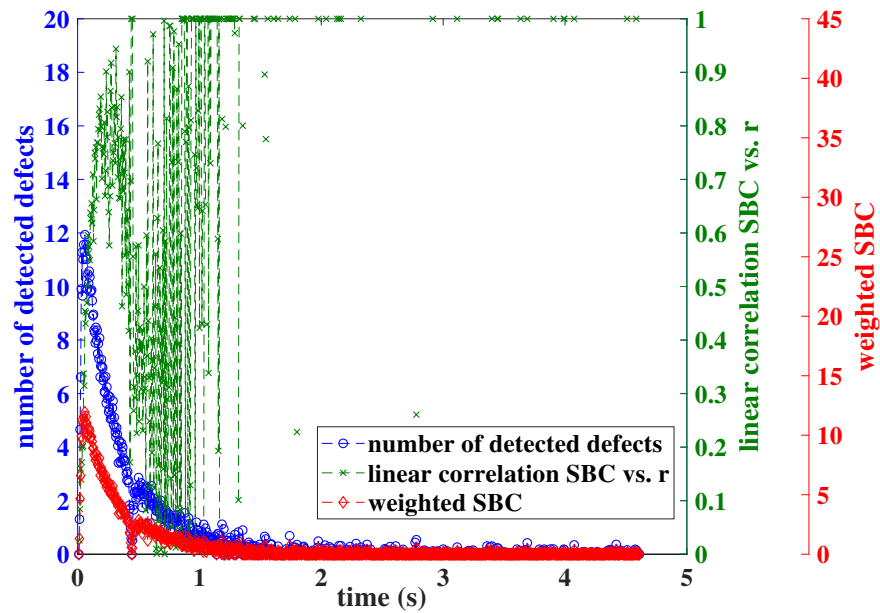


Figure 3.39: Phase overview; linear correlation SBC vs. r (R^2 index), detected defect number and weighted SBC during the entire observation time.

Looking at the previous figures (Fig. 3.35-Fig. 3.39), the first question is: how long each algorithm takes to see the greatest number of defects with an $SBC > 2$? Or in other words: how long it is necessary to acquire with the chosen frame rate if it is requested to see the greatest number of defects after applying the slope and R^2 algorithm? What are the advantages compared to a TSR® or PPT analysis? If the aim is to see a good number of defects with also a good linear correlation within the analysis SBC versus aspect ratio (r) and with a good weighted SBC, probably the answer is different from the previous one and the more useful choice in terms of truncation window size is different from the one indicated above. In this regard, it is necessary to compare the different analyzes carried out and the different post processing algorithms in terms of defect detectability, trying to summarize the results illustrated so far and giving an indication for a correct thermographic analysis, especially in terms of acquisition times and therefore of analysis, although the variables to be considered are different and influence each other. It is necessary to highlight that the comparison shown in this latest paragraph sees a different approach from the previous one: the slope and the R^2 algorithms have been analyzed frame by frame, instead the TSR® and PPT algorithm are performed by evaluating the entire sequence. Therefore, to evaluate the influence of the “analysis window” also for the other algorithms (PPT, TSR® and PCT), the results illustrated in the previous session (Section 3.3) remain valid and will be compared in the last paragraph.

These are two slightly different approaches of analysis and two quantitative comparisons with the same direction but 2 different ways, since all the algorithms must be used to the best of their ability, but to make a comparison on an equal footing it is necessary to have the same methodology of analysis.

3.5 Results and discussion: by comparing different thermographic algorithms in terms of defect detectability

In order to do a final overview, all the obtained results have to be summarized, and so the used algorithms have to be compared in terms of maximum SBC, number of detected defects and the correlation SBC vs. r .

A final comparison among the different analysis algorithms will be illustrated, considering separately the results obtained for the TSR® and PPT algorithms, evaluating different analysis intervals or, alternatively, evaluating the entire sequence of raw data and choosing the map that shows the best results.

In Fig. 3.40, the results, as 2D maps, are represented for each algorithm, by considering the 7 different analysis intervals indicated previously (16-32-64-128-256-512-1024 frames) and chosen to evaluate the influence of this parameter on the various analysis algorithms, including TSR® and PPT. In particular, it is chosen to show the maps in which the greatest number of defects is detected, as already illustrated within the bar plot reported in Fig. 3.15. For some of the analyzed algorithms (TSR® and PPT), there is more than one frames interval in which the greatest number of defects is detected. In this particular case, the map corresponding to the smaller truncation window size is shown for each algorithm.

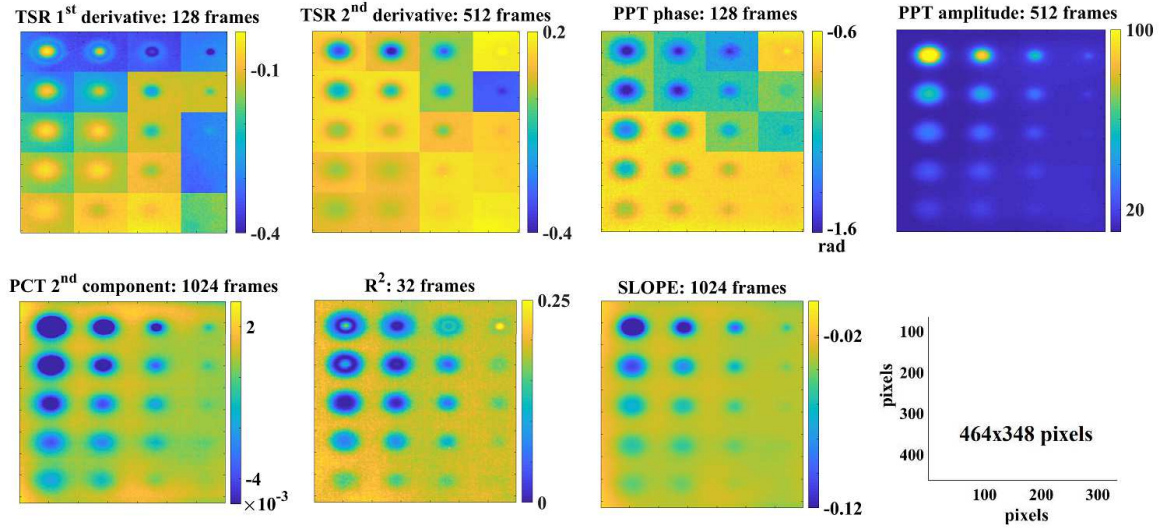


Figure 3.40: Best maps for each algorithm of analysis by considering the truncation window size for which the greatest number of defects were detected.

Similar considerations are reported in Tab. 3.4, however specified the optimal truncation window size (TWS) in order to obtain a linear correlation and the higher number of detected defects, within the chosen analysis:

Algorithm	TWS (linear correlation optimization)	Linear Correlation (R^2 index)	TWS (higher number of detected defects)	Number of detected defects
TSR® 1 st derivative	1024 frames	0.86	128 frames	18
TSR® 2 nd derivative	256 frames	0.92	512 frames	19
PPT phase	128 frames	0.49	128 frames	18
PPT amplitude	512 frames	0.98	256 frames	17
PCT (2 nd principal component)	1024 frames	0.96	1024 frames	19
R^2	512 frames	0.64	32 frames	19
Slope	1024 frames	0.98	1024 frames	17

Table 3.4: Final comparison among the different algorithms.

The strengths and the weakness of each algorithm can be summarized as follows:

- the PCT algorithm shows the maximum SBC value;
- the R^2 algorithm is the faster one since it allows to find the greatest number of defects 480 (19/20) with only 32 analyses frames;
- the 2nd derivative (TSR®), the slope, the amplitude and the PCT algorithms seem to get a very good correlation between the SBC and the aspect ratio r with a square correlation coefficient of $R^2 > 0.9$.

- the PCT algorithm, in this case, has returned a very good compromise: the greatest number of detected defects with a very good SBC value and a good correlation between the SBC and the aspect ratio r , but with 1024 frames of analysis.

The results reported in Fig. 3.40 and in Tab. 3.4 have been obtained by considering the first type of approach, or 7 different truncation window sizes equal to all post processing algorithms, although 16 data of analysis represent a small number and therefore a choice that is not entirely optimal for an analysis that involves a polynomial fitting, such as the TSR® one.

Similar results can be obtained by using slope and R^2 in the same way, and by increasing this type of analysis frame by frame, but by adopting a different type of approach for TSR® and PPT (Section 3.4). In this regard, it is possible to show a comparison entirely similar to the previous one and which takes into account the analysis windows, the number of defects, the maximum weighted contrast and the SBC- r correlation, but with a slightly different approach. The final comparison is show in Tab. 3.5, by summarizing the reached results described in Section 3.4.

ALGORITHM	maximum number of defects		minimum aspect ratio	
	number	time	number	time
TSR® 1 st derivative	19	0.02 s after 10 s of analysis	1	0.015 s after 10 s of analysis
TSR® 2 nd derivative	19	0.045 s after 10 s of analysis	1	0.04 s after 10 s of analysis
PPT phase	18	0.06 s after 10 s of analysis	1.33	0.06 s after 10 s of analysis
Slope	19	0.14 s	1	0.125 s
R^2	19	1.65 s	1	1.65 s

Table 3.5: Maximum detected defect number and minimum aspect ratio with the relative time interval necessary.

As shown in the second column of Tab. 3.5, also the time necessary to see the minimum detectable aspect ratio is reported. With the application of all algorithms, except the phase (PPT) one, is possible to see 19/20 defects with a minimum aspect ratio equal to 1. Probably it is necessary to choose a correct interval also for the PPT analysis in order to have the same results of the other algorithms.

In Tab. 3.6-1 some compromise choices are indicated: if the aim is to see a good number of defects with a good correlation between the aspect ratio and the SBC and with a good weighted SBC, the truncation windowing size is different from the one indicated above and also the results are not the same.

ALGORITHM	compromise choice			
	number of defects	linearity	weighted contrast	time (s)
TSR® 1 st derivative	19	0.93	18.96	0.395 s of 10
TSR® 2 nd derivative	19	0.90	18.87	0.045 s of 10
PPT phase	18	0.45	11.93	0.06 s of 10
Slope	19	0.97	17.05	2.16 s
R^2	19	0.80	21.59	8.045 s

Table 3.6: Compromise choice by highlighting the best truncation window size that allows to have the maximum detected defect number with a good weighted contrast and a good linearity.

From a final analysis, it is possible to say that in order to see 19/20 by analyzing only the slope of the cooling down, it is sufficient to acquire in this particular case only 0.14 seconds, or 28 frames with a very low acquisition

frequency and by investigating a material with very high diffusivity with minimum aspect ratio equal to 1.

These final plots show a further comparison among this last achieved result after the application of the slope algorithm by considering only 0.14 seconds of analysis and the analysis with the same interval, but with the application of the TSR® algorithm, however shown in terms of 1st and 2nd derivative and the PPT one, in terms of phase, always with the same truncation window size of analysis. The three principal aims have always been considered.

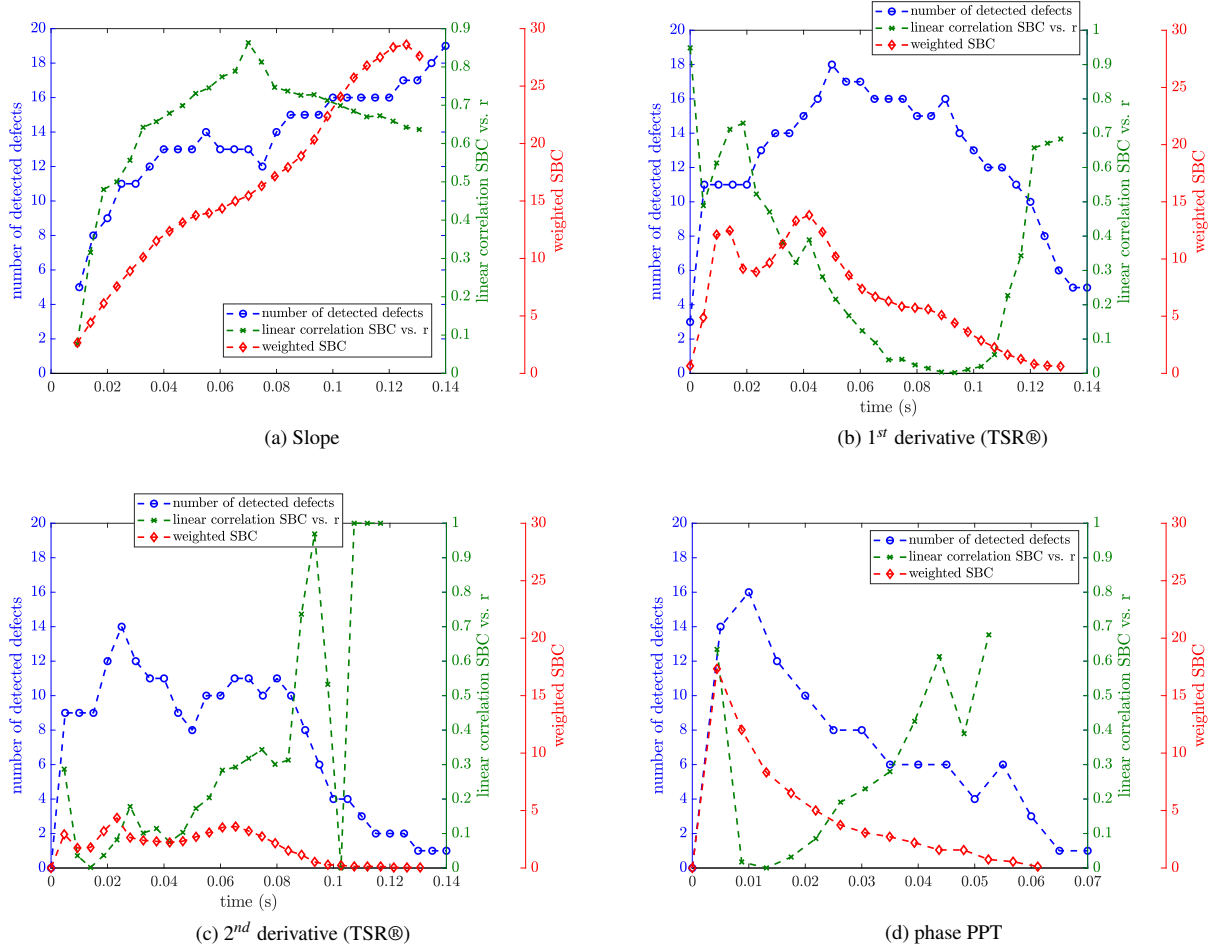


Figure 3.41: A comparison among different post processing algorithms after only 0.14s of analysis.

The 1st derivative allow to see 18/20 defects, one less than the slope, but with a very low weighted SBC and a not good linearity. The 2nd derivative shows worse results, probably due to the use of a low polynomial degree equal to 5 (the 2nd derivative is a polynomial equal to 3). If, instead, the principal aim is to obtain good results by analyzing the R^2 map, it is necessary to acquire about for 2 seconds obtaining in general not good results in terms of correlation between the SBC and the aspect ratio [19, 20, 21].

The last Fig. 3.42 shows the thermographic maps related to the column 1 of the Tab. 3.5 as best results obtained from the previous analyses.

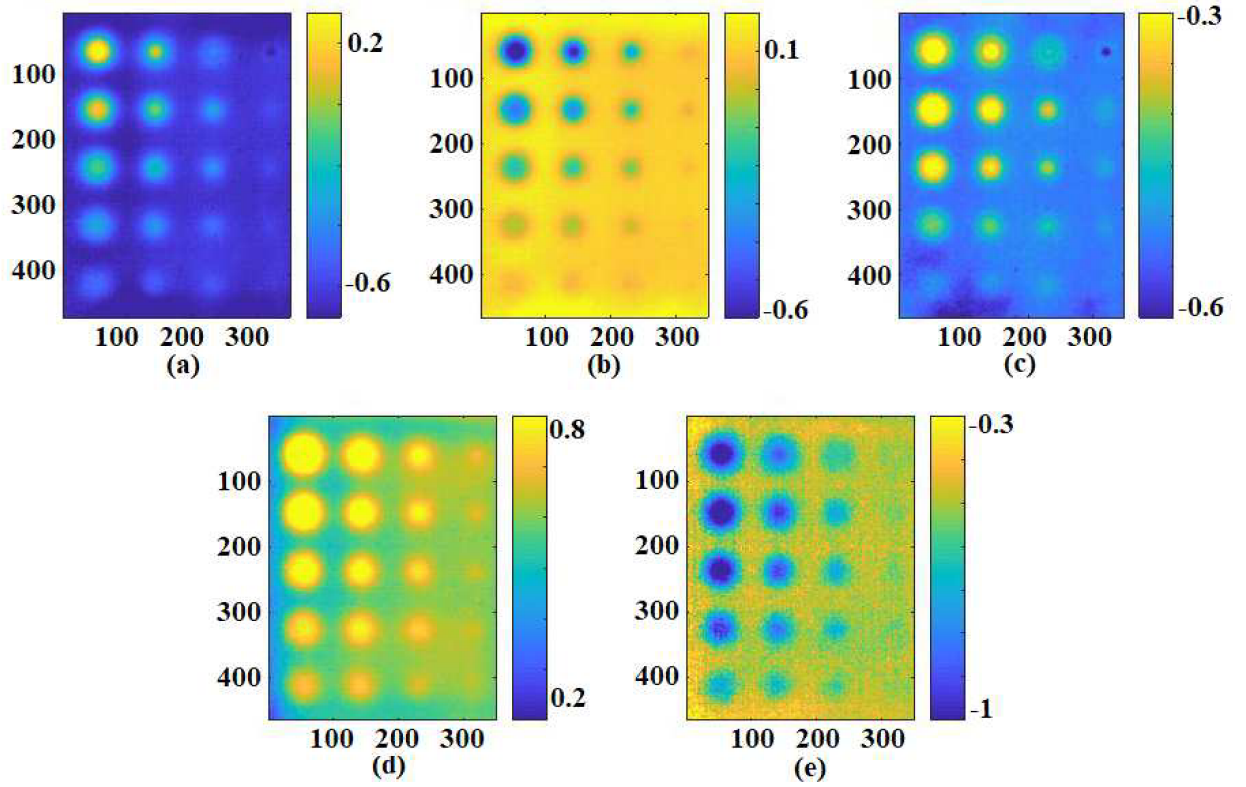


Figure 3.42: Thermographic maps related to the first column of the Tab. 3.5: (a) 1st derivative TSR®, (b) 2nd derivative TSR®, (c) slope, (d) R^2 , (e) phase (PPT).

By concluding, in literature, there are some works that show a comparison among the different thermographic techniques and post processing algorithms in terms of the capability to detect a defect [8, 9, 10, 11, 12, 13, 14, 15, 16]. However, most of them regards a qualitative evaluation of the results, avoiding the quantitative characterization of the detected defects in terms of size and depth estimation. Here, quantitative criteria have been used to underline the strengths and the weakness of each algorithm. Besides, two different types of approach are adopted to show the results that come from a comparison among different post processing algorithms; the first one sees the assessment of these criteria by considering the same type of analysis for all the algorithms, in terms of truncation window size and data processing; instead, the second one sees the analysis of the TSR® and PPT algorithms by considering the entire sequence of raw data and stressing the advantage of having as a final result a sequence of maps after a single analysis, although the results of an analysis that considers different intervals are profoundly different. This latest approach takes into account of the mathematical formulations of a polynomial fitting, that requires a good number of data (frames) to follow the same in a correct way and to carry out good results.

This first part of the work proposes an attempt to evaluate the influence of the processed number of frames on the capability of the technique in quantifying the defects. In particular, a single pulsed thermographic test has been carried out (with 3 replications) on an aluminum specimen. This type of material has a high diffusivity and so the observed physical phenomenon ends within the first cooling frames. In order to test how is the right number of frames to choose, different sizes and depths of the imposed defects have been investigated; to detect the presence of superficial defects, few frames are enough to obtain a significant signal contrast. In contrast, deeper defects became

visible after a few seconds and then a wider number of frames have to be considered. Moreover, the number of processed frames changes within different algorithms.

An important result regards the possibility to use the linear correlation between the SBC and the relative defect aspect ratio as calibration curve to make a new procedure to quantify the defect. In fact, the obtained results in terms of linear correlation seem very promising and in some cases, for some algorithms and precise truncation window size of analysis, very good. However, it will be necessary to separate depth and size information in order to quantify the defect thus characterized (Chapter 4).

Chapter 4

By using a calibration approach to estimate defect size and depth

Subsurface defects can be detected by the pulsed thermography technique analyzing the raw thermal data with the application of different post processing algorithms. In this regard, different methods, based on one dimensional models, are used in literature to estimate the depth and size of defects. Two of the most established methods refer to TSR® (Thermal Signal Reconstruction) and PPT (Pulsed Phase Thermography) algorithms. These latter require a carefully set up of the testing parameters such as sampling frequency, truncation window size and energy density to obtain a good depth estimation.

Even if many works have already investigated these methods, there are few works in which the correct procedures to obtain size and depth of defects are deeply explained, above all for high diffusivity materials, such as aluminum.

The aim of this work is to propose a new procedure to obtain depth and size estimation of defects and to overcome the limits shown by the classical and well-established methods. Moreover, the influence of different thermographic parameters on the quantitative results has been studied, by using two experimental setups, in terms of heat sources and infrared detectors.

The proposed procedure starts by the experimental observation that there is a linear correlation between the defect contrasts and the relative aspect ratios, for a suitable truncation window size, after the application of specific post processing algorithms on the raw thermal data.

By using some models already present in literature and adapting them appropriately to the studied case, the linear correlation between the defect slope contrast and the relative aspect ratio has been also demonstrated.

In order to obtain quantitative suitable information, the slope algorithm has been used to analyze the raw thermal data, with the aim to quantify imposed defects in an aluminum sample.

Finally, a comparison with the well-established techniques, TSR® and PPT has been performed and its limitation in terms of depth estimation for this type of material and for precise boundary conditions, such as pulse length and acquisition frequency will be shown.

This part of dissertation wants also to emphasize that it is necessary to have a sample with imposed defects to calibrate the thermographic parameters and to obtain the calibration curves, useful to estimate and characterize the detected defects.

4.1 A new procedure to quantify the defects in a material with high diffusivity

4.1.1 Theoretical and experimental motivations

Within the previous Chapter (Chapter 3) an investigation about the possibility to characterize the defects in an aluminum sample, by using pulsed thermography and its post-processing algorithms has been shown and the obtained results have been widely illustrated. The obtained results have demonstrated that a linear correlation between the achieved SBC for a precise post-processing algorithm and the relative set of defect aspect ratios exist for a suitable truncation window of analysis.

Besides, the graphs reported in Section 3.5 consider the slope and R^2 algorithms showing the trends that can be obtained frame by frame in the case of precise features of investigation such as the number of detected defects above a certain noise threshold, the achieved SBC and the possible linear correlation SBC-r (Fig. 3.36-Fig. 3.40). It is precisely from the analysis of these experimental trends that it is discovered that there is a suitable analysis window for which occurs the optimum in terms of linear correlation SBC-r, when a good number of defects are diagnosed.

It has also been experimentally demonstrated that there is a window of analysis which can be associated with the concept of a “blind frequency” but in the time domain, and that this changes with the depth and the size of the defect (Fig. 3.30-Fig. 3.31).

These experimental evidences have been studied mainly in the case of the slope algorithm (Fig. 3.30), usually used for a qualitative analysis of the raw thermographic data and they should be theoretically explained if the aim is to find and to propose a procedure for a quantitative characterization in terms of defect size and depth evaluation.

By considering the Almond 2D model for a semi-infinite body Eq. 1.21 [38, 39, 40], it is possible to simulate the thermal behaviors of different defect aspect ratios and using the post processing algorithms [4, 5, 6, 7, 8, 9, 10, 11, 12, 13, 14, 15, 16, 17], for investigating the correlation between the signal contrast and the aspect ratio. In the previous section, it has been demonstrated as for a suitable truncation window size there is a linear correlation between the signal contrast and the defect aspect ratio. This relation occurs for different outputs deriving from different algorithms [19, 20, 21]

The slope algorithm has been considered, but the results can be extended to other algorithms.

Within the previous Chapter (Chapter 3), the slope behavior has been already studied, by computing a linear fitting of the raw thermal data frame by frame, in order to obtain the slope trend for each defect and for the relative sound. In this way, it is possible to obtain a sequence of slope maps that shows the behavior of this thermographic parameter over the time.

In Fig. 4.1, the data processing procedure to obtain the slope contrast trend for each defect is shown. Here the abbreviation “t.w.s.” is used to indicate the truncation window size.

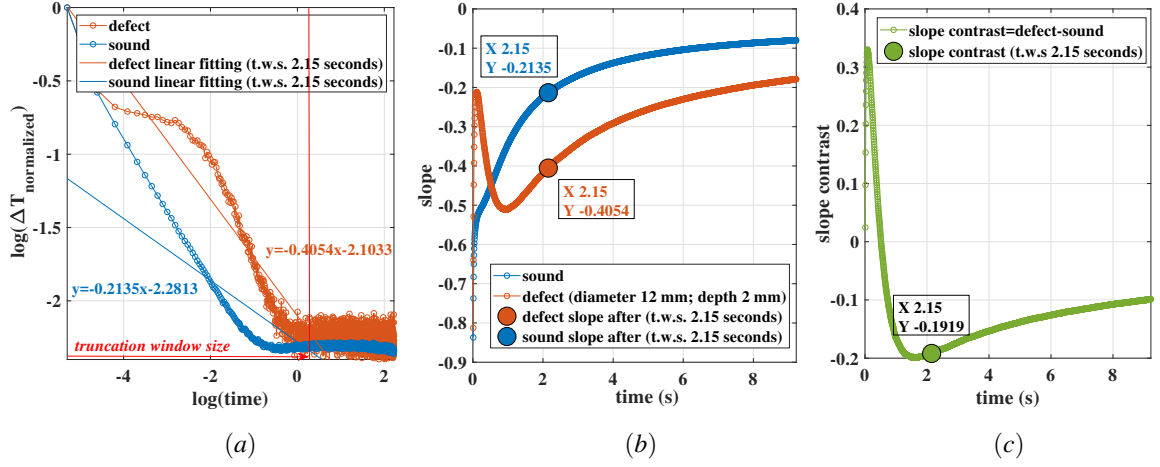


Figure 4.1: Thermal trends (a), Slope trends (b) and the relative slope contrast over the time (c) for a defect and relative sound (diameter 12 mm, depth 2 mm).

By considering the other defects of the tested aluminum sample, it is possible to obtain similar trends to the previous one, reported in green (Fig. 4.1a). The slope contrast has been computed, frame by frame, by using the model in Eq. 1.21 for different aspect ratios and by using these parameters: $\rho = 2700 (kg/m^3)$, $k = 190 (W/mK)$, $c_p = 880 (J/kgK)$, $f = 200 Hz$, $Q = 6400 J/m^2$; the theoretical sound slope equal to -0.5 has been subtracted to obtain the simulated contrast slope trends, for each defect.

In Fig. 4.2, the simulated slope contrast, frame by frame, for a defect depth equal to 3 mm and different sizes, is shown. In the same figure (Fig. 4.2), the simulated slope contrasts are compared with the experimental one.

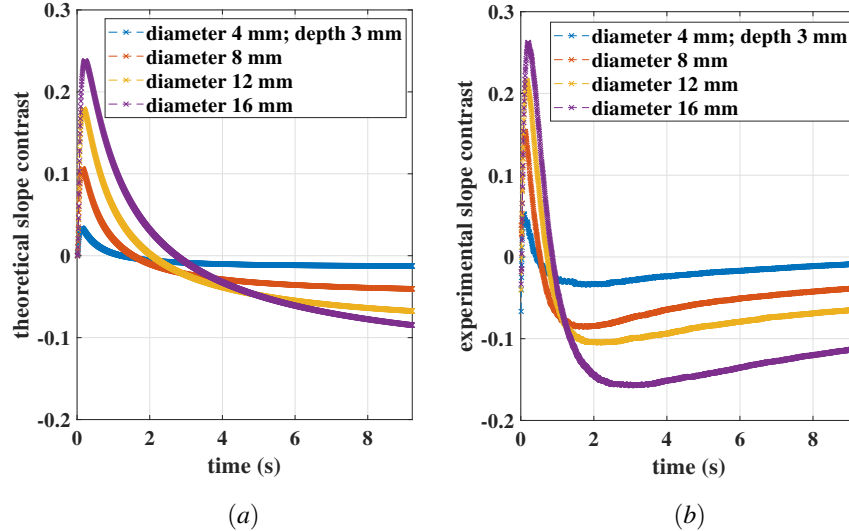


Figure 4.2: Comparison between simulated (a) and experimental slope contrast (b) for different aspect ratios; depth 3 mm.

Theoretically, it is possible also to obtain the trend that describes the linear correlation between the slope contrast

and the defect aspect ratio, by studying as this correlation evolves frame by frame over the time manipulating the Almond models. This linear correlation is expressed in terms of R^2 and can be obtained by a linear fitting in a double logarithmic scale and computing the slope contrast for each defect aspect ratio and plotting the relation that exists between these values and the chosen aspect ratios for each frame.

In Fig. 4.3, the correlation that occurs between the slope contrast and the chosen aspect ratios is shown for 3 different truncation window sizes, in order to understand the logical and chronological process that leads to the result shown above and here recalled for the slope algorithm (Fig. 4.4).

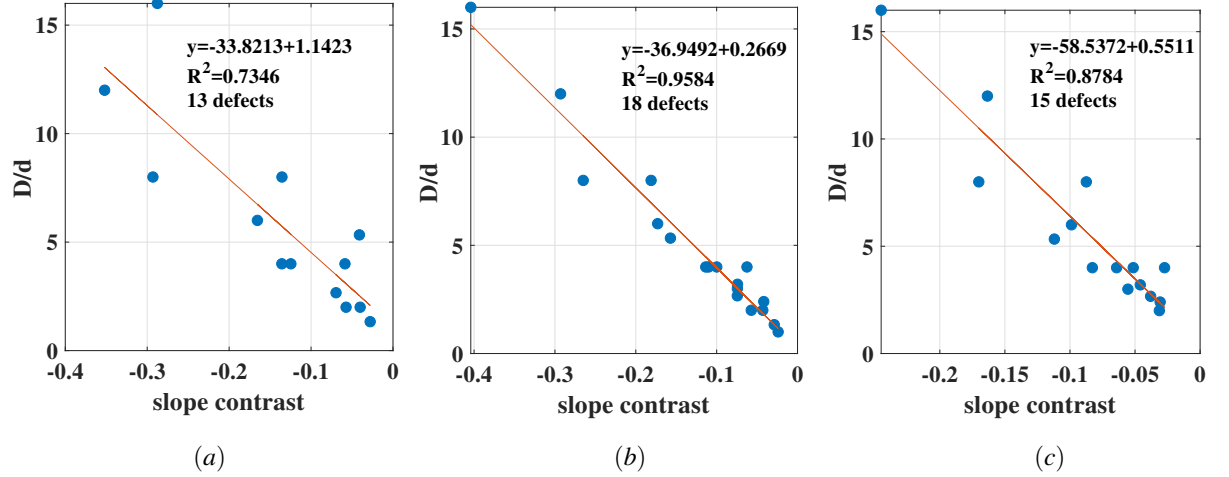


Figure 4.3: Correlation between slope contrasts and relative defect aspect ratios for different truncation window sizes, chosen as example (1 second-200 frames (a), 2 seconds-400 frames (b), about 9 seconds-1845 frames (c)).

As we can see by analyzing Fig. 4.3, the graphs show in the abscissa (x-axis) the simple contrast and not the relative normalized one (however, the linear relationship remains the same) and in ordinate (y-axis) the defect aspect ratio r , so the axes are inverted respect to those previously reported (results in Chapter 3), in order to have as output the one useful for the final calibration.

By computing this correlation frame by frame, it is possible to find, experimentally, the precise truncation window size in which the maximum linear correlation (R^2 value) occurs (red line in the next Fig. 4.4b).

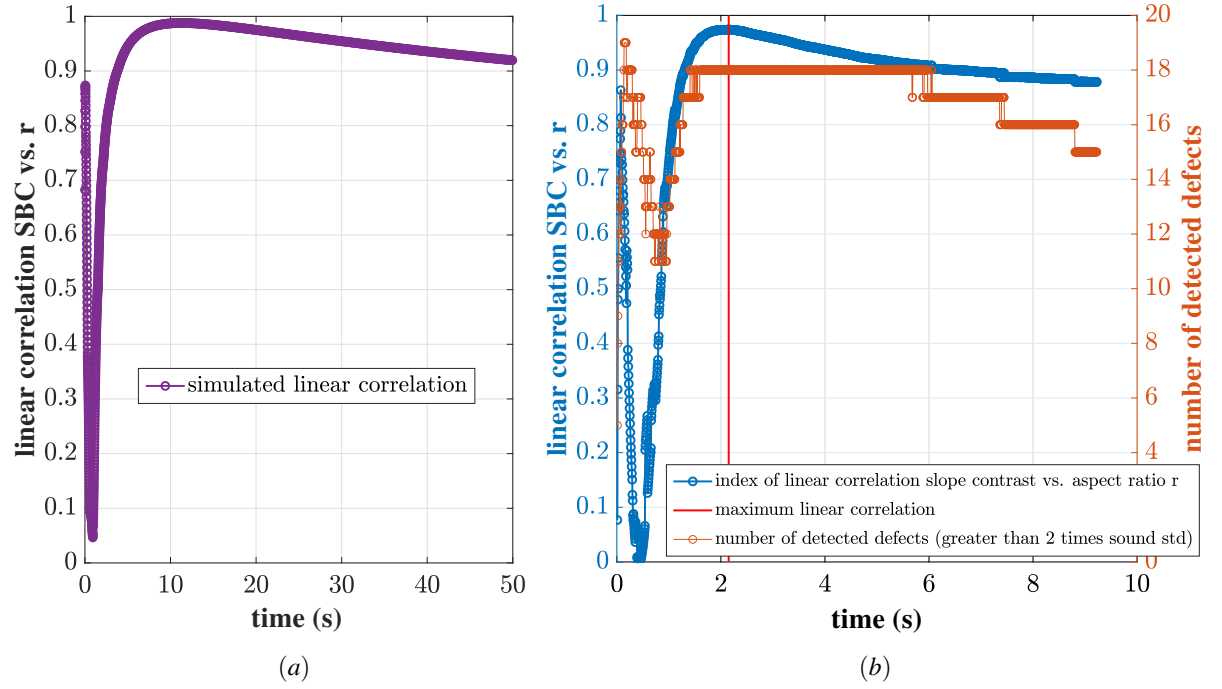


Figure 4.4: simulated (a) and experimental linearity (b) between the defect aspect ratios and the relative slope contrasts.

In the simulated case, the linear correlation is obtained by considering all 20 defect aspect ratios and the relative simulated slope contrasts.

It is necessary to stress that the experimental trends have been obtained by taking into account the real detected defects with a contrast higher than 2 times of the sound standard deviation (the orange trend in Fig. 4.4b).

By comparing Fig. 4.2 and Fig. 4.4, it is evident as there is a discrepancy between simulated and experimental results, above all if we consider the times in which the maximum linear correlation and the slope contrast changes in sign. This discrepancy is due to the two hypotheses that are not verified for the experimental tests: semi-infinite plate and Dirac pulse, as well as the noise dependency (measured in terms of sound standard deviation).

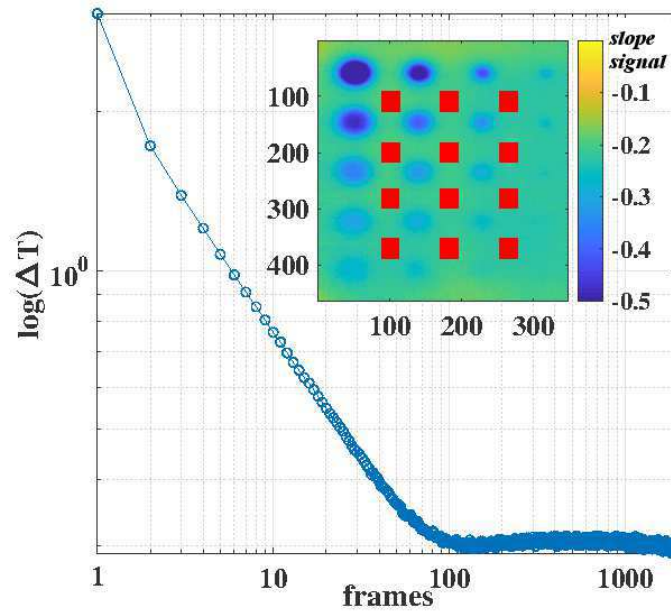


Figure 4.5: Experimental delta temperature over time (expressed as frames number) related to the sound regions highlighted in red in a thermographic map showed as example (double log-scales).

Fig. 4.5 shows the experimental thermal contrast of the sound (indicated with red squares) during the cooling phase. It is clear as in less 100 frames (0.5 seconds), the thermal phenomena can be considered concluded.

The experimental conditions are very far from the hypothesis of a semi-infinite body expressed by the Eq. 1.21, and so the experimental slope is very different from the theoretical value equal to -0.5 . For these reasons, to have a better comparison of the simulated results with the experimental ones, it is possible to consider the body with a finite thickness by means of Eq. 1.20.

Fig. 4.6 shows the theoretical temperature and the thermal contrast trends by simulating aluminum plates with different thicknesses and by adopting a sample rate of 200 Hz.

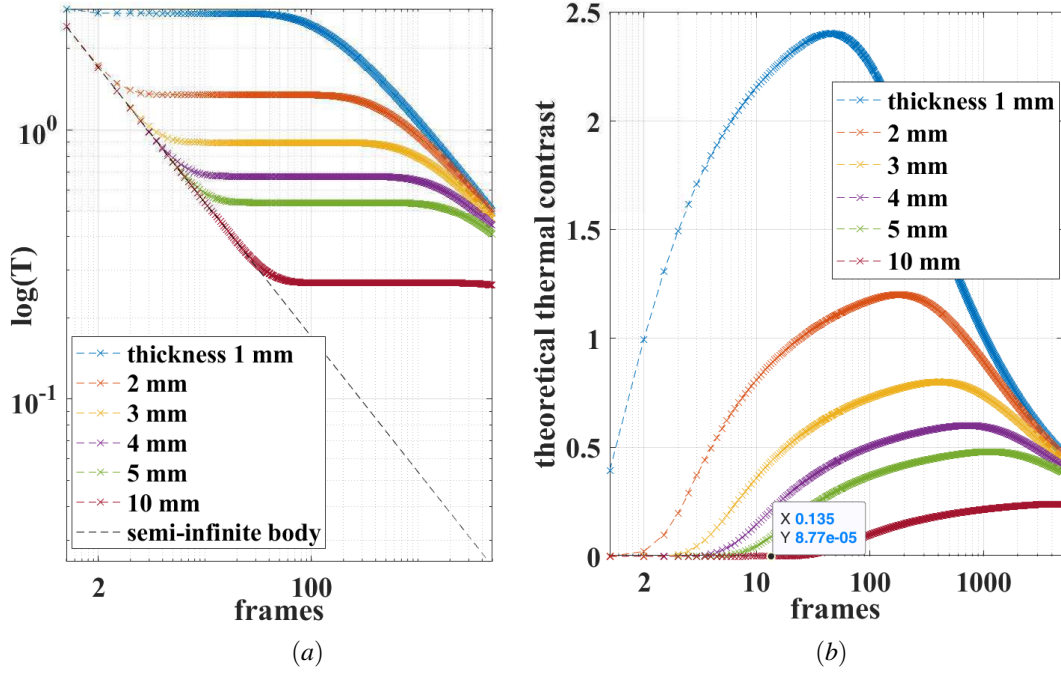


Figure 4.6: Thermal defect trends (a) and relative contrasts (b) for a finite body.

In Fig. 4.6, it is simple to verify that the thermal wave reaches the sample bottom (10 mm) within 0.135 seconds and then after only 27 frames.

By using both the models described with Eq. 1.21 and the Eq. 1.20, it is therefore possible to explain better the experimental behavior of material.

For this reason, it is necessary to modify the Eq. 1.21, in order to evaluate the influence of the real sample thickness on the defect thermal behavior [41]; in this way, the thermal contrast is re-defined by considering as sound the temperature over a plate of specified thickness L , by using the Eq.7.

In this way, to obtain the defect thermal behavior in terms of temperature, it is necessary to simulate the thermal sound behavior by using the Eq. 1.20 for a finite thickness of 10 mm and the thermal contrast by using the Eq.7 for the different defects aspect ratios (Fig. 4.10, red box). The final used model can be expressed with these following equations:

$$\Delta T(t) = 2 \frac{Q}{e\sqrt{\pi t}} \left(\sum_{n=1}^{\infty} R^n e^{-\frac{(nd)^2}{\alpha t}} - \sum_{n=1}^{\infty} R^n e^{-\frac{(nL)^2}{\alpha t}} \right) \left(1 - e^{-\frac{(Pd)^2}{16\alpha t}} \right) \text{ for each defect aspect ratio with } L = 10 \text{ mm} \quad (4.1)$$

$$T(t) = \frac{Q}{e\sqrt{\pi t}} \left[1 + 2 \sum_{n=1}^{\infty} R^n e^{-\frac{(nL)^2}{\alpha t}} \right] \text{ with } L = 10 \text{ mm} \quad (4.2)$$

By using these equations, a better correspondence has been obtained between simulated and experimental data, as shown in Fig. 4.7 and Fig. 4.8. In particular, both the maximum and minimum slope contrasts (as absolute values) are anticipated in the time (Fig. 4.7).

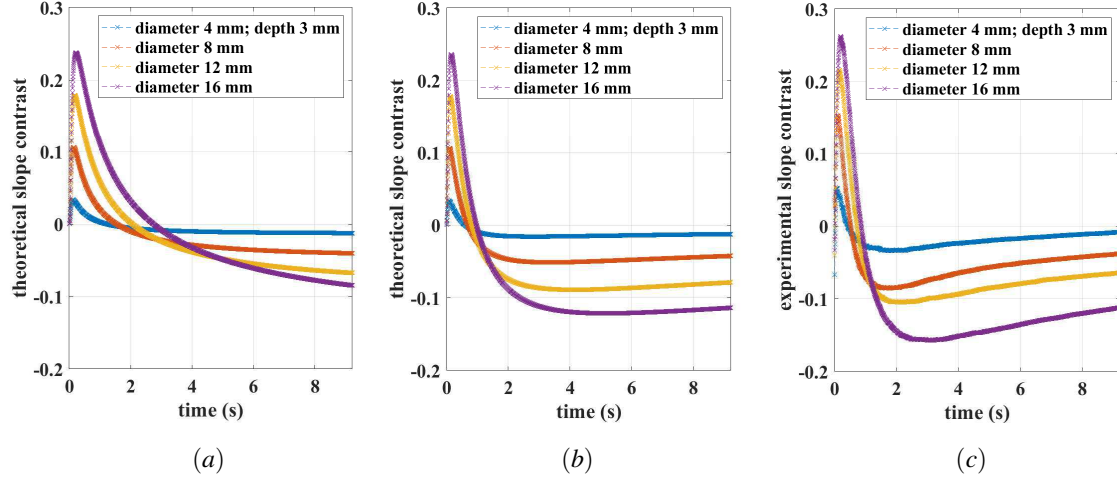


Figure 4.7: Simulated (a, semi-infinite body and b, finite body) and experimental slope contrast (c) for different aspect ratios; depth 3 mm.

In a similar way, also the linear correlation between the slope contrasts and the relative defect aspect ratios can be obtained for simulated and experimental data (Fig. 4.8).

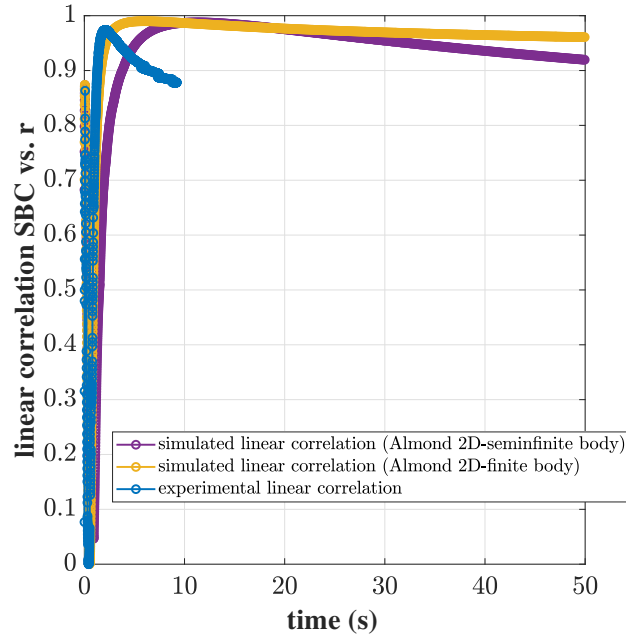


Figure 4.8: Simulated and experimental linear correlation between the defect aspect ratios and the relative slope contrasts: a comparison between Almond 2D model-semifinite body, Almond 2D-finite body model and experimental one.

Some differences between the simulated and the experimental results remain, since a finite pulse of 5 ms cannot be approximated with a Dirac pulse for this material. Besides, the experimental results are affected by the noise, that

involves a decrease in the signal contrast and number of detected defects. In this regard, by using Eq.8, the sound behavior can be obtained, frame by frame, by applying the slope algorithm.

In Fig. 4.9, it is possible to observe that, the slope sound of the experimental data differs from the theoretical one (-0.5) above all in the early frames of cooling (blue trend). Also, in Fig. 4.9 the simulated sound slope trend is reported in green, obtained by using the Eq.8.

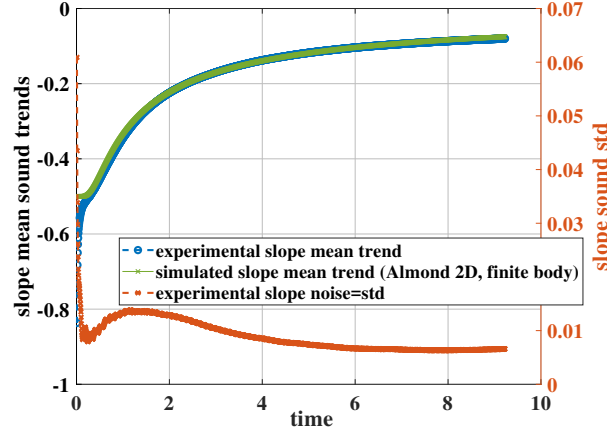


Figure 4.9: Experimental slope results shown in terms of mean and standard deviation for the considered sound area.

The experimental data are computed by considering the same red area indicated in the previous Fig. 4.5. In Fig. 4.9, the trend of the sound standard deviation is also reported. This trend is a measure of the experimental noise due to the acquisition and data post processing.

Some discrepancies that still remain are also due to not a perfect estimation of the material thermal properties, but the green simulated trend follows very well the blue experimental one.

In this way, by studying the slope behavior over the time with well-established Almond models [39, 41, 42, 43, 44, 45, 46, 47, 48], it has been possible to estimate the correct temporal window within the maximum linear correlation occurs (10 seconds are sufficient for this type of material and thickness) and also the one when the slope contrast changes in sign.

4.1.2 By using two different set-ups and very different thermographic equipment: two different frame rates and pulse durations

Several tests have been carried out on the same aluminum sample reported in Fig. 3.1, with different flat bottom holes, characterized by different sizes and depths. The proposed procedure consists of a first phase in which a calibration curve is obtained, by using the defect aspect ratio within the sample. Then, to validate it and obtain the size and depth defect estimation, defects with a different aspect ratio were considered as validation data set. These defects have been specially created in a sound part of the sample, choosing aspect ratios different from those used for obtaining the calibration curve and with very small values, between 2 and 3, around the minimum value known in the literature as the detectability threshold of the pulsed thermographic technique. The nominal defect sizes and depths of the defects used as validation data set are reported in , with the previous one already shown.

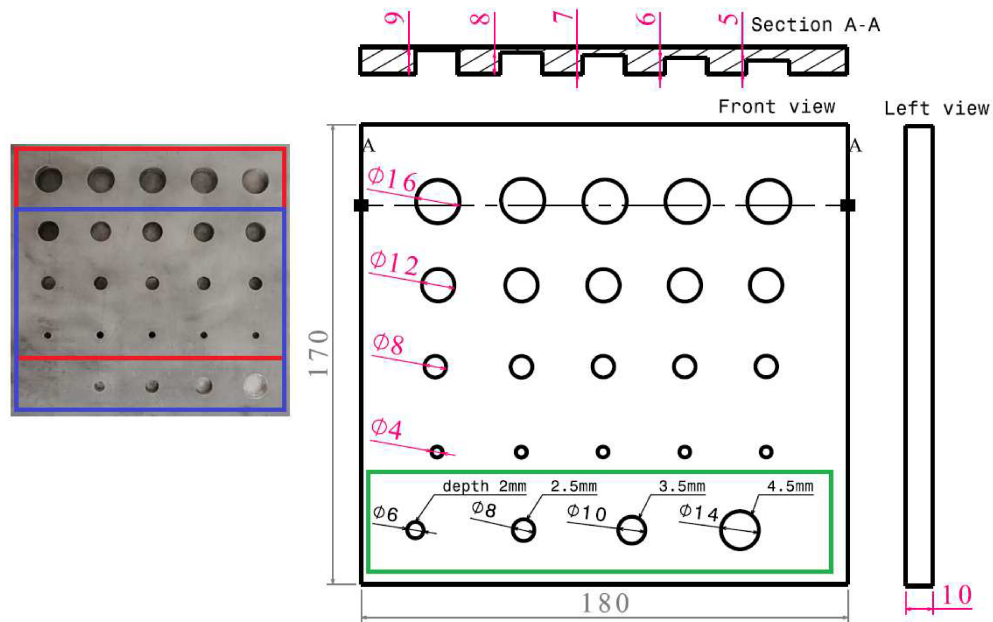


Figure 4.10: Aluminum sample with simulated defects (nominal sizes and depths) used for thermographic tests.

The thermographic tests have been performed using the same set-up and thermographic parameters indicated in the previous chapter (Chapter 3). It was necessary to perform two different and separate tests, in order to obtain firstly the calibration curve and then the validation of the propose procedure. The same frame window has been kept for these two tests so, as it is shown in Fig. 4.10, the defects within the red box have been used for creating the calibration curve, while the ones within the blue one for showing the validation.

A second more performing set-up, Fig. 4.11, has been used for obtaining a comparison with the other two techniques PPT and TSR®, considered as reference.



Figure 4.11: The used set-up for the comparative thermographic pulsed tests.

This setup is composed by the Infratec ImageIR 8300 hp IR camera with a cooled detector, a full frame window of 640x512 pixels with a wavelength range of 2 to 5 μm and an NETD < 30 mK. The pulsed tests have been performed by using the same acquisition frame rate (200 Hz), in order to have the whole sample in an only acquisition. To increase the frame rate up to 1000 Hz, four different frame windows of dimensions 160x128 and then four different tests have been carried out to cover the whole specimen.

Four synchronized flash lamps with a pulsed duration of 3 ms and a total converted energy of 24 kJ have been used. To reduce the thermal afterglow of the lamps, poly-methyl methacrylate (PMMA) plates were mounted between the flash lamps and the test specimens [75]. Thermal sequences of 15 s were acquired. The IR camera has been positioned at a distance of about 45 cm to the sample surface, while the distance between lamps-sample was equal to 35 cm. The camera and energy source specifications are reported with a major detail in Appendix A.

In the next sessions, the new procedure will be exposed together with a quantitative comparison with the traditional methods.

4.1.3 Experimental results and validation

As it already explained in the previous section, the proposed procedure is based on the linear correlation between the defects aspect ratio and the relative slope contrasts.

By analyzing the cooling phase of a pulsed thermographic test there is a truncation window size in which the maximum of the linearity is reached Fig. 4.4. As it just demonstrated, this latter depends strongly by the thickness of the sample. In our case, this time interval is about 2 seconds (2.15 s, 430 frames).

In Fig. 4.1, the sound slope signal over time is reported with the slope signal of defect with diameter 12 mm and depth 2 mm. It is interesting to underline as the maximum of the linearity occurs away from the time in which the maximum slope contrast (and maximum thermal contrast) is obtained. Indeed, the first part of the cooling phase is usually used in literature to quantify size and depth. However, the slope contrast is more stable in the second part of the cooling phase and this explains the better correlation in this zone between the aspect ratio and the slope contrast.

Moreover, as it shown in Fig. 4.4, a good defect detection is obtained in correspondence of the maximum R^2 . This topic will be deeply investigated in the next section.

Unlike the previous sections (Chapter 3), in which it was necessary to introduce the concept of the Signal Background Contrast (SBC) in order to compare the different algorithms [19, 20, 21], in this one it is sufficient to refer to the simple contrast between each defect and relative sound. The chosen defective and sound areas are the same specified in the previous sections. The pre-processing procedure, in terms of cold frame subtraction and normalization of the raw thermal data, is already explained in Section 3.2. As already specified, the results shown within this Chapter 4 they are not see the application of the final Gaussian filter.

Fig. 4.12 shows the linear correlation between the aspect ratios and the slope contrasts for the defects enclosed in the red box Fig. 4.10, used for obtaining the calibration curve. Only the detected defects have been used, as explained in the previous Chapter 3 and reported in [19, 20, 21].

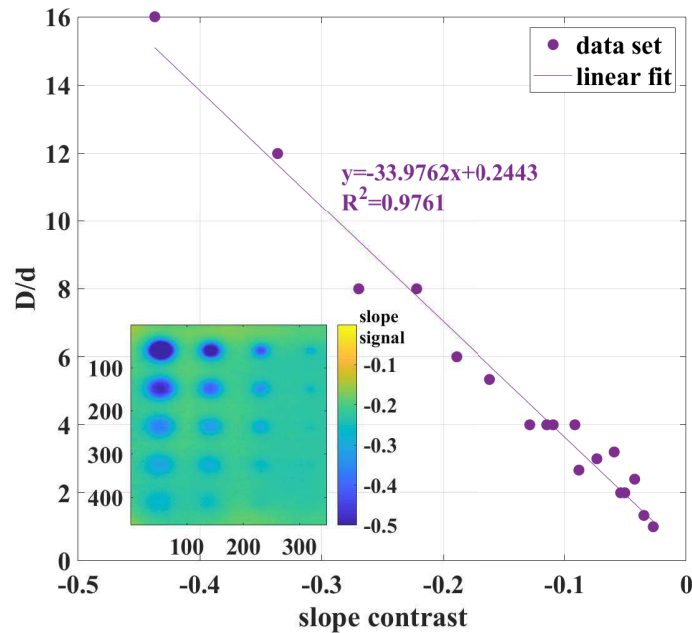


Figure 4.12: Slope results after an analysis interval of 2.15 seconds: linear correlation between defect slope contrasts and relative aspect ratios and corresponding slope map (1 test).

To verify the test repeatability, in Fig. 4.13 are reported the results of 3 replications obtained by keeping the same setup and carrying out 3 pulsed tests. The mean result, obtained from these 3 replications, is also reported in black.

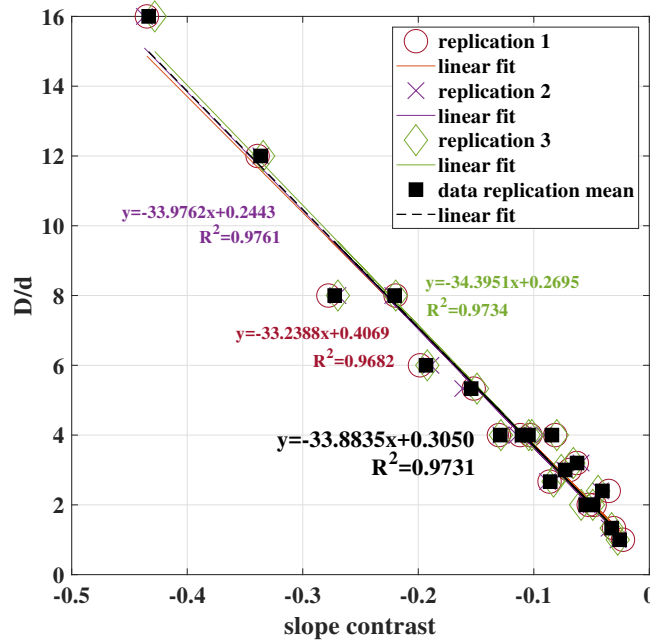


Figure 4.13: Mean calibration curve (aspect ratio vs. slope contrast) and relative replication results (3 tests).

In the next Fig. 4.14, the mean values obtained with these 3 replications and for each defect, are reported together with the mean calibration curve (the one in black). The obtained linear model is reported with its confidence and prediction bounds. These latter are larger than the confidence bounds because take into account not only the error for the estimation of the model, but also the error associated to future observations [134, 135].

In the same graph, the slope contrasts of defects used for validation are reported with their standard deviation calculated for three replications. It is necessary to stress, again, that these last measurements and relative post-processing values are obtained by performing other tests with a different camera window, and so these are different acquisitions.

The calibration curve can be used for estimating the aspect ratio of a detected defect, by knowing the achieved slope signal contrast, after a pulse test and the application of the chosen post processing algorithm of data analysis.

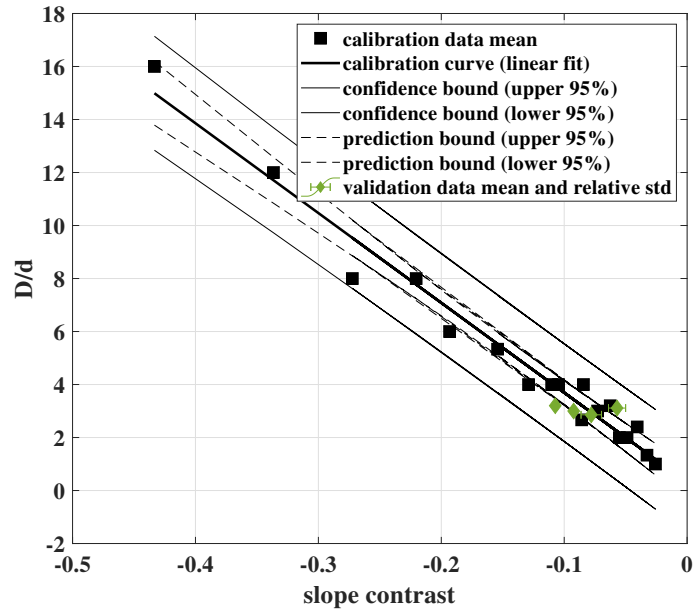


Figure 4.14: Calibration curve (aspect ratio vs. slope contrast) with the estimated regression line (linear model), the prediction bounds (external curves) and the 95% confidence bounds.

Now, it is necessary to separate size and depth information in order to characterize and quantify the defect.

The size of a defect can be estimated by adopting several procedures or methods present in literature [74, 127]. In this case, the semi-contrast method has been used: the contrast between the defect and the relative sound is evaluated as explained before and a threshold equal to half of this value is chosen to discern defect and sound pixels [127]. Known the resolution of the test, in terms of mm/pixel ratio, it is possible, then, to determine the defect size. The same procedure has been used for all the defects considered as validation data set.

Fig. 4.15 shows an example of the obtained binary map, choosing the threshold determined by applying the semi-contrast method for the defect reported as example within a yellow circle.

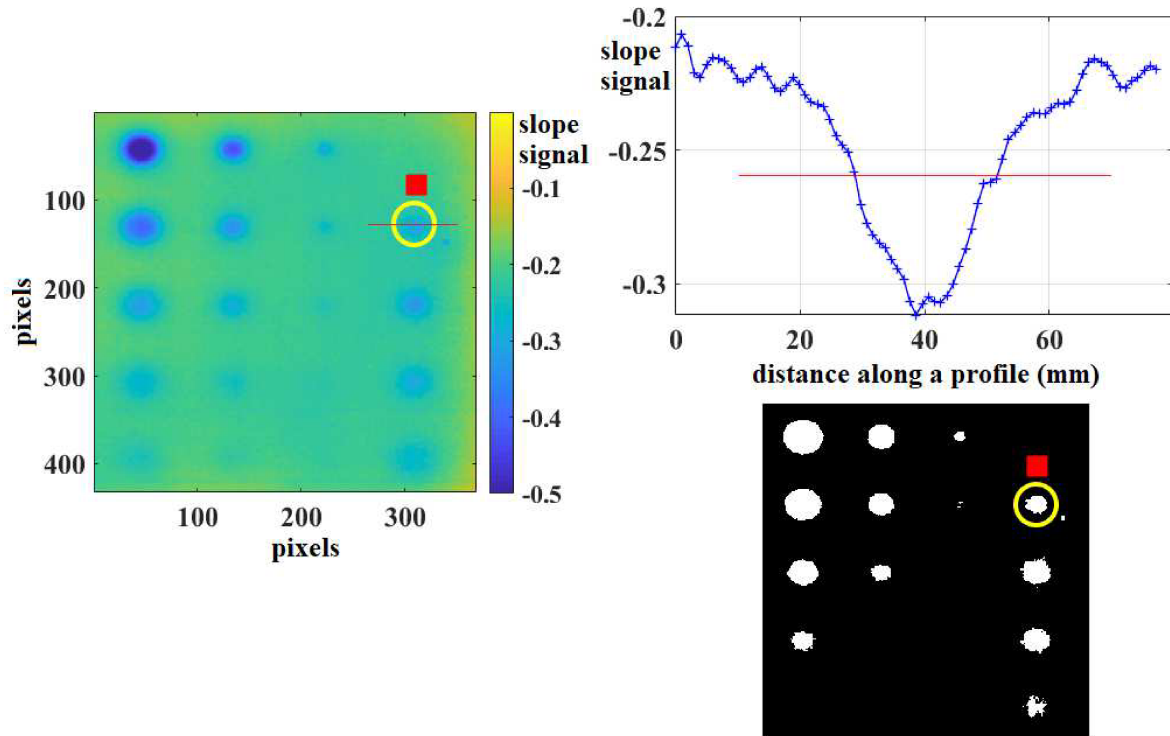


Figure 4.15: Defect size estimation by using the semi contrast method (an example of the obtained results by considering the underline defect and the relative sound).

The proposed quantitative procedure can be summarized by the following steps and can be used if a generic component with thickness L is considered:

1. Obtaining a sample specimen with imposed defects (with known size and depths) and with the same thickness of the component is necessary for the calibration phase
2. Using the well-established Almond models, to study the thermal behavior of material and have an idea of the correct test parameters
3. Carrying out pulsed thermographic tests (at least 3 replications)
4. Applying a post processing algorithm, like the slope one, analyzing the thermal behavior over the time frame by frame, in order to obtain the precise temporal window (exact number of frames) for which there is the maximum linear correlation between the signal contrast (here the slope contrast) and the defect aspect ratios
5. Obtaining the calibration curve by means of a linear fitting of all data in correspondence of the maximum linear correlation (replications allow for improving the results)
6. Carrying out pulsed tests on the considered component by keeping the same set-up used for the calibration phase.

7. Analyzing data by considering the same temporal window (truncation window) used for the calibration procedure (replications are recommended to reduce the standard deviation).
8. Selecting an area that can be considered as sound, in order to obtain the signal contrast.
9. Obtaining the defect aspect ratio by using the calibration curve.
10. Obtaining the defect size by applying a threshold algorithm (binary data).
11. Obtaining the defect depth by knowing the defect size and the defect aspect ratio.

In Tab. 4.1 are reported the errors derived by using the proposed procedure on the chosen validation data set (4 defects); the reference values have been measured with a digital caliper, after the drilling, in order to have 2 significative decimal places, after the comma.

estimated aspect ratio	aspect ratio	% error D/d (mean value)	estimated size	size	% error size (mean value)	estimated depth	depth	% error depth (mean value)
3.45	2.94	17.35	6.82 mm	5.97 mm	14.24	1.98 mm	2.03 mm	-2.46
3.60	3.15	14.29	7.87 mm	7.90 mm	-0.38	2.19 mm	2.51 mm	-12.74
2.62	2.71	-3.32	9.74 mm	9.77 mm	-2.60	3.71 mm	3.61 mm	2.77
2.39	2.98	-19.80	11.30 mm	13.96 mm	-19.05	4.72 mm	4.68 mm	-0.85

Table 4.1: % errors on the mean value in terms of aspect ratio, size and depth by using the mean calibration curve (3 replications in both cases).

These results have been obtained using the mean data of 3 replications carried out both in the case of calibration analysis that in the validation one.

Anyway, in Tab. 4.2 are reported the errors obtained if only a measurement is performed.

estimated aspect ratio	aspect ratio	% error D/d (single measure)	estimated size	size	% error size (single measure)	estimated depth	depth	% error depth (single measure)
3.44	2.94	17.01	6.84 mm	5.97 mm	14.57	1.99 mm	2.03 mm	-1.97
3.61	3.15	14.60	7.54 mm	7.90 mm	-4.56	2.09 mm	2.51 mm	-16.73
2.76	2.71	-1.84	9.33 mm	9.77 mm	-4.50	3.38 mm	3.61 mm	-6.37
2.38	2.98	-20.13	11.02 mm	13.96 mm	-21.06	4.63 mm	4.68 mm	-1.07

Table 4.2: % errors in terms of size and depth by using the calibration curve after only a single measurement.

It is necessary to underline that the committed errors in size and depth estimation are to be attributed to a double source: the proposed procedure used to estimate the defect aspect ratio and also the method used to estimate the defect size.

The semi-contrast method has the advantage to process the same data (slope contrast) used for obtaining the calibration curve.

4.2 The limits of PPT and TSR® methods for a correct depth estimation in aluminum material

In this section, two well-established algorithms (TSR® and PPT) will be used for quantifying the defect depths and comparing the obtained results with those obtained in the previous one.

In particular, difficulties and limits due to the high diffusivity of aluminum will be shown by adopting two different setups.

4.2.1 Influence of the pulse duration

A first attempt has been carried out by keeping the same setup used for the proposed procedure Fig. 3.2, and after the more performing one, to do a comparison Fig. 4.11.

TSR® allows for obtaining information about the defect depth by analyzing the first and second derivative of a polynomial fitting of the raw thermal data in a double log scale [56, 71, 115, 116].

The analysis has been performed in Matlab® using the polyfit function on the raw thermal data with a polynomial fitting of 5 degree. The aim is to estimate the defect depth by using the classical Eq. 2.5, starting from the second derivative peak evaluation. In Fig. 4.16, the results in terms of second derivative are reported, for one of the defects (defect size 6 mm, depth 2 mm) and different truncation window sizes.

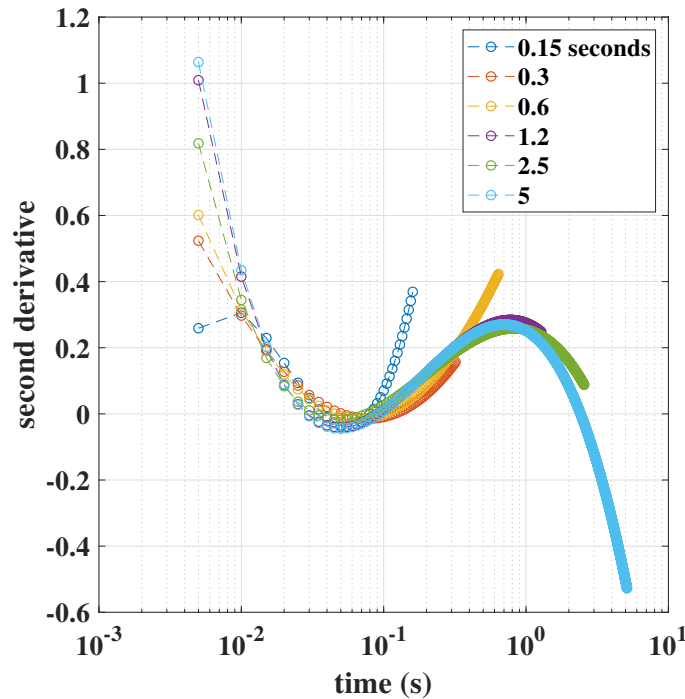


Figure 4.16: Second derivative trends (defect size 6 mm, depth 2 mm). Set-up showed in Fig. 3.2.

The flash duration for this type of material is decisive: the second derivative peak is completely lost. This is due to the flash duration (5 ms) too long for this material and for the considered defect.

For this reason, the same pulsed tests have been repeated by using the set up showed in Fig. 4.11, with a shorter pulsed duration (3 ms), an energy 8 times higher (24 kJ) and also a maximum available frame rate up to 1000 Hz. The chosen frequency remains equal to a low value of 200 Hz, in order to evaluate all depth defect in one acquisition. The same previous defect has been considered to show the second derivative trends and also different truncation window sizes have been considered (Fig. 4.17).

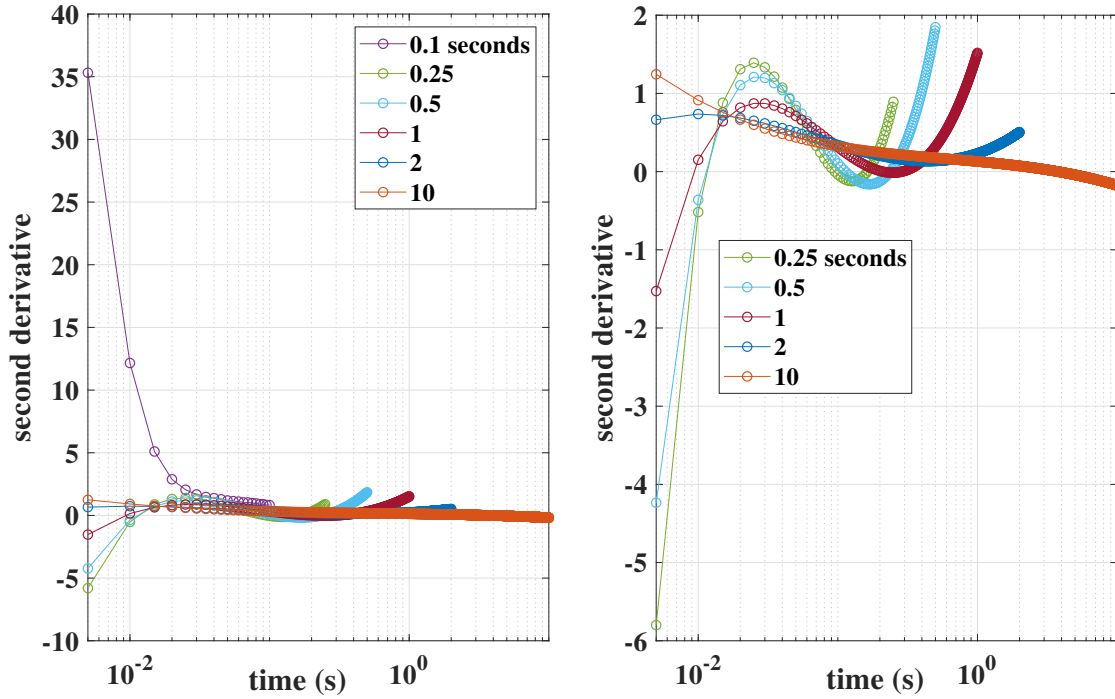


Figure 4.17: Second derivative trends (defect size 6 mm, depth 2 mm). Set-up showed in Fig. 4.11 (200 Hz).

In this case, it is possible to see the second derivative defect peak, but it is necessary to choose the correct truncation window size: in fact, by analyzing only 0.1 seconds or instead 2 seconds, mathematically too few and too much frames, it is not possible to identify the defect peak, anymore. So it seems that, by adopting a more performing thermal camera and choosing the correct analysis window, after a thermal diffusivity estimation, it is possible to have a depth estimation, with a very low acquisition frequency; unfortunately, if different defect depths are considered, the time in which the second derivative peak still remains equal the same.

In the following section (Section 4.2.2), the problem of the acquisition frequency will be illustrated.

4.2.2 Influence of the frame rate

In the following Fig. 4.18, the results are showed for the defects with a size of 12 mm and by considering different depths; the chosen truncation window size is equal to 0.5 seconds.

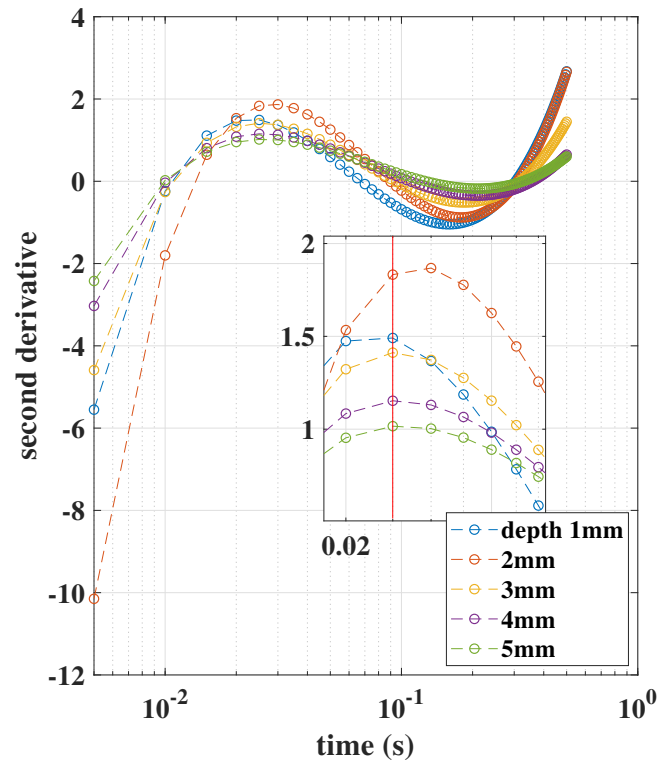


Figure 4.18: Second derivative trends (defect size 12 mm, different depth 1-5 mm). Set up showed in Fig. 4.11 (200 Hz).

As shown, by using a low frequency of 200 Hz, the second derivative time peak occurs always in the same position, so it is not possible to have a depth estimation in this way.

Moreover, the sample rate has been increased up to 1000 Hz by using a different IR camera (Infratec ImageIR 8800, see Chapter 5, section 1) and 4 different windows for the acquisition, within the same set-up in terms of main distances and thermal excitation.

Fig. 4.19 shows for the defects included in the red box in Fig. 3.2, and for a temporal window of 0.5 seconds that it is not possible to use the second derivative peak, in both cases. We are able to see the second derivative peak, but when a low frame rate is used Fig. 4.19a, it occurs always in the same position. Instead, when the frame rate increases up to 1000Hz, Fig. 4.19b, the data result uncorrelated due to the high level of noise.

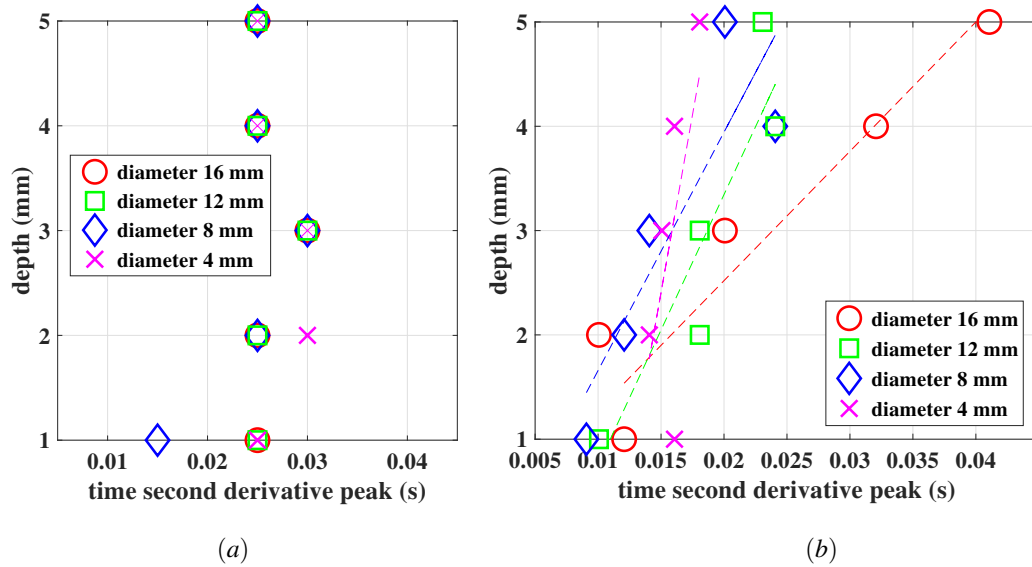


Figure 4.19: Defect main parameters vs Time second derivative peak; set up showed in Fig.3 with a low frame rate 200 Hz (a) and 1000 Hz (b).

In Fig. 4.20, the second derivative trends are reported for the defects used as validation data set, as well the frequency is set to 1000 Hz. It seems obvious that it is very difficult to discern 3 different times in which the second derivative peak occurs when the defects depths are in the range 2-3.5 mm, and the aspect ratio is around 3.

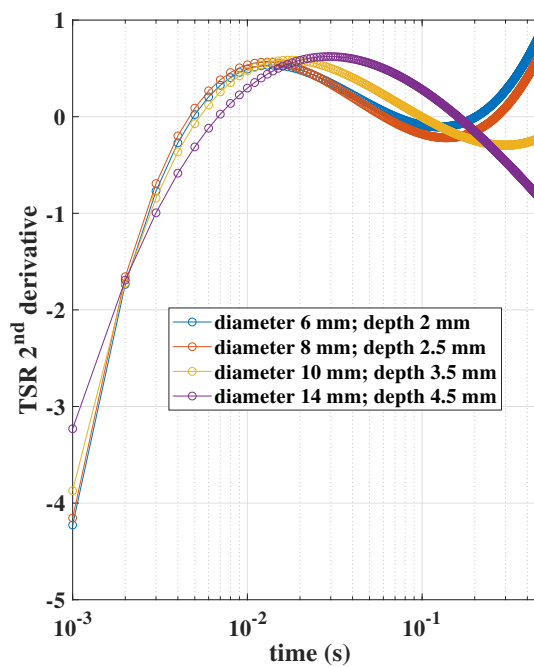


Figure 4.20: TSR® second derivative trends for the defects chosen as validation data set (truncation window size 0.5 seconds).

The same analysis has been carried out by using the PPT algorithm in terms of phase data, in order to obtain the depth estimation by using the so-called blind frequency [142, 143, 144].

In Fig.19, the phase contrast is reported by considering the set up showed in Fig. 3.2, and so a power of only 3000 J. The different trends obtained for the defects used as validation have been considered, by choosing a frames number of 1024 frames (about 1 second with a frame rate of 200 Hz), multiple of $2N$ [17].

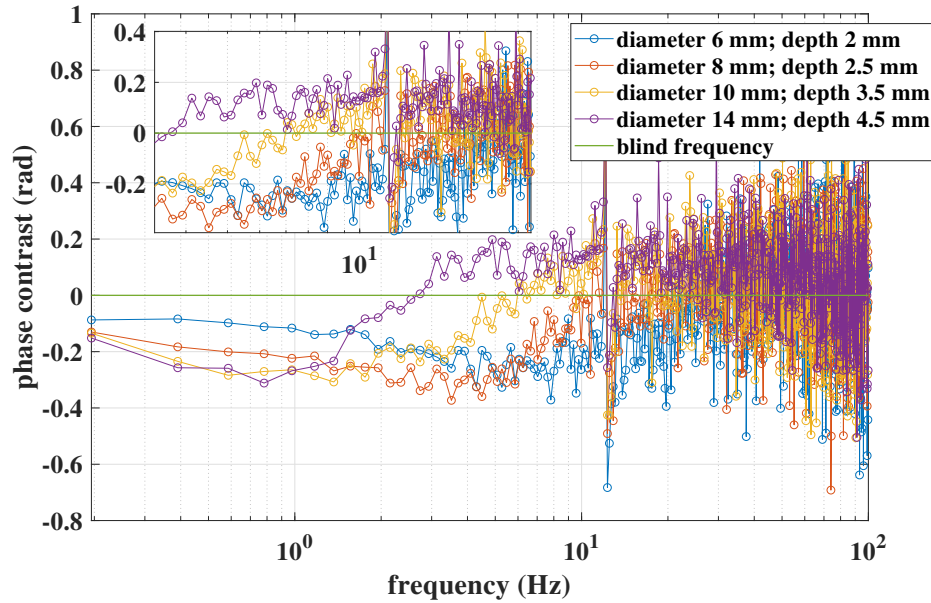


Figure 4.21: Phase contrast trends; set up showed in Fig. 3.2 (3 kJ).

The obtained results in terms of phase contrast are very noisy, due to an inadequate heat power.

Increasing the power up to 24 kJ and the sample rate to 1000 Hz, a clear phase trend was obtained (Fig. 4.22), by choosing the same truncation window size (1024 frames). However, in correspondence of the blind frequency the phase signal still results very noisy, because the material is characterized by a very high diffusivity and so it is not simple to discern all the different depths.

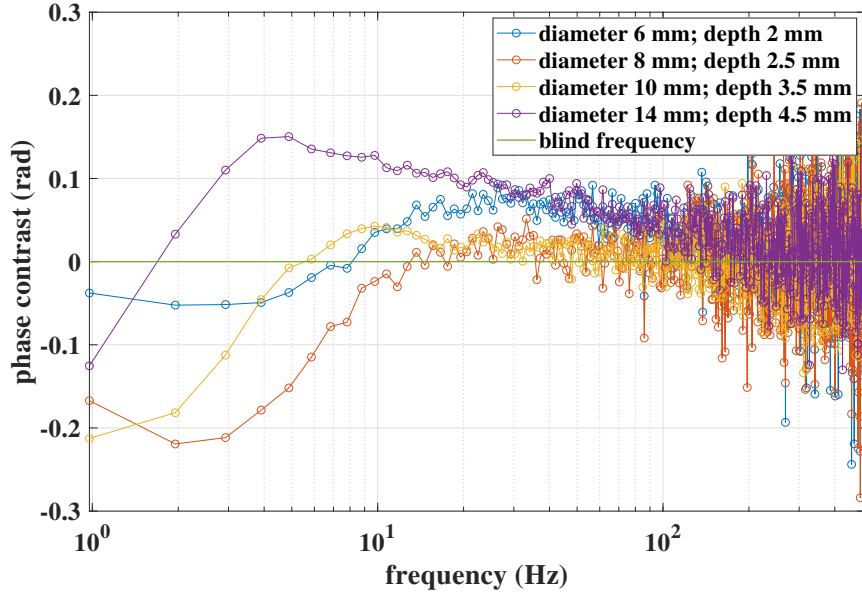


Figure 4.22: Phase contrast trends; set up showed in Fig. 4.11 (24 kJ).

As proposed in the work of Ibarra [92], it is possible to choose a threshold level different from 0, in order to try an estimation of the blind frequency for this type of materials, but this choice remains arbitrary, as the one that regards the best truncation window size. Another problem is the coefficient $C1$, that depends on materials properties and test parameters, so it is also a random variable. Both TSR® and PPT methods, need the knowledge of the thermal diffusivity of the material [62, 63, 64] to retrieve the depth estimation. The thermal diffusivity can be assessed experimentally with the Parker method [62, 63, 64], but also in this case, the measurement requires a more performing setup.

4.3 Final remarks

A new procedure has been proposed to quantify defects in very high diffusivity materials with the pulsed thermographic technique. Such a procedure is based on the linear correlation between the defects aspect ratio and the signals contrast and needs sample specimens with imposed known defects to obtain the calibration curves.

Different tests were carried out on a sample specimen made of aluminum with different flat bottom holes. The slope algorithm has been used for data processing and a comparison with the theoretical models used in literature has been shown. Finally, the limits of traditional quantitative methods have been discussed, by comparing different experimental setups, test parameters and conditions. The main results can be summarized as follow:

- The extensive comparison between the obtained experimental results in terms of slope algorithms and the simulated one has allowed to obtain information about the thermal behavior of the investigated material and simulated defects
- The proposed procedure has been applied on post processing data obtained by the slope algorithm, but it remains still valid for post processing algorithms that provide a signal contrast linearly related to the defect

aspect ratios

- This proposed procedure has been also theoretical explained and motivated; the linear correlation occurs within a precise interval of analysis, changes based on the material properties and the test parameters, but it still occurs and can be explained starting from the analysis of simple models
- The proposed procedure allows for obtaining the quantitative analysis of high diffusivity materials by using a not expensive set up with only 3 kJ in terms of energy source and 200 Hz of acquisition frequency
- Errors up to 20% have been obtained in size and depth estimation, by choosing a very critical value of aspect ratio (around 3) and a material with very high diffusivity

Chapter 5

Case studies

5.1 By using pulsed thermography to detect typical defects of Metal Additive Manufacturing process

One of the most advanced technologies of Metal Additive Manufacturing (AM) is the Laser Powder Bed Fusion process (L-PBF), also known as Selective Laser Melting (SLM). This process involves the deposition and fusion, layer by layer, of very fine metal powders and structure and quality of the final component strongly depends on several processing parameters, for example the laser parameters. Due to the complexity of the process it is necessary to assure the absence of defects in the final component, in order to accept or discard it. Thermography is a very fast non-destructive testing (NDT) technique. Its applicability for defect detection in AM produced parts would significantly reduce costs and time required for NDT, making it versatile and very competitive.

5.1.1 Metal Additive Manufacturing: Laser Powder Bed Fusion (L-PBF) process and its typical defects

Additive manufacturing (AM) processes build three-dimensional (3D) parts by progressively adding thin layers of materials starting from a digital model [136]. This unique feature allows production of complex, small and customized parts directly from the design without the need for expensive tooling or forms such as punches, dies or casting molds and reduces the need for many conventional processing steps.

The AM processes sees the use of materials such as powder, wire or sheets into a dense metallic part by melting and solidification by using an energy source such as laser, electron beam or electric arc, or with ultrasonic vibration in a layer by layer manner.

The AM processes fall into two categories defined by ASTM Standard F2792 [137] as Directed Energy Deposition (DED) and Powder Bed Fusion (PBF). A further distinction is provided as a function of the primary heat source; in particular the nomenclature for laser (L), electron beam (EB), plasma arc (PA), and gas metal arc (GMA) heat sources as PBF-L, PBF-EB, DED-L, DED-EB, DED-PA and DED-GMA.

Among the PBF technologies, Laser-Power Bed Fusion process (L-PBF) also known as Selective laser melting (SLM) allows the manufacture of functional components with various materials and with a complex shape suitable for high demanding applications in mechanical, aerospace, medical, and racing fields.

Generally, L-PBF is an Additive Manufacturing process that uses a laser to melt thin layers of powder. Once

the layer is solidified, a new powder layer is spread, and the process repeats until the part is created. A particular class of PBF processes uses high power energy beams to fully melt the powder particles, which then fuse together to the previous layer(s) when the molten material cools, e.g., selective laser melting (SLM), direct metal laser sintering (DMLS), or electron-beam melting (EBM). Repeating this process, layer-by-layer, directly results in a part with near 100% density, even in metals. These processes are of primary interest to this study [137].

There are several different types of PBF commercial systems that can produce either metal parts. A selective laser melting machine (SLM) was first introduced by Fockele and Schwarze (F&S) of Germany in 1999 with the support of the Fraunhofer Institute of Laser Technology.

According to literature in the field, PBF processes have a high degree of sensitivity to disturbances and input process parameters such as laser power, laser scanning path, and scan speed. It is usual to categorize process parameters into either controllable (possible to modify), such as laser power and scan speed, or predefined (set at the beginning of each build) material properties, such as powder size and distribution.

The vast number of controllable and predefined process parameters as summarized by Mani et al. [138] have a complex influence over the transient thermal behavior of the melt pool, often resulting in unexpected presence of different defects, such as pores, high surface roughness, thermal cracking and delamination.

Porosity and lack of fusion voids are typical and spread defects in AM. There are two main mechanisms by which these defects are produced. First, when some AM processes are operated at very high power density, by increasing the laser scan speed, deposition or melting may be performed in keyhole mode. Without careful control of keyhole mode melting, keyholes can become unstable and repeatedly form and collapse, causing voids inside the deposit that consist of entrapped vapor. Therefore, those porosities are almost spherical in shape. Fig. 6.1a shows keyhole porosity formed during laser assisted AM of 316L stainless steel. The size of keyhole porosity can vary depending on the shape and size of the keyhole. Second, lack of fusion defects can be caused by inadequate penetration of the molten pool of an upper layer into either the substrate or the previously deposited layer as shown in Fig. 6.1b [139, 140, 141, 142].

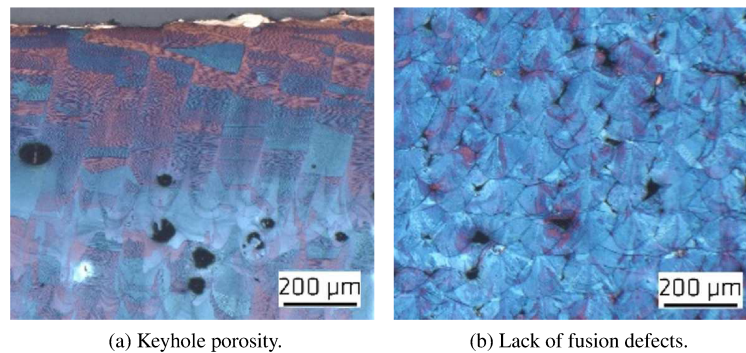


Figure 5.1: Typical defects in Metal Additive Manufacturing process.

There are several non-destructive techniques available to have a measure of this porosity.

The Archimedes method [143] is the simplest method for measuring porosity of an entire specimen. The volume percentage of porosity is estimated by starting from the density of the component. However, the shape, size and distribution of the pores cannot be determined using this method.

Optical microscopy [144] is a widely used destructive method to measure porosity; therefore, the volume of the

pores cannot be accurately measured using this technique. Also, another problem is that this method is not suitable for measuring very small pores.

X-ray computer tomography (X-ray CT) can measure pores as small as 10 μm , and has been used to study porosity formation in laser welds as well [145, 146, 147].

In [148], Synchrotron Radiation micro-Tomography (SR μ T) is used to measure keyhole porosity. This method can be used to measure in-situ formation of porosity.

As shown in [149], by using a scanning electron microscope (SEM) is possible to detect lack of fusion defect.

SEM, X-ray CT and SR μ T can accurately measure shape, size and distribution of very small pores. However, these methods are expensive because of the high capital cost of the equipment.

Alternatively, passive and active thermography can be applied. It could be a promising choice both for on-site control (passive thermography) [150] and offline (active thermography) [5] due to its versatility, costs and the time required for testing and analysis, which are remarkably competitive with other methods of NDT.

5.1.2 Materials and methods

In the following study, several samples made of AISI 316L steel have been produced by means of the L-PBF technique, varying the process parameters at certain positions within the component in order to induce the presence of typical defects of different size, shape, thickness and depth. High and low energy settings of the laser were used to induce different types of porosity (keyhole and lack of fusion pores). By changing also different defects geometrical characteristics, such as depth, shape, size and height (in terms of interested layers number), it is possible to have different combinations and so different case studies.

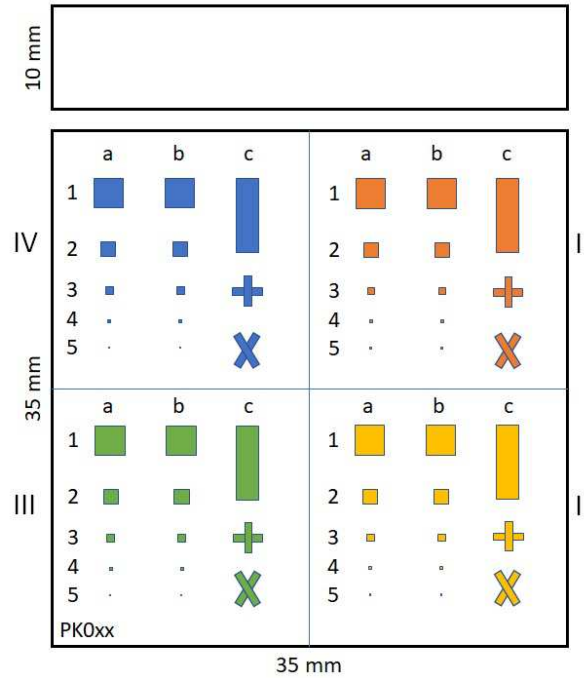
To build these components a selective laser melting machine (SLM) is used (Fig. 5.2), by setting a laser power of 275 W and a scanning speed of 700 mm/s. The different samples have different defects inside. There are some samples with buried regions with keyhole defects, produced by locally increased energy density during the build (275 W; 300 mm/s) and there are some other samples with lack of fusion defects, produced by locally decreased energy density during the build (150 W; 700 mm/s). Besides, some samples have inside very small defects, produced by a gap during the laser illumination.



Figure 5.2: SLM Solutions Group AG, Type 280 HL.

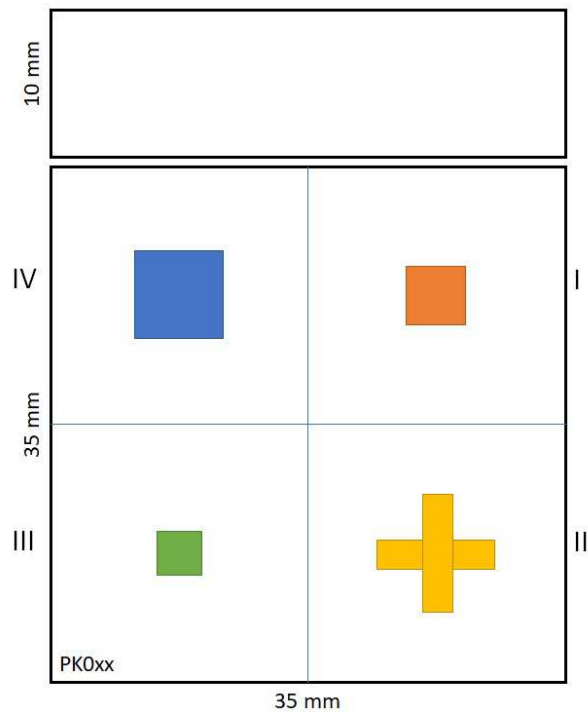
The main defect characteristics in terms of geometry (size, depth and height) and in terms of energy inside are reported in Tab. 5.1, Tab. 5.2 and Tab. 5.3, together with the chosen sample nomenclature. In Fig. 5.3(a-h) some of

the tested samples are shown. The samples are covered with black graphite in order to avoid the reflection problems that characterize the real surface.



	Defect height (mm)	Row 1 a/b (mm)	Row 2 a/b (mm)	Row 3 a/b (mm)	Row 4 a/b (mm)	Row 5 a/b (mm)	Row 1c (mm)	Row 3c (mm)	Row 5c (mm)
I	0.15	2.0x2.0	1.0x1.0	0.5x0.5	0.2x0.2	0.1x0.1	1.5x5.0	2.0x2.0/0.5	1.75x2.5/0.5
II	0.25	2.0x2.0	1.0x1.0	0.5x0.5	0.2x0.2	0.1x0.1	1.5x5.0	2.0x2.0/0.5	1.75x2.5/0.5
III	0.40	2.0x2.0	1.0x1.0	0.5x0.5	0.2x0.2	0.1x0.1	1.5x5.0	2.0x2.0/0.5	1.75x2.5/0.5
IV	0.60	2.0x2.0	1.0x1.0	0.5x0.5	0.2x0.2	0.1x0.1	1.5x5.0	2.0x2.0/0.5	1.75x2.5/0.5

Table 5.1: PK001-PK004 defects geometry in terms of size and height.



	Size (mm)
I	4x4
II	8x8/2
III	3x3
IV	6x6

Table 5.2: PK005-PK016 defects sizes.

Sample Name	Type	Defect depth (mm)	Defect height (mm)	Energy input at defect	Comments
PK001	Gaps in illumination	0.1	different	none	
PK002	Gaps in illumination	0.2	different	none	
PK003	Gaps in illumination	0.3	different	none	
PK004	Gaps in illumination	0.4	different	none	
PK005	Defects with differing energy	0.1	1	high	Cross is illuminated with high energy
PK006	Defects with differing energy	0.2	1	high	
PK007	Defects with differing energy	0.4	1	high	
PK008	Defects with differing energy	0.1	1	low	
PK009	Defects with differing energy	0.2	1	low	
PK010	Defects with differing energy	0.4	1	low	
PK011	Defects with differing energy	0.1	0.25	high	Unwanted defects (lines) in part
PK012	Defects with differing energy	0.2	0.25	high	
PK013	Defects with differing energy	0.4	0.25	high	
PK014	Defects with differing energy	0.1	0.25	low	Unwanted defects (lines) in part
PK015	Defects with differing energy	0.2	0.25	low	Unwanted defects (lines) in part
PK016	Defects with differing energy	0.4	0.25	low	Unwanted defects (lines) in part

Table 5.3: PK001-PK016 defects characteristics in terms of depth, height and energy.

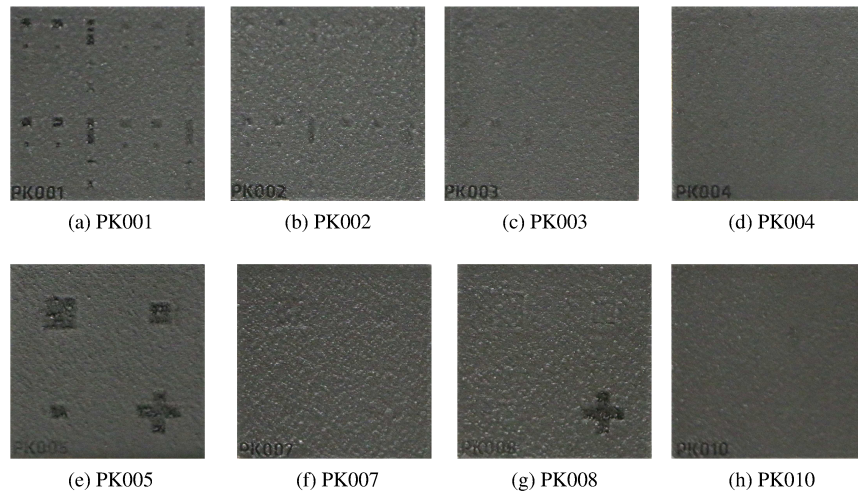


Figure 5.3: Some of the tested samples.

Different thermographic pulsed tests have been carried out by using different energy sources and also different thermal imaging cameras in order to analyze the influence of these choices on the possible results. We have to analyze a different type of defect, that shows a different thermal behavior respect of the normal one; for this reason, it is important to evaluate different types of thermographic analysis, such as the analysis of the cooling down after a pulsed test with flash lamps, the analysis of the cooling down after a test with laser source, by using different pulse durations and different laser power (long pulse analysis) and finally the analysis of the heating phase during the same laser tests (stepped analysis).

The used equipment during the different tests consists of: two different cooling cameras, flash lamps, a widened laser beam and a wave generator. The equipment specifications are shown in detail in Appendix A.

The used flash set-up is shown in Fig. 5.4, with main parameters and distances in Tab 5.4.



Figure 5.4: Pulsed thermographic set-up with 4 flash lamps.

Camera: Infratec ImageIR 8800 Frame rate 1000 Hz Duration 10000 frames Resolution 0.35 mm/pixel Quarter Frame 160x128 pixels	Excitation: Flash lamps Hensel EH Pro 4x6 kJ Impulse Duration 3 ms	Distances: Flash lamps to sample 25 cm Camera to sample 45 cm
---	---	--

Table 5.4: Thermographic parameters and set-up distances for pulsed flash thermography.

To reduce the thermal afterglow of the lamps, poly-methyl methacrylate (PMMA) plates were mounted between the flash lamps and the test specimens [75].

The used laser set-up is shown in Fig. 5.5, with main parameters and distances in Tab 5.5. The test plane, in terms of laser powers and pulse durations is reported in Tab 5.5.

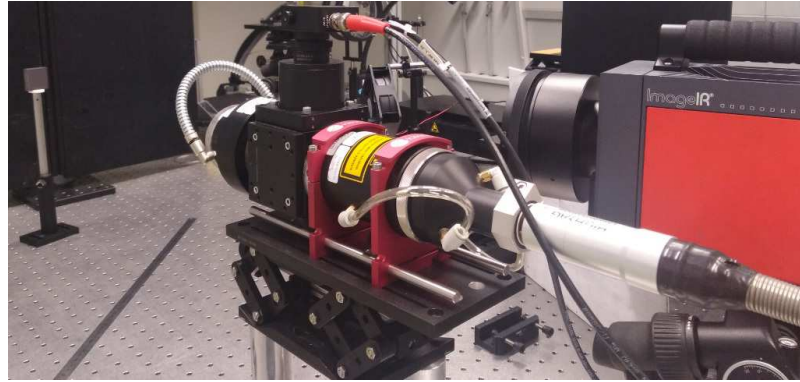


Figure 5.5: Pulsed thermographic set-up with a widened laser beam.

Camera: Infratec ImageIR 8300 hp Frame rate 500 Hz Duration 5000 frames Resolution 0.11 mm/pixel Windowing 320x320 pixels Calibration file -10-60 °C Integration time 600 μ s, 7.93 °C	Excitation: DIODE LDM LASER (935 nm) Square to phat profile 39 x 39 mm^2 Laser focusing lens 600 mm		Distances: Laser to sample 60 cm Camera to sample 80 cm
	Impulse duration 100 ms	Power 300 W	
	Impulse duration 300 ms	Power 300 W	
	Impulse duration 500 ms	Power 300 W	
	Impulse duration 1000 ms	Power 300 W	
	Impulse duration 100 ms	Power 500 W	
	Impulse duration 300 ms	Power 500 W	
	Impulse duration 500 ms	Power 500 W	
	Impulse duration 1000 ms	Power 500 W	
	Impulse duration 1000 ms	Power 500 W	

Table 5.5: Thermographic parameters and set-up distances for pulsed laser thermography.

5.1.3 Theoretical remarks and experimental investigations

In this paragraph the obtained results by using pulsed thermography will be shown.

The simple analysis of the raw thermal data, as many times specified, does not allow to a quantitative analysis; especially in this type of application, where the investigated defect can be considered a small reflector and with a reflection coefficient value very low, it is necessary a post processing of the acquired data in order to detect and characterize these typical defects.

The analyzed defects are very particular, and their thermal behavior is very different, for example, from the case of a flat bottom hole. In particular, the analyzed reflector doesn't have a flat shape, but its shape depends on the process and on the powder quality.

As specified in Chapter 1, the surface temperature due to the back-wall at depth for a homogeneous plate is given by the Eq. 1.20 [5]. Here, in fact, the value of the reflection coefficient R is decisive. Fig. 5.6 shows the plots of temperature decay in the logarithmic domain with different values of R . It can be clearly observed that the time of temperature deviation, representing the depth, is independent to the value of R . Furthermore, the value of R determines the slope of the curve after the temperature deviation. If is 1, the slope is zero, which indicates 100% thermal wave is reflected by the defect or back wall. If is zero, there is no temperature deviation occurred [151].

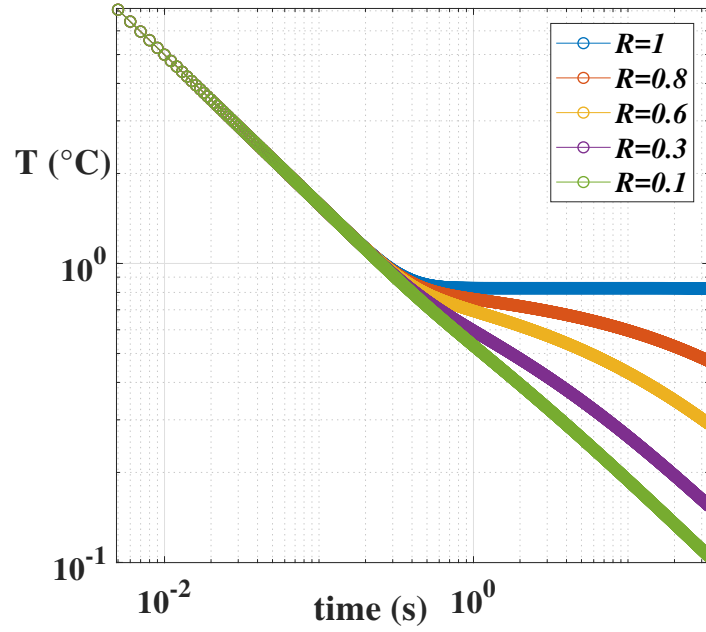


Figure 5.6: The comparison of numerical simulation with different values of R , where other parameters are shown in Tab. 1.2 for a steel 316 L, $Q=6400 \text{ J/m}^2$, $f=1000 \text{ Hz}$.

As it is easily understandable, small values of reflection coefficient request higher thermal stimuli and the defect detectability is not simple, anymore.

Different post-processing algorithms have been applied in order to study the cooling thermal behavior and to find a tool able to detect these type of very shallow and particular defects.

It is necessary also to evaluate the influence of the truncation window size on this type of analysis, because the thermal phenomenon in terms of difference between the defect and relative sound zone runs out in the first frames, being the defects depths very superficial (the maximum one is 0.4 mm). Another problem is the relative defect height, in terms of interested layers, maximum equal to 1 mm; this problem influences inevitably the minimum thermal contrast that can be reached.

As comparative measure the Signal Background Contrast has been chosen, in order to compare the different results on the same scale. This parameter is computed pixel by pixel in order to show the obtained maps in terms of SBC (Eq. 5.1).

$$SBC = \frac{P_{xydef} - MS_s}{SD_s} \quad (5.1)$$

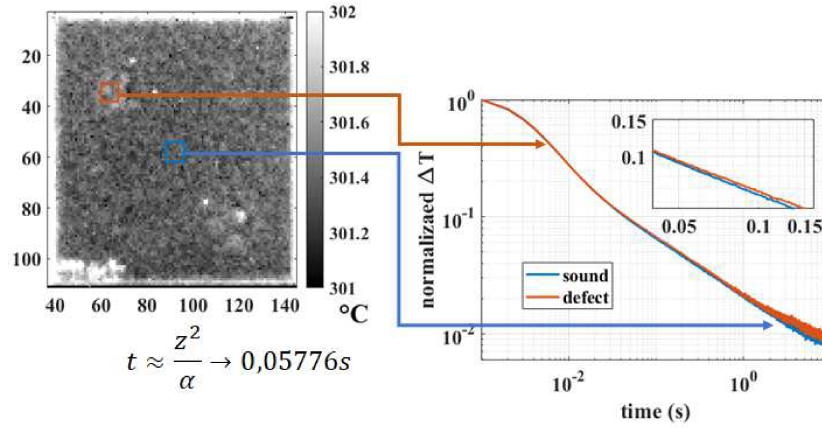
where P_{xy} indicates the value of the chosen parameter as post processing algorithm for each pixel, MS_s the mean value in the chosen sound area taken as reference and SD_s the standard deviation value in the same area.

Here the results obtained for the sample PK003, PK004, PK007, PK008, PK009 and PK010 will be summarized. The chosen criteria shall take account of:

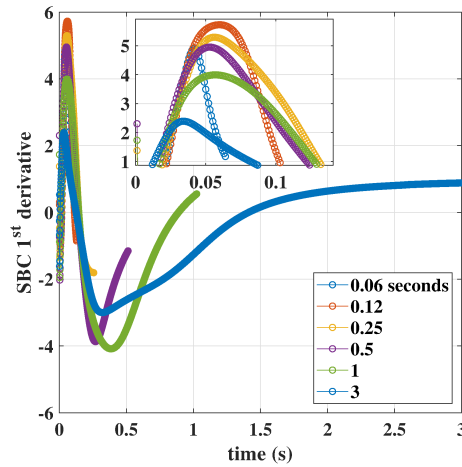
- different samples (PK007 and PK010), keyhole defects (PK010) and defects build for lack of fusion (PK007), same depth.
- different samples (PK008, PK009 and PK010), defects build for lack of fusion (PK007), different depths.
- same sample (PK003 and PK004), defects build by illumination gaps, same depth, but different heights in terms of interested layers.
- different samples (PK003 and PK004), defects build by illumination gaps, different depths.

5.1.4 Pulsed thermographic results by using a flash source

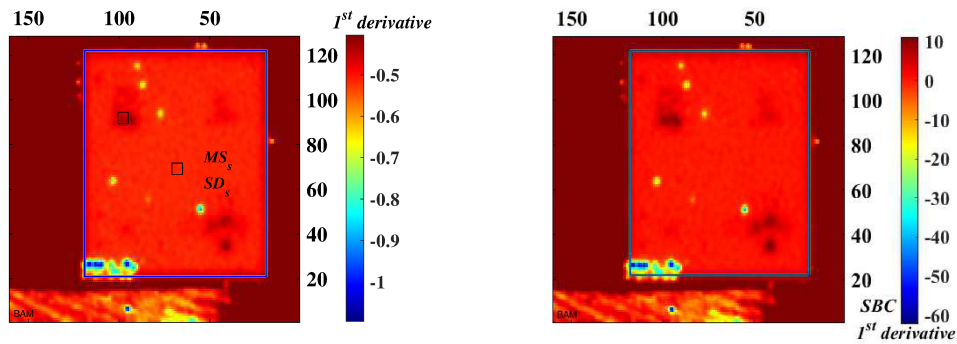
Here, the achieved results by using a flash source and the set-up reported in was first type of post-processing analysis, it is chosen to apply the Thermal Signal Reconstruction (TSR®) [56, 71], by using a polynomial fitting in MATLAB® of 5 degree and by analyzing different truncation window sizes of analysis. The reached results are shown in terms of first and second derivative maps, by choosing the best ones in terms of reached SBC. In Fig. 5.7, the used criteria is chosen in a graphical form, by taking the sample PK007 results as example. Also the raw signal is reported, in order to show the quality of the same and the very small differences that we have tried to study between the defect and the relative sound. A matrix of 3x3 pixels for the defect and the relative sound is considered. The map shown in Fig. 5.7a is related to the frame taking in correspondence of the time which, according to the one-dimensional model, is linked to the thermal diffusivity of the material, for the examined depth.



(a) Trends related to the raw thermal data in correspondence of a defect and the relative sound (SubFig. 5.7c).



(b) First derivative trends.



(c) 1st derivative map, taking in correspondence of the maximum SBC.

(d) SBC map

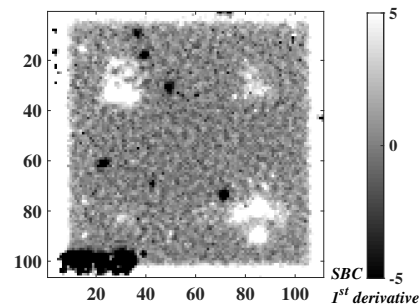
Figure 5.7: Data fitting with a polynomial of 5 degree and analysis of the relative first derivative for different truncation window sizes (time intervals); thermographic maps corresponding to the maximum reached SBC by considering the sound region highlighted in a black square.

As we can see from the analyzes reported in SubFig. 5.7b, the chosen truncation window size influences the maximum achieved SBC, although, as is known, the TSR® algorithm leads to obtaining a sequence of thermographic maps and the polynomial fitting still requires a certain number of data to follow the thermal raw decay, for mathematical reasons. In fact, for the examined case, the choice which leads to the best result correspond to 0.12 seconds of analysis.

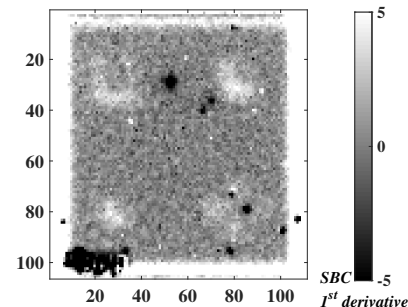
Although the graph shown in Fig. 5.7a changes according to the defect considered and the depth examined, the results shown below consider for all samples (PK007-PK010) the same defect indicated in SubFig. 5.7b, and, from time to time, the various depths examined.

So, for each sample, the different truncation window sizes indicated in SubFig. 5.7b have been considered as analysis intervals and it has been chosen to show the map taking in correspondence of the maximum SBC, by examined the defect within the fourth quadrant. For the samples PK001-PK004 an average of the contrast was considered, referring to all small defects present in the fourth quadrant.

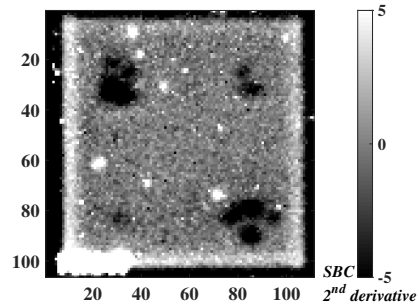
By applying the previous procedure to the raw thermal data related to the samples PK007 and PK010, it is possible to obtain the results shown in Fig. 5.8. First of all, it is chosen to analyze these two samples, in order to evaluate the influence of the energy inside the defects (keyhole and lack of fusion mode), at the same defect depth and height, on the possible results.



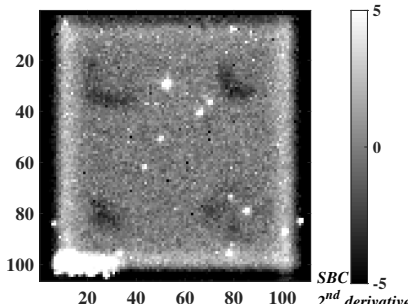
(a) PK007, 1st derivative (TSR®), map 60 after 0.12 s of analysis.



(b) PK010, 1st derivative (TSR®), map 45 after 0.12 s of analysis.



(c) PK007, 2nd derivative (TSR®), map 132 after 0.5 s of analysis.



(d) PK010, 2nd derivative analysis, map 96 after 0.5 s of analysis.

Figure 5.8: A comparison between the sample PK007 (keyhole defects) and PK010 (lack of fusion defects); maps related to the maximum achieved SBC, TSR® algorithm, analysis of the first and second derivative for different time intervals.

In fact, it appears evident that, if other defect characteristics such as shape, depth (0.4 mm) and height are equal, the defects in keyhole mode have a greater contrast than those generated by lack of fusion, as well as a more delineated form. However the quality of the defect influences, inevitably, the final result; the reflector shape is not always very precise, and, in particular, only for the defect below left, the shape seems more pronounced when the defect build for lack of fusion is considered.

Fig. 5.9 shows, instead, the comparison with the same energy (lack of fusion), considering different samples (PK008, PK009 and PK010), with defects at different depths. The analysis is carried out by considering the feature that shows the best results in terms of SBC, by considering different time intervals.

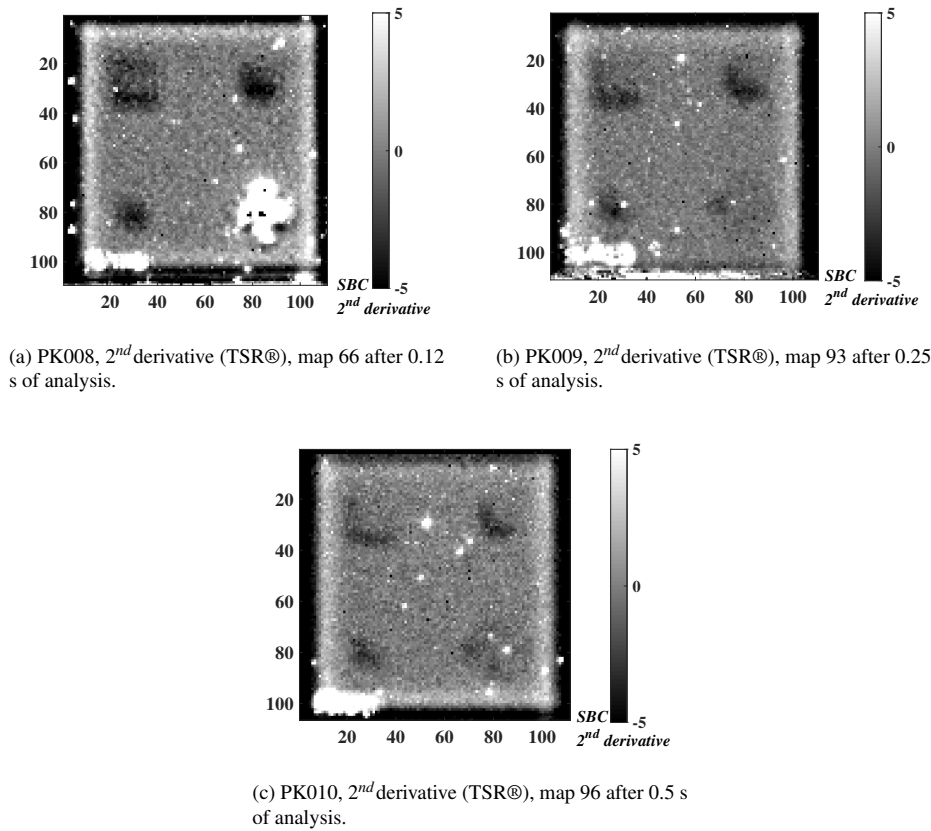


Figure 5.9: A comparison among the samples PK008, PK009 and PK010, lack of fusion defects at different depths; the maximum SBC, analysis of the second derivative sequences.

At the same energy, the more shallow defects show a higher contrast than the deeper one. The cross at the bottom right of the sample PK008 was produced in keyhole mode for a mistake (Tab. 5.3), increasing the laser scanning speed and not decreasing it, for this reason, this defects shows a higher contrast than the other one at the same depth, as well it results already visible to a visual analysis (Fig. 5.3g). For the same reason the comparison of the samples with defects produced in keyhole mode is not reported, since with depths less than 0.4 mm, the defects are already visible to a visual analysis Fig. 5.3e.

The last comparison regards the samples PK001, PK002, PK003 and PK004, with very small defects. Also the reached results in the case of the samples PK001 and PK002 are shown for completeness of information, despite on

a simple visual control the most defects are visible.

In Fig. 5.10 the reached best results are shown, by using the same type of analysis and criteria of the previous one. As reference defect area, a mean value of the ones that show a considerable SBC has been chosen in order to evaluate the maximum SBC.

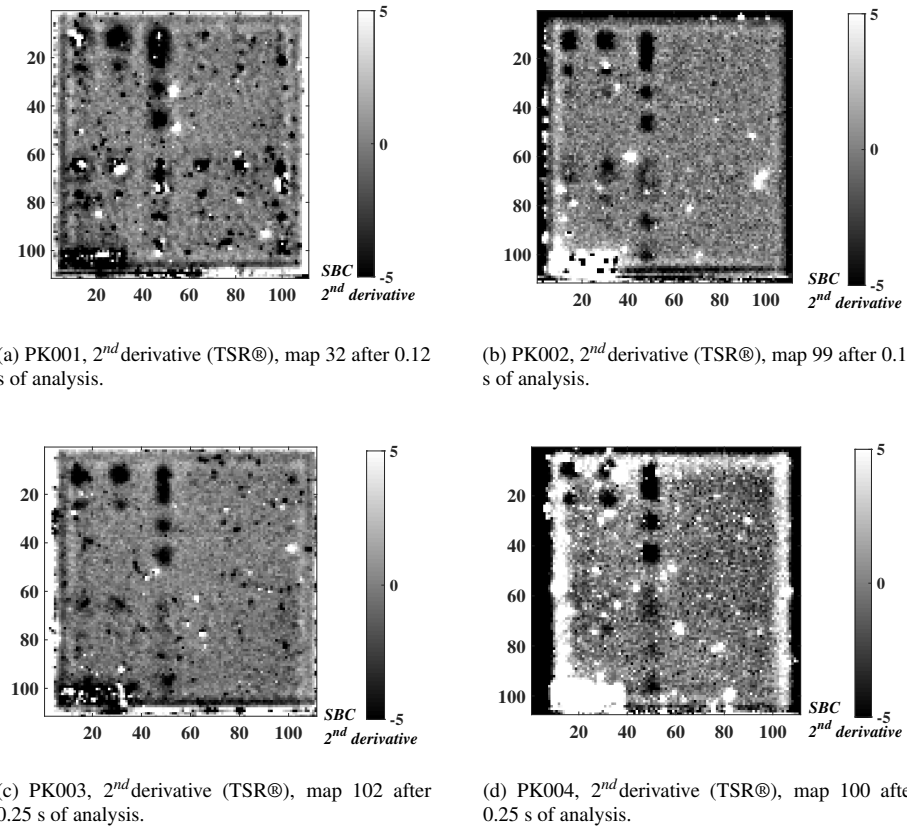


Figure 5.10: A comparison among the samples PK001-PK004, with defects at different depths and heights, produced by a gap during the laser illumination.

These samples have inside several defects produced by laser illumination gaps; within the same sample, it is possible to distinguish 4 different sectors where the defects have different heights, while the 4 samples differ from each other for the defect depth. Obviously, if the height of the defect is higher, the contrasts, expressed in terms of SBC, are greater. In all cases, we are able to see the defects with a high between 0.4 and 0.6 mm, instead the height of only 0.15 mm is not sufficient to show, clearly, the presence of a defect.

The choice to use the TSR® as a post processing algorithm is subordinate to the possibility of having as output, within the same analysis, a sequence of multiple maps, because the presence of the analyzed defect (it is a not plane reflector) is not easy to diagnose. However, the results obtained with the other post processing algorithms were also considered, but it was decided not to show them, because they show a worse quality than those obtained from a TSR® analysis.

5.1.5 Pulsed thermographic results by using a laser source

Comparing stepped and long pulse results

In order to increase the energy density, it is chosen to analyze the same samples by using another energy source, or a widened laser beam, in line with the sample and with a square spot of a size comparable of the sample one.

The plane tests has been structured in such a way to have a comparison in term of power and pulse duration, in order to study the influence of these test parameters on these type of analysis (both heating-stepped and cooling down-long pulse).

As already explained in SubSec. 2.4.1.2, during a step heating analysis, by using an energy source with an extended heating pulse duration, the thermal behavior of a defect zone is different from a relative sound one; in particular, if the heating pulse duration is sufficient to reach, theoretically, the defect, we are able to see a thermal contrast also during the heating phase and, in particular, if the sound area is more thermally diffusive than the defect one, at the end of this heating phase, the surface above the defect is warmer than the sound material, and exchanges heat by conduction and convection more quickly than the sound material.

Two profile in correspondence of the same defect and the same sound taking in the previous analysis are shown in Fig. 5.11, in order to explain the differences between the defect and the relative sound also in this case.

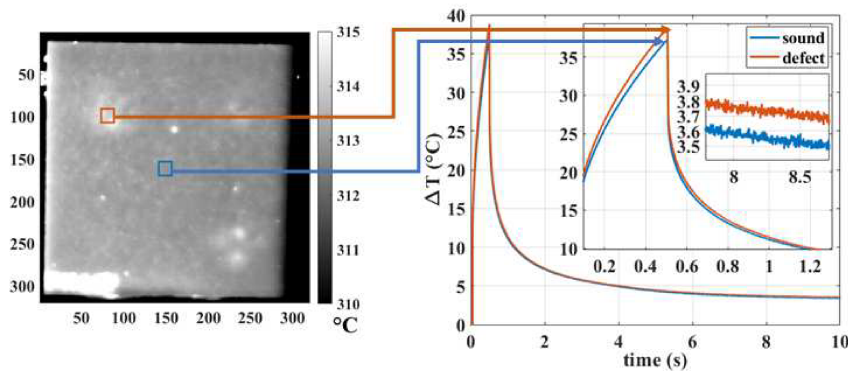


Figure 5.11: Raw thermal data by using a laser source, power 550 W, period of 500 ms, PK007.

As you can see from the analysis of the simple raw thermal data, already analyzing only the raw thermal trend, it is possible to notice differences between the defect indicated within an orange square and the relative sound zone. In this regard it was decided to show for the sample PK007 the frame corresponding to the end of the heating phase, and therefore the first in correspondence with the cooling one Fig. 5.11.

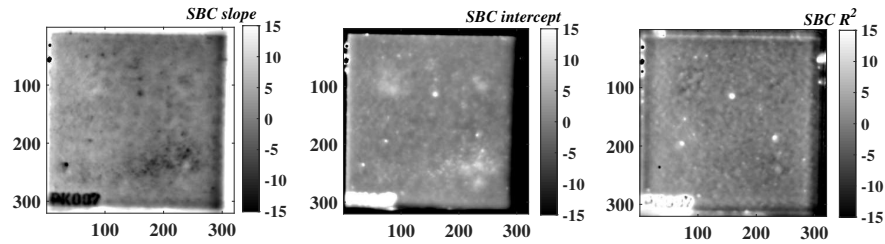
As already specified, the difference in temperature reached during the heating and the following cooling behavior will depend on the different thermophysical properties between defective and sound material, as well as on the depth and type of defect. If, during a step-heating, this thermal behavior is analyzed with a linear fitting in a double log-scale, in a presence of a defect, the slope and square correlation coefficient R^2 values will be different respect of the theoretical ones that characterize a sound material, respectively equal to $+0.5$ and 1 [74, 76, 77]. It will be possible to underline some differences of these analysis indices also during the cooling down, although for the chosen pulse durations the theoretical values taken in correspondence of sound zones of the component (slope -0.5 , R^2 1) are

very far from those foreseen by the one-dimensional models that are based on a thermal stimulation of a theoretical infinitesimal duration [76, 77].

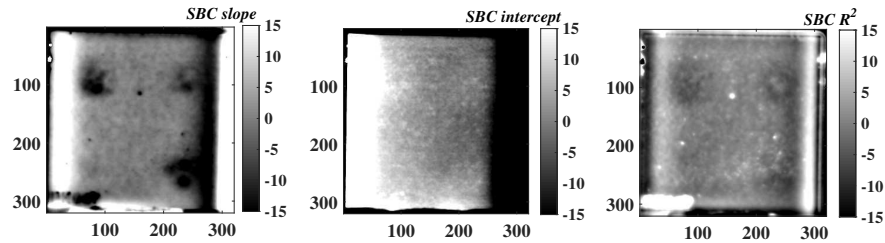
For this reason, in order to study the heating and the cooling down phenomena of this type of material and defects, it is chosen to use these algorithms, and so the slope, the R^2 and also the value of the intercept, after a polynomial fitting of the raw thermal data, in both the phases of thermographic interest [74].

For the sample PK007, all the results will be shown, by comparing the different pulse durations (heating periods) and also the relative combinations by changing the input laser power, both during the heating phase and during the cooling one. As criteria in terms of truncation window size during the cooling down, it is chosen to analyze a time interval (in terms of frames) equal to the pulse duration; in this way the frames number of both analyses is the same. In order to have the same scale also by comparing this type of algorithm and analyses, it is chosen to refer to the SBC, by computing this parameter pixel by pixel, like the pulse flash analyses.

For brevity, it is chosen to show only the results achieved by using a period of 1000 ms and the maximum available laser power, of about 550 W, that theoretically, is the better condition that allow this type of set-up and technique (Fig. 5.12).



(a) Stepped analysis, pulse duration 1000ms, laser power 550 W.



(b) Long pulse analysis, pulse duration 1000ms, laser power 550 W.

Figure 5.12: PK007, 1000 ms, 500 W, stepped and long pulse analysis; slope, intercept and R^2 (linear fitting of 500 frames)

The achieved results show that the long pulse analysis is better than the stepped one. In fact, except in the case of the intercept map, however showed in terms of SBC, during the heating phase the detected defects show a low contrast respect of the cooling one.

The same analysis have been repeated also by studying the other combinations, in terms of heating periods and laser power. In all cases, the stepped analysis doesn't allow to see the defects better than the long pulse one, as shown in the previous Fig. 5.12, and also in the following paragraphs, where the reached results are compared by analyzing other different points of view.

Influence of the laser pulse duration

This paragraph regards the investigation of the influence of the laser pulse duration (heating periods) on the achieved results. In terms of algorithms, it is chosen to show the best results both in the case of stepped heating analysis, where the intercept show the best SBC, that in the long pulse one, where the maps related to the R^2 achieve a very good SBC. In these shown analyzes, the laser power is fixed to 500 W, instead the pulse duration is made vary according the chosen heating periods, indicated previously (100 ms, 300 ms, 500 ms, 1000 ms).

The results reported in Fig. 5.13 confirm that, at the maximum available power, regardless of the laser power, the qualitative best results are obtained with the long pulse analysis.

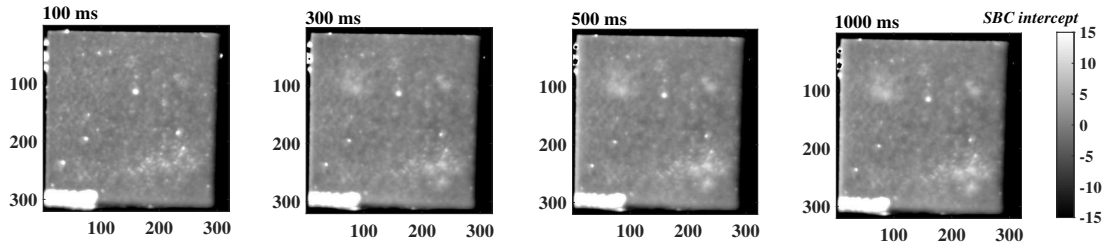


Figure 5.13: Influence of the laser pulse duration, by analyzing the same parameter at the same laser power (500 W); stepped analysis.

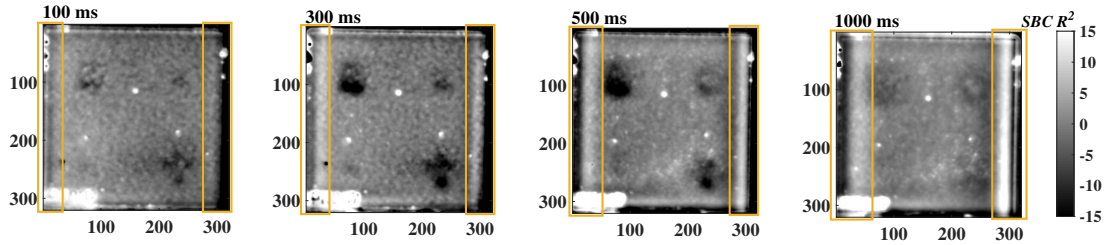


Figure 5.14: Influence of the laser pulse duration, by analyzing the same parameter at the same laser power (500 W); long pulse analysis.

By comparing the reached results related to the influence of the laser power on the long pulse analysis, seems that, by increasing the laser pulse duration, the results are more and more influenced by the small heating inhomogeneities, from the left to the right part of the sample. These heating inhomogeneities are due to the relative position sample-camera-laser, that is, obviously, not perfect in line. Besides, the choice of analyze a truncation window equal to the pulse length is, surely, not the best one for the longer pulse analysis; in fact for reasons due to the thermal diffusivity of the material and the shallowness of the defects, a truncation window equal to 1 s (500 frames) seems too long if it is compared to the previous one, in terms of defect detectability.

Influence of the laser power

Here there is an evaluation about the influence of the laser power on the results. In fact, it is not always possible

to have a laser with a very high laser power, because it requires a significant commitment in terms of costs.

For this reason, it is important to find that, in this case, at the same pulse heating period (set to 500 ms), the results are comparable in terms of maximum reached SBC, as shown in Fig. 5.15 and even more clear in Tab. 5.6, where the result obtained in terms of maximum SBC, as absolute value, is reported, analyzing the defect indicated as an example within the relative thermographic maps.

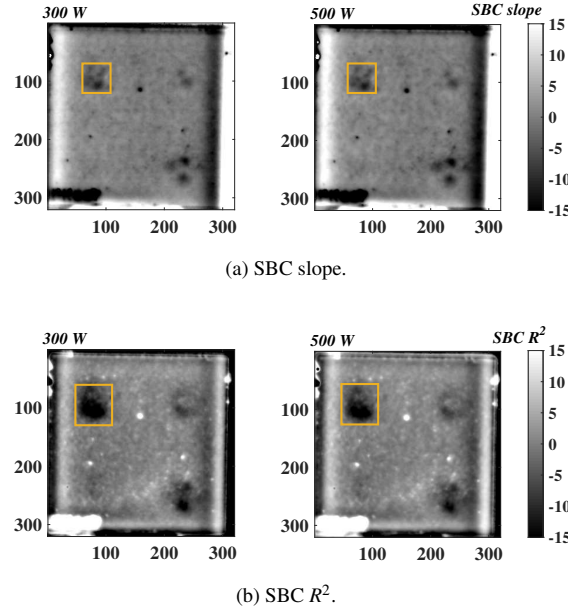


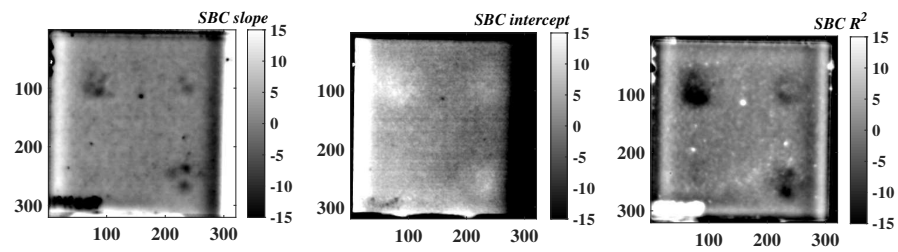
Figure 5.15: Influence of the laser power, same laser duration (500ms), long pulse analysis.

300 W, 500 ms, slope	500 W, 500 ms, slope
$ SBC_{max} =11.84$	$ SBC_{max} =12.56$
500 ms, 300 W, R^2	500 W, 500 ms, R^2
$ SBC_{max} =19.79$	$ SBC_{max} =21.72$

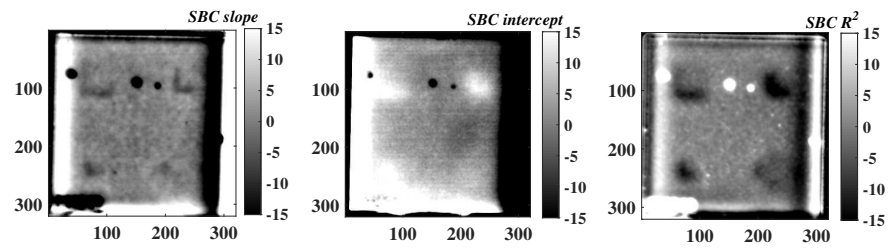
Table 5.6: Influence of the laser power, same laser duration (500ms), long pulse analysis, maximum achieved SBC.

By comparing the results reached by analyzing the different defect typical conditions and dimensions

All the analyses are also repeated for the other samples PK003, PK004, PK008, PK009, PK010, in order to analyze the most signification combinations. Only the best results, so the long pulse one, are reported below for brevity, by using a laser power of 500 W and a heating period of 500 ms, for the motivations that have been shown before.



(a) PK007.



(b) PK010.

Figure 5.16: A comparison between the sample PK007 (keyhole defects) and PK010 (lack of fusion defects).

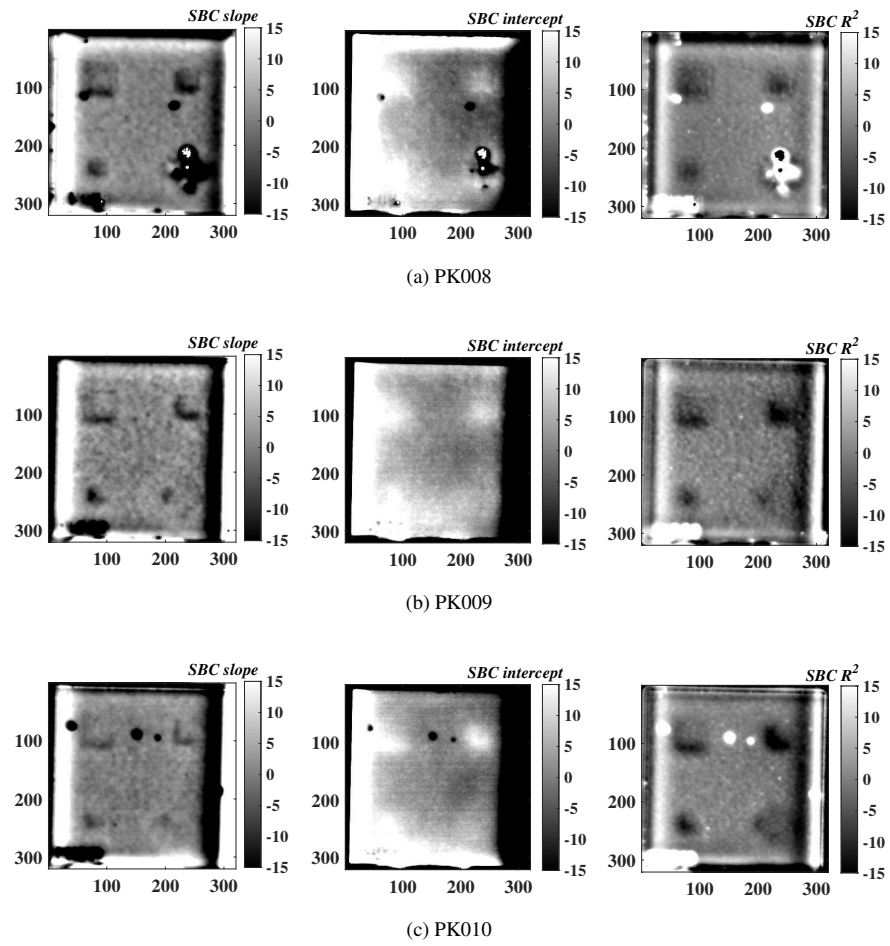


Figure 5.17: A comparison among the samples PK008, PK009 and PK010, lack of fusion defects at different depths; the maximum SBC.

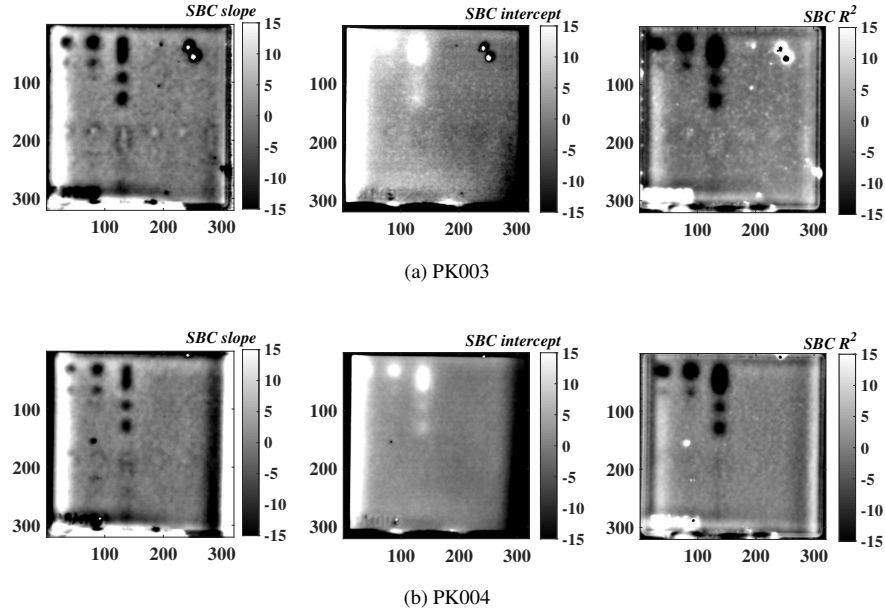


Figure 5.18: A comparison between the samples PK003 and PK004, with defects at different depths and heights, produced by a gap during the laser illumination.

Qualitatively, the analyzes carried out by using a laser source and a long pulse approach seem more promising than the one obtained after a flash excitation. It is necessary also to underline the difference in terms of thermal imaging camera used within the two different used set-ups, as well as the excitation source one. In the next section, where the data are treated with a quantitative approach, it will explain how these choices affect the results obtained.

5.1.6 By comparing the achieved results: a quantitative approach

The achieved results are compared in terms of used set-up and so in terms of heating pulse duration, in order to have an idea of the more useful solution for this application. In this regard, it is necessary to perform a quantitative analysis. As quantitative parameter, it is chosen to use the achieved SBC. This is one of the possible indications which can provide a measure of how the defect is seen within a thermographic analysis.

By comparing the reached results in terms of SBC seems to be evident that the geometrical resolution (mm/pixel) and the energy density are decisive for this type of defects and application [152]; in fact the shallow depth does not require the use of a very high speed camera, instead the small size need a good resolution.

In this context, the use of a thermal imaging camera in the mid-infrared, with its integration time and the possibility to decide the precise window of analysis (*pixels x pixels*) show significant advantages respect of the use of a long-wave one, more performative in terms of frame rate (until 1000 Hz, instead 500 HZ), but with a less resolution, due to the possibility to choose only 4 precise windows (*pixels x pixels*).

Besides, the particular quality of the studied reflector requires very high thermal stimuli in terms of energy source. In this context, the possibility to use a laser source having high performances, like the one summarized in Tab. 5.5 seems very promising. In fact, by applying the combination “middle wave camera+laser source” (set-up 2), the achieved SBC is clearly higher than the “long wave+flash” one (set-up 1) (Tab 5.8).

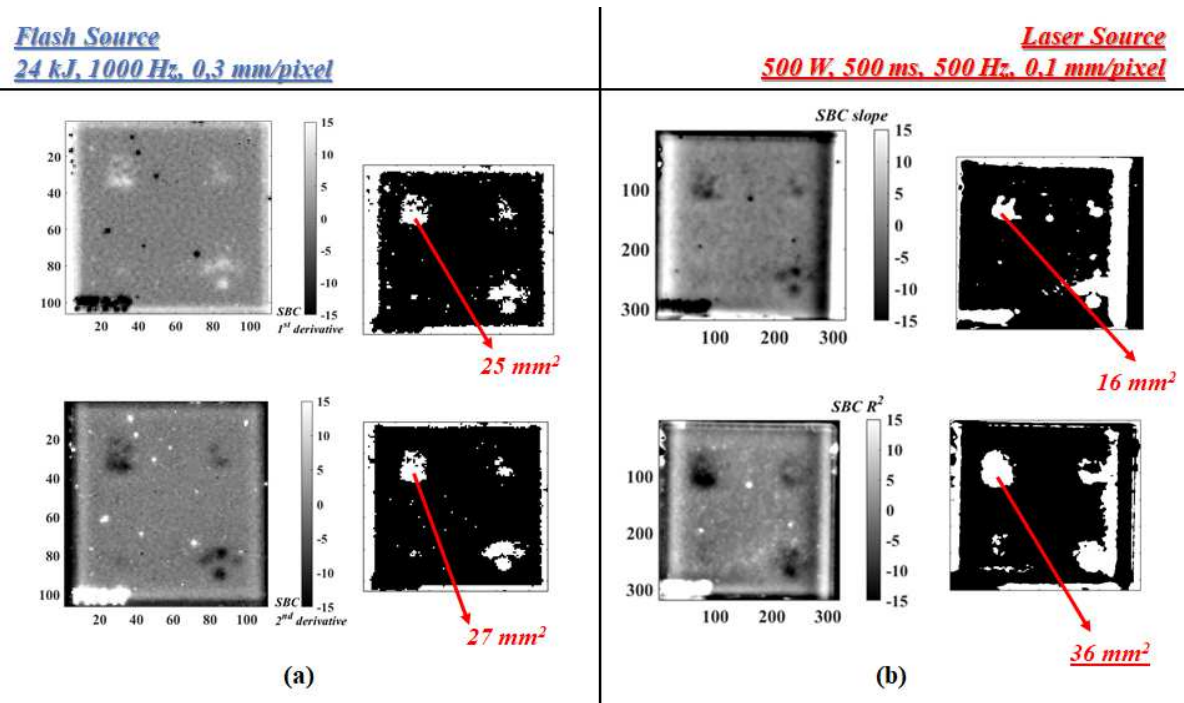


Figure 5.19: By comparing the different solution in terms of used set-up, sample PK007, size estimation, (a) flash set-up, (b) laser set-up.

Flash set-up		Laser set-up	
1 st derivative	$ SBC_{max} =11.51$	slope	$ SBC_{max} =12.56$
2 nd derivative	$ SBC_{max} =12.04$	R^2	$ SBC_{max} =21.72$

Table 5.7: By comparing the different solution in terms of used set-up, sample PK007, maximum $|SBC|$.

Besides, a first tentative to do a quantitative analysis by using the achieved results in terms of maximum SBC is shown in Fig. 5.19. In this regard, a simple threshold value equal to 3 times the sound standard deviation (taking as measure of the noise within the considered map) is chosen to binarize the previous results and to have a size estimation of the defect taken as example. The defect area is calculated as the sum of the white pixels that have a unit value and greater than the average plus 3 times the standard deviation of the sound zone. The value obtained by analyzing the R^2 map after a long pulse test allows to obtain the best result, with a size estimation value perfectly equal to the nominal one. In this regard, this latest result confirms what was obtained simply by comparing the results in terms of SBC. However, if we try to analyze also the influence of the defect shape, seems to be evident that the different analyzes carried out are complementary to each other; in fact the defect in the shape of a cross seems more outlined within a 1st derivative (TSR®) or a slope map than the R^2 one.

The reached results have to be compared also in terms of depth estimation. Two different set-ups by using the same equipment previously chosen and described have been used, leaving the combinations unchanged “longwave camera-flash source” and “mid-wave camera-laser source”. The used thermographic parameters are indicated within Tab 5.8 and Tab 5.9 and are shown in Fig. 5.20 and Fig. 5.21.

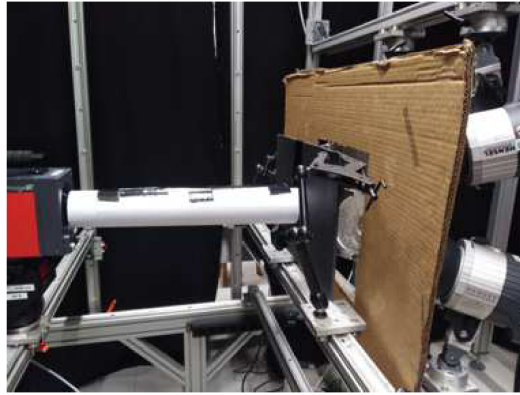


Figure 5.20: Transmission set-up by using a flash source.

Camera: Infratec ImageIR 8800 Lens 25 mm Integration time 0-60 °C Frame rate 100 Hz Duration 10000 frames Resolution 0.35 mm/pixel Quarter Frame 160x128 pixels	Excitation: Flash lamps Hensel EH Pro 4x6 kJ Impulse Duration 3 ms	Distances: Flash lamps to sample 19 cm Camera to sample 45 cm
--	---	--

Table 5.8: Thermographic parameters and set-up distances for pulsed flash thermography.

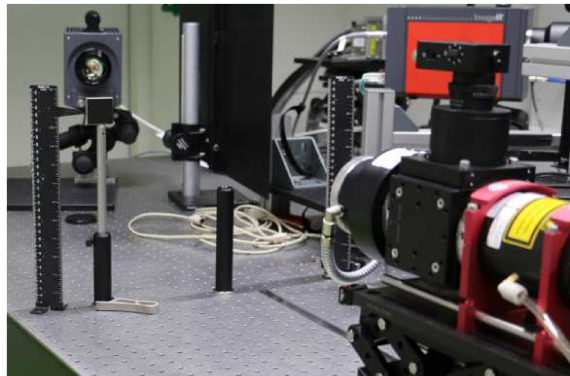


Figure 5.21: Transmission set-up by using a laser source.

Camera: Infratec ImageIR 8300 hp Lens 25 mm Integration time 0-60 °C Frame rate 100 Hz Duration 10000 frames Resolution 0.15 mm/pixel Quarter Frame 160x128 pixels	Excitation: DIODE LDM LASER (935 nm) Square to phat profile 39 x 39 mm ² Laser focusing lens 600 mm Pulse duration 50 ms Power 450 W	Distances: Laser to sample 60 cm Camera to sample 30 cm
---	---	--

Table 5.9: Thermographic parameters and set-up distances for pulsed flash thermography.

In order to evaluate the starting point of the cooling down after a long pulse excitation with a laser source has been used a black tape placed near the sample, at its same height and contained within the chosen thermographic window Fig. 5.21. For both the used set-ups, the frame rate is setted to 100 Hz, because the observed thermal phenomenon is very slow. As method of analysis, the Parker one has been used. In both cases, despite the “long” pulse duration due to the use of a laser source, the obtained values are quite similar, and, in any case, not far from that indicated in the literature for AISI 316L steel. As final value, in both cases, it is chosen to use a average on 5 different measurements, by considering 5 different samples; by using a flash source $\alpha = 2.77 \times 10^{-6} (m^2/s)$, instead by using a laser one $\alpha = 3.03 \times 10^{-6} (m^2/s)$. However, the differences are further shortened if the depth estimation is evaluated by using the 2nd derivative TSR® method. In Fig. 5.22, the time corresponding to the second derivative peak is theoretically indicated in blue and the second derivative trends obtained in both cases are reported, by also considering different time intervals of analysis, expressed as number of frames. As known, during a “pulse” heating, the contrast created by the defect occurs right after reaching the semi-infinite medium regime for pulse-heating, but much later for the step-heating. This will have no influence for the detection of the defect, indeed in this particular case it allows a higher contrast, but it will make the quantitative characterization (depth identification) more difficult. The pulse duration is decisive in this case, because the hypotheses at the base of the proposed one-dimensional method are totally lost if the pulse duration is 50 ms (Fig. 5.22b). However, we can also note that, also in this case, the choice of the truncation window size is decisive and changes the results in terms of depth estimation; in fact by analyzing the Fig. 5.22a, it appears evident that, considered right the result in terms of thermal diffusivity, the most suitable analysis window is included between 0.5-1 seconds (512-1024 frames); however, truncation window sizes that are too long or, alternatively, too short are completely incorrect.

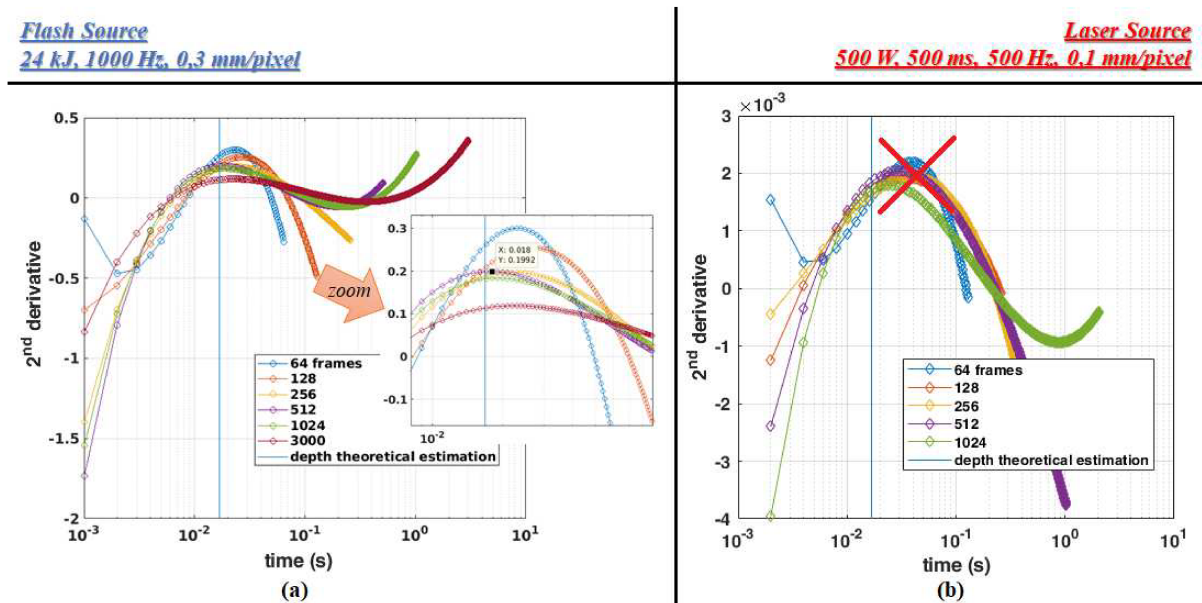


Figure 5.22: By comparing the different solution in terms of used set-up, sample PK007, depth estimation.

5.1.7 Final remarks and future steps

The reached results can be summarized as follow:

- For the first time, the thermography is been used to talk about of “quality assurance” within the field of Metal Additive Manufacturing, in order to evaluate its effectiveness for detecting typical defects of L-PBF process (small and not-plane reflectors).
- The influence of different thermographic parameters, in terms of acquisition frequency, truncation window size, resolution, energy source and post processing algorithms are evaluated in order to try different solution and to show the limits and the advantages of the possible combinations.
- By applying different types of thermographic analyses, we are able to see with a good contrast (SBC) the typical defects of the L-PBF process, discerning the defects in keyhole mode from the one generated due to lack of fusion. The defects in keyhole mode (high energy) show a higher contrast than the lack of fusion one (low energy) because the amount of air inside (porosity) influences the results.
- The defect height, in terms of interested number of layers, influences the defect detectability, and so the reached SBC.
- The resolution (mm/pixel) and the energy density, in terms of energy source, are decisive for this type of defects, because the shallow depth does not require a high speed camera, instead a one with a high resolution. In this regard, a mid-wave camera seems more promising than a log-wave one. By applying a laser source, together with a mid-wave camera, the achieved SBC is clearly higher than the flash one.
- During a pulse heating, the contrast created by the defect occurs right after reaching the semi-infinite medium regime for pulse-heating, but much later for the step-heating. This will have no influence for the detection of the defect, indeed in this particular case it allows a higher contrast, but it will make the quantitative characterization (depth identification) more difficult.

Future steps will investigate the influence of the truncation window size for the analysis of a long pulse test (or a stepped one), when the slope or the R^2 algorithms are used [21]. In Fig. 5.23, an example that shows this further investigation is shown, by considering a long pulse test with a laser power of 500 W and a pulse duration of 500 ms and by performing a polynomial fitting of one degree, frame by frame, capable to provide slope and R^2 maps, like the approach shown within Chapter 4.

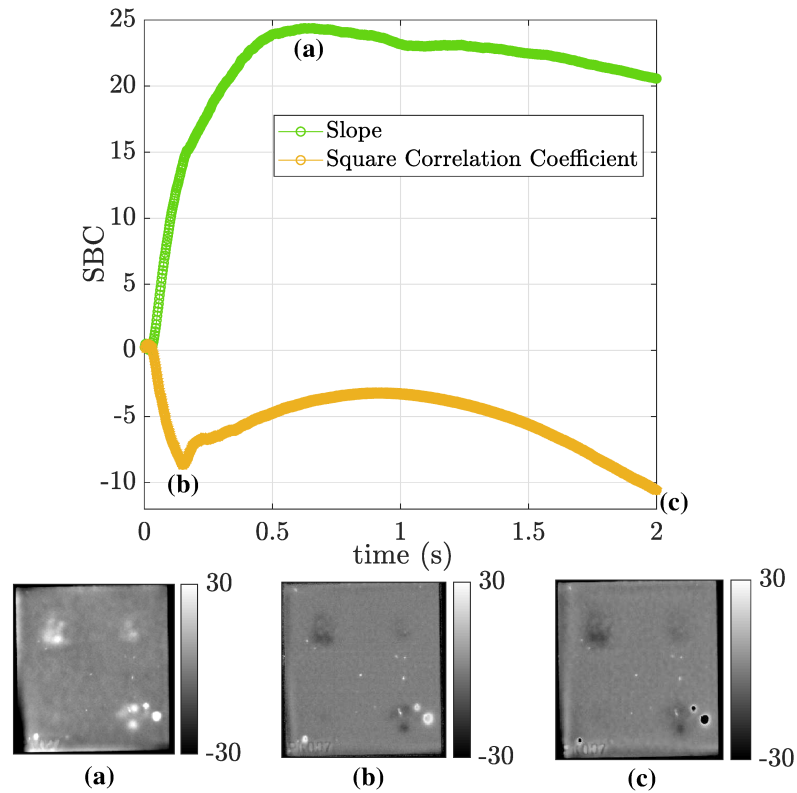


Figure 5.23: The influence of the truncation window size on the slope and R^2 algorithms, long pulse analysis; (a) slope map, frame 329, 0.658 s, (b) R^2 map, frame 75, 0.15 s (c) R^2 map, frame 1000, 2 s, maps taking in correspondence of the maximum ISBCI.

Will be also assessed the possibility to use different post-processing algorithms, such as PPT and PCT, with the aim to detecting these typical defects, when a long pulse test is performed. An example of preliminar results is shown in Fig. 5.24, by using the same previous raw thermal data (laser power of 500 W and pulse duration of 500 ms) and an analysis frame by frame, like the previous one, always by considering PK007 sample.

Also the defects for lack of fusion mode will be analyzed in this way, in order to improve the results already achieved.

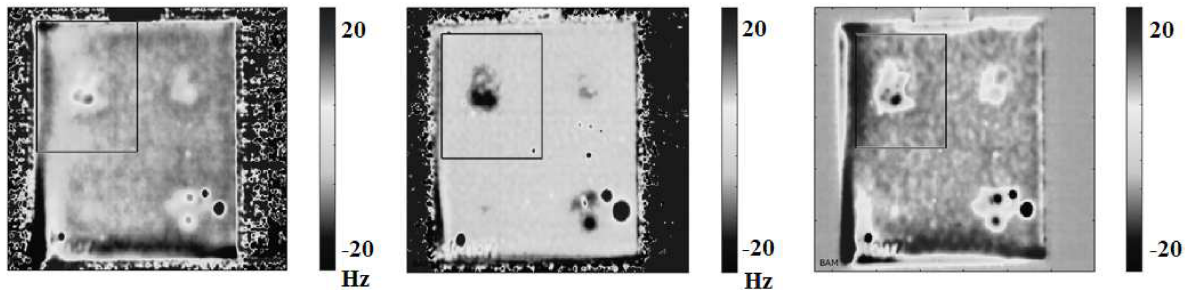


Figure 5.24: SBC phase map $f=0.4883$ Hz (positive) , SBC phase map $f=7.8125$ Hz (negative), SBC PCT map, frame 672, 1.34 s, Gaussian filter $\text{std}=1$.

5.1.8 Activity acknowledgements

This research was funded by BAM (Bundesanstalt für Materialforschung und -prüfung) within the focus area Materials.

All the experimental investigations have been conducted in BAM thanks to the equipment present in the labs of division 8.7 and to the availability of all the researchers of the division, especially Dr. rer. nat. Christiane Maierhofer and Dr. rer. nat. Simon Altenburg. The various tests involved the specimens that were built for the BAM PromoAm project, thanks to the availability, the SLM machines and the skills of Gunther Mohr and Kai Hilgenberg, from the BAM division 9.3.

5.2 Pulsed Phase Thermography Approach for the Characterization of Delaminations in CFRP and Comparison to Phased Array Ultrasonic Testing

5.2.1 Materials and methods

Pulsed phase thermography (PPT) is a well-established algorithm used for processing thermographic data in frequency domain with the aim to extract information about the defect size and depth. However, few works demonstrated the capability of PPT in defects evaluation and characterization in real components. The aim of this work is the assessment of capability of PPT in determining delaminations in CFRP components used in aeronautics. Composite materials are widely used in aeronautics due to their high strength-to-weight ratio. However, such materials require control with non-destructive (NDT) techniques in order to detect typical defects generated during production or due to severe operating conditions. Among NDT techniques, ultrasonic tests (UT) are considered as a technique already established in the aeronautical field, thanks also to the recent development of new instruments such as the phased array [153, 154, 155, 156, 157] which allows scanning of large surfaces in relatively short times. The phased array ultrasonic technique allows to detect all the typical defects of the composite materials and to determine their size and position with high accuracy [155, 156, 157], faster and easier respect to the traditional pulse echo method. In recent years, thermography has appeared particularly attractive among the non-destructive testing (NDT) methods for the detection of defects in materials. It offers the advantages of low cost, easy operation, high speed, and wide area coverage. The most widely used form of thermographic NDT is pulsed thermography in which the surface of a tested part is heated with a brief pulse of light usually from a high power source. Then, the heat flux on the surface tends to diffuse into the material. The time-dependent surface temperature response is captured as a series of thermal images by an infrared camera. The defects hinder the heat flow of from the flash heated surface, causing a reduction in the cooling rate of the surface above the defects, that is revealed as an area of thermal contrast in the thermal images of the surface [50]. The temperature contrast between the defected and non defected regions enables defects detection based on thermographic data. However, thermal images usually involve significant measurement noise and non-uniform backgrounds caused by uneven heating. As a result, it is difficult to recognize the defective regions clearly [158]. Hence, different types of thermographic image analysis methods have been proposed for signal

enhancement, e.g. thermographic signal reconstruction (TSR) [6, 7, 11, 12, 13, 21, 159], pulsed phase thermography (PPT) [2, 9, 36, 86, 93], principal component thermography (PCT) [88, 89, 90], the slope (m) and the linear correlation R^2 of data [19, 20, 21, 87], based on the assumption that the presence of the defect determines a modification of thermal profile during cooling with a typical non-linear behavior.

In this part of dissertation, the pulsed phase thermography (PPT) algorithm has been used for the analysis of thermographic data. The algorithm combines the techniques of pulsed thermography and lock-in thermography, analyzing in the frequency domain and through the phase and amplitude parameters, the cooling transient of the specimen subjected to a variable duration thermal pulse of and allows to extract information related to the size and depth of defects [2, 10, 160, 161, 162, 163, 164, 165]. In the literature, there are several works that show the capability of PPT technique in evaluating defect depth and dimensions on CFRP materials [2, 133, 164, 165, 166, 167, 168, 169]. However, most of them regards applications on sample specimens with simulated defects realized by means of Teflon foils or flat bottom holes, generally with well-known shapes (circular or square). Real defects present an in plane and in depth irregular shape that affects the signal contrast and then defects detection.

Very few works [96, 170, 171, 172] showed applications on real components and a comparison in defect evaluation between two different non-destructive technique such as thermography and UT. In this context, the component chosen for implementing the technique has a non-uniform geometry and the defects inside it are not simulated, but they are real and generated during the production process. Within the surface of the investigated component, spread delaminations are diagnosed. Delamination is the major failure mechanism in composite aeronautical components and eventually leads to material failure [173, 174, 175, 176, 177]. An early-detection and a better understanding of this phenomenon can be provided through a non-destructive assessment, by applying different techniques and types of control. The specimen has been investigated through the application of both the ultrasonic technique and the thermographic one. Thermographic phase images elaborated with a suitable computational processing have been compared with Ultrasonic C-scan images and, the agreement between the location and depth of defects has been verified. Besides, the ultrasonic technique has been used to validate the PPT results: the agreement between the location of defects has been verified.

5.2.1.1 Samples

The specimens were stringer assy made of Carbon Fiber Reinforced Polymer (CFRP). Two main areas, cap and web, can be identified on the samples Fig. 5.25. The testing was carried out on the cap. The cap length was 98 mm with a thickness of 2.76 mm (15 PLY), while the web thickness was 5.2 mm (30 PLY). Some detailed information about materials and manufacturing process have to be hidden due to a non-disclosure agreement signed with the aeronautical industrial partner involved in the research project. The project have seen the analysis and the study of 4 different stringers (072 073 074 075), with same geometrical characteristics, but characterized by diffuse delaminations over the entire surface in a scattered manner. Within this part of the work, the obtained results will be shown only for the component 075, because they show the comparison more interesting between ultrasound and thermographic techniques.

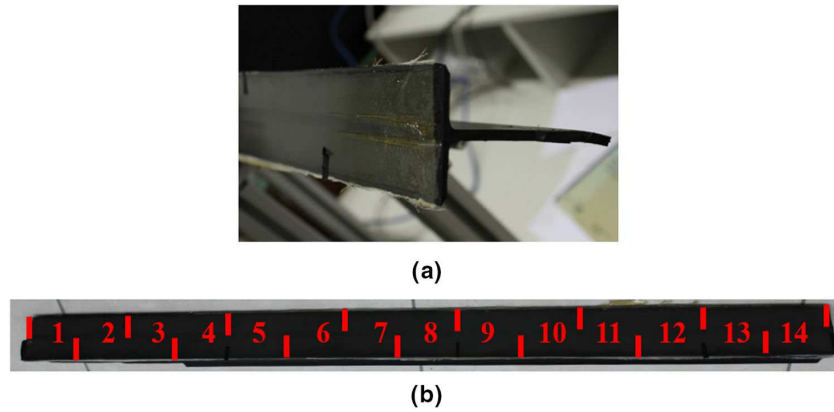


Figure 5.25: Lateral (a) and top (b) view of analyzed component.

5.2.1.2 Ultrasonic testing equipment

The experimental set-up (Fig. 5.26a) was based on the Olympus OmniScan MX2 system with a Phased Array module. The sample was inspected by means of a phased array flat probe with 64 individual elements, operating at a frequency of 3.5 MHz (Fig. 5.26b).

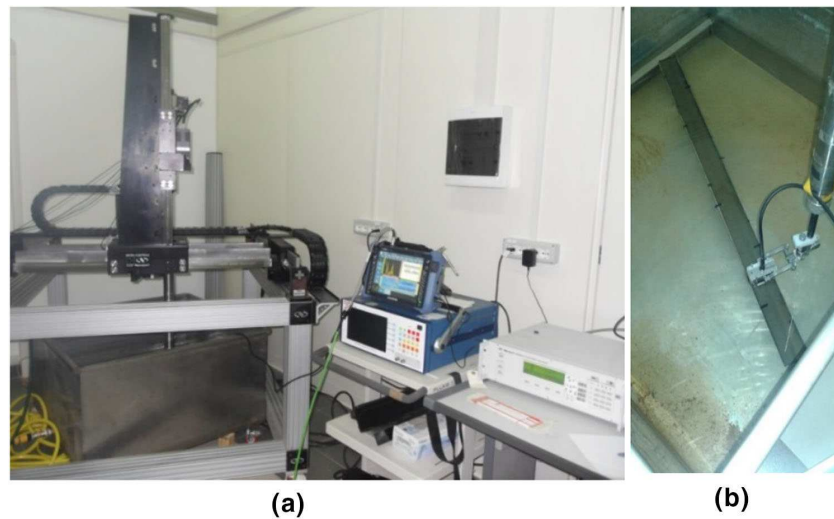


Figure 5.26: Ultrasonic set up (a) and a particular of the probe and its support (b).

The UT inspection technique, chosen for this study, was the “pulse - echo” in immersion mode. A mechanical displacement system allowed the transducer to move in an x-y raster scan pattern over the test piece. The scan operation was done by using two Mini-Wheel encoders, which were connected to the pulse-receiver instrument, to synchronize the probe data acquisition with the probe bidirectional motion. The axial resolution obtained with the used probe is of about 0.3 mm, that is comparable with a third of the ultrasound wave length in the investigated material, while the lateral resolution was 1 mm, since the pitch of the probe was 1 mm. Before performing the

ultrasonic testing, the probe sensitivity and the ultrasonic velocity (3030 m/s) in the tested material was calibrated. At the end of scan, UT data are saved in files containing the whole set of complete UT wave forms. The software allows the visualization in the A-Scan, B-Scan, C-Scan mode (Fig. 5.27). The 3.5 MHz probe has allowed the complete UT signal penetration in the specimen. Ultrasonic data were acquired and saved with the Omniscan MX2 flaw detector and offline elaboration has been processed by OmniPC and TomoView Software (Olympus). From the UT file, UT C-scan images for any portion of the material thickness can be obtained and analyzed. The chosen C-scan images to be analyzed were those related to a step of 0.3 mm (axial resolution) in order to display the defects present at each depth. C-scan images of the section of interest show, according to the scale, areas with a great amplitude of the reflected signal (pulse height in the A-scan), and areas with low amplitude of the signal. The first type of images (yellow–red color bar) are indicative of areas in which the defectiveness has occurred, the second type refers to sound area (Fig. 5.27). Tilted surfaces respect to the beam axis direction produce an increase in attenuation. Therefore, the boundary echo in correspondence to the T section and the fillet radii in correspondence to the thickness variation are not visible.

C-scan nondestructive analysis, realized by means of phased array ultrasonic technique, reveals some significant discontinuities in correspondence to the middle and the two extremities of the stringer (Fig. 5.27). Fig. 5.27a shows the C-scan image for almost all the stringer length. B-scan displayed on top right is chosen along the black line indicated on C-scan (on the bottom) and it corresponds to a defected section. A-scan (on top-left) is referred to position indicated by red line on B-scan (on top right), corresponding to a defect position. The first peak represents the water-stringer interface, the low peak corresponds to the defect and the third one corresponds to the back-wall interface. The two extremities are better analyses in some separate scans and the UTimages for sector 14 are displayed in Fig. 5.27b.

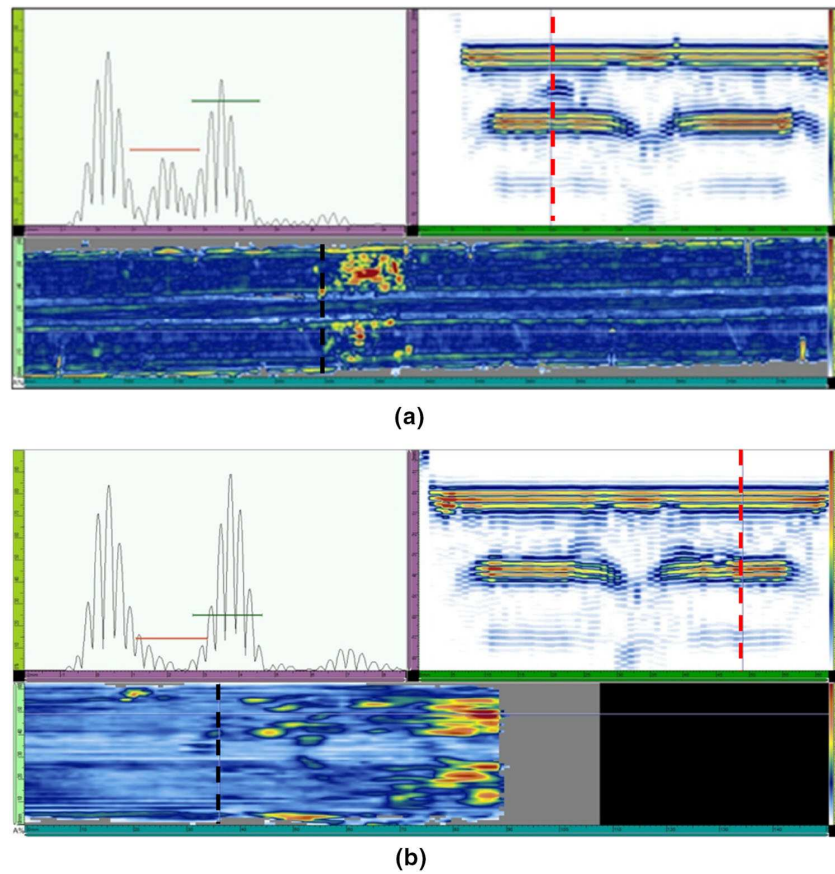


Figure 5.27: Visualization in the A-Scan, B-Scan, C-Scan mode of the entire stringer (a) and one of its extremities (b).

5.2.1.3 Thermographic set-up

A cooled IR camera (camera specifications in Appendix A) with an indium-ammonium detector and a spatial resolution of 640×512 pixels (Flir X6540 SC) sensitive in the range of $3\text{--}5\text{ }\mu\text{m}$ was used to monitor the temperature transient of the sample surface at a frame rate of 100 Hz after a flash test. The observation time was set at 5 s for each test (final resolution 0.17 mm/pixel). As thermal source, it was used a Bowens equipment with two flash lamps with a total energy of 3000 J. In order to obtain a good geometrical resolution (mm/pixel), it was necessary to divide the entire cap length into 14 sectors with a length of 70 mm each one.

The experimental set up is shown in Fig. 5.28, with its main distances. This thermographic set-up allowed to acquire the data sequences in a short time (about 5 min for each component), simply by moving the specimen during the several acquisitions and by using a common equipment (IR camera and flash lamps).



Figure 5.28: Set-up used for PPT acquisition (lamp angle 30° , sample-camera 900 mm, sample-flash lamps 150 mm)

5.2.2 By using Pulsed Phase Thermography to estimate depth delaminations

PPT processing consists on analyzing the material response in the frequency domain. The extraction of the different frequencies is performed with a discrete one-dimensional Fourier transform on each pixel of the thermograms sequence, by using the equations described within the Chapter 2. The algorithm described allowed to obtain amplitude and phase maps and it has been developed in Matlab®, by using the *fft* function. As already specified, the algorithm results particularly efficient if the number of thermograms N is a power of 2. Therefore, it has been decided to analyze only 256 frames of the entirely acquired sequence, that are sufficient to describe the entire physical phenomenon.

In order to compare in qualitative way thermographic and ultrasonic data, three sectors of the examined component have been chosen.

According to UT axial resolution, C-scan images have been extracted each 0.3 mm in order to analyze defects present at each depth. In this way, it was possible to extract 12 ultrasonic maps in the whole specimen. As it is shown in Fig. 5.25b, two sectors, named as 1 and 14, present spread delaminations while the sector 13 is free from defects.

As it has been described in a previous section, PPT algorithm provides phase maps for each analyzed frequencies determined, based on the obtained resolution in the frequency domain that changes with the frame rate and the truncation window size. To compare results of the two adopted techniques, it is necessary to estimate the depth resolution obtained with PPT algorithm, related to the frequency one with the “blind frequency” relation.

It is important to underline as, generally, a reference specimen made of the same material of the component, allows for evaluating thermal diffusivity (α) and the constant C in the “blind frequency” equation or for obtaining a calibration curve by previous known depths of simulated defects. However, in evaluating real components, in most cases, it is not available a reference specimen and then it is not possible to assess α and C . In view of this, it is

proposed a practical approach capable for estimating the depth resolution and then the defect depth. This approach is based on a number of literature data and results obtained by applying PPT algorithm on CFRP specimens. From the analysis of this data set, reliable values of the thermal diffusivity and calibration constant (C) are respectively $4 * 10E - 7 m^2/s$ [5] and 2. Based on the used parameters in terms of frame rate and analysis interval, these values provide a maximum searchable depth of about 1.2 mm and a depth resolution of about 0.3 mm, this last very close to UT value.

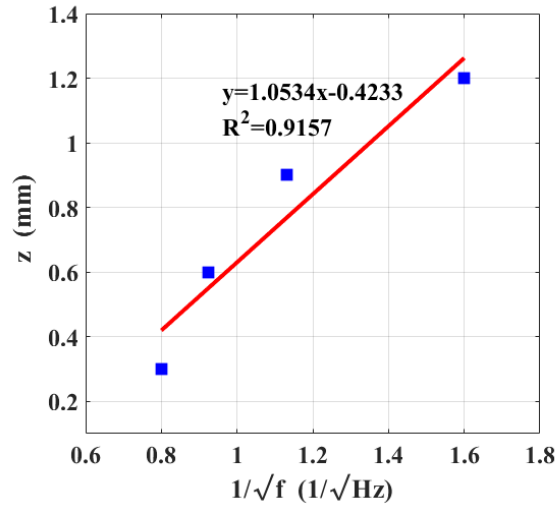


Figure 5.29: Depth and frequency relation (PPT algorithm).

Then, associating at each frequency obtained with PPT algorithm, the relative estimated depth, thermographic and ultrasonic results can be compared.

In Fig. 5.29 and Fig. 5.30 the comparison between ultrasonic data (C-scan) and thermographic ones (phase maps) is shown for different investigated depths. As example, only sectors 13 and 1 are reported as non-defected and defected areas.

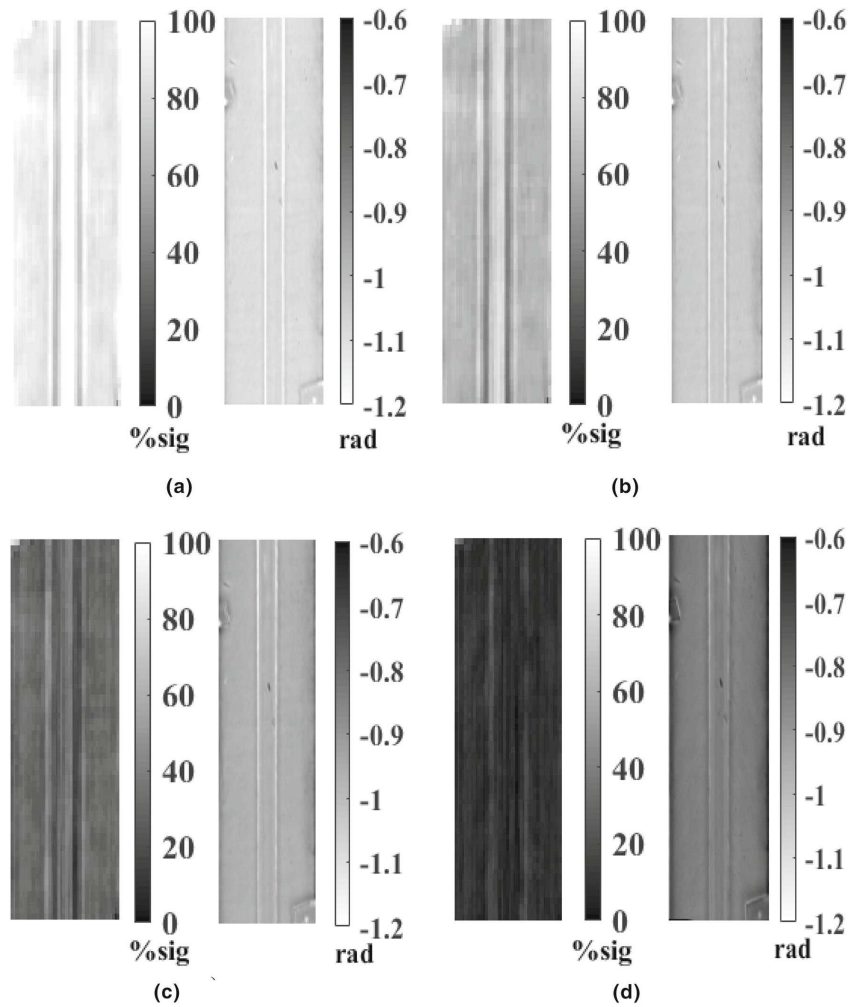


Figure 5.30: Comparison between ultrasonic and thermographic map at different depths; sound sector 13. a 0.9–1.2 mm/0.3916 Hz; b 0.6–0.9 mm/0.7812 Hz; c 0.3–0.6 mm/1.1718 Hz; d 0–0.3 mm/1.5612 Hz.

Both UT and phase data are reported in grey scale palette. C-scan data with colors moved towards white are indicative of the presence of defects, while the most attenuated signals moved toward black colors. In the same way, for the thermographic data the lighter colors are associated with a higher phase signal (in absolute value) and can be associated with the presence of defects.

Fig. 5.29 and Fig. 5.30 show a good agreement between UT and thermographic phase maps. Particularly, both techniques provide areas free from defects for sector 13 (named as sound areas). By considering UT maps, it can be noted that the delaminations are present above all on the top of the image related to the sector 1 of the component. Phase maps report similar indications but with a reduced contrast. A better contrast with respect to UT data is obtained only on the central part of the cap due to very shallow defects. In the next section, a suitable approach is proposed with the aim to introduce a particular procedure to analyze the data of a real component.

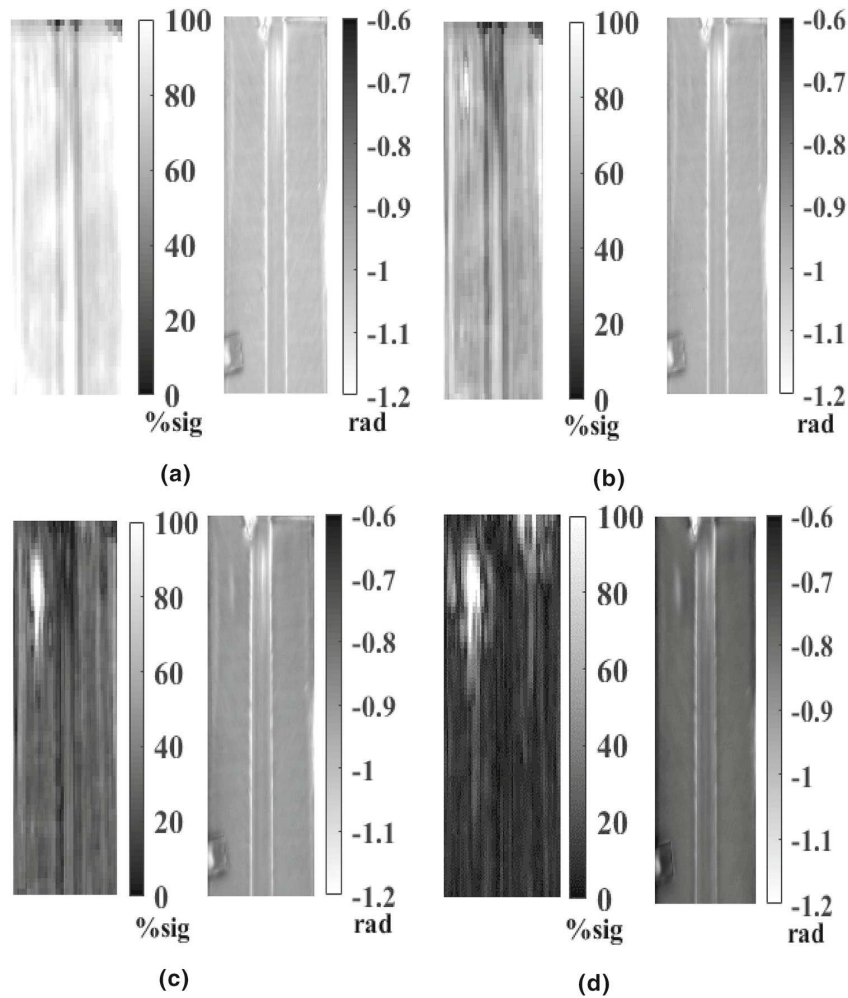


Figure 5.31: Comparison between ultrasonic and thermographic map at different depths; defective sector 1. a 0.9–1.2 mm/0.3916 Hz; b 0.6–0.9 mm/0.7812 Hz; c 0.3–0.6 mm/1.1718 Hz; d 0–0.3 mm/1.5612 Hz.

5.2.3 A comparison between the ultrasonic and PPT results in terms of depth estimation

Generally, the quantitative analysis of thermographic data requires a further processing aimed at evaluating the phase contrast. The processing procedure consists of choosing a reference sound zone for assessing the phase contrast as difference of phase signal between defect and sound (Fig. 5.32).

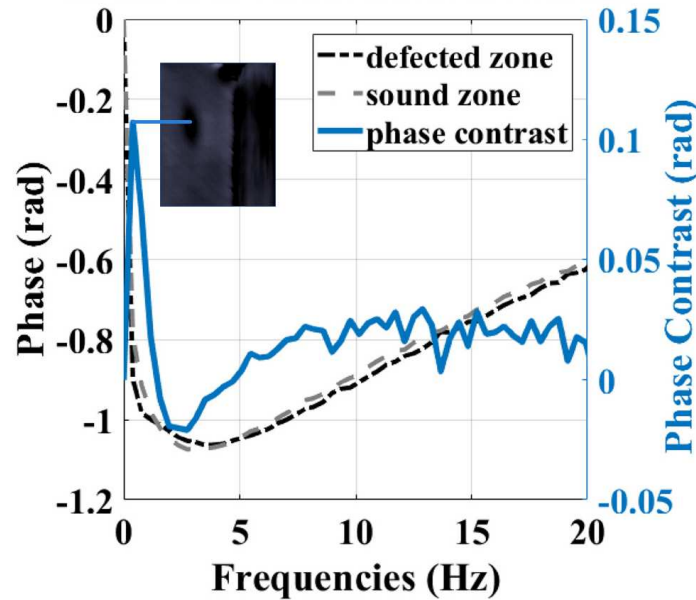


Figure 5.32: Phase and phase contrast trends for a defect chosen as an example.

Then, for each defect, the frequency map obtained in correspondence with the phase maximum contrast is usually used for evaluating defect dimension. At the same manner, the blind frequency, obtained in correspondence of zero phase contrast can be used to assess defect depth.

It is important to notice as the phase signal changes along the transverse direction, while it is constant along the longitudinal direction due to the geometry of the component. In this case, then, the sound signal can be represented by a sound profile along the x direction (Fig. 5.33).

Hence, to obtain phase contrast images for each analyzed frequency, the follow procedure has been used (Fig. 5.33):

1. Considering a sound area (free from defects) as reference. In this case, the sector 13 in Fig. 5.25b has been chosen as the reference for assessing the sound signal.
2. Considering an average sound profile obtained by averaging all profiles along the y direction of the sector 13.
3. Obtaining for each analyses frequency the phase contrast map by subtracting the reference profile from the phase maps of defected sectors, row by row, along the y direction.

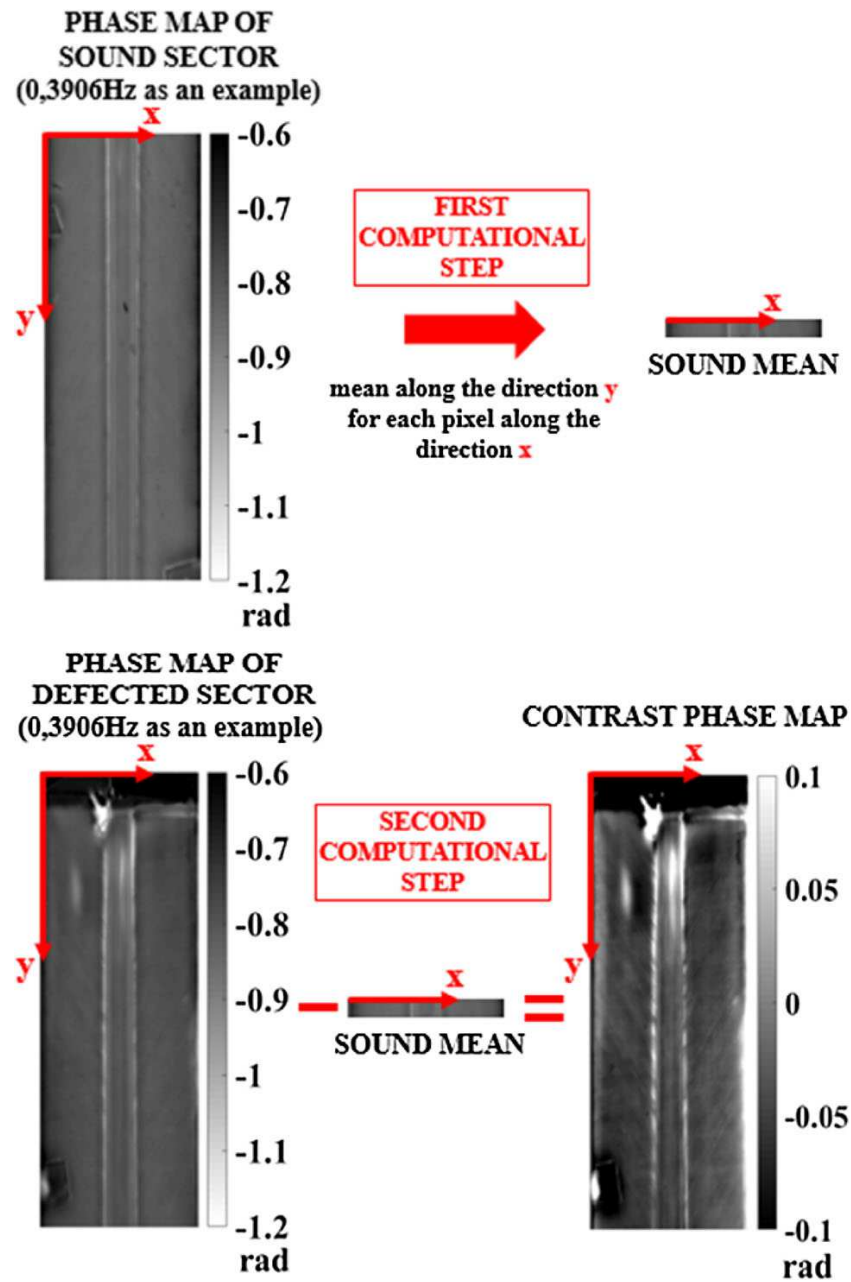


Figure 5.33: A scheme of the procedure used to get contrast phase maps for a real sample.

It is noteworthy, that these are two thermographic tests acquired at different time and so the matching operation has been computed in Matlab® as a post-processing operation by using the commands `rot90`, `imrotate` and `cut` already implemented in this software (Fig. 5.34).

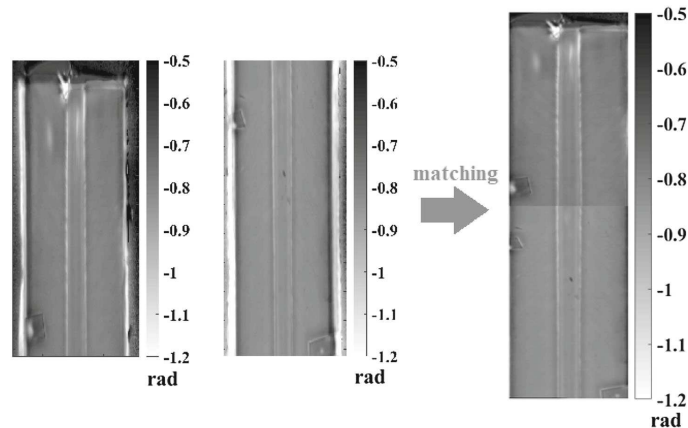


Figure 5.34: Matching thermographic maps-a frequency example (3.906 Hz).

In this way, the phase contrast trend along frequencies has been obtained pixel by pixel and it is possible to obtain the phase maximum contrast and the blind frequency pixel by pixel and then, the relative maps. As example, in Fig. 5.35 are shown the maximum phase contrast (MPC) and the blind frequency (BF) maps obtained for sectors 1 and 14.

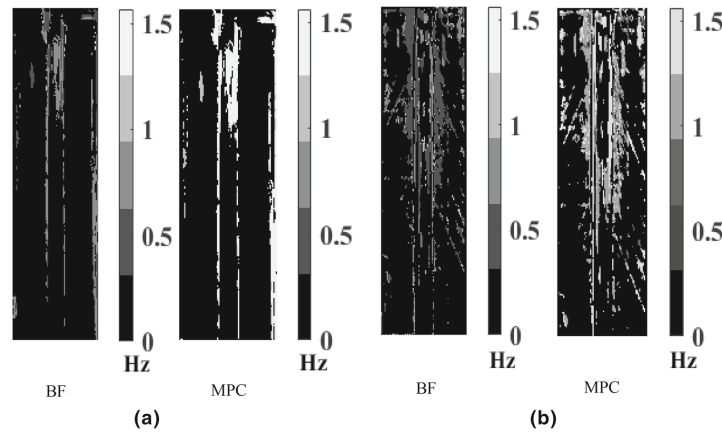


Figure 5.35: Blind frequencies (BF) and maximum phase contrast (MPC) maps for the defected sectors. (a) sector 1, (b) sector 14

The main advantage of this approach is to assemble in two maps the whole information deriving from the application of the PPT algorithm and then to have a rapid investigation about dimensions and depths of defects.

The analysis of the phase contrast maps allows the knowledge of areas at the maximum phase contrast with its corresponding frequency and areas at the zero-phase contrast with its corresponding frequency, the so-called blind frequency. The blind frequency map provides the depths of the individual delamination, while the frequency map at the maximum phase contrasts is useful to derive the right frequency where the size evaluation of the detected defects is possible.

In the same way, by using TomoViewSoftware (Olympus), it is possible to obtain a map showing the presence of defects corresponding to a chosen threshold percentage of the UT amplitude peak. The defects are representative of

all the discontinuities in the entire depth of the specimen.

In Fig. 5.36, for sector 1, the map scanned along the entire depth is shown with a threshold value set at 60% of the peak amplitude.

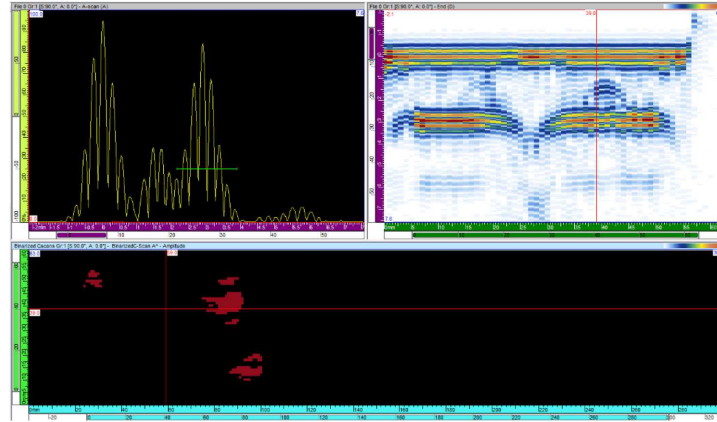


Figure 5.36: Map scanned along the entire depth-threshold value set at 60% of the peak amplitude, sector 1.

The same operations have been done in the case of the sector 14, and the results are shown in Fig. 5.37.

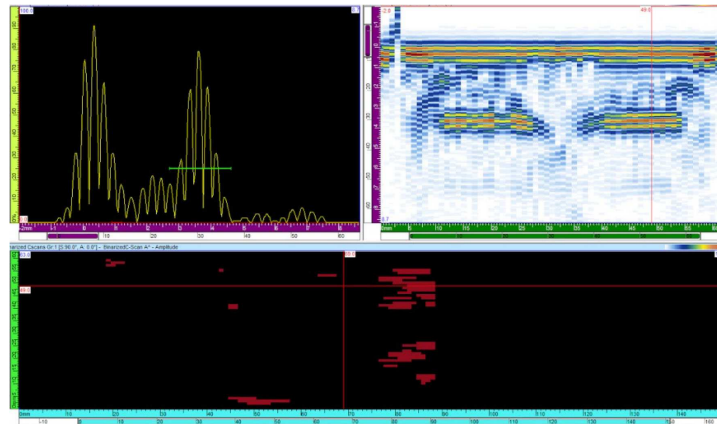


Figure 5.37: Map scanned along the entire depth-threshold value set at 60% of the peak amplitude, sector 14.

From the analysis of these maps (thermographic and ultrasonic results), there is a correspondence between the location of the detected defects for the both analyzed sectors (1 and 14). It is important to highlight as two different geometric resolutions have been used for the two techniques (0.17 mm/pixel for thermographic technique and 1 mm for ultrasonic one) and this explains a better definition of defects obtained with the PPT procedure with respect to the ultrasonic one.

Summarizing, UT allows for obtaining better results in terms of defect size and depth identification, but it requires a more complex set-up with respect to the thermographic technique. In this regard, thermography seems more suitable for analyzing very large components on-site.

5.2.4 Some final considerations

In the present part of dissertation, the results of the experimental activity carried out on a real component in CFRP have been presented and discussed to determine the capability of PPT in evaluating the presence of delaminations. The specimen has been investigated through the application of both the ultrasonic technique and the thermographic one. Both techniques confirm the presence of defects.

Thermographic phase images and Ultrasonic C-scan images, elaborated with a suitable computational approach, have been compared. In particular, a suitable approach has been proposed to processing phase maps derived from PPT analysis. This approach allows for extracting the sound area from the same component to get information about defect size and depth of a defective part having the same geometry. Ultrasonic C-scan tests were also used in order to validate thermographic results. PPT algorithm provides results in good agreement with UT C-scan inspection. The agreement between the location of defects has been verified. PPT has shown itself to be an excellent NDT tool to evaluate the condition of a CFRP real component: it can provide information with respect to the ‘correctness’ of the manufacturing process and it can give indication about the acceptance of the component after a non-destructive control. However, the PPT algorithm has to be optimized in order to allow not only a qualitative accordance between the defects revealed with the two techniques, but also a quantitative one. Summarizing, the main results of comparison of the two techniques are:

- In terms of defect depth, the obtained results show a good correspondence between the so-called blind frequencies and the defects depths found with the C-scan maps, even if ultrasonic technique allowed to detect deeper defects. In fact, it seems that the thermographic technique allowed to estimate real defects (delaminations) with a depth equal to 1.2 mm as well as to identify other shallow defects (probably excess of resin), some of which did not emerge by analyzing the ultrasonic maps (depth < 0.3 mm).
- UT allows for obtaining better results in terms of defect size and depth identification, but it requires a more complex set-up with respect to the thermographic technique. In this regard, thermography seems more suitable for analyzing very large components on-site.

For this reason and to perform a complete quantitative analysis, a further work is already in progress with the application of other thermographic algorithms and with the improvement of the set-up parameters.

5.3 A new thermographic procedure for the non-destructive evaluation of RSW joints

Resistance Spot Welding (RSW) is one of most used method to weld two sheet material thanks to its reliability and rapid production that makes it economical [178]. The process is based on the heat generated according to the Joule's law between the metals sheet interfaces. The principle of RSW is that two electrodes clamp two or more metal sheets together. Forcing a large electric current through the electrodes (and thus the metal sheets), the metal between the electrodes will melt and a weld nugget is formed when the metal has cooled down sufficiently. Then the electrodes release the nugget. An attractive feature of RSW is that a large amount energy can be delivered to the spot in a very short time (fractions of a second). That permits the welding to occur without excessive heating of the remainder of the sheet [178, 179, 180, 181, 182, 183, 184].

The quality of the produced joints depends on time, electrode pressure, current and surface conditions since each one is related on the heat generated during the process. A measure of the quality of a spot weld is the diameter of the weld nugget since it directly relates to the strength.

There is an ever increasing need for efficient quality control in the automotive and aerospace industries, for several reasons. One such reason is that reducing the weight of the manufactured structures as a means of reducing fuel consumption and material costs has high priority. Reduced structural weight results in decreased margins with respect to the structural strength, which leads to an increased need for product quality control. Another reason for quality control is the safety aspects. With a higher demand for quality control follows a need for general inspection of all manufactured products (not only a sparsely sampled subset), which requires automatic inspection cells in order to be time and cost effective.

Generally, the quality of joints is assessed by means of destructive testing on lap-specimens and peel-specimens [184]. However, more than thousands of spots are presented in one automobile so, a destructive control on the 100% of the joints would be too expensive in term of times and costs. In fact, typically, a car body contains about more than 4300 spot welds joining sheets of different thicknesses for making just one car and this trend is expected to be continued.

In this regard, non-destructive tests (NDT) allow for controlling the welded joints with reduced times and for the on-line monitoring of the RSW process. In literature, the main NDT techniques used for the RSW process are eddy currents, ultrasounds and infrared thermography.

In the work of Tsukada et al. [181], a new method has been developed for evaluating the quality of joints. This method, named (ECT) is capable to combine two different techniques based on the magnetic flux penetration and eddy currents. In particular, a good correlation with the destructive shear tests has been obtained with the magnetic flux penetration method. The ultrasonic C-scan technique has been used in the work [182] for NDT of aluminum joints. The proposed technique allows for obtaining the quality assessment of RSW joints even if a flat contact surface needs to be guarantee.

In the work of Wan et al. [185], the dynamic resistance variation has been used to investigate the weld nugget formation in titanium joints. In particular, a regression analysis has been carried out to obtain different features correlated to the quality of joints. In this work the attention was focused on the stimulated thermographic techniques and in particular on the pulsed thermography technique performed with flash lamps.

Stimulated techniques have some peculiarities with respect to traditional NDT since they provide a full-field information about the defect areas without a direct contact in rapid way [5, 19, 20, 21, 110, 115].

In literature there are few works about the thermographic techniques used for controlling joints obtained with the RSW process.

An automatic approach using thermography has been proposed in the work of Runnemalm et al., [183]. The pulsed technique has been used adopting a reflection set-up and the shape and nugget dimension has been assessed with an algorithm.

A different approach with a transmission set-up has been used in the work of Schlichting [186], in which, the quality of joints has been classified by means of a statistical analysis.

Both the approaches, in transmission and reflection set-up, with two different heat sources (laser flash lamps) were adopted in the work of Jonietz [187]. In particular, a new analysis procedure of thermographic data has been developed to take into account effects due to emissivity variations. In this regard, these variations involve also a different absorption of the heat although a uniform heat distribution is applied with a consequent problem on results interpretation.

Woo et al. [188] suggested different excitation techniques, e.g. flash lamp and ice cubes. All experiments were conducted with a transmission set-up, double sided.

Runnemalm et al. [183] propose a single-sided set up of a thermography system for spot weld inspection. The set-up is arranged to be possible to mount on an industrial robot in order to achieve a fully automatic inspection system. In this work, an analysis algorithm has been developed with the aim to find the spatial region in the acquired images that corresponds to the successfully welded area (the nugget size). The presented system is capable to inspect more than four spot welds per minute.

Lee et al. [189] used lock-in thermography to measure the nugget size of a spot weld. They used a single-side experimental set up, and compared ultrasound-infrared, photo-infrared, and lock-in thermography methods. Their conclusion was that the lock-in method was the most suitable for nugget sizing. However, lock-in thermography has one major disadvantage when it comes to automation; it is more time consuming than pulsed thermography which is used in this part of dissertation.

In fact, here the aim is to propose a new procedure for testing and processing of pulsed thermographic data, capable of assessing the quality of joints produced with RSW technique. Different steel joints were obtained from the RSW process by varying the main process parameters such as, current and time. The proposed procedure is based on a data processing of pulsed thermographic tests and does not require the preparation of the specimen surface with black coating. Thermographic data were acquired adopting a transmission set-up by means of a cooled infrared camera capable to acquire thermographic sequences at 64 Hz with a geometrical resolution equal to 0.062 mm/pixel. A flash lamp has been used to produce a thermal pulse of 3000 J with duration 5 ms. The procedure is based on the study of the characteristic behavior of the obtained thermal signal over time in the welded area. By fitting the thermal signal with a mathematical model, several features or indexes can be extracted, able to describe the thermal behavior of joints. A correlation between these indexes and the process parameters can be demonstrated.

5.3.1 Materials and methods

RSW welded joints were obtained from two steel sheet with thickness of 0.8 mm by imposing for each test a constant electrode pressure and varying current and time. Tab. 5.10 shows the specimen used for the experimental campaign and the relative process parameters. It is possible to note that the joints named with 2, 3 and 5 have very different conditions. In fact, the specimen 5 has been obtained with process parameters close to the optimum conditions, while specimens 2 and 3 represent two opposite conditions in which a poor quality is obtained. In particular, the specimen 2 has been obtained with low current and time values with a weld area characterized by

the absence of the nugget (stick weld). Conversely, the specimen 3 has been obtained with high value of process parameters and consequent welded area with material expulsion.

Specimen Number	Current (I) [kA]	Time (t_c) [s]	Electrode Force [kg]
1	8.9	12	270
2	7	6	270
3	15	15	270
4	8.9	9	270
5	9.7	15	270

Table 5.10: Process parameters used for obtaining the RSW joints.

Fig. 5.38 shows the surface conditions of the joints and the section variation at the nugget.

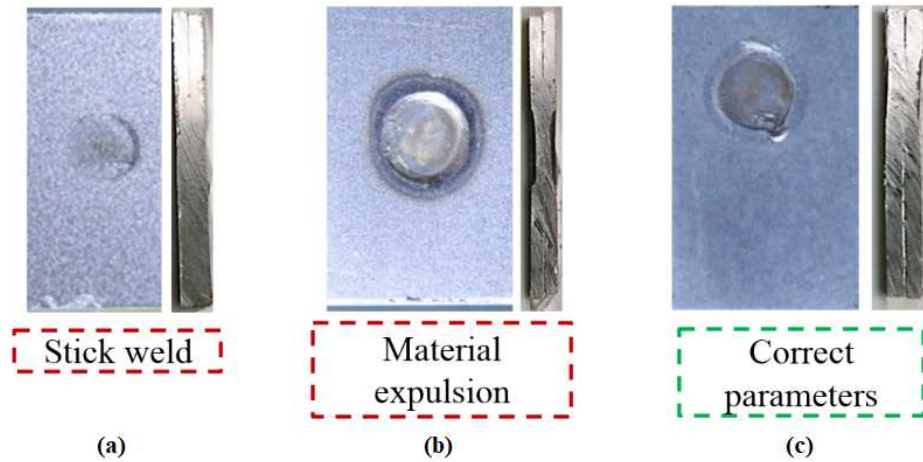


Figure 5.38: Specimens investigated and cross section of the welded area; (a) specimen 2, stick weld, (b) specimen 3, material expulsion, (c) specimen 5, correct parameters.

In reality, the test campaign was more extensive, and saw the examination of another 4 specimens, and for each examined combination of 3 identical specimens. However, the process parameters of the other 4 specimens can be traced back to the main cases studied, and for this reason the obtained results are not shown.

In Fig. 5.39 is shown the experimental set-up used for pulsed thermographic tests. A single flash lamp with energy of 3000 J and pulse duration of 5 ms has been used as heat source while, a cooled IR detector has been used for acquiring thermal sequences (FLIR X6540sc). A geometrical resolution of 0.062 mm/pixel has been obtained by using an optical lens of 50 mm and an extension ring of 12 mm. Thermal sequences were acquired with a frame rate of 64 Hz for a total duration of 30 seconds. Three repetitions were carried out for each specimen, and also 3 replications were performed by using the 3 different specimens with same name and parameter conditions (for example, we have specimens 2a, 2b, 2c, and so on).



Figure 5.39: Experimental transmission set-up adopted for thermographic tests.

However, the first test set-up used in order to analyze these specimens was carried out in a reflection configuration, using a 1064 nm wavelength Ytterbium pulsed fiber laser with a power of 30 W, the same infrared camera FLIR X6540SC, an optical bench, having the function of eliminating every single vibration, making the precise test as much as possible, and a micro metric table. The tests were conducted using different heating times with a laser beam of 25 ms, 500 ms, 1000 ms, with the same laser power. For the camera, a frame rate of 400 Hz and a time acquisition of 30 s were used.

The configuration is shown within the following figures (Fig. 5.40a and Fig. 5.40b):

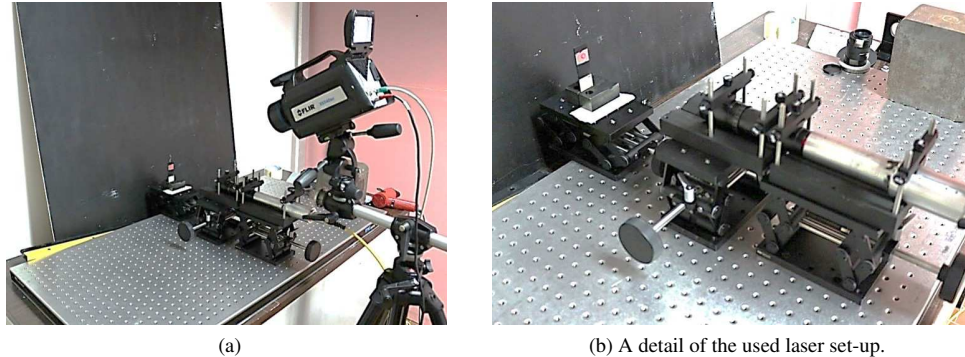


Figure 5.40: Laser set-up adopted for experimental reflection tests (a), with a particular detail (b).

A similar set-up, in reflection configuration with the same IR camera, but by adopting a flash source with 2 lamps was also used to perform the same tests.

Because of problems related to the emissivity of the spot surface, which varies greatly between the specimens, it is not easy to draw considerations about the welding nugget. It would be necessary to compensate for the differences in emissivity, which depends on factors such as the temperature, the angle of emission, the wavelength and the surface finishing of the object observed. In particular, each single point (pixel) on the spot surface absorbs heat differently and, in turn, emits infrared radiation in different ways. Surface finishing means both the surface roughness (average value, shape and direction of the roughness) of the body, and the presence of extraneous inclusions.

Within the following sections (5.3.2 and 5.3.3), the problem of emissivity variation and its influence on thermo-

graphic analysis will be shown and some procedures for its compensation will be discussed.

5.3.2 The problem of emissivity variation and its influence on thermographic analysis

The weld nugget provides the mechanical joint between the two steel sheets. At the same time, it constitutes a thermal bridge between the two welded sheets, which is exploited in this method. The better thermal contact between the sheets at the weld nugget contrasts with the surrounding material, where the heat transfer between the two sheets is comparatively low. This means that in transmission configuration, the position and size of the spot weld can be identified in the thermal image by a contrast of higher relative temperature, whereas in reflection configuration, the enhanced heat diffusion through the spot weld leads to a contrast of lower relative temperature for the spot weld.

When putting this idea into practice, two major obstacles for observing the above explained effect are encountered.

First of all, reflections of the surroundings at the bare steel surface are dominant and interfere with the signal induced by the spot weld. This effect is eliminated by subtracting a thermal image or a mean of the thermal images before the heating; in this way, the thermal reflections of the surroundings are treated as a background, which is subtracted, in order to obtain the classical delta temperature over the time.

Besides, the varying surface emissivity, which dominates the thermal signature in the case of a bare surface, has to be compensated. A compensation emissivity operation is necessary in order to void surface inhomogeneities, like scratches, surface impurities, surface color changes, and, most prominent, the dark discoloration of the impression of the welding electrodes that can mask the effect of the thermal bridge, until they make it almost undetectable.

One solution would be coating the surface with a material with high emissivity, for example black graphite [186]. In this way, the emissivity of the surface is homogenized and besides, the signal strength results increased drastically, as a bare steel surface has a rather low emissivity.

In the work [187], Jonietz et al. demonstrated that the coating solution on the investigated surface can be avoided by a proper normalization of the data. The advantage of avoiding the surface coating is a fast and cheap testing procedure, where the surface stays free of contamination by coating material. Within the cited work, two different procedures of normalization for both transmission and reflection configuration are shown:

1. Normalization for transmission configuration: background subtraction and division by a thermal image taken after 75 s of the cooling down, where the temperature has almost homogenized by lateral heat transfer and the time gradient of the temperature is almost zero. However, the temperature has not reached room temperature yet, in fact, the temperature of the sample has homogenized at a temperature still significantly above room temperature. This means, that the pronounced signatures in the thermal image taken at time of maximal intensity (immediately after the thermal radiation) are not caused by temperature differences, but by emissivity differences. The final thermal image obtained in this way results nearly free of surface properties, which indicates the real heat flow in the sample, i.e., in this transmission setup, the heat flux primarily through the spot weld across the thermal bridge toward the IR-camera.
2. Normalization for reflection configuration: background subtraction and division by considering an emissivity image taken 2 s after stopping the laser radiation. In reflection configuration, the real heat flow in the sample primarily through the spot weld is apparent by a lower relative temperature compared to the rest of the illuminated area. It has to be added that the sample geometry has a significant influence on the normalization. Especially if the emissivity image is taken after a long cooling down, the sample temperature will significantly

differ depending on the actual sample dimensions. For small samples, the lateral heat transfers are stopped after a short distance at the edge of the sample, leading to a larger heat accumulation. In contrast, in larger samples, the lateral heat transfers are stopped after a greater distance, which leads to a faster cooling of the sample. Thus, in practical use, the heating power and the time when the emissivity image is taken, have to be adapted to the size and geometry of the work piece examined.

5.3.3 A new procedure to emissivity compensation

The same problems described in the previous section characterize also our specimens and our thermographic results; for this reason, a procedure to compensate the emissivity in reflection configuration has been adopted:

1. evenly painting in an uniform way the tested samples in correspondence of the areas not interested by welding;
2. heating the specimens with a warm gun until reaching an uniform temperature of about 50 °C; therefore, the cooling down is recorded up to reach the room temperature (approx. T=25 °C);
3. from the registered sequence, extracting a hot frame (the warmest and most uniform possible) and a cold one (the coldest and most uniform possible), by considering the same area as reference within the painted region (the indicative emissivity value of this area is known);
4. calculating the radiant difference (I) by subjecting the average values registered in the considered area (hot and cold) and dividing for the known emissivity value in the case of a black body ($\epsilon = 0.95$), $I = \frac{HotMeanValue - ColdMeanValue}{\epsilon}$;
5. obtaining the emission map, subtracting the images related to the hot and cold frames, pixel by pixel, and dividing the obtained result for the previous radiant value of the point 4;
6. dividing the interested thermographic result, however considered as a map, with the emissivity map obtained as result in the point 5 and considered as map of compensation.

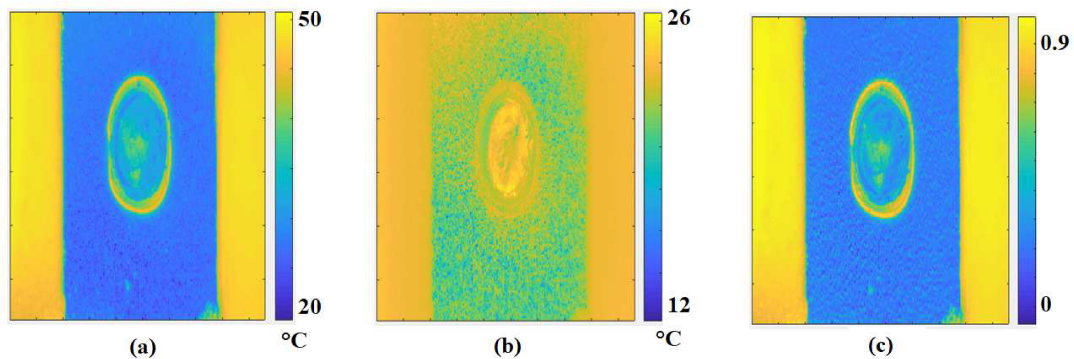


Figure 5.41: Emissivity compensation: (a) hot frame, (b) cold frame, (c) emissivity map.

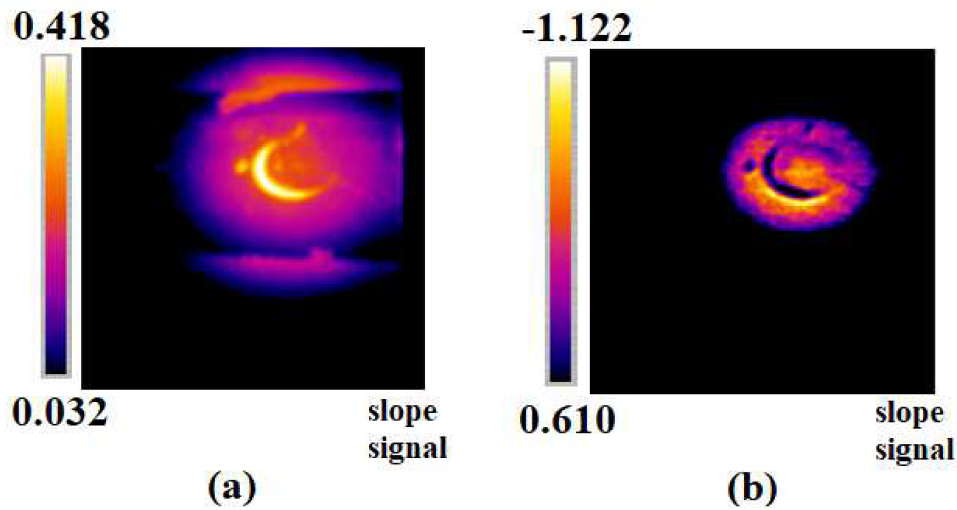


Figure 5.42: The final result of emissivity compensation; long pulse analysis by using slope algorithm, laser excitation of 500 ms.

The described procedure was carried out for each examined component and for analyzing the different set-up configurations, in order to have comparable and useful images to compensate the different emissivity of the initial thermographic maps. Within Fig. 5.42, a significative result of the emissivity compensation is shown, by using the slope map that it is possible to obtain by fitting the raw thermal data during the cooling down (long pulse analysis) with a line in a double log scale pixel by pixel, after a laser excitation of 500 ms.

However, these procedures, although effective and useful for estimating the size of the nugget, require time for the tests and additional post processing analyses.

From a practical point of view, it was decided to adopt a transmission set-up, using a single flash lamp placed on the opposite side of the infrared camera (set-up in transmission by flash lamp). By using a transmission configuration with a flash lamp as heating source, the emissivity does not affect the tests and the results in the same way that it affects the same in the reflection ones. In fact, the infrared camera and the exciting source are placed on opposite sides and for this reason we don't have the same problems.

5.3.4 The proposed thermographic procedure in order to characterize the joint quality by avoiding the emissivity compensation

Pulsed thermography is based on a short heat pulse generated by a heat source (for example flash lamps) and on studying the characteristic behavior of material during cooling. In particular, the surface temperatures decrease uniformly on areas without internal defects, while, in presence of internal anomalies, a temperature pattern is produced on the sample surface. The shape of this pattern can be linked to the geometrical properties of the related defects in the three dimensions. The equations and the models that can describe the temperature variation over the time of the surface opposite to the heat source (transmission configuration), under appropriate hypotheses, are already shown in Section 1.4.2.

Eq. 1.24 shows as the temperature rise depends on the material properties and the thickness of the specimen.

In particular, the time in which the maximum temperature is reached depends on thickness of plate, it decreases as the thickness decreases (Fig. 1.13). Fig. 1.13 shows the temperature trends in the case of an aluminum material for different thickness of plate, under the hypothesis of a homogeneous and isotropic semi-infinite plate with thickness L , subjected to a Dirac impulse, under adiabatic conditions. In the same way, only by changing the material properties with the steel generic one ($\rho = 7900 [kg/m^3]$, $k = 46 [W/mK]$, $c_p = 440 [J/kgK]$), it is possible to obtain similar trends (Fig. 5.43) [50].

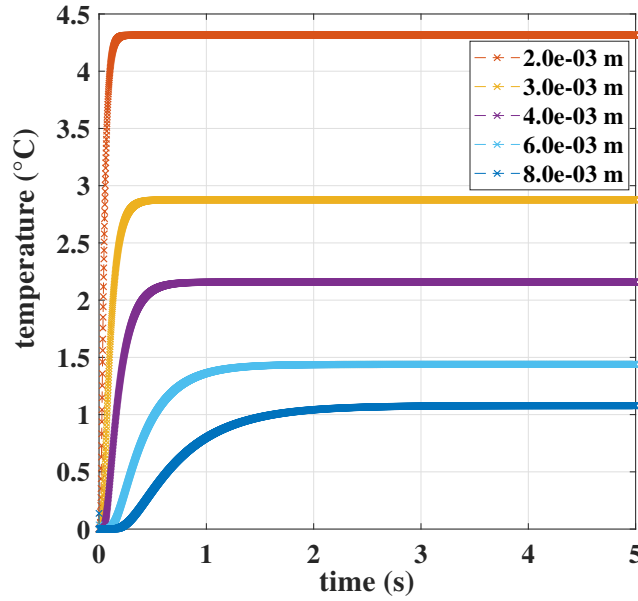


Figure 5.43: Temperature trend over time for a pulsed test in transmission mode (Eq. 1.24), steel material.

As shown in Fig. 5.43, the temperature reaches its maximum value in very short times and then reaches a steady-state value.

In our case, with respect to the model of Eq. 1.24, the heat exchanges cannot be neglected, and we have two steel plates welded with RSW process. As already said, in the previous section, the variation of the process parameters is correlated with the heat generated and can cause typical defect such as stick weld or material expulsion and then thickness reduction. In the first case the thermal resistance to heat flow will be higher than the second one so, the thermal behavior and thermal profiles will be different.

In Fig. 5.44, the thermal profiles related to the investigated specimens are shown, after the flash test in transmission configuration. In particular, the means value of temperature in a square area at the centre of the weld zone has been considered to plot the thermal profile over time.

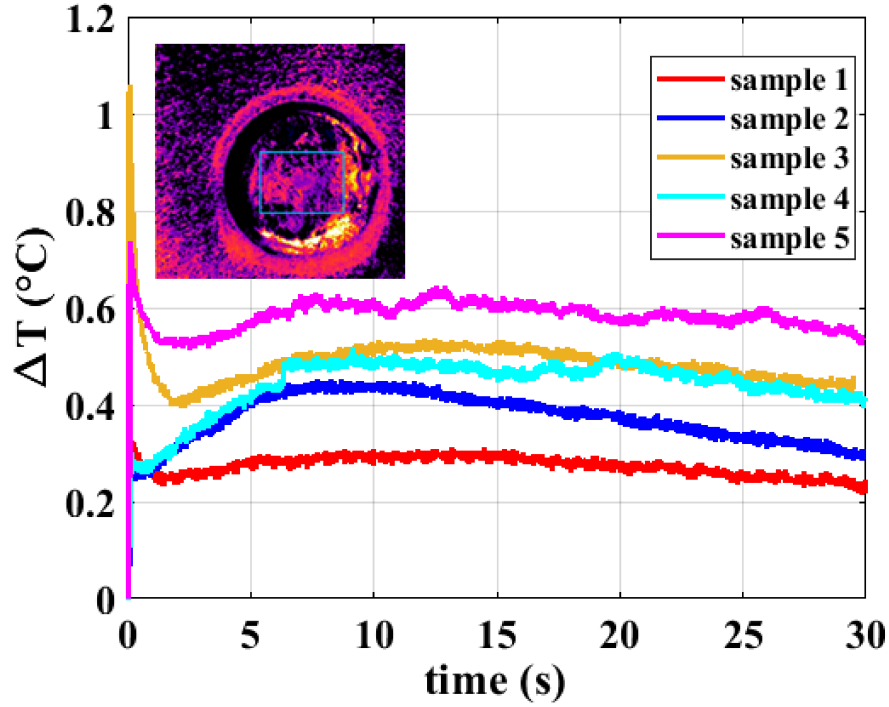


Figure 5.44: Comparison among the mean values of temperature over time for the investigated specimens, after the flash test in transmission configuration.

It is clear as the trend of thermal profiles is correlated with the process parameters. The profile related to the joint 5 can be considered as reference. As just said, the maximum temperature is reached for a relative short time then, temperature decreases for the heat exchanges for conduction, convention and radiation. However, after some seconds the temperature back to increase. This behavior occurs because the flash lamp heats all the specimen. In other words, also the areas far the welded ones are involved in heat transmission phenomena. These areas present a higher thermal resistance with respect to the welded ones and transfer heat by conduction trough the welded area causing the relative temperature increase. The thermal profile of the specimen 2 describes the thermal behavior in the case of low value of the process parameters. The higher thermal resistance leads to low temperatures and the lack of the cooling phase. On the contrary indeed, the joint 3 presents a high maximum temperature, a significative cooling phase and a well discernible minimum value.

The analysis of thermal profiles show as the thermal behavior is related to the process parameters and then to the quality of the joints. To extract the information from the thermal profile, a mathematical and empirical model has been used to describe the temperature evolution over time. The used model is:

$$T(t) = (at^2 + bt + c)e^{-\frac{d}{t}} \quad (5.2)$$

where t is the time and a, b, c, d are coefficients that can be found by adopting a least square algorithm. These coefficients represent the indexes used to describe the thermal behavior of the joint. Another index that can be used is the time in which the minimum value of temperature is reached. The proposed procedure of data analysis consists

on:

1. Exporting thermal sequence as a 3D matrix in Matlab®;
2. Applying a move mean mobile filter (on 5 data) on temperature data to reduce noise;
3. Searching the maximum value of temperature and then the time coordinate by using the mean value of temperature on a square area at the centre of the joint;
4. Applying the model, pixel by pixel, on temperature data to find the coefficients (indexes);
5. Searching the minimum value of temperature and the relative value of the time, pixel by pixel;
6. Obtaining for each index the 2D map of results.

In Fig. 5.45 is reported the temperature trend for the specimen 3 and a comparison among the raw data, after applying the move mean filter and then the result of fitting by using the proposed empirical model.

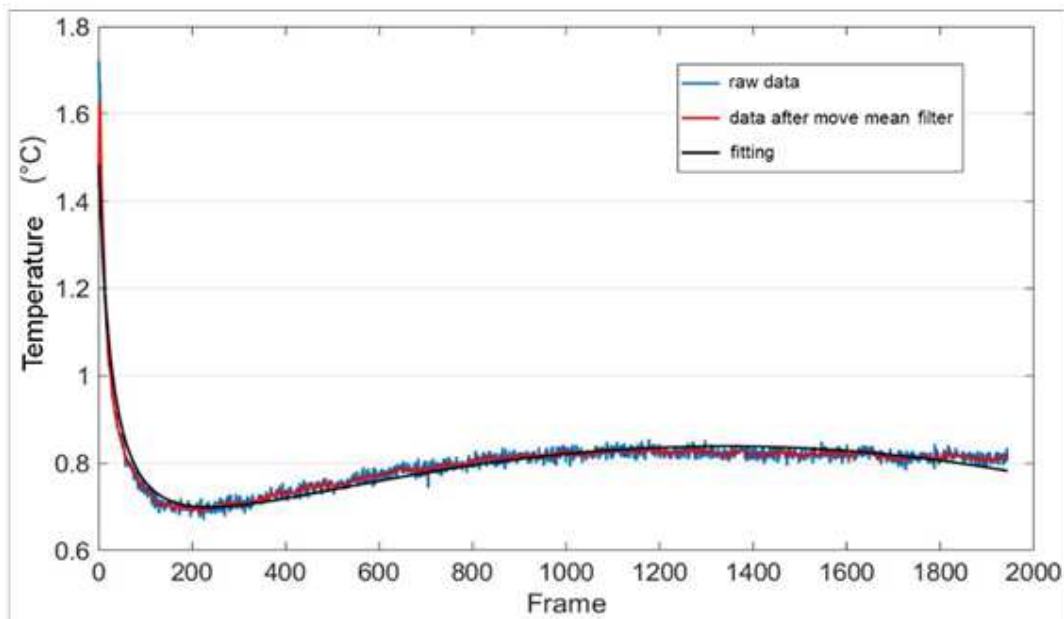


Figure 5.45: Comparison among the mean value of temperature over time for the specimen 3, after the move mean filter and data fitting.

5.3.5 By using thermographic technique and relative thermal indices to control RSW process

In Fig. 5.46, the results obtained from the proposed procedure described in the previous section are summarized. These latter are represented as 2D maps representative of the model coefficients (a and b) plus the 2D map related

to the time (or frame) in which the minimum temperature is obtained (t_{min}). The results and then, each coefficient (index) seem capable of discerning among the different process conditions. In particular, for the specimen 2 each index provides a 2D map in which the weld spot is not visible. This result is due to the lack of welding in the joint and to the presence of a stick weld. By contrast, the specimen 3 is characterized by the material expulsion in the weld area with reduction of the thickness. In Fig. 5.46 is evident as the specimen 5 shows an intermediate thermal behavior with respect to specimens 2 and 3.

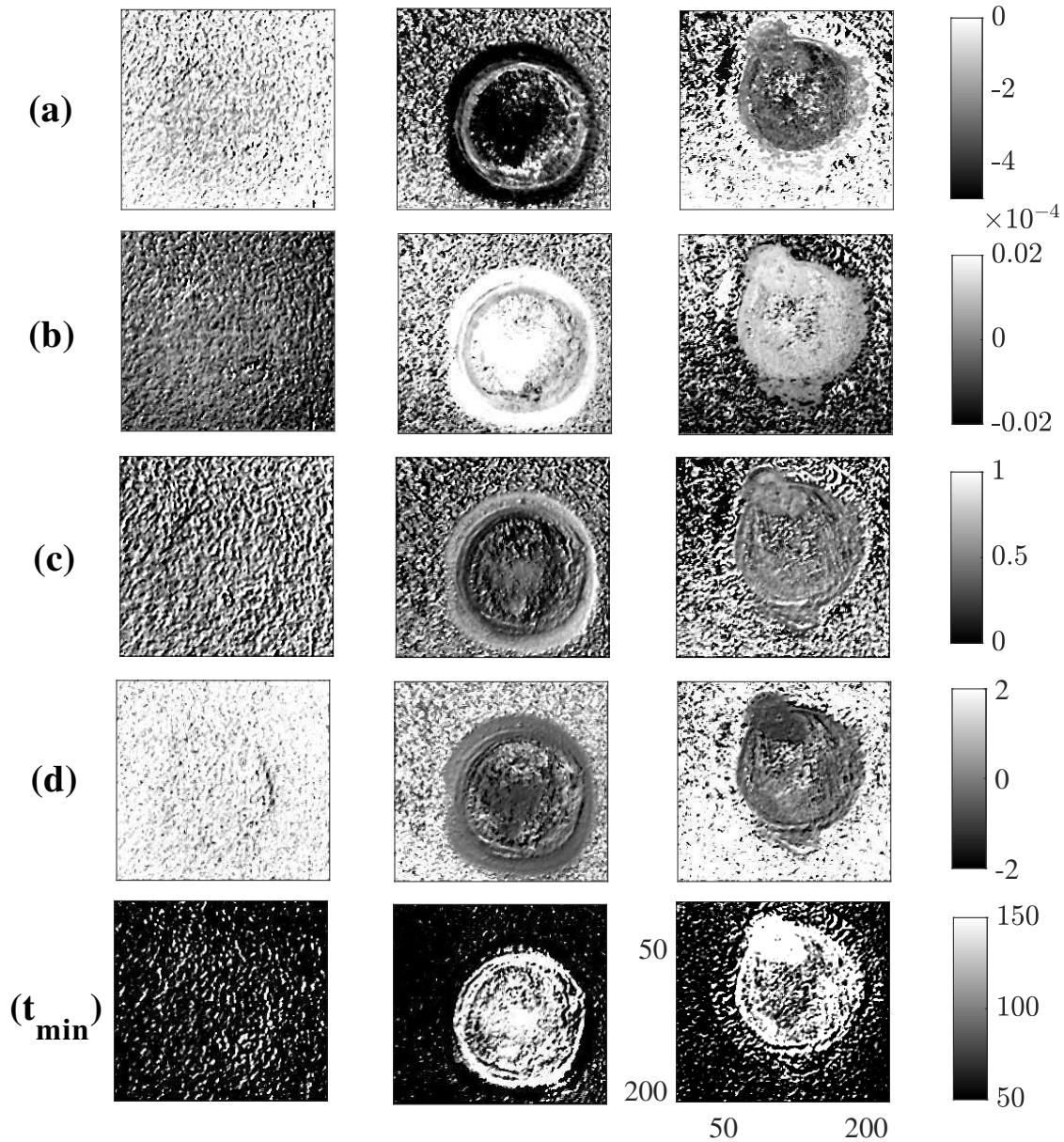


Figure 5.46: Results in terms of 2D maps for each index.

Tab. 5.11 shows the average values and the standard deviation one by considering an area on the welding spot

(Fig. 5.46) for each coefficient.

<i>specimen 1</i>	<i>a</i>	<i>b</i>	<i>c</i>	<i>d</i>	$t_{min}(frame)$
mean	9,78E-05	-1,02E-02	4,13E-01	1,22E+00	128,09
std	6,65E-05	2,40E-02	3,61E-02	2,79E-05	8,61
<i>specimen 2</i>					
mean	-1,13E-04	-4,53E-03	5,62E-01	1,59E+00	45,32
std	2,98E-05	2,29E-03	1,29E-02	1,24E-01	4,91
<i>specimen 3</i>					
mean	-6,10E-04	2,42E-02	2,65E-01	-1,07E+00	158,90
std	3,25E-05	9,61E-04	3,71E-02	3,69E-01	5,72
<i>specimen 4</i>					
mean	1,09E+04	-2,56E-02	7,67E-01	1,66E+00	49,06
std	1,89E+04	4,36E-04	6,51E-03	9,71E-02	25,47
<i>specimen 5</i>					
mean	-3,05E-04	1,01E-02	4,72E-01	-2,33E-01	124,65
std	5,05E-05	2,08E-03	4,13E-02	1,90E-01	3,03

Table 5.11: Results obtained for each thermal index in terms of mean and standard deviation values.

By way of example, to show the significance of the difference among the average values of the specimens analyzed, a histogram graph relating to the t_{min} parameter expressed as the number of frames is shown in Fig. 5.47. In particular, the height of each column represents the average value of the signal obtained as described above, while the error bands have an amplitude equal to 3 times the standard deviation. In this case, therefore, it is possible to adopt a threshold value equal to plus or minus 3 times the standard deviation beyond which it is possible to discern, respectively, a weld with material leakage or a gluing.

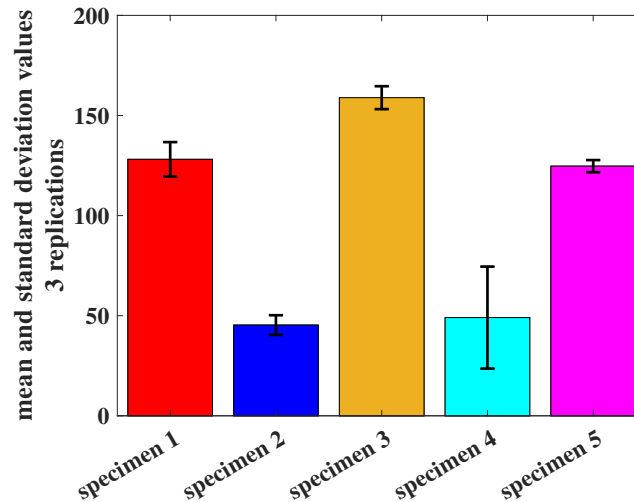


Figure 5.47: Results obtained for the examined specimens, by considering the index t_{min} .

Having 3 specimens available for each process condition, it was decided to compare the thermographic results (non destructive one) with the one obtained by applying the classic destructive controls provided for this type of

joints. The 3 specimens representing the 3 significant study cases were cut in correspondence of the nugget to perform micro graphic analysis of the same. The procedure to be carried out includes the incorporation of the cut part in a mold, then the resin is immersed inside and the solidification of the same is awaited. Once the embedded specimen is obtained, the upper part of the sectioned weld is polished. The process of polishing is carried out with a lapping machine, that is a rotating circular table and abrasive papers with different grain sizes and diamond cloths. After the polishing, the micro graphs in correspondence of the nugget were performed with optical microscope. The results obtained in correspondence of the 3 nuggets are shown in Fig. 5.48 and are in complete agreement with those obtained by thermography: specimen 2 nugget lenght $0\mu m$, specimen 5 nugget lenght $5878.6\mu m$, specimen 3 nugget lenght $6534.7\mu m$.

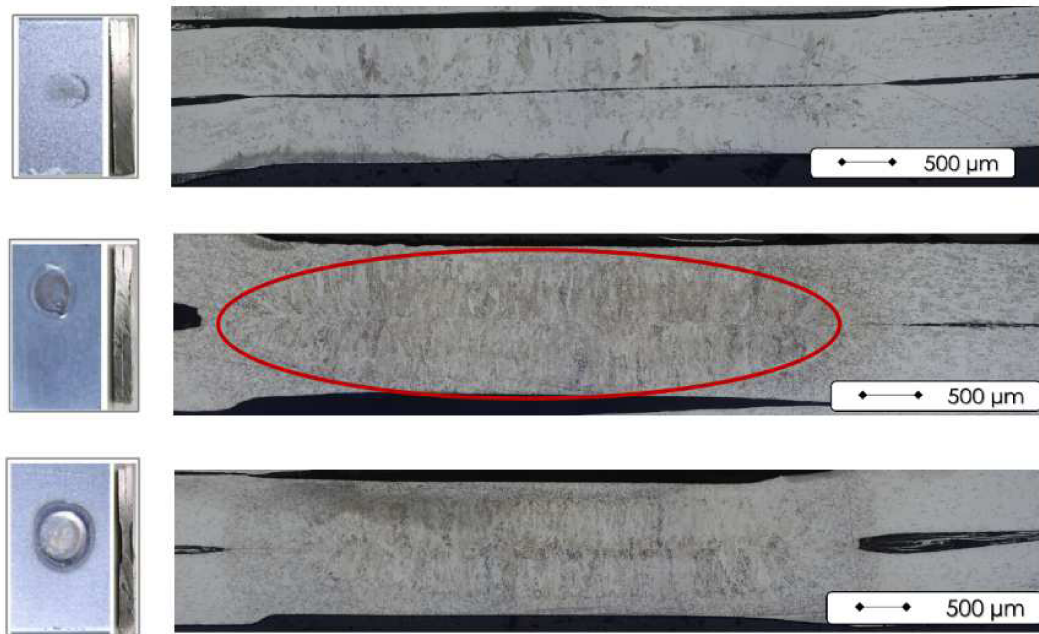


Figure 5.48: Micro graphs in corrispondence of the nuggets; in order from upwards to below: specimen 2 (stick weld), specimen 5 (the one taking as reference, with in red circle the weld zone), specimen 3 (material expulsion).

As already demonstrated, the thermal behavior is strictly related to the process parameters that directly affect the heat generated during the process. In this regard, the current and time have a similar effect on the heat produced during the process. So, as first approximation, it is possible to obtain empirical models relating the indexes t_{min} and d to the product $I * t_c$.

In Fig. 5.49 are represented two linear model obtained by considering the mean values of two indexes (coefficient d and t_{min}). The results seem very promise to use the proposed procedure to control the RSW process. However, an extensive experimental campaign is needed by involving also other specimens with different combination of the process parameters. In this way, it will be possible carry out a wide statistical analysis to investigate the significance of the proposed indexes.

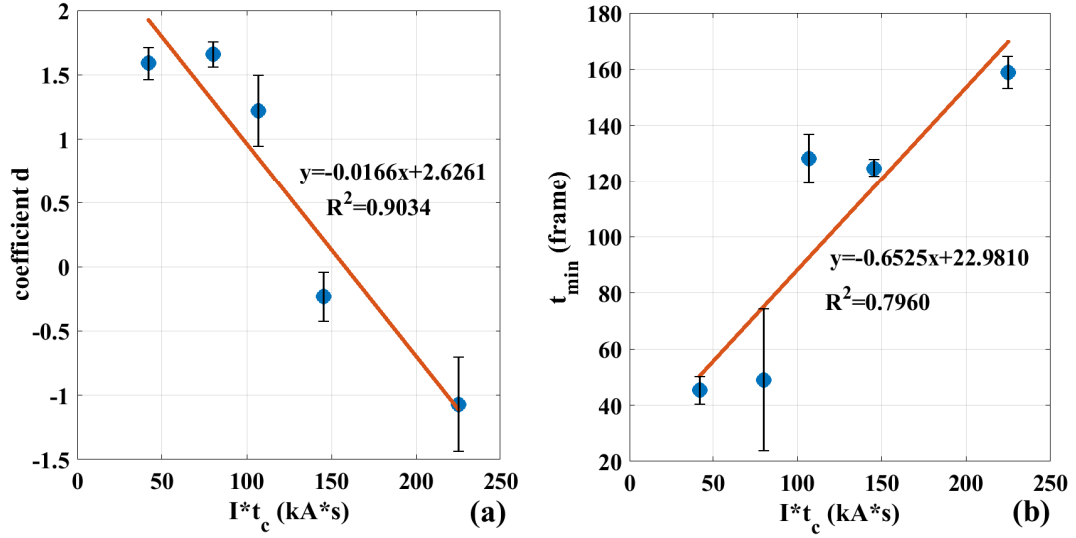


Figure 5.49: Correlation among the thermographic indexes and the process parameters ($I \cdot t_c$), transmission set-up: (a) coefficient d versus $I \cdot t_c$, (b) t_{min} versus $I \cdot t_c$.

With the same idea and the same aim, it is possible to obtain a linear correlation with thermographic parameters (such as the slope one) by using the laser results and applying the proposed procedure for the emissivity compensation. In Fig. 5.50, an example is reported by analyzing the slope map related to the thermal behavior of the three specimen taking as limit cases and studied in detail. However, also in this case, it is necessary to expand the test campaign and then the analysis one, in order to give a more accurate e precise measure about the possibility of using the thermography for controlling the RSW process.

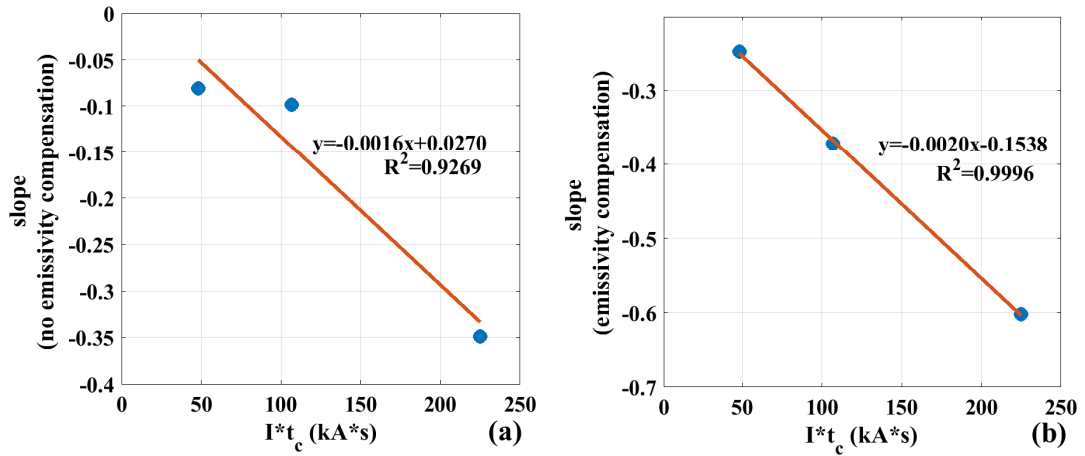


Figure 5.50: Correlation among the thermographic indexes and the process parameters ($I \cdot t_c$), reflection configuration and laser spot source (cooling down-long pulse analysis): (a) slope versus $I \cdot t_c$ before emissivity compensation, (b) t_{min} versus $I \cdot t_c$ after emissivity compensation.

5.3.6 Some final considerations and future steps

A new procedure has been proposed for evaluating the quality of RSW joints. The proposed procedure is based on the analysis of thermographic data deriving from the pulsed technique with a flash lamp and in transmission mode. The proposed analysis allows for evaluating the thermal behavior of joints by means of thermal indexes obtained by fitting the thermal data.

The main results can be summarized as follow:

- The thermal behavior over time during a pulsed test is related to the process parameters;
- The thermal indexes allow for detecting the quality of joints. In particular, the stick weld and the expulsion of material in the weld area;
- The possibility of using the thermal indexes for controlling the RSW process has been explored, by using a very low cost set-up: a cooling camera with a low acquisition frequency of 64 Hz and a flash set-up with only 3000 J as energy amount.

Moreover, the possibility of using a laser source has been investigated, and a new procedure for emissivity compensation has been described and discussed. Future works will be focused on a wide experimental campaign and statistical analysis in order to optimize the proposed procedure, as well also by increasing the acquisition frequency in order to obtain a more clear thermographic signal.

5.4 A thermographic procedure for the measurement of the tungsten carbide coating thickness

Mechanical components are subjected to severe abrasive wear in a number of industrial fields, such as shipping, metallurgy, energy, and construction industry, and it is one of the most serious issues for equipment failure. Because wear only occurs on the surface of components, surface engineering techniques have become the most effective solutions for the wear problems [190, 191, 192].

Cermet based WC–Co–Cr thermally sprayed coating is considered to be potential wear resistant coating material since can offer a combination of high hardness and excellent toughness. The hard WC particles in the coatings lead to high coating hardness and high wear resistance, while the metal binder Co–Cr supplies the necessary coating toughness [193].

The tungsten carbide cermet powder can be sprayed using different spray processes such as conventional flame spraying, plasma spraying and High velocity oxy-fuel (HVOF) spraying process. The coating properties are influenced not only by the properties of the used powders but also significantly by the used spray process and spray parameters [194, 195].

HVOF-sprayed WC-based cermet (e.g. WC–Co, WC–CoCr) have been shown to possess excellent tribological properties; indeed, they combine very high hardness with satisfactory toughness, as Co-based metal matrixes possesses ductility and excellent wettability toward the carbide grains [196].

One very important aspect, which has not been explicitly considered yet in literature, is the effect of the coating thickness on its properties, in particular on the tribological performance: this issue is particularly critical when dealing with soft substrates, as Al alloys are [197, 198].

Anyway, the coating plays a very important role in improving a component's survivability and operational performance. The coatings thickness is not only a parameter of the geometrical property of the coatings itself, but also an important indicator for evaluating the coatings' quality, performance and service life.

Therefore, effective non-destructive testing of the coatings thickness is of great significance for the performance of the components.

The coating thickness needs to be controlled and mastered because it has a great influence on the final product performance (weight, friction, corrosion, aspect, etc.). Commercially available thickness meters, including cross-section microscopy or gravimetric (mass) measurement, might be destructive by inducing surface damage and are limited in spatial sampling resolution. These methods are used when nondestructive methods are not possible, or as a way of confirming non-destructive results [199].

In order to ensure the safety and reliability of the coating work, it is necessary to use nondestructive testing method to characterize and evaluate the state of TBC in both manufacturing and service. Failure of a TBC could lead to a costly unplanned outage and could lead to catastrophic events. It is therefore necessary to monitor the condition of the TBC so as to avoid such failures and, if possible, to provide pre-cursor information that would suggest whether spallation is imminent. Due to the porous nature of TBC, conventional nondestructive testing methods, such as ultrasonic [191] and X-ray [192] method, are difficult to be competent. Besides, non-destructive measuring techniques are also used for coating thickness evaluation: eddy current methods [200], ultrasound testing [201], spettroscopy method [202].

The choice among these measurement methods depends on the coating thickness, the cost of instrumentation and the accuracy required.

The infrared thermography technique is an alternative nondestructive evaluation method. The thermal response of an exited material depends on different parameters of the material such as thermal conductivity, diffusivity, emissivity, and specific heat. Besides, the above properties manifest themselves in the thermal response depending upon different factors including the coating heterogeneities [203]. Infrared thermography based measurement presents several benefits: remote sensing, twodimensional data acquisition, rapid response, non-contact, high resolution, large temperature range, post-processing versatility and portability [20].

The well established thermographic technique is the pulsed technique, although, it has only been used for the evaluation of thermal barrier coating thickness [203, 204, 205]. In particular, Marinetti et al. even proposed the thermographic inspection method to discriminate reliably between TBC thickness changes coated gas turbine blades and adhesion defects [84]. To the knowledge of the authors this technique has been never used for the evaluation of thickness for metal/metal configuration.

In literature the possibility of measuring the coating thickness has been widely explored but, very few authors investigated the precision and accuracy in thickness evaluation. The proposed method is based on the cooling rate evaluation after the application of a long pulse heating. This means that during the heating the thermal waves reach the substrate. The accumulated heat depends on the thermal capacity of both the coating and substrate. If the thickness of substrate is constant (the used specimens have this peculiarity), the follow cooling behavior will only depend on the thickness of the coating. In particular, it has been considered the average cooling behavior by evaluating the slope of cooling in a fixed temporal window. This allows us to use a lower frame rate for acquiring thermal data with respect to the literature methods.

A procedure based on the “long pulse” thermographic approach for the measurement of the tungsten carbide coating thickness has been proposed and a comparison has been made with the performance of the traditional pulsed thermographic technique. In fact, very interesting results have been obtained by applying the thermographic “long pulse” technique, as the parameters extracted from acquired thermal responses have the ability of identifying the different coating thicknesses investigated. A calibration has been performed to evaluate the thickness of the coating and a prediction model has been proposed.

5.4.1 Materials and methods

The 9 samples considered in this study are disks composed by a steel substrate with 9.75 mm thickness coated with WC 86% - Co10% - Cr 4%. The tungsten carbide has been deposited by HVOF process. The specimens have been realized by coating the basic metallic material with different thicknesses varying between 1,00E-01mm and 10,10E-01mm.

In Tab. 5.12, the thicknesses of WC 86% - Co10% - Cr 4% coating are reported.

Specimen	Thickness of WC-Co-Cr coating (mm)
TH1	1,00E-01
TH2	2,00E-01
TH3	3,00E-01
TH4	4,00E-01
TH5	6,00E-01
TH6	7,00E-01
TH7	8,70E-01
TH8	9,50E-01
TH9	10,10E-01

Table 5.12: Thicknesses of WC-Co-Cr coatings.

The thermophysical properties [2] of the analyzed coating and the steel substrate are indicated in Tab. 5.13.

	Density (kg/m^3)	Specific heat capacity ($J/(kgK)$)	Thermal diffusivity ($m^2/s * 10^{-7}$)	Thermal conductivity ($W/(mK)$)
WC-Co-Cr coating	13640	239	89.2	29.2
Steel substrate	8055	480	39	15.1

Table 5.13: Thermophysical data properties of WC-Co-Cr coatings and steel substrate [2].

Fig. 5.51 shows the final appearance of the samples.



Figure 5.51: Picture of one of the reference-coated samples.

The techniques applied are the pulsed Infrared thermography and the “long pulse” Infrared thermography.

Two different set-ups have been realized, as shown in Fig. 5.52 and Fig. 5.53.

The first test bench for implementing the pulsed Infrared thermography consists of a flash source (flash lamps 1500 J x 2) generating a pulse excitation of duration 5ms and a cooled IR camera (Flir X6540 SC) with an indium-antimonium detector and resolution of 640x512 pixels sensitive in the range of 3-5 μm with Noise Equivalent Temperature Difference (NETD) <25 mK. The distance between the camera and the sample is 70 cm. The lamps have been placed as proximal as possible to the sample. The camera has been used with a lens of 50mm to reach a small spatial target and hence to obtain sufficient spatial resolution. The use of such a high performance thermal imaging camera allowed to obtain a reduced window (64x80 pixels) for the observation of the phenomenon Fig. 5.52, achieving a resolution 0.19 mm/pixel. The windowing is necessary to reduce the acquired data (in terms of dimension

pixel x pixel) and allow the use of a higher frame rate of 980 Hz. The observation time of the thermal cooling has been of 2 seconds.



Figure 5.52: Pulsed Infrared thermography set-up.

The other test equipment for implementing “long pulse” tests consists of a 1064 nm wavelength Ytterbium pulsed fiber laser, generating a pulse excitation of 500 ms with a collimated laser spot having a diameter of about 8 mm. In terms of IR camera, a microbolometric one has been used. The camera model is A655 FLIR (Fig. A.5) and its technical specifications are reported in Tab. A.2. The distance between the camera and the sample is 100 cm. The laser source has been placed at a distance of 15 cm from the sample and the laser beam strikes the sample perpendicularly. The camera has been used with a lens of 13.1 mm to reach a spatial resolution of 0.37 mm/pixel (Fig. 5.53).

Though the used camera allows to reduce the window of observation, it has been and forced to acquire the thermal sequences at a frame rate of 50 Hz, avoiding the windowing. The aim has been to acquire at the most slow frame rate.

As you can see from the set-up image (Fig. 5.53), the same acquisitions are carried out also by using the cooled detector Flir X6540 SC, in order to compare, in a future work, the results reached by using two very different IR

cameras, with also two different acquisition frequencies.



Figura 5.53: Laser setup to perform “long pulse” tests.

In this last case, the infrared image sequences have been acquired five times for each sample, and so five repetitions of the measure operation under identical condition have been carried out. The purpose of acquiring infrared image sequences five times is to evaluate the test repeatability and to improve the measurement procedure.

The observation time of the thermal transient has been of 5 seconds. In the wavelength intervals in which both the infrared cameras work, the spectral emissivity of the samples can be considered constant.

5.4.2 The limits of well-established methods (apparent thermal effusivity and TSR®) for estimating metal coating thickness

The apparent thermal effusivity algorithm, based on the above theoretical remarks (Section 1.4.3.5), has been applied in order to study the thermal behavior that come from the analysis of the pulsed thermographic tests performing with flash lamps.

The thermal sequences are those acquired for each thickness of the coating.

A pre processing procedure has been implemented before the application of the effusivity algorithm. The steps of this procedure can be summarized as follows:

- Importing of the thermographic sequence (3D matrix) in Matlab®;
- Subtracting of the average of the first ten cold frames to the whole sequence to obtain the ΔT values over time;
- Adding an offset ΔT value (zero machine) to avoid ΔT values close to zero; this step is applied pixel by pixel to each temperature decay curve and allows to avoid negative values in the logarithmic scale.

The mean temperature decay trend observed for the first 700 frames of the cooling stage are plotted in Fig. 5.54. The choice of the frame number is due to the certainty that in this time interval the thermal cooling phenomenon can be

considered terminated. The trends refer to each one of the 9 different thickness of the coating. Each trend represents the average of the temperature behavior of the surface in the windowed area (80x64 pixels).

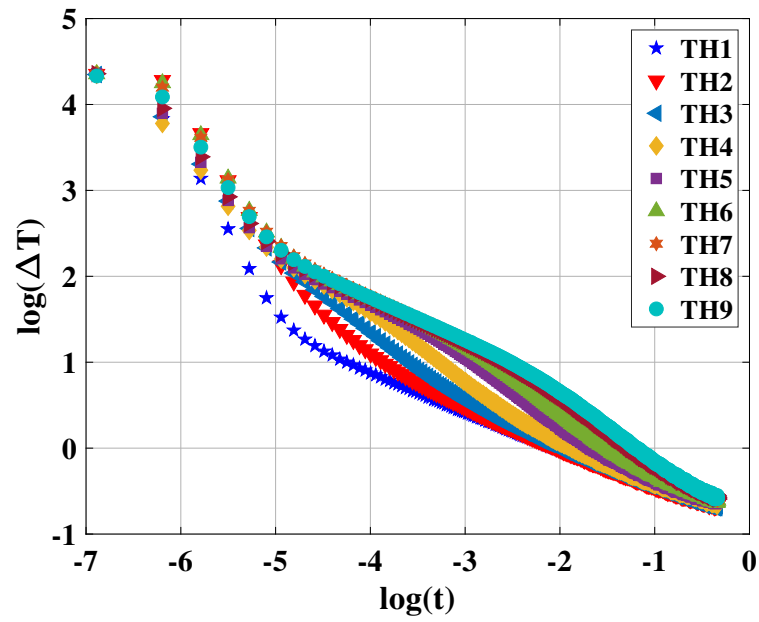


Figure 5.54: Mean temperature decay trends observed for the first 700 frame of the cooling stage for all the specimens.

The apparent effusivity profiles extracted for the 9 thickness are plotted in Fig. 5.55, where the influence of a thickness variation of the coating (from 1,00E-01mm to 10,10E-01 mm) on the apparent effusivity profiles is shown.

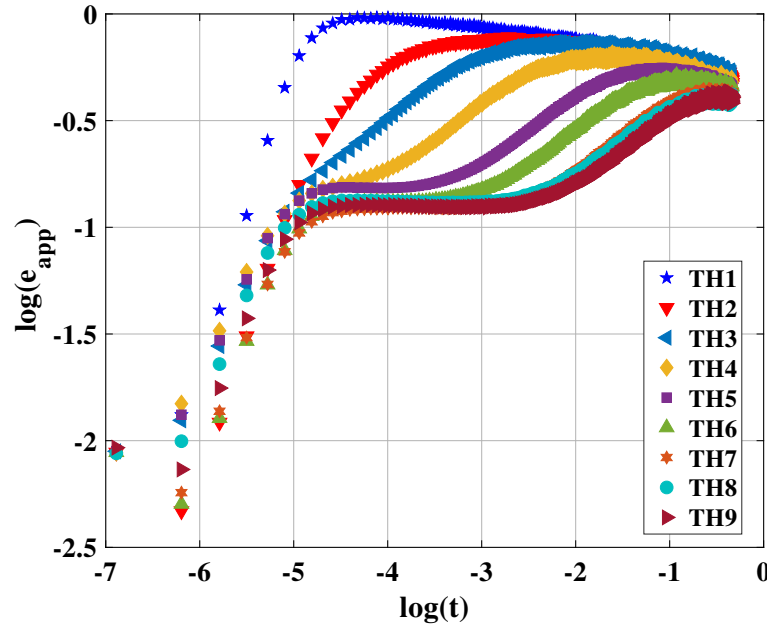


Figure 5.55: Influence of a thickness variation of the coating (from 1,00E-01 mm to 10,10E-01 mm) on the apparent effusivity profiles.

Fig. 5.55 shows in a logarithmic representation the experimental curves of apparent effusivity (e_{app}) over time for the considered areas (80x64pixels) for all the nine thickness, respectively. Each curve refers to the apparent effusivity value averaged on 5376 pixels. As expected, e_{app} curves do not show any minimum, but only a shift caused by the different coating thickness.

Anyway, the reached results show an important limitation; the thermal effusivity doesn't allow to evaluate the too thin (1,00E-01 mm 3,00E-01 mm) coating and the too thick coating (9,50E-01 mm 10,10E-01 mm): in the first case, the thermal excitation is too long and the calculated effusivity is not referred to the coating, but it is an expression of both the involved materials; in the second case, the thermal excitation is too weak and the pulse doesn't reach the interface between the coating and the substrate returning the same effusivity. An increasing of the energy of the pulse can induce a damage on the coating. If the reflection coefficient R results too small, it is impossible to resolve the differences between the thicknesses in any case. Besides, it is necessary to consider the high diffusivity of both materials, the coating and the basic one, that is crucial for the correct application and analysis of the data that come from a pulsed test. However, in both cases, it is impossible to resolve the difference among the different thickness. The technique remains valid for the coating whose thickness varies from 3,00E-01 mm to 7,00E-010 mm. In addition, another crucial issue has to be reported, this approach based on the analysis of the apparent effusivity in the time domain needs a thermographic acquisition with an elevated frame rate, of about 1000 Hz, in order to capture the cooling behavior of the material. This is possible only by using a high performance and so expensive IR camera. Besides, an essential point of the effusivity method is that you need to know the thermophysical properties of the coating and the substrate in order to estimate the coating thickness; however, once known the material thermophysical properties, it is possible to calculate directly, without any calibration, the value of the unknown coating thickness.

Same considerations come from the analysis of 1st derivative trends, by fitting the raw thermal data with a polynomial of 5 degree. Also in this case there are only a few points that outline the first part of the different curves

(despite the high acquisition frequency) and so it is not possible to distinguish a net inflection point. Besides, if we want to discern the different trends by considering the minimum points, the thick thickness ($7,00E-018,70E-01$ $10,10E-01$) don't show this typical behavior.

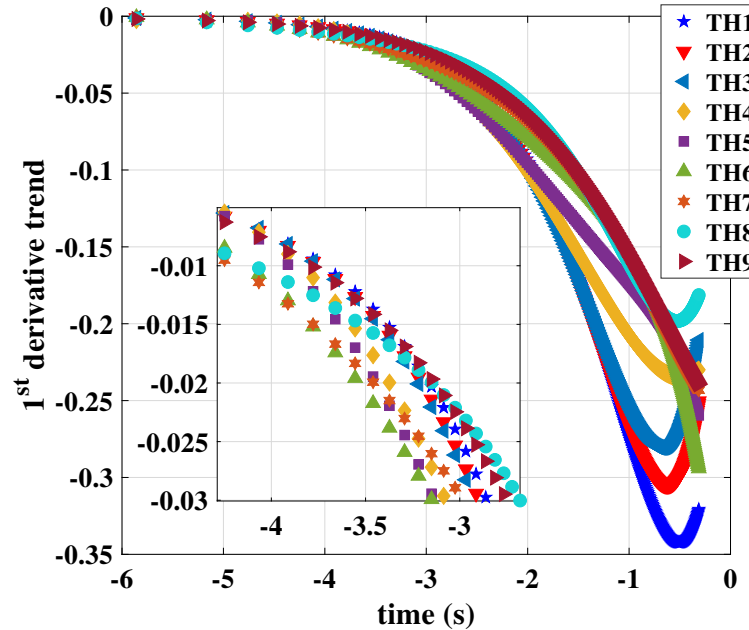


Figure 5.56: Influence of a thickness variation of the coating (from $1,00E-01$ mm to $10,10E-01$ mm) on the 1st derivative (TSR®) trends.

5.4.3 By using slope algorithm and a calibration procedure to the thickness coating estimation

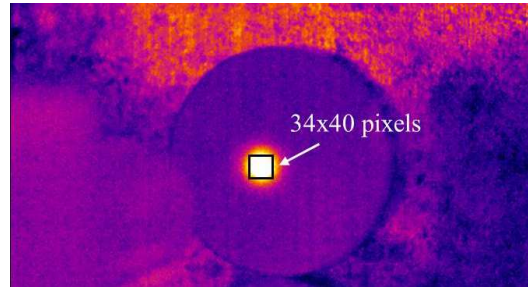
The thermal sequences obtained by using a “long pulse” approach have been pre-processed with the same procedure summarized in the previous paragraph.

In order to achieve the goal of proposing a prediction model and so a new procedure that require a training (calibration) data set and a validation one, only 7 specimens have been used as training data set, while the remaining two specimens have been used as validation one. The validation set consists of the specimens having the coating thickness of $3,00E-01$ mm and that having the coating thickness of $8,70E-01$ mm, in order to consider two opposite cases.

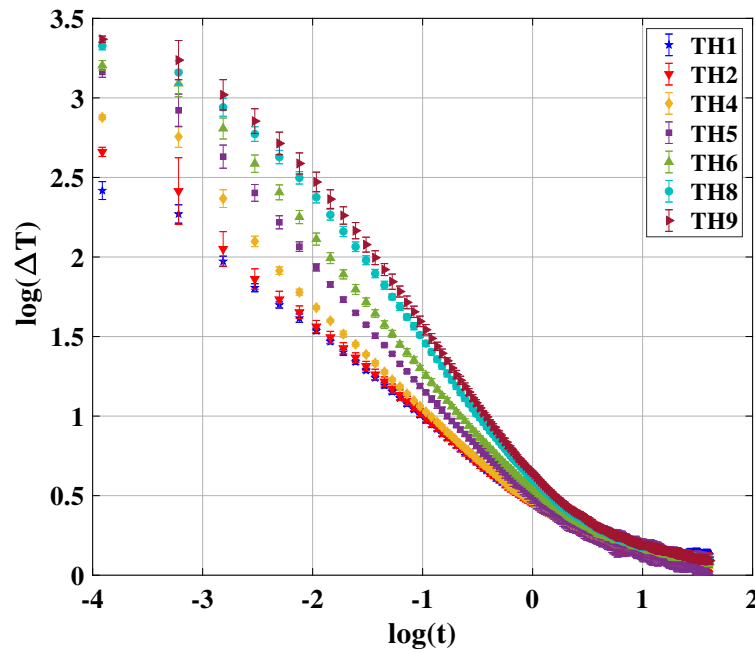
The mean temperature decay trends observed on the 7 samples for the first 250 frame (5 seconds) of the cooling steady are plotted using a double log scale, in Fig. 5.57. The choice of the observation time has come by observing that the physical phenomenon of cooling was exhausted, anyway studies are in progress to indicate the best final frame for improving the procedure.

The plots have been obtained choosing the pixel with the maximum temperature value by considering a rettangular area inside the spot of the laser (34×40 pixels) on the surface of the sample. Each value of temperature reported

in each plotted trend is the mean of the five repetitions carried out, so they are represented together with the relative error bars, in order to show the data variability. The error bars represent the uncertainty of the mean due to random effects [134, 135]. The reported uncertainty provides a level of confidence of approximately 95%.



(a) Selected area inside the thermogram acquired with the microbolometric infrared camera (640x480).



(b) Long pulse analysis.

Figure 5.57: Mean temperature decay by considering the pixel with maximum temperature value and relative error bars on 5 replications; training data set.

The analysis of the temperature plots relative to the samples with 7 different thicknesses allows to notice that the thickness variation results in a change of the cooling rate of the material (Fig. 5.57). On this logarithmic scale graphic, it can be notice that the central portion of the temperature decay follows a line. The value of the slope of the different lines has a correspondence with the different coating thickness.

The evaluation of the slope has been obtained by processing the thermal sequences in Matlab® and using the commands “polyfit” and “polyval” for fitting the same with a polynomial of 1 degree and for evaluating the polynomial coefficients performing an ordinary least squares calculation. The fitting has been applied by considering the

all data set (5 replications), avoiding the previous calculation of the mean. The least squares process solves for the slope and intercept of the best fit line. The slope obtained has been chosen as the indicator to explain the variation of thickness. In particular, the slope values decrease with the increasing of thickness.

Then, the validation samples have been investigated by adopting the same procedure in all its step and by using the same experimental parameters. The temperature decay trends, calculated for five repetitions, for the validation samples are reported in Fig. 5.58.

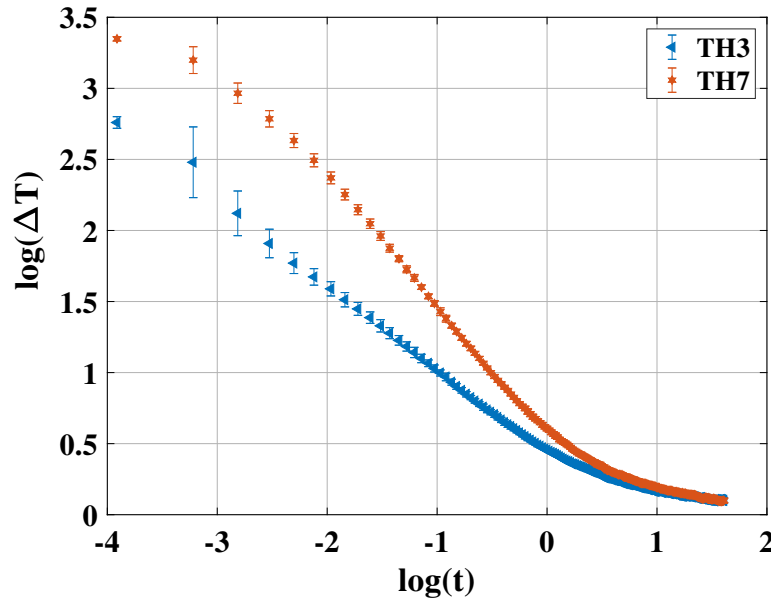


Figure 5.58: Mean temperature decay by considering the pixel with maximum temperature value and relative error bars on 5 replications; validation data set.

An attempt to create possible mathematical models to describe the behavior of coating thickness depending on the slope values of the temperature cooling profiles has been investigated, by considering the results that come from the considered validation data set.

The models (calibration curves) have been obtained by considering the WC-Co-Cr thickness as a function of the slope values.

The models have been extrapolated using data provided by the training set. Two different models seem to explain the observed behavior: a linear model and a second order polynomial model (Fig. 5.59 and Fig. 5.60); the results show a goodness of fit very high. The two models are reported with their confidence bounds and their prediction bounds. This last are larger than the confidence bounds because take into account not only the error for the estimation of the model, but also the error associated to future observations [134, 135].

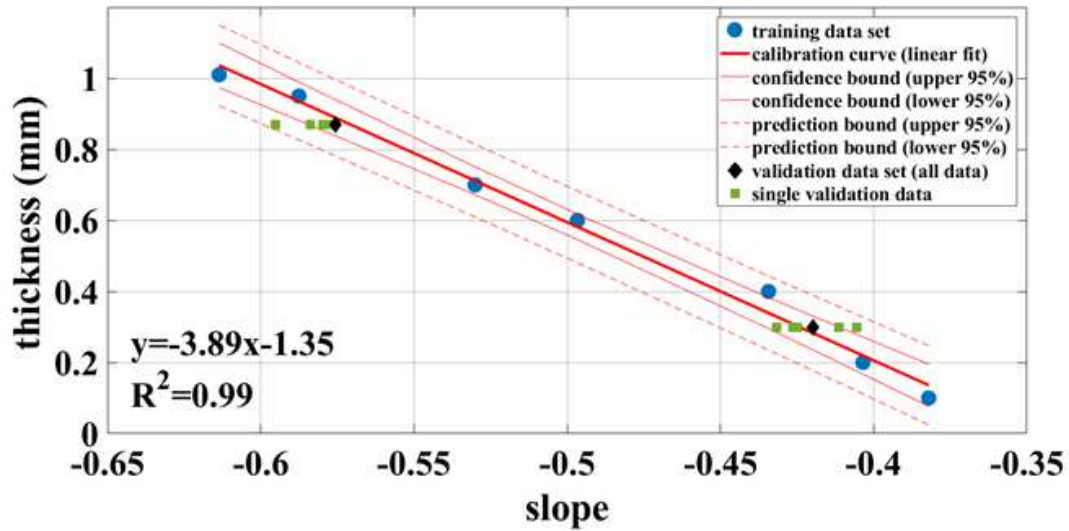


Figure 5.59: Data dispersion plot (thickness vs slope) with the estimated regression line (linear model), the prediction bounds (external curves) and the 95% confidence bounds.

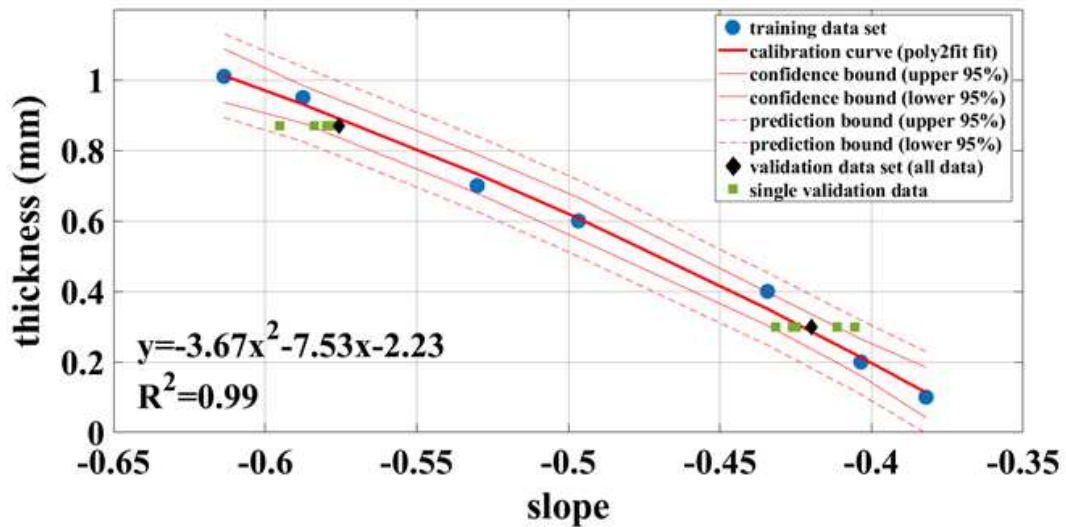


Figure 5.60: Data dispersion plot (thickness vs slope) with the estimated regression line (second order polynomial model), the prediction bounds (external curves) and the 95% confidence bounds.

The evaluated slope results related to the validation data set (green squares) are reported in the same previous plots, in order to show, graphically, where these values, in terms of new observations, are collocated; in both cases, the values are within the prediction bounds. These evaluated slope values are also reported in Tab. 5.14, accompanied with the associated confidence bounds. As we can see, there is a good resolution in solving two adjacent

thickness. The result of fitting is good for both the obtained models, however the error committed, in the evaluation of thickness, by choosing the linear model is a little bit greater than the error made with the polynomial model for small thickness values. The errors have been calculated using the validation data set (two samples) and compared with the nominal thickness. The difference between the mean of the measurements and the reference value (accuracy of the measurement procedure), expressed as percentage, and the precision of the models are reported in Tab. 5.15. The obtained results return errors lower than 6%.

For completeness of information, the evaluated slope values related to the validation thickness are reported in Tab. 5.14, with the relative 95% confidence bounds related to the initial fitting (fitting of 1 degree on the 5 replications carried out).

Specimen	Slope	Upper bound, 95% CI on mean	Lower bound, 95% CI on mean
TH3	-4.20E-01	-4.13E-01	-4.27E-01
TH7	-5.76E-01	-5.66E-01	-5.68E-01

Table 5.14: Slope values related to validation samples and 95% confidence bounds on them.

Specimen	Nominal thickness	Polynomial model expectation (mm) value and 95% confidence bounds		Percentage error (%)	Linear model expectation (mm) value and 95% confidence bounds		Percentage error (%)
TH3	3.00E-01	2.87E-01	$\frac{3.40E-01}{2.26E-01}$	4.33	2.83E-01	$\frac{3.32E-01}{2.35E-01}$	5.56
TH7	8.70E-01	8.92E-01	$\frac{9.50E-01}{8.28E-01}$	2.52	8.89E-01	$\frac{9.40E-01}{8.39E-01}$	2.21

Table 5.15: Expected values of the thickness by using the models accompanied by their accuracy and precision with respect to the nominal values.

The results reported in table 4 and in table 5 have been obtained using the data of the five repetition performed in the experimental acquisition. Anyway, if it is impossible to perform the five measurements, the error that occurs, in the case in which only a measurement is performed and the same calibration model is used, has been evaluated. The percentage errors, reported in table 6, are higher if the linear model is used, while they results lower if the polynomial model is used. The accuracy worsens also for the thin thickness. It is graphically shown, as already said, in Fig. 5.59 and Fig. 5.60.

Specimen	Nominal thickness (mm)	Polynomial model expectation (mm)	Percentage error (%)	Linear model expectation	Percentage error (%)
TH3	3.00E-01	3.07E-01	2.33	3.03E-01	1.00
		2.86E-01	4.67	3.29E-01	9.67
		3.03E-01	1.00	3.08E-01	2.67
		3.66E-01	22.00	2.27E-01	24.33
		3.48E-01	16.00	2.50E-01	16.67
TH7	8.70E-01	9.51E-01	9.31	9.65E-01	10.09
		9.14E-01	5.06	9.19E-01	5.63
		9.02E-01	3.68	9.05E-01	4.02
		8.98E-01	3.22	9.01E-01	3.56
		8.94E-01	2.76	8.95E-01	2.87

Table 5.16: Expected values of the thickness by using the models accompanied by their accuracy with respect to the nominal values if single measurements are carried out.

This new and simple procedure based on the evaluation of the slope of the linearized temperature profile, as previously shown, needs a calibration model to be useful, but the provided results show the capability of the method in measuring the real thickness of an unknown coating. A further condition to ensure the good functioning of the developed model based on “long pulse” thermography is the thickness of the substrate whose value has to be the same for all the investigated samples.

It is noteworthy that this approach, on the contrary of the other one, doesn’t require an elevate frame rate for data acquisition, so a cheap IR camera is sufficient to implement the procedure if the accuracy requested is comparable with the obtained results. A chance to improve the accuracy and the precision of the model is given by using a more performant camera, and so, for this reason, a future development regard the analysis of the same data, acquired in the same time, by using the cooled IR camera.

5.4.4 Final remarks

A novel procedure to estimate WC-Co-Cr coating thickness over a metallic substrate has been proposed and described, in detail. The methodology consists in evaluating the changes in slope of the linear fitting that describes the cooling behavior, in a double logarithmic scale, of the surface of the sample after a laser heating, by using a microbollometric camera with a very low speed as temperature detector.

A linear and a second degree polynomial dependency of the coating thickness with respect to the evaluated slope is demonstrated. An experimental analysis has been conducted on samples constituted by a steel substrate and WC-Co-Cr different coating thickness. The results obtained for the measured thickness return values with a precision of one hundredth of a millimeter. This achievement demonstrates the high potential of the method to estimate in a simple, fast and robust way the WC-Co-Cr coating thickness over metallic substrates. Besides, the procedure shows a significant advantage over the alternative pulsed technique that doesn’t work well in the case of thin and thick coatings with also very similar thermophysical properties, with the aggravating factor of needing a very performing and expensive infrared camera.

However, it is necessary to underline as the application of which the results have been shown, although it seems narrow, in reality it is placed in a wider context of industrial interest. In fact, when performing in-field tests on thermal barrier coatings (TBCs), we can encounter several cases of coatings deposited on gas turbine blades and the

main problem could be the difficulty to correctly interpret the experimental data that come from a thermographic inspection. The coating thickness changes, which are not regarded as anomalies, are one of the most common sources of false alarms. They are very challenging to recognize because, unlike stains, eroded areas and optical property variations, they are not detectable in the visible band. Furthermore, their thermal signal is similar to the one produced by an adhesion defect. It would be very interesting, for the power generation industry, to be able to interpret the coating thickness variations by means of PT, with also a very high final precision. Although the results concerned the analysis of specimens with imposed thickness, the approach adopted lends itself well to the application of a real case, after a previous calibration of the chosen quantitative thermographic index, and so it could be a promising choice in order to investigate, for example, serviced turbine blades still mounted on their turbine rotor, for a robust quantitative assessment of their coatings within this very interesting industrial application.

Chapter 6

Conclusions and future developments

Here the key results of this thesis are summarized to provide to the reader an overall picture of the conclusions that can be drawn from the present manuscript.

In this dissertation, a new thermographic quantitative approach has been developed, capable to provide interesting results for defect detection, and more in general, for ensuring structural integrity within different applications of industrial interest.

An essential question that needs to be asked before to start a research analysis is: there is someone who did it before you, or who did something similar, within the same topic?

If the answer is positive, you have to investigate his work and to study his methodology, try applying it to your precise case.

If maybe it didn't work you have to find out why and give the right reasons, with physical and mathematical explanations.

Again, if it works, you can try to do it in a different way, perhaps by applying another technique or, more simply, a different analysis methodology and you can compare the results, stressing the advantages and, why not, also the disadvantages of both the procedures.

And finally, if nobody did your idea before you, ask yourself again why, and try to do it.

Basically, this is the aim of a research work and within this thesis, I tried to answer these questions.

For this reason, within Chapter 2, a careful study of the state of art has been presented, by showing methodologies and procedures already used for a quantitative thermographic analysis, together with strengths and weaknesses of the same. The influence of some experimental and analysis choices have been investigated in detail, in order to understand and stressing where the literature has arrived and the encountered problems. The analysis of the works in the literature has shown that there are unidimensional models often used for the quantitative analysis of thermographic data and that provide an estimation of the depth and size of the defect. When these relations are applied to experimental data, where 3D phenomena are involved, the first problems arise. Besides, the application of these models very often require the use of a high performance set-up, in terms of energy source and acquisition frame rate, and boundary conditions that are not easy to obtain and to replicate.

The work carried out in the literature study has therefore demonstrated the presence of different post processing algorithms for the analysis of thermographic data. However, most of these literature works have seen a comparative study of the various analysis algorithms above all qualitative and that, in most cases, has concerned the investigation of low diffusivity materials such as FRP composites..

So, what should be the guidelines or the basis for this kind of a comparative study? The first thing, the experiments should be clear. Or better, the experimental procedures should be clear. It should be presented in a way that the reader or the user can replicate and/or reproduce that result. And the evaluation criteria should be very clear, straightforward.

Things like “better” or “worse” does not mean anything to the audience. Also the choice of the specimen to be tested should be made with criteria. Definitely, the quantitative real analysis in terms of depth and size values, that represents what in the end users are looking for, should be presented.

For this reason, within Chapter 3, where an extended comparison among different post processing algorithms has been shown, we tried to make a comparison work that would answer the questions asked.

First of all, we have to choose a sample. We tried to investigate an aluminium sample with different imposed defects, since this type of material is highly diffusive and therefore some choices such as the acquisition frequency, the analysis window and the duration of the pulse create problems for the purpose of a complete diagnosis and characterization of the sound material and the defective one.

The test parameters such as the acquisition frequency, the pulse length, the duration of the acquisition have been specified, and also the comparison among the use of different thermographic set-ups has been described, in detail (Chapter 4).

Some criteria have to be defined; for this reason, the weighted maximum SBC, the number of detected defects above a certain threshold or the possibility to have a correlation among the investigated defect indices have been clearly defined, in order to have a quantitative comparison. The results have showed a clear dependence from the analysis window and the same in turn demonstrated a clear dependence on the chosen algorithm for data analysis, on the investigated aspect ratio. The conclusions did not lead to say that one method or algorithm was better than the other, but different results were shown for which one is preferable to the other.

The quantitative analysis in terms of depth and size has been shown in Chapter 4. A new procedure to quantify the results has been proposed and described in detail, giving, at the end, a measure of the defect dimensions and the related error respect to the nominal size values. The proposed procedure allows for obtaining the quantitative analysis of high diffusivity materials by using a not expensive set up with only 3 kJ in terms of energy source and 200 Hz of acquisition frequency. Errors up to 20% have been obtained in size and depth estimation, by choosing a very critical value of aspect ratio (around 3) and a material with very high diffusivity. In this way, a new algorithm of data processing such as the slope one has been declared as a quantitative algorithm and its effectiveness has been demonstrated both with simulations and with experimental results. Besides, the limits of TSR® and PPT as quantitative algorithms of data analysis have been shown, however stressing that is a specific case, with a specific material and particular set-up conditions.

The same common thread is also found in the following chapters, where the results obtained by investigating a sample with imposed defects have been used within studied cases of industrial interest and in the analysis of real defects.

For the first time, as knowledge of the author, the Thermography, as non destructive control, has been used for detecting and characterizing the defects typical of Metal Additive Manufacturing process, in particular of the L-PBF one. The results have shown how the use of a laser source, together with the one of a thermal imaging camera in the mid-infrared are more effective for a small and non-flat reflector, and so for the analysis of components that commonly have complex shapes and small dimensions. By using Thermography, we are able to discern defects in keyhole mode respect of the one for lack of fusion, and we are able to detect defects very shallow (until a depth of

0.4 mm, with a step of 0.1 mm) with a good SBC (that is a measure of SNR-Signal Noise Ratio), which would not be easy to assessment by adopting an ultrasonic control (Chapter 5, section 1).

The capability of PPT algorithm to give information about the depth of a defect has been demonstrated within an analysis of a real component, by proposing a new approach for the identification of a sound material suitable for the analysis of a component that show a variable geometry (Chapter 5, section 2).

The results obtained by applying a new procedure for the analysis of RSW joints have demonstrated the possibility to identify the typical thermophysical behavior of this type of welded joints and to discern among stick weld, weld with material expulsion and a weld produced with correct process parameters. The proposed new procedure doesn't require the use of a coating, as well as emissivity map compensation (Chapter 5, section 3).

An empirical procedure that uses the slope algorithm for processing raw thermal data has been developed to discern the coating thickness. The obtained results by applying this new procedure return errors lower than 6%. Besides, the limits of the classical procedures used for this assessment have been shown, when the substrate and the relative coating have thermophysical properties very close and the coating thickness are too thin ($1,00E-01$ mm $3,00E-01$ mm) or too thick ($9,50E-01$ mm $10,10E-01$ mm) (Chapter 5, section 4).

All the proposed procedures are the sum of a detail study of the problem, of the relative state of art and how Thermography can solve it.

Bibliography

- [1] Meola, C., Carlomagno, G. M., & Giorleo, L. (2004). The use of infrared thermography for materials characterization. *Journal of materials processing Technology*, 155, 1132-1137.
- [2] Ibarra Castanedo, C. (2005). Quantitative subsurface defect evaluation by pulsed phase thermography: depth retrieval with the phase.
- [3] Spring, R. W. (1995, March). American Society for Nondestructive Testing (ASNT) certification of thermographers. In *Thermosense XVII: An International Conference on Thermal Sensing and Imaging Diagnostic Applications* (Vol. 2473, pp. 131-134). International Society for Optics and Photonics.
- [4] Gavrilov, D., & Maev, R. (2018). Extraction of Independent Structural Images for Principal Component Thermography. *Applied Sciences*, 8(3), 459.
- [5] Maldague, X. (2001). *Theory and practice of infrared technology for nondestructive testing*.
- [6] Oswald-Tranta, B. (2017). Time and frequency behaviour in TSR® and PPT evaluation for flash thermography. *Quantitative InfraRed Thermography Journal*, 14(2), 164-184.
- [7] Oswald-Tranta, B. (2016, May). Comparison of time and frequency behavior in TSR® and PPT evaluation. In *Thermosense: Thermal Infrared Applications XXXVIII* (Vol. 9861, p. 98610P). International Society for Optics and Photonics.
- [8] Maierhofer, C., Reinhardt, H. W., & Dobmann, G. (Eds.). (2010). *Non-Destructive Evaluation of Reinforced Concrete Structures: Non-Destructive Testing Methods*. Elsevier.
- [9] Ibarra-Castanedo, C., & Maldague, X. (2004). Pulsed phase thermography reviewed. *Quantitative Infrared Thermography Journal*, 1(1), 47-70.
- [10] Marinetti, S., Plotnikov, Y. A., Winfree, W. P., & Braggiotti, A. (1999, January). Pulse phase thermography for defect detection and visualization. In *Nondestructive Evaluation of Aging Aircraft, Airports, and Aerospace Hardware III* (Vol. 3586, pp. 230-238). International Society for Optics and Photonics.
- [11] Shepard, S. M., Lhota, J. R., Rubadeux, B. A., Wang, D., & Ahmed, T. (2003). Reconstruction and enhancement of active thermographic image sequences. *Optical Engineering*, 42(5), 1337-1343.
- [12] Shepard, S. M., Hou, J., Lhota, J. R., & Golden, J. M. (2007). Automated processing of thermographic derivatives for quality assurance. *Optical Engineering*, 46(5).

- [13] Balageas, D., Chapuis, B., Deban, G., & Passilly, F. (2010). Improvement of the detection of defects by pulse thermography thanks to the TSR® approach in the case of a smart composite repair patch. *Quantitative InfraRed Thermography Journal*, 7(2), 167-187.
- [14] Maierhofer, C., Myrach, P., Reischel, M., Steinfurth, H., Röllig, M., & Kunert, M. (2014). Characterizing damage in CFRP structures using flash thermography in reflection and transmission configurations. *Composites Part B: Engineering*, 57, 35-46.
- [15] Maierhofer, C., Röllig, M., Gower, M., Lodeiro, M., Baker, G., Monte, C., ... & Blahut, A. (2018). Evaluation of different techniques of active thermography for quantification of artificial defects in fiber-reinforced composites using thermal and phase contrast data analysis. *International Journal of Thermophysics*, 39(5), 61.
- [16] TOMIĆ, L. D., JOVANOVIĆ, D. B., KARKALIĆ, R. M., DAMNJANOVIĆ, V. M., KOVAČEVIĆ, B. V., FILIPOVIĆ, D. D., & RADAKOVIĆ, S. S. (2015). APPLICATION OF PULSED FLASH THERMOGRAPHY METHOD FOR SPECIFIC DEFECT ESTIMATION IN ALUMINUM. *Thermal Science*, 19(5).
- [17] Ibarra-Castanedo, C., & Maldague, X. P. (2004, April). Defect depth retrieval from pulsed phase thermographic data on plexiglas and aluminum samples. In *Thermosense XXVI* (Vol. 5405, pp. 348-356). International Society for Optics and Photonics.
- [18] Zeng, Z., Tao, N., Feng, L., & Zhang, C. (2012). Specified value based defect depth prediction using pulsed thermography. *Journal of Applied Physics*, 112(2), 023112.
- [19] D'Accardi, E., Palumbo, D., Tamborrino, R., & Galietti, U. (2018). Quantitative analysis of thermographic data through different algorithms. *Procedia Structural Integrity*, 8, 354-367.
- [20] D'Accardi, E., Palumbo, D., Tamborrino, R., & Galietti, U. (2018). A quantitative comparison among different algorithms for defects detection on aluminum with the pulsed thermography technique. *Metals*, 8(10), 859.
- [21] D'Accardi, E., Palumbo, D., Tamborrino, R., & Galietti, U. (2019, May). The influence of the truncation window size on the quantitative thermographic results after a pulsed test on an aluminium sample: comparison among different post-processing algorithms. In *Thermosense: Thermal Infrared Applications XLI* (Vol. 11004, p. 110040M). International Society for Optics and Photonics.
- [22] Mahan, J. R. (2002). *Radiation heat transfer: a statistical approach*. John Wiley & Sons.
- [23] Kombucha Mushroom P., Goliath National Bank (GNB), teaching material, 2014, available on: <https://www.slideshare.net/kombuchamushroom>, assessed 14/08/2017.
- [24] Halliday, D., Resnick, R., & Walker, J. (2013). *Fundamentals of physics*. John Wiley & Sons.
- [25] Siegel, R. H. J. R., & Howell, J. R. (1992). *Thermal radiation heat transfer*, Hemisphere Pub. Corp., Washington DC.
- [26] Balaji, C. (2014). *Essentials of radiation heat transfer*. John Wiley & Sons.
- [27] Czichos, H. (Ed.). (2013). *Handbook of technical diagnostics: fundamentals and application to structures and systems*. Springer Science & Business Media.

- [28] Incropera, F. P., Lavine, A. S., Bergman, T. L., & DeWitt, D. P. (2007). Fundamentals of heat and mass transfer. Wiley.
- [29] Rogalski A., "Infrared detectors: an overview," *Infrared Physics & Technology*, vol. 43, no. 3, pp. 187–210, 2002.
- [30] Dowden, J. (2009). The theory of laser materials processing. *Heat and Mass Transfer in Modern Technology*, Springer, 95-128.
- [31] ASTM E2582-07. (2014). Standard practice for infrared flash thermography of composite panels and repair patches used in aerospace applications. West Conshohocken (PA): International A.
- [32] Bein, B. K., Gibkes, J., Gu, J. H., Hüttner, R., Pelzl, J., Balageas, D. L., & Deom, A. A. (1992). Thermal wave characterization of plasma-facing materials by IR radiometry. *Journal of nuclear materials*, 191, 315-319.
- [33] Williams, T. (2009). Thermal imaging cameras: characteristics and performance. CRC Press.
- [34] Vollmer, M., & Möllmann, K. P. (2017). Infrared thermal imaging: fundamentals, research and applications. John Wiley & Sons.
- [35] Ibarra-Castanedo, C., Gonzalez, D., Klein, M., Pilla, M., Vallerand, S., & Maldague, X. (2004). Infrared image processing and data analysis. *Infrared physics & technology*, 46(1-2), 75-83.
- [36] Ibarra-Castanedo, C., Gonzalez, D., & Maldague, X. (2004). Infrared Image Processing for Nondestructive Applications. In *NDE 2004 National Indian Society annual conference*.
- [37] Cielo, P., Maldague, X., Déom, A., & Lewak, R. (1987). Thermographic NDE of industrial materials and structures. *Materials evaluation*, 45(12), 452-480.
- [38] Allport, J., & McHugh, J. (1988). Quantitative evaluation of transient video thermography. *Review of Progress in Quantitative Non-Destructive Evaluation*, 253-262.
- [39] Lau, S. K., Almond, D. P., & Milne, J. M. (1991). A quantitative analysis of pulsed video thermography. *Ndt & E International*, 24(4), 195-202.
- [40] Almond, D. P., & Pickering, S. G. (2012). An analytical study of the pulsed thermography defect detection limit. *Journal of applied physics*, 111(9), 093510.
- [41] Almond, D. P., Angioni, S. L., & Pickering, S. G. (2017). Long pulse excitation thermographic non-destructive evaluation. *NDT & E International*, 87, 7-14.
- [42] Lau, S. K., Almond, D. P., & Patel, P. M. (1991). Transient thermal wave techniques for the evaluation of surface coatings. *Journal of Physics D: Applied Physics*, 24(3), 428.
- [43] Almond, D. P., & Lau, S. K. (1993). Edge effects and a method of defect sizing for transient thermography. *Applied physics letters*, 62(25), 3369-3371.
- [44] Almond, D. P., & Lau, S. K. (1994). Defect sizing by transient thermography. I. An analytical treatment. *Journal of Physics D: Applied Physics*, 27(5), 1063.

- [45] Saintey, M. B., & Almond, D. P. (1995). Defect sizing by transient thermography. II. A numerical treatment. *Journal of Physics D: Applied Physics*, 28(12), 2539.
- [46] Angioni, S. L., Ciampa, F., Pinto, F., Scarselli, G., Almond, D. P., & Meo, M. (2016). An analytical model for defect depth estimation using pulsed thermography. *Experimental Mechanics*, 56(6), 1111-1122.
- [47] Almond, D. P., & Pickering, S. G. (2014, February). Analysis of the defect detection capabilities of pulse stimulated thermographic NDE techniques. In *AIP Conference Proceedings* (Vol. 1581, No. 1, pp. 1617-1623). AIP.
- [48] Ciampa, F., Angioni, S. L., Pinto, F., Scarselli, G., Almond, D. P., & Meo, M. (2015, April). Modeling of thermal wave propagation in damaged composites with internal source. In *Structural Health Monitoring and Inspection of Advanced Materials, Aerospace, and Civil Infrastructure 2015* (Vol. 9437, p. 943709). International Society for Optics and Photonics.
- [49] Shepard, S. M., Hou, Y. L., Lhota, J. R., Wang, D., & Ahmed, T. (2005, March). Thermographic measurement of thermal barrier coating thickness. In *Thermosense XXVII* (Vol. 5782, pp. 407-410). International Society for Optics and Photonics.
- [50] Vavilov, V. P., & Burleigh, D. D. (2015). Review of pulsed thermal NDT: Physical principles, theory and data processing. *Ndt & E International*, 73, 28-52.
- [51] Fernandes, H., Zhang, H., Figueiredo, A., Ibarra-Castanedo, C., Guimaraes, G., & Maldague, X. (2016). Carbon fiber composites inspection and defect characterization using active infrared thermography: numerical simulations and experimental results. *Applied optics*, 55(34), D46-D53.
- [52] Sun, J. G. (2006). Analysis of pulsed thermography methods for defect depth prediction. *Journal of Heat Transfer*, 128(4), 329-338.
- [53] Broberg, P. (2014). Analytic model for pulsed thermography of subsurface defects. In *Conference QIRT 2014* (Bordeaux, France), 7-11 July 2014 (pp. 1-5). QIRT.
- [54] Weiser, M., Röllig, M., Arndt, R., & Erdmann, B. (2010). Development and test of a numerical model for pulse thermography in civil engineering. *Heat and mass transfer*, 46(11-12), 1419-1428.
- [55] Lopez, F., de Paulo Nicolau, V., Ibarra-Castanedo, C., & Maldague, X. (2014). Thermal–numerical model and computational simulation of pulsed thermography inspection of carbon fiber-reinforced composites. *International Journal of Thermal Sciences*, 86, 325-340.
- [56] Shepard, S. M., & Beemer, M. F. (2015, May). Advances in thermographic signal reconstruction. In *Thermosense: Thermal Infrared Applications XXXVII* (Vol. 9485, p. 94850R). International Society for Optics and Photonics.
- [57] Crinière, A., Dumoulin, J., Ibarra-Castanedo, C., & Maldague, X. (2014). Inverse model for defect characterisation of externally glued CFRP on reinforced concrete structures: comparative study of square pulsed and pulsed thermography. *Quantitative InfraRed Thermography Journal*, 11(1), 84-114.

- [58] Crowther, D. J., Favro, L. D., Kuo, P. K., & Thomas, R. L. (1993). Inverse scattering algorithm applied to infrared thermal wave images. *Journal of applied physics*, 74(9), 5828-5834.
- [59] Sundaravalli, S., Majumder, M. C., & Vijayaraghavan, G. K. (2013). Modeling and simulation of delaminations in FML using step pulsed active thermography. *Int Sch Sci Res Innov*, 7(4), 288-97.
- [60] Feuillet, V., Dujardin, N., Fois, M., Ibos, L., Poilâne, C., & Candau, Y. (2012, June). Pulsed thermography: A useful tool to determine porosity in composite materials. In *Proceedings of the 11th International Conference on Quantitative InfraRed Thermography*, Naples, Italy (Vol. 1114, p. 9).
- [61] Standard, A. S. T. M. (2013). E1461 (2013) Standard test method for thermal diffusivity by the flash method. ASTM International, West Conshohocken, PA, doi, 10.
- [62] Parker, W. J., Jenkins, R. J., Butler, C. P., & Abbott, G. L. (1961). Flash method of determining thermal diffusivity, heat capacity, and thermal conductivity. *Journal of applied physics*, 32(9), 1679-1684.
- [63] Pawar, S. S., & Vavilov, V. P. A novel one-sided diffusivity evaluation technique versus Parker's method in application to carbon/epoxy composite.
- [64] Lee T.R., Purdue University Ph.D. Thesis, "Thermal Diffusivity of Dispersed and Layered Composites", University Microfilms International, 1977.
- [65] Donaldson, A. B. (1972). Two-dimensional thermal attenuation of a laser pulse in a solid. *Journal of the Franklin Institute*, 294(4), 275-281.
- [66] Donaldson, A. B. (1972). Radial conduction effects in the pulse method of measuring thermal diffusivity. *Journal of Applied Physics*, 43(10), 4226-4228.
- [67] Donaldson, A. B., & Taylor, R. E. (1975). Thermal diffusivity measurement by a radial heat flow method. *Journal of Applied Physics*, 46(10), 4584-4589.
- [68] Tao, N., Li, X. L., & Sun, J. G. (2017). Simultaneous measurement of thermal conductivity and heat capacity by flash thermal imaging methods. *Review of Scientific Instruments*, 88(6), 064903.
- [69] Maillet, D., Andre, S., Batsale, J. C., Degiovanni, A., & Moyne, C. (2000). *Thermal quadrupoles, Solving the heat Equations through Integral Transforms*, edition Wiley.
- [70] Feuillet, V., Ibos, L., Fois, M., Dumoulin, J., & Candau, Y. (2012). Defect detection and characterization in composite materials using square pulse thermography coupled with singular value decomposition analysis and thermal quadrupole modeling. *NDT & E International*, 51, 58-67.
- [71] Shepard, S. M. (2003). U.S. Patent No. 6,516,084. Washington, DC: U.S. Patent and Trademark Office.
- [72] Altenburg, S. J., & Krankenhagen, R. (2018). Continuous and Laplace transformable approximation for the temporal pulse shape of Xe-flash lamps for flash thermography. *Quantitative InfraRed Thermography Journal*, 15(1), 121-131.
- [73] Balageas, D. L. (2010, July). Thickness or diffusivity measurements from front-face flash experiments using the TSR® (thermographic signal reconstruction) approach. In *Proceedings of 10th Quantitative InfraRed Thermography conference*, paper QIRT2010-011 Québec (Canada).

- [74] Palumbo, D., Cavallo, P., & Galietti, U. (2019). An investigation of the stepped thermography technique for defects evaluation in GFRP materials. *NDT & E International*, 102, 254-263.
- [75] Maierhofer, C., Krankenhagen, R., Röllig, M., Heckel, T., Brackrock, D., & Gaal, M. (2018). Quantification of impact damages in CFRP and GFRP structures with thermography and ultrasonics.
- [76] Balageas, D. L., & Roche, J. M. (2014). Common tools for quantitative time-resolved pulse and step-heating thermography—part I: theoretical basis. *Quantitative InfraRed Thermography Journal*, 11(1), 43-56.
- [77] Roche, J. M., & Balageas, D. L. (2015). Common tools for quantitative pulse and step-heating thermography—part II: experimental investigation. *Quantitative InfraRed Thermography Journal*, 12(1), 1-23.
- [78] Tamborrino, R., D'Accardi, E., Palumbo, D., & Galietti, U. (2019). A thermographic procedure for the measurement of the tungsten carbide coating thickness. *Infrared Physics & Technology*, 98, 114-120.
- [79] Vavilov, V. (1979). Infrared nondestructive testing of bonded structures: aspects of theory and practice. *NDT'79*, Nottingham, 180-183.
- [80] Vavilov, V. P., & Taylor, R. (1982). Theoretical and practical aspects of the thermal nondestructive testing of bonded structures. *Academic Press, Research Techniques in Nondestructive Testing*, 5, 239-279.
- [81] Osiander, R., & Spicer, J. W. (1998). Time-resolved infrared radiometry with step heating. A review. *Revue Générale de Thermique*, 37(8), 680-692.
- [82] Badghaish, A. A., & Fleming, D. C. (2008). Non-destructive inspection of composites using step heating thermography. *Journal of composite materials*, 42(13), 1337-1357.
- [83] Balageas, D. L., Krapez, J. C., & Cielo, P. (1986). Pulsed photothermal modeling of layered materials. *Journal of Applied Physics*, 59(2), 348-357.
- [84] Marinetti, S., Robba, D., Cernuschi, F., Bison, P. G., & Grinzato, E. (2007). Thermographic inspection of TBC coated gas turbine blades: Discrimination between coating over-thicknesses and adhesion defects. *Infrared physics & technology*, 49(3), 281-285.
- [85] Palumbo, D., Ancona, F., & Galietti, U. (2015). Quantitative damage evaluation of composite materials with microwave thermographic technique: feasibility and new data analysis. *Meccanica*, 50(2), 443-459.
- [86] D'Accardi, E., Palumbo, D., Tamborrino, R., Cavallo, P., & Galietti, U. (2018). Pulsed Thermography: Evaluation and quantitative analysis of defects through different post-processing algorithms. In *Proceedings of the Conference QIRT*.
- [87] Palumbo, D., & Galietti, U. (2016). Damage investigation in composite materials by means of new thermal data processing procedures. *Strain*, 52(4), 276-285.
- [88] Rajic, N. (2002). Principal component thermography (No. DSTO-TR-1298). DEFENCE SCIENCE AND TECHNOLOGY ORGANISATION VICTORIA (AUSTRALIA) AERONAUTICAL AND MARITIME RESEARCH LAB.
- [89] Parvataneni, R. (2009). Principal component thermography for steady thermal perturbation scenarios.

- [90] Rajic, N. (2002). Principal component thermography for flaw contrast enhancement and flaw depth characterisation in composite structures. *Composite structures*, 58(4), 521-528.
- [91] Duan, Y. (2014). Probability of detection analysis for infrared nondestructive testing and evaluation with applications including a comparison with ultrasonic testing.
- [92] Ibarra-Castanedo, C., Bendada, A., & Maldague, X. (2007, October). Thermographic image processing for NDT. In *IV Conferencia Panamericana de END* (Vol. 79, pp. 1-12).
- [93] Ibarra-Castanedo, C., González, D. A., Galmiche, F., Bendada, A., & Maldague, X. P. (2006). On signal transforms applied to pulsed thermography. *Recent research developments in applied physics*, 9, 101-27.
- [94] Sun, J. (2008). U.S. Patent No. 7,365,330. Washington, DC: U.S. Patent and Trademark Office.
- [95] Han, X., Favro, L. D., Kuo, P. K., & Thomas, R. L. (1996). Early-time pulse-echo thermal wave imaging. In *Review of progress in quantitative nondestructive evaluation* (pp. 519-524). Springer, Boston, MA.
- [96] Palumbo, D., Tamborrino, R., Galietti, U., Aversa, P., Tatì, A., & Luprano, V. A. M. (2016). Ultrasonic analysis and lock-in thermography for debonding evaluation of composite adhesive joints. *Ndt & E International*, 78, 1-9.
- [97] Meola, C., & Carlomagno, G. M. (2004). Recent advances in the use of infrared thermography. *Measurement science and technology*, 15(9), R27.
- [98] Favro, L. D., & Han, X. (1998). Thermal wave materials characterization and thermal wave imaging. *Sensing for Materials Characterization, Processing and Manufacturing, ASNT TONES*, 1, 399-415.
- [99] Wu, D., & Busse, G. (1998). Lock-in thermography for nondestructive evaluation of materials. *Revue générale de thermique*, 37(8), 693-703.
- [100] BuSse, G., Wu, D., & Karpen, W. (1992). Thermal wave imaging with phase sensitive modulated thermography. *Journal of Applied Physics*, 71(8), 3962-3965.
- [101] Busse, G. (1979). Optoacoustic phase angle measurement for probing a metal. *Applied Physics Letters*, 35(10), 759-760.
- [102] Busse, G. (1982). Optoacoustic and photothermal material inspection techniques. *Applied optics*, 21(1), 107-110.
- [103] Rosencwaig, A., & Busse, G. (1980). High-resolution photoacoustic thermal-wave microscopy. *Applied Physics Letters*, 36(9), 725-727.
- [104] Thomas, R. L., Pouch, J. J., Wong, Y. H., Favro, L. D., Kuo, P. K., & Rosencwaig, A. (1980). Subsurface flaw detection in metals by photoacoustic microscopy. *Journal of Applied Physics*, 51(2), 1152-1156.
- [105] Spiessberger, C., Gleiter, A., & Busse, G. (2008). Data fusion of lockin-thermography phase images. *Quantitative InfraRed Thermography Journal*, 6.

- [106] Duan, Y., Huebner, S., Hassler, U., Osman, A., Ibarra-Castanedo, C., & Maldague, X. P. (2013). Quantitative evaluation of optical lock-in and pulsed thermography for aluminum foam material. *Infrared Physics & Technology*, 60, 275-280.
- [107] Menaka, M., Sharath, D., Venkratraman, B., & Raj, B. (2014). Defect depth detectability in Austenitic stainless steel by lock in thermography. *Proceedings 12th QIRT, Bordeaux*.
- [108] Ibarra-Castanedo, C., Piau, J. M., Guilbert, S., Avdelidis, N. P., Genest, M., Bendada, A., & Maldague, X. P. (2009). Comparative study of active thermography techniques for the nondestructive evaluation of honeycomb structures. *Research in Nondestructive Evaluation*, 20(1), 1-31.
- [109] Mulaveesala, R., & Tuli, S. (2006). Theory of frequency modulated thermal wave imaging for nondestructive subsurface defect detection. *Applied Physics Letters*, 89(19), 191913.
- [110] Pitarresi, G. (2015). Lock-in signal post-processing techniques in infra-red thermography for materials structural evaluation. *Experimental Mechanics*, 55(4), 667-680.
- [111] Pitarresi, G. (2010). Thermal NDE of thick GRP panels by means of a Pulse Modulated Lock-In Thermography technique. In *EPJ Web of Conferences* (Vol. 6, p. 38014). EDP Sciences.
- [112] Ibarra-Castanedo, C., Genest, M., Piau, J. M., Guilbert, S., Bendada, A., & Maldague, X. P. (2007). Active infrared thermography techniques for the nondestructive testing of materials. In *Ultrasonic and advanced methods for nondestructive testing and material characterization* (pp. 325-348).
- [113] Maldague, X., & Marinetti, S. (1996). Pulse phase infrared thermography. *Journal of applied physics*, 79(5), 2694-2698.
- [114] Ibarra-Castanedo, C., Bendada, A., & Maldague, X. (2005). Image and signal processing techniques in pulsed thermography. *GESTS Int'l Trans. Computer Science and Engr*, 22(1), 89-100.
- [115] Krapez, J. C., Balageas, D., Deom, A., & Lepoutre, F. (1994). Early detection by stimulated infrared thermography. Comparison with ultrasonics and holo/shearography. In *Advances in Signal Processing for Nondestructive Evaluation of Materials* (pp. 303-321). Springer, Dordrecht.
- [116] Martin, R. E., Gyekenyesi, A. L., & Shepard, S. M. (2003). Interpreting the results of pulsed thermography data. *Materials evaluation*, 61(5), 611-616.
- [117] Krapez, J. C., Boscher, D., Delpech, P., Déom, A., Gardette, G., & Balageas, D. (1992). Time-resolved pulsed stimulated infrared thermography applied to carbon-epoxy non destructive evaluation. *ONERA TP*.
- [118] Theodorakeas, P., & Kouli, M. (2018). Depth Retrieval Procedures in Pulsed Thermography: Remarks in Time and Frequency Domain Analyses. *Applied Sciences*, 8(3), 409.
- [119] Benítez, H. D., Ibarra-Castanedo, C., Bendada, A., Maldague, X., Loaiza, H., & Caicedo, E. (2008). Definition of a new thermal contrast and pulse correction for defect quantification in pulsed thermography. *Infrared Physics & Technology*, 51(3), 160-167.
- [120] Theodorakeas, P., & Kouli, M. (2018). Depth Retrieval Procedures in Pulsed Thermography: Remarks in Time and Frequency Domain Analyses. *Applied Sciences*, 8(3), 409.

- [121] Krapez, J. C., Lepoutre, F., & Balageas, D. (1994). Early detection of thermal contrast in pulsed stimulated thermography. *Le Journal de Physique IV*, 4(C7), C7-47.
- [122] Plotnikov, Y. A., & Winfree, W. P. (2000, May). Temporal treatment of a thermal response for defect depth estimation. In *AIP Conference Proceedings* (Vol. 509, No. 1, pp. 587-594). AIP.
- [123] Favro, L. D., Han, X., Kuo, P. K., & Thomas, R. L. (1995, March). Imaging the early time behavior of reflected thermal wave pulses. In *Thermosense XVII: An International Conference on Thermal Sensing and Imaging Diagnostic Applications* (Vol. 2473, pp. 162-166). International Society for Optics and Photonics.
- [124] Ringermacher, H. I., Archacki Jr, R. J., & Veronesi, W. A. (1998). U.S. Patent No. 5,711,603. Washington, DC: U.S. Patent and Trademark Office. González
- [125] Bai, W., & Wong, B. S. (2001). Evaluation of defects in composite plates under convective environments using lock-in thermography. *Measurement science and technology*, 12(2), 142.
- [126] Wong, B. S., Tui, C. G., Bai, W., Tan, P. H., Low, B. S., & Tan, K. S. (1999). Thermographic evaluation of defects in composite materials. *Insight*, 41(8), 504-509.
- [127] Giorleo, G., & Meola, C. (2002). Comparison between pulsed and modulated thermography in glass-epoxy laminates. *NDT & E International*, 35(5), 287-292.
- [128] Castleman, K. R. (1996). *Digital Image. Processing* Englewood Cliffs, New York.
- [129] Pierce, J., & Crane, N. B. (2019). Impact of Pulse Length on the Accuracy of Defect Depth Measurements in Pulsed Thermography. *Journal of Heat Transfer*, 141(4), 042002.
- [130] Masamune, S., & Smith, J. M. (1963). Thermal conductivity of beds of spherical particles. *Industrial & Engineering Chemistry Fundamentals*, 2(2), 136-143.
- [131] Edgar, J., & Tint, S. (2015). Additive manufacturing technologies: 3D printing, rapid prototyping, and direct digital manufacturing. *Johnson Matthey Technology Review*, 59(3), 193-198.
- [132] Kim, J. W., Yun, K. W., & Jung, H. C. (2013). Investigation of optimal thermal injection conditions and the capability of IR thermography for detecting wall-thinning defects in small-diameter piping components. *Nuclear Engineering and Design*, 262, 39-51.
- [133] Ciampa, F., Mahmoodi, P., Pinto, F., & Meo, M. (2018). Recent advances in active infrared thermography for non-destructive testing of aerospace components. *Sensors*, 18(2), 609.
- [134] JCGM 100:2008 (E). Guide to the expression of uncertainty in measurement.
- [135] Montgomery D. C. and Runger G. C. (2011). *Applied Statistics and Probability for Engineers*, 5th edition (Wiley, New York).
- [136] DebRoy, T., Wei, H. L., Zuback, J. S., Mukherjee, T., Elmer, J. W., Milewski, J. O., ... & Zhang, W. (2018). Additive manufacturing of metallic components—process, structure and properties. *Progress in Materials Science*, 92, 112-224.

- [137] ASTM Committee F42 on Additive Manufacturing Technologies, & ASTM Committee F42 on Additive Manufacturing Technologies. Subcommittee F42. 91 on Terminology. (2012). Standard terminology for additive manufacturing technologies. ASTM International.
- [138] Mani, M., Feng, S., Lane, B., Donmez, A., Moylan, S., & Fesperman, R. (2015). Measurement science needs for real-time control of additive manufacturing powder bed fusion processes.
- [139] Vlasea, M. L., Lane, B., Lopez, F., Mekhontsev, S., & Donmez, A. (2015, August). Development of powder bed fusion additive manufacturing test bed for enhanced real-time process control. In Proceedings of the International Solid Freeform Fabrication Symposium, Austin, TX, USA (pp. 13-15).
- [140] King, W. E., Barth, H. D., Castillo, V. M., Gallegos, G. F., Gibbs, J. W., Hahn, D. E., ... & Rubenchik, A. M. (2014). Observation of keyhole-mode laser melting in laser powder-bed fusion additive manufacturing. *Journal of Materials Processing Technology*, 214(12), 2915-2925.
- [141] Coeck, S., Bisht, M., Plas, J., & Verbist, F. (2019). Prediction of lack of fusion porosity in selective laser melting based on melt pool monitoring data. *Additive Manufacturing*, 25, 347-356.
- [142] Thanki, A., Goossens, L., Mertens, R., Probst, G., Dewulf, W., Witvrouw, A., & Yang, S. (2019). Study of keyhole-porosities in selective laser melting using X-ray computed tomography. *Proceedings of iCT 2019*, 1-7.
- [143] Slotwinski, J. A., Garboczi, E. J., & Hebenstreit, K. M. (2014). Porosity measurements and analysis for metal additive manufacturing process control. *Journal of research of the National Institute of Standards and Technology*, 119, 494.
- [144] Thijs, L., Verhaeghe, F., Craeghs, T., Van Humbeeck, J., & Kruth, J. P. (2010). A study of the microstructural evolution during selective laser melting of Ti-6Al-4V. *Acta materialia*, 58(9), 3303-3312.
- [145] Elmer, J. W., Vaja, J., Carlton, H. D., & Pong, R. (2015). The effect of Ar and N₂ shielding gas on laser weld porosity in steel, stainless steels, and nickel. *Weld J*, 94(10), 313s-325s.
- [146] Elmer, J. W., Vaja, J., & Carlton, H. D. (2016). The effect of reduced pressure on laser keyhole weld porosity and weld geometry in commercially pure titanium and nickel. *Welding Journal*, 95(11), 419S-430S.
- [147] Girardin, E., Renghini, C., Dyson, J., Calbucci, V., Moroncini, F., & Albertini, G. (2011). Characterization of porosity in a laser sintered MMCp using X-ray synchrotron phase contrast microtomography. *Materials Sciences and Applications*, 2(9), 1322-1330.
- [148] King, W. E., Barth, H. D., Castillo, V. M., Gallegos, G. F., Gibbs, J. W., Hahn, D. E., ... & Rubenchik, A. M. (2014). Observation of keyhole-mode laser melting in laser powder-bed fusion additive manufacturing. *Journal of Materials Processing Technology*, 214(12), 2915-2925.
- [149] Aboulkhair, N. T., Everitt, N. M., Ashcroft, I., & Tuck, C. (2014). Reducing porosity in AlSi10Mg parts processed by selective laser melting. *Additive Manufacturing*, 1, 77-86.
- [150] Altenburg, S. J., Maierhofer, C., & Gumenyuk, A. (2018). Comparison of MWIR thermography and high-speed NIR thermography in a laser metal deposition (LMD) process.

- [151] Sirikham, A., Zhao, Y., & Mehnen, J. (2017). Determination of thermal wave reflection coefficient to better estimate defect depth using pulsed thermography. *Infrared Physics & Technology*, 86, 1-10.
- [152] D'Accardi, E., Altenburg, S., Maierhofer, C., Palumbo, D., & Galietti, U. (2019). Detection of Typical Metal Additive Manufacturing Defects by the Application of Thermographic Techniques. In *Multidisciplinary Digital Publishing Institute Proceedings* (Vol. 27, No. 1, p. 24).
- [153] Jolly, M. R., Prabhakar, A., Sturzu, B., Hollstein, K., Singh, R., Thomas, S., ... & Shaw, A. (2015). Review of non-destructive testing (NDT) techniques and their applicability to thick walled composites. *Procedia CIRP*, 38, 129-136.
- [154] Gholizadeh, S. (2016). A review of non-destructive testing methods of composite materials. *Procedia Structural Integrity*, 1, 50-57.
- [155] Boychuk, A. S., Generalov, A. S., Stepanov, A. V., & Juhackova, O. V. (2013, September). Nondestructive testing of FRP by using phased array ultrasonic technology. In *Proceedings of the 12th International Conference of the Slovenian Society for Non-Destructive Testing*, Portoroz, Slovenia (pp. 4-6).
- [156] Scarponi, C., & Briotti, G. (2000). Ultrasonic technique for the evaluation of delaminations on CFRP, GFRP, KFRP composite materials. *Composites Part B: Engineering*, 31(3), 237-243.
- [157] Carofalo, A., Dattoma, V., Palano, F., & Panella, F. W. (2014, June). ND testing advances on CFRP with ultrasonic and thermal techniques. In *Proceedings of the 16th European Conference on Composite Materials, ECCM, Seville, Spain* (pp. 22-26).
- [158] Zheng, K., Chang, Y. S., & Yao, Y. (2015). Defect detection in CFRP structures using pulsed thermographic data enhanced by penalized least squares methods. *Composites Part B: Engineering*, 79, 351-358.
- [159] Shepard, S. M. (2001, March). Advances in pulsed thermography. In *Thermosense XXIII* (Vol. 4360, pp. 511-515). International Society for Optics and Photonics.
- [160] Rodríguez, F. L., Nicolau, V. P., & Maldague, X. (2012, June). Pulsed Phase Thermography applied on complex structures: modelling and numerical analysis. In *Proceedings of the 11th International Conference on Quantitative InfraRed Thermography* (pp. 11-14).
- [161] Maldague, X., Galmiche, F., & Ziadi, A. (2002). Advances in pulsed phase thermography. *Infrared physics & technology*, 43(3-5), 175-181.
- [162] Ibarra-Castanedo, C., Gonzalez, D., & Maldague, X. (2004, August). Automatic algorithm for quantitative pulsed phase thermography calculations. In *Proc. 16th World Conference on Nondestructive Testing (WC-NDT)* (Vol. 16).
- [163] Ibarra-Castanedo, C., Gonzalez, D., Klein, M., Pilla, M., Vallerand, S., & Maldague, X. (2004). Infrared image processing and data analysis. *Infrared physics & technology*, 46(1-2), 75-83.
- [164] Waugh, R. C., Dulieu-Barton, J. M., & Quinn, S. (2014). Modelling and evaluation of pulsed and pulse phase thermography through application of composite and metallic case studies. *Ndt & E International*, 66, 52-66.

- [165] Sharath, D., Menaka, M., & Venkatraman, B. (2013). Defect characterization using pulsed thermography. *Journal of Nondestructive Evaluation*, 32(2), 134-141.
- [166] Liu, B., Zhang, H., Fernandes, H., & Maldague, X. (2016). Experimental evaluation of pulsed thermography, lock-in thermography and vibrothermography on foreign object defect (FOD) in CFRP. *Sensors*, 16(5), 743.
- [167] Liu, B., Zhang, H., Fernandes, H., & Maldague, X. (2016). Experimental evaluation of pulsed thermography, lock-in thermography and vibrothermography on foreign object defect (FOD) in CFRP. *Sensors*, 16(5), 743.
- [168] Ibarra-Castanedo, C., Aydelidis, N. P., Grinzato, E. G., Bison, P. G., Marinetti, S., Chen, L., ... & Maldague, X. (2006). Quantitative inspection of non-planar composite specimens by pulsed phase thermography. *Quantitative InfraRed Thermography Journal*, 3(1), 25-40.
- [169] Gruber, J., Stotter, B., Mayr, G., & Hendorfer, G. (2013, January). Prospects of pulse phase thermography for finding disbonds in CFRP-sandwich parts with aluminum honeycomb cores compared to ultrasonic. In *AIP Conference Proceedings* (Vol. 1511, No. 1, pp. 547-554). AIP.
- [170] Zalameda, J. N., & Winfree, W. P. (1990). Thermal diffusivity measurements on composite porosity samples. In *Review of Progress in Quantitative Nondestructive Evaluation* (pp. 1541-1548). Springer, Boston, MA
- [171] Dattoma, V., Nobile, R., Panella, F. W., & Saponaro, A. (2018). NDT thermographic techniques on CFRP structural components for aeronautical application. *Procedia Structural Integrity*, 8, 452-461.
- [172] Dattoma, V., Nobile, R., Panella, F. W., Pirinu, A., & Saponaro, A. ADVANCED NDT PROCEDURES AND THERMAL DATA PROCESSING ON CFRP AERONAUTICAL COMPONENTS.
- [173] Colombo, C., Bhujangrao, T., Libonati, F., & Vergani, L. (2019). Effect of delamination on the fatigue life of GFRP: A thermographic and numerical study. *Composite Structures*, 218, 152-161.
- [174] Colombo, C., & Vergani, L. (2014). Influence of delamination on fatigue properties of a fibreglass composite. *Composite Structures*, 107, 325-333.
- [175] Vergani, L., Colombo, C., & Libonati, F. (2014). A review of thermographic techniques for damage investigation in composites. *Fract. Struct. Integr. Ann*, 8.
- [176] Colombo, C., Crivelli, D., Gobbi, G., Guagliano, M., & Vergani, L. A. U. R. A. (2013). Application of thermography and acoustic emission to detect impact damage in CFRP. In *3rd International Conference of Engineering Against Failure (ICEAF III)* (pp. 14-22). S. Pantelakis, G. Gibson.
- [177] Dattoma, V., Giancane, S., Nobile, R., & Panella, F. W. Application of Thermography and Digital Image Correlation on the study of fatigue damage in fiber reinforced composites.
- [178] Al-Mukhtar, A. M. (2016). Review of resistance spot welding sheets: processes and failure mode. In *Advanced Engineering Forum* (Vol. 17, pp. 31-57). Trans Tech Publications.
- [179] Williams, N. T., & Parker, J. D. (2004). Review of resistance spot welding of steel sheets Part 1 Modelling and control of weld nugget formation. *International materials reviews*, 49(2), 45-75.

- [180] Williams, N. T., & Parker, J. D. (2004). Review of resistance spot welding of steel sheets Part 2 Factors influencing electrode life. *International Materials Reviews*, 49(2), 77-108.
- [181] Tsukada, K., Miyake, K., Harada, D., Sakai, K., & Kiwa, T. (2013). Magnetic nondestructive test for resistance spot welds using magnetic flux penetration and eddy current methods. *Journal of Nondestructive Evaluation*, 32(3), 286-293.
- [182] Thornton, M., Han, L., & Shergold, M. (2012). Progress in NDT of resistance spot welding of aluminium using ultrasonic C-scan. *Ndt & E International*, 48, 30-38.
- [183] Runnemalm, A., Ahlberg, J., Appelgren, A., & Sjökvist, S. (2014). Automatic inspection of spot welds by thermography. *Journal of nondestructive evaluation*, 33(3), 398-406.
- [184] ISO: ISO 10447:2006 resistance welding peel and chisel testing of resistance spot and projection welds (2006).
- [185] Wan, X., Wang, Y., Zhao, D., Huang, Y., & Yin, Z. (2017). Weld quality monitoring research in small scale resistance spot welding by dynamic resistance and neural network. *Measurement*, 99, 120-127.
- [186] Schlichting, J., Brauser, S., Pepke, L. A., Maierhofer, C., Rethmeier, M., & Kreutzbruck, M. (2012). Thermographic testing of spot welds. *NDT & E International*, 48, 23-29.
- [187] Jonietz, F., Myrach, P., Suwala, H., & Ziegler, M. (2016). Examination of spot welded joints with active thermography. *Journal of Nondestructive Evaluation*, 35(1), 1.
- [188] Woo, W., Chin, C. W., Feng, Z., Wang, H., Zhang, W., Xu, H., & Sklad, P. S. (2009, April). Application of infrared imaging for quality inspection in resistance spot welds. In *Thermosense XXXI* (Vol. 7299, p. 729912). International Society for Optics and Photonics.
- [189] Lee, S., Nam, J., Hwang, W., Kim, J., & Lee, B. (2011). A study on integrity assessment of the resistance spot weld by Infrared Thermography. *Procedia Engineering*, 10, 1748-1753.
- [190] Kamdi, Z., Shipway, P. H., Voisey, K. T., & Sturgeon, A. J. (2011). Abrasive wear behaviour of conventional and large-particle tungsten carbide-based cermet coatings as a function of abrasive size and type. *Wear*, 271(9-10), 1264-1272.
- [191] Wang, Q., Chen, Z. H., & Ding, Z. X. (2009). Performance of abrasive wear of WC-12Co coatings sprayed by HVOF. *Tribology International*, 42(7), 1046-1051.
- [192] Stewart, D. A., Shipway, P. H., & McCartney, D. G. (1999). Abrasive wear behaviour of conventional and nanocomposite HVOF-sprayed WC-Co coatings. *Wear*, 225, 789-798.
- [193] Zhao, L., Maurer, M., Fischer, F., Dicks, R., & Lugscheider, E. (2004). Influence of spray parameters on the particle in-flight properties and the properties of HVOF coating of WC-CoCr. *Wear*, 257(1-2), 41-46.
- [194] Davis, J. R. (Ed.). (2004). *Handbook of thermal spray technology*. ASM international.
- [195] Wesmann, J. A. R., & Espallargas, N. (2016). Effect of atmosphere, temperature and carbide size on the sliding friction of self-mated HVOF WC-CoCr contacts. *Tribology International*, 101, 301-313.

- [196] Wank, A., Wielage, B., Pokhmurska, H., Friesen, E., & Reisel, G. (2006). Comparison of hardmetal and hard chromium coatings under different tribological conditions. *Surface and Coatings Technology*, 201(5), 1975-1980.
- [197] Fischer-Cripps, A. C., Lawn, B. R., Pajares, A., & Wei, L. (1996). Stress analysis of elastic-plastic contact damage in ceramic coatings on metal substrates. *Journal of the American ceramic society*, 79(10), 2619-2625.
- [198] Holmberg, K., Laukkanen, A., Ronkainen, H., Wallin, K., Varjus, S., & Koskinen, J. (2006). Tribological contact analysis of a rigid ball sliding on a hard coated surface: Part II: Material deformations, influence of coating thickness and Young's modulus. *Surface and Coatings Technology*, 200(12-13), 3810-3823.
- [199] Bolelli, G., Lusvarghi, L., & Barletta, M. (2009). HVOF-sprayed WC-CoCr coatings on Al alloy: effect of the coating thickness on the tribological properties. *Wear*, 267(5-8), 944-953.
- [200] Dodd, C. V., & Simpson Jr, W. A. (1972). THICKNESS MEASUREMENTS USING EDDY-CURRENT TECHNIQUES (No. ORNL-TM-3712). Oak Ridge National Lab., Tenn..
- [201] Ming-Xuan, L., Xiao-Min, W., & Jie, M. (2004). Thickness measurement of a film on a substrate by low-frequency ultrasound. *Chinese Physics Letters*, 21(5), 870.
- [202] Izutani, Y., Akagi, M., & Kitagishi, K. (2012, September). Measurements of paint thickness of automobiles by using THz time-domain spectroscopy. In 2012 37th International Conference on Infrared, Millimeter, and Terahertz Waves (pp. 1-2). IEEE.
- [203] Mezghani, S., Perrin, E., Vrabie, V., Bodnar, J. L., Marthe, J., & Cauwe, B. (2016). Evaluation of paint coating thickness variations based on pulsed Infrared thermography laser technique. *Infrared Physics & Technology*, 76, 393-401.
- [204] Tang, Q., Liu, J., Dai, J., & Yu, Z. (2017). Theoretical and experimental study on thermal barrier coating (TBC) uneven thickness detection using pulsed infrared thermography technology. *Applied Thermal Engineering*, 114, 770-775.
- [205] Palumbo, D., Tamborrino, R., & Galletti, U. (2017, May). Coating defect evaluation based on stimulated thermography. In *Thermosense: Thermal Infrared Applications XXXIX* (Vol. 10214, p. 102140X). International Society for Optics and Photonics.

Appendix A: IR cameras and energy sources specifications

Camera FLIR X6540 SC



Figure 1: IR camera FLIR X6540 SC

IMAGING AND OPTICAL DATA

IR RESOLUTION	640X512
THERMAL SENSIVITY/NETD	<25 mK (18 mK typical)
DETECTOR TYPE	Focal plane array (FPA)
SENSOR MATERIAL	InSb
DETECTOR PITCH	15 μ m
IMAGE FREQUENCY	Up to 120Hz by windowing
MAXIMUM IMAGE FREQUENCY (FULL FRAME)	126 Hz
MAXIMUM IMAGE FREQUENCY	4011 Hz
MAXIMUM FRAME RATE	126 Hz
SPECTRAL RANGE	1.5–5.5 μ m

MEASUREMENT

MAXIMUM TEMPERATURE WITHOUT FILTER	300°C
OPERATING TEMPERATURE RANGE	–20°C/+50°C (–4°F/122°F) (–4°F/122°F)
ACCURACY	±1°C (1.8°F) or ±1%

Tabella 1: FLIR X6540 SC

Camera Mirko

- Model: Infratec ImageIR 8800
- Detector IR: (MCT)-Focal-Plane-Array telluride mercury-cooled cadmium

- Detector size: 640 x 512 (step 16 μ m)
- Spectral range: LWIR, 8-9,4 μ m
- Temperature resolution: NETD @ 30°C < 60mK, (at 140 μ s) 80 mK (at 70 μ s) measured on single pixels
- Integration times: 1 200 μ s (step by 1 μ s)
- Conversion A/D: 14 bit
- Storage temperature / humidity: -40°C 70°C / 10 ... 95% rel (no condensation)
- Operating temperature: -20°C 40°C
- Power supply: 230V / 50Hz
- Weight: 4 kg
- Sizes: 244mm x 130mm x 160mm (L x P x A)
- Series Number: 880981 (90466.103)
- Freq/Windowing: 100Hz / FullFrame, 350Hz / HalfFrame, 1200Hz / QuarterFrame, 8 kHz / LineScan (8 x 1.024(h x w))

Camera Objective

MWIR Objective 25 mm

- Focal length: f=25 mm
- Light intensity: f/1,4
- Opening angle: 23,1° x 18,6°
- Optimized for LWIR spectral range LWIR
- IFOV: 6,3 rad
- Image field (d=1 m): (384 x 307) mm, geometrical resolution 0,3 mrad
- Nominal focus range: approx. 20 cm - ∞



Figure 2: Layout of Camera Infratec ImageIR.

Flash Lamps

For the pulsed flash tests a source of optical thermal excitation is used, with 4 flash lamps Hensel EH PRO 6 kJ.

- Capacity up to 6000 Ws
- 5m lamp cable (long plug)
- Housing made of aluminum drawn profile, 2.6 mm thick
- Plug-in flash tube
- Modeling light up to 650 W
- Clear glass cover
- Reflector quick-change automatic, 360° for EH



Figure 3: Lamp Hensel EH Pro 6000.

Camera Kasimir

- Model: Infratec ImageIR 8300 hp
- Spectral range: (2.0 ... 5.7) μm
- Pitch: 15 μm
- Detector MCT or InSb
- Detector format (IR pixels) (640 \times 512)
- Detector cooling: Stirling cooler
- Temperature measuring range: -40 ... 1,500 $^{\circ}\text{C}$
- Measurement accuracy: ± 1 $^{\circ}\text{C}$ or ± 1 %
- Temperature resolution @ 30 $^{\circ}\text{C}$: Better than 0.02 K
- Frame rate: Up to 125 / 404 / 1,051 / 2,996 Hz
- Window mode: Yes
- Integration time: (0.6 ... 20,000) μs
- Power supply 24 V DC, wide-range power supply (100 ... 240) V AC
- Storage and operation temperature (-40 ... 70) $^{\circ}\text{C}$, (-20 ... 50) $^{\circ}\text{C}$
- Dimensions: 235 \times 120 \times 160 mm
- Weight: 3.3 kg (without lens)

Camera Objective

MWIR Objective 25 mm

- Focal length: $f=25$ mm
- FOV: 21.7 \times 17.5
- IFOV: 0.6 mrad

Diode laser system LDM 500-20

- Laser line
- Technology: Fiber-coupled BA high-power diode laser array with 2D scanner head and homogenizing optics
- Optical fiber cable: 200 μm fiber core diameter, 10 m length, NA 0.22 +/- 0.02
- Power up to 500 W
- Wavelength 935 nm

In order to control the laser power and the pulse duration, it is chosen to use a pulse generator and a function generator, connected as shown in Fig. A.4. The technical specification of both are reported below:

Pulse generator

Quantum composers 9520 series Digital Delay Pulse Generator

- 8 independent channels
- Resolution: 250 ps
- Accuracy: $1\text{ns} + 0.0001 \times \text{setpoint}$
- Jitter: < 50 ps

Function generator

Rhode & Schwarz HMF2525 Arbitrary Function Generator

- Frequency range: 10 μHz to 25 MHz [50 MHz];
- Triangle and ramp signal up to 10 MHz;
- Pulse: frequency range from 100 μHz to 12.5 MHz [25 MHz];
- Output voltage: 5 mVPP to 10 VPP (into 50 Ω load);
- DC offset: $\pm 5\text{ mV}$ to 5 V;
- Output impedance steplessly adaptable (1 Ω to 10 k Ω);
- Total harmonic distortion: 0.04% ($f < 100\text{ kHz}$);
- Waveform modes: sine, square, pulse, triangle, ramp and arbitrary wave forms (incl. standard curves: white noise, pink noise, cardiac, exponential rise and fall, etc.);

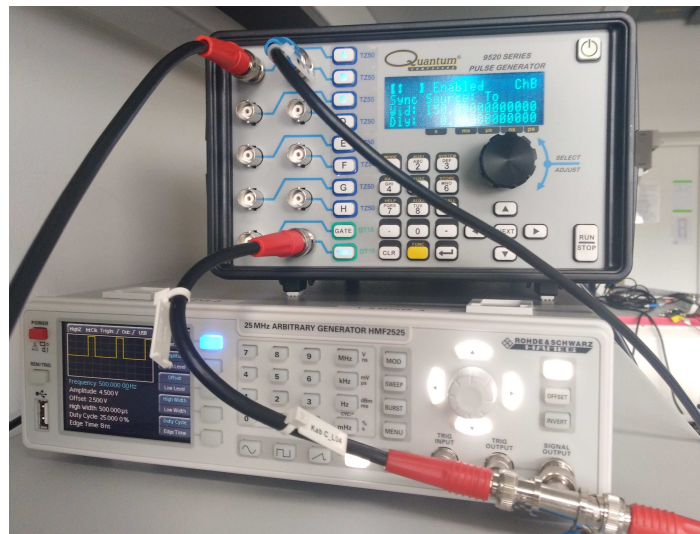
- Modulation modes: AM, FM, pulse, PWM, FSK (internal and external);
- Arbitrary waveform generator: 250 MSa/s, 14 bit, 256 kSa;
- Easily create your own wave forms using standard PC software;
- Oscillographic signal display;
- Front USB to easily save and recall wave forms and settings, RS-232/USB dual interface for remote control;
- BNC connectors: modulation input, sweep output, trigger (input, output), 10MHz reference (input, output, ± 1 ppm TCXO).



(a) Pulse generator.



(b) Function generator.



(c) Connection pulse generator-function generator.

Figure 4: Scheme and components for square wave pulse generation: pulse and function generator.

Camera FLIR SC655



Figura 5: FLIR SC655.

IMAGING AND OPTICAL DATA

IR RESOLUTION	640X480
THERMAL SENSIVITY/NETD	<0.05°C + 30°C/ 50 mK
FIELD OF VIEW (FOV)/MINIMUM FOCUS DISTANCE	25° x 18.8°
SPATIAL RESOLUTION (IFOV)	0.69 mrad
IMAGE FREQUENCY	50 Hz
FOCUS	Automatic or manual (build in monitor)
FOCAL PLANE ARRAY (FPA)/SPECTRAL RANGE	7.5 - 13 µm

MEASUREMENT

TEMPERATURE RANGE	-20°C to +150°C 0°C to +650°C
ACCURACY	± 2°C or ± 2% of reading

Tabella 2: Technical Specification FLIR SC655.

Appendix B: Matlab® Code

```

clear all
2 fclose all;
directory=input('inserting the directory file Irta: ', 's'); %import thermal sequence in Matlab
    (file .irt)
4 name_test=input('inserting the test name: ', 's');
name_sequence=strcat(directory, '/', name_test, '0', '.irt');
6 name_sequence_irt=strcat(directory, '/', name_sequence);
fid=fopen(name_sequence); %read file 0 (size sequence and time vector t)
8 B=fread(fid, [1, 3], 'integer*4'); %get size sequence (pixel by pixel)
t=fread(fid, [4, ceil((B(3)/4))], 'double'); %extract time
10 t=reshape(t, 4*ceil((B(3)/4)), 1);
fclose(fid);

```

```

12 initial_frame=input('initial frame: '); %initial frame of analysis (Tmax if it is a pulsed test)
   final_frame=input('final frame: '); %final frame of analysis
14 matrix=zeros(1,1);
   for i=initial_frame:final_frame %read thermal sequence frame by frame
16 string=[name_sequence_irt int2str(i) '.irt'];
   fid1=fopen(string);
18 film=cat(2,matrix,fid1);
   film=film(2:size(matrix,2));
20 film2D(:,i)=fread(film,'double');
   fclose(fid1);
22 end
   film3D=film2D(:,frame_iniziale:frame_finale); %film2D into film3D by considering own initial and
       final frames
24 film3D=permute(film3D,[1 2 3]);
   film3D=permute(film3D,[1 3 2]);
26 film3D=reshape(film3D,B(2),B(1),initial_frame-final_frame+1);
   t=t(initial_frame:final_frame); %time related to the considered sequence

```

importing_film(irt_to_matlab).m

```

   directory=input('Inserire directory file Irt output: ', 's'); %exporting Matlab result (for
       example 1st derivative sequence) in IRTA
2 name_sequence_file0=strcat(directory,'\','file0','irt'); %creating a file (file 0) with time
       and matrix sizes (row by column)
   name_sequence=strcat(directory,'\','file');
4
6 fid1=fopen(name_sequence_file0,'wb'); %write file 0
   fwrite(fid1,size(matlab_result,2),'integer*4'); %matlab result number of columns (size 2)
8   fwrite(fid1,size(matlab_result,1),'integer*4'); %matlab result number of columns (size 1)
   fwrite(fid1,size(matlab_result,3),'integer*4'); %matlab result number of frames (size 3)
10  fwrite(fid1,t,'double'); %writing time
   fclose(fid1);
12  for i=1:size(matlab_result,3) %writing Matlab result
   stringa=[name_sequence int2str(i) '.irt'];
14  fid2=fopen(stringa,'wb');
   postprocessing_result=matlab_result(:, :, i);
16  fwrite(fid2,postprocessing_result,'double');
   fclose(fid2);
18  end

```

exporting_film(matlab_to_irt).m

```

fclose all
2 film=original_sequence;
   time=original_sequence_time;
4 initial_frame=input('starting frame: ');
   final_frame=input('final frame: ');
6 cold_frame=input('cold frame: ');
   cooling_film=film(:, :, initial_frame:final_frame)-film(:, :, cold_frame); %deltaT sequence (
       cooling)
8 for i=1:size(cooling_film,3)

```



```

    final_film (:, :, i) = ((cooling_film (:, :, i)) ./ (cooling_film (:, :, 1))); %normalization
10 end

12 for i=1:size (final_film ,3)
    for j=1:size (final_film ,2)
14         for k=1:size (final_film ,1)
                if final_film (k,j ,i) <=0
16                     final_film (k,j ,i) = 10^-12;
                        end
18         end
    end
20 end

22 frame_rate=input('camera frame rate: ');
    polynomial_degree=input('polynomial degree: ');
24 t=time (initial_frame : final_frame );
    t=t-(t(1)-1/frame_rate);

26
    s1=size (final_film ,1);
28 s2=size (final_film ,2);
    s3=size (final_film ,3);
30

32 for b=1:s1
    for c=1:s2
34         TEMP=final_film (b,c,:);
            TEMP=TEMP(:);
36         ln_T=log (TEMP);
            ln_time=log (t);
38         polynomial_coeff=polyfit (ln_time , ln_T , polynomial_degree);
            polynomial_values=polyval (polynomial_coeff ,ln_time);
40         polynomial_values=transpose (polynomial_values);

42         first_derivative_coeff=polyder (polynomial_coeff);
            first_derivative_values=polyval (first_derivative_coeff ,ln_time);
44         first_derivative_values=transpose (first_derivative_values);

46         second_derivative_coeff=polyder (first_derivative_coeff);
            second_derivative_values=polyval (second_derivative_coeff ,ln_time);
48         second_derivative_values=transpose (second_derivative_values);

50         m=1;
            s=1;
52         for m=1:polynomial_degree+1
                polynomial_coeff_matrix (b,c,m)=polynomial_coeff (1,s); %matrix for polynomial
coefficients
54             s=s+1;
        end

56
        x=1;
58         g=1;
        for x=1:polynomial_degree

```

```

60         first_polynomial_coeff_matrix(b,c,x)=first_derivative_coeff(1,g);    %matrix for
first derivative polynomial coefficients
        g=g+1;
62     end

64     d=1;
w=1;
66     for d=1:size(final_film,3)
        polynomial_matrix(b,c,d)=polynomial_values(1,w);    %matrix for polynomial sequence
68         w=w+1;
        end

70
k=1;
72     z=1;
        for k=1:size(final_film,3)
74         first_derivative_matrix(b,c,k)=first_derivative_values(1,z);    %matrix for first
derivative sequence
        z=z+1;
76     end

78     j=1;
l=1;
80     for j=1:size(final_film,3)
        second_derivative_matrix(b,c,j)=second_derivative_values(1,l);    %matrix for second
derivative sequence
82         l=l+1;
        end
84     end
end

```

Matlab_Code_Post_processing.m

Acknowledgements

Throughout the writing of this final dissertation, I have received a great deal of support and assistance. The work presented in this document would not have been possible and, above all, it would not have had the same value without the guidance, assistance, and support of others.

First of all, I would like to thank my supervisor, Prof. Umberto Galietti, for their valuable guidance. He provided me with the tools that I needed to choose the right direction and successfully complete my research work. It was a privilege to work alongside him, I believe that the continuous confrontation is fundamental for researchers.

A heartfelt thanks go to my first “mentor”, Dr. Davide Palumbo, whose expertise was invaluable in the formulating of the research topic and methodology. His meaningful suggestions and his clever understanding of the Thermography theory supported my work, and gave me the opportunity to discover an important part of this field. Never stop doing what you do every day for research and for our group, Davide.

I would like to acknowledge my colleagues from my research group, past, present and partly future, Rosanna Tamborrino, Rosa De Finis, Francesca Di Carolo and Giuseppe Dell’Avvocato; even if sometime it was difficult due to the different point of views, I believe that to work in a heterogeneous team like ours is a great fortune and a privilege. I also take this opportunity to thank the guys from DES (Diagnostic Engineering Solutions S.r.l.), for their availability and their technical support.

I wish to thank Dr. rer. nat. Christiane Maierhofer, which hosted me during my stay abroad, at BAM (Bundesanstalt für Materialforschung und -prüfung), in my beloved Berlin. It was a pleasure to work for 6 months with the “Thermos” of the division 8.7; in particular a big thank you also goes to Dr. Simon Altenburg for involving me within a very interesting project, giving me the opportunity to confront myself with a new problem and above all by providing me with all the means necessary to do so.

In addition, I would like to thank my parents for their wise counsels and sympathetic ear. You are always there for me. Finally, there are my friends and roommates, past and present, near and far, scattered not only in Italy, but also in the world after my experience in the cold Berlin; thank you for listening, offering me advice, and supporting me through this entire process. Thank you for your thoughts, well-wishes/prayers, phone calls, e-mails, texts, visits, editing advice, and being there whenever I needed a friend.

Let me conclude as I started, by expressing my thanks to my colleagues who accompanied me from the beginning to the end of this journey, or the Ph.D. students of XXXII cycle, now famous. And therefore thanks to my two pillars of this fantastic group, Giovanni e Guido, who have supported and endured me every holy day, with their strange ways, but to them I owe a lot. They are two great colleagues and, even before that, two fantastic people, whom I hold in high esteem and to whom I really care.

Hoping that I had not disappointed and failed to meet the expectations of anyone and especially my parents.

Ester.

Ringraziamenti

Voglio iniziare questa parte dedicata ai ringraziamenti finali, riprendendo le parole di una presentazione ascoltata all'ultima "AIAS", da Ph.D. student alla quale ho partecipato quest'anno, il 5 settembre ad Assisi. La presentazione conteneva, all'interno della slide dedicata allo stato dell'arte, 3 precise e specifiche domande, che possono sembrare banali, ma non lo sono: "DOVE", "QUANDO", "QUANTO". La presentazione riguardava il confronto di 3 tecniche non distruttive con lo scopo di localizzare e quantificare il danno in componenti in materiale composito. Alla fine di questa presentazione, l'autore ha dato delle risposte precise alle domande che si era posto, argomentandole con risultati quantitativi. Non ero autrice del lavoro in questione, non sapevo l'attività sperimentale e i risultati presentati (in quel periodo mi trovavo a Berlino), ma conosco il relatore.

Non era chissà quale presentazione, non conteneva nessun effetto speciale o chissà quale formulone matematico, ma aveva il suo contributo innovativo, aveva qualcosa da dire di "nuovo" alla comunità scientifica ed era spiegata con rigore metodologico, risultati quantitativi e soprattutto rispondeva in modo semplice ed efficace alle 3 domande poste all'inizio, "DOVE", "QUANDO" e "QUANTO".

Questo è quello che ho provato a fare anche io in questi anni di attività di ricerca, prima di pensare e quindi di provare a pubblicare (perché non è una cosa affatto automatica) qualsiasi lavoro, comunque e sempre supportato da un'attività sperimentale.

Un attento ricercatore avrà già notato che alle 3 domande precedenti ne manca, forse, una fondamentale: "PERCHÉ". In realtà, non è che questa domanda manchi o non sia stata posta all'interno della presentazione alla quale faccio riferimento; semplicemente una persona presente alla discussione o chiunque abbia avuto il piacere di lavorare nella sua vita, anche solo per puro caso, con questa persona, avrà sicuramente notato come questo avverbio, interrogativo e di congiunzione, sia il filo conduttore delle 17 slides proiettate durante la conferenza e che anima, ogni giorno, la sua instancabile attività da ricercatore, cultore della materia e colonna portante del nostro gruppo.

Non è semplice lavorare all'interno di un Gruppo di ricerca; qualcuno potrebbe pensare "che bello vi dividete il lavoro da fare" o ancora "che fortuna, voi vi potete citare a vicenda", ma vi garantisco che mi sono bastati 2 o 3 mesi per capire che la giostra avrebbe girato diversamente e come è giusto che sia. E non lo dico perché si tratta del mio gruppo di ricerca.

Come dice il mio supervisor e di questa frase sono profondamente orgogliosa "Noi ci siamo scelti a vicenda" e per citare, in parallelo, quella di un nuovo acquisto, "noi, ogni giorno, ci svegliamo e decidiamo di restare in questo gruppo e di continuare a farlo crescere, insieme". In realtà, quest'ultima frase l'ho un attimino riarrangiata e riadattata al caso specifico, perché il collega in questione la utilizza spesso in un altro contesto, ma sono certa che apprezzerà e sposerà il presta citazione.

Inizio quindi col ringraziare il mio tutor Professor Umberto Galietti, docente e ancora prima persona che stimo molto per avermi dato l'opportunità di lavorare all'interno di questo gruppo di ricerca e di confrontarmi con un lavoro

impegnativo, permettendomi di migliorarmi non solo professionalmente, ma ancor prima umanamente. Grazie per questi 3 anni insieme, che in realtà il 2 Novembre saranno 4, per i continui confronti agli orari più improponibili, per la sua esperienza, le sue conoscenze ed il tempo concessomi. Grazie per avermi dato la fiducia di girare un pò il mondo insieme a lei, dandomi la possibilità di presentare i nostri lavori in diverse conferenze sia nazionali che internazionali; e grazie anche per i “no, non va bene” servono a molto anche quelli.

I ringraziamenti più importanti e sentiti vanno a Davide; per la sua infinita pazienza e disponibilità, per avermi insegnato il valore vero della ricerca, per avermi trasmesso incondizionatamente, cosa non affatto banale in questo strano mondo universitario, le sue conoscenze e una piccola fetta di quello che in questi 12 anni di carriera ha imparato, con una voglia ed una dedizione alla materia difficili da eguagliare. Perchè questo è un mondo assai particolare dove non è affatto semplice trovare qualcuno che vi resti alle volte anche solo per il puro piacere ed amore per la ricerca. Grazie per i continui consigli, per le intere serate passate davanti ad un PC o nei tetri laboratori di Japigia ad analizzare quello stupido “champion sample” con i buchi dietro che tanto ho odiato. Grazie per avermi dedicato una buona parte del tuo prezioso TEMPO, senza di te questo lavoro non sarebbe stato possibile e sappi che per me, anzi per noi, hai già vinto tutto.

Ringrazio quindi la restante parte del mio gruppo di ricerca, passata e presente: Rosanna, Rossella, Francesca e il “nuovo acquisto” Giuseppe; grazie per il infiniti pranzi, soprattutto quelli del Venerdì, per avermi accompagnato quasi per mano, durante questi anni di dottorato, per avermi fatto conoscere la vostra attività e per essere stati confidenti dei miei dubbi e dei miei momenti di rabbia, prima ancora che colleghi. Grazie per i consigli da persone un pò più grandi di me e grazie per i continui confronti durante quelle che dovrebbero essere le nostre pause, ma che puntualmente si trasformano in riunioni e “melodrammi”, che fanno di tutto, tranne che di una giusta e meritata pausa. Grazie per aver deciso di “continuare”, da voi devo ancora imparare qualcosa.

Grazie anche ai colleghi e ai ragazzi della nostra “vicina di casa” DES, per la disponibilità dei laboratori e per il supporto tecnico durante alcune attività sperimentali.

Colgo l’occasione per ringraziare la Dr. rer. nat. Christiane Maierhofer del BAM di Berlino e tutti i Thermos della divisione 8.7; in particolare un grazie va Simon Altenburg che ha messo a mia disposizione i mezzi del BAM e mi ha coinvolto all’interno di un progetto nuovo e di grande interesse, sia scientifico che industriale.

Un grazie a tutti i docenti e ricercatori del DMMM senza i quali non avrei potuto concludere il mio dottorato all’interno dell’ormai famoso dipartimento di eccellenza.

Grazie agli amici, lontani e vicini, in particolare Melania, Federica, Samanta e Danila, con le quali ormai da diversi anni condivido le mie esperienze e sono cresciuta, giorno dopo giorno, cercando, con i loro consigli e la loro presenza, di migliorarmi costantemente. Grazie per i momenti di svago trascorsi insieme, grazie per i continui incoraggiamenti e grazie per esserci state sempre, a voi devo molto e so per certo che le nostre strade continueranno ad incrociarsi sempre...e tranquille, questa è l’ultima laurea che mi prendo!

Grazie quindi al “Berlinissimo” group, I mean, grazie a tutte quelle persone con le quali ho condiviso anche solo una cena per sbaglio di quei 6 importantissimi mesi del mio percorso di vita all’estero; grazie a voi sono cresciuta tanto e senza Berlino non sarei ciò che oggi sono diventata. E’ vero, non è semplice vivere 6 mesi lontana da quelli che sono gli affetti più cari, ma è un’esperienza che ti cambia la vita.

Ben più di un semplice grazie va alla mia famiglia e ai miei genitori, che mi hanno insegnato il valore vero del sacrificio e che non hanno mai smesso di credere in me, sin dal primo giorno; grazie Mamma e grazie Papà, i miei sacrifici e i miei risultati sono anche i vostri.

A tutti i ragazzi e gli amici della “Camera dei Dottorandi”, che hanno rappresentato per me la mia famiglia in

questi ultimi mesi di dottorato, forse i più brutti ed intensi e mi hanno concesso il privilegio di vivere e condividere con loro la quotidianità di tutti i giorni. Sono certa che il 23 Ottobre consegnerete anche voi qualcosa.

Grazie ai miei compagni e colleghi di corso del XXXII ciclo. Non credo di peccare di presunzione in quello che sto per dire, ma forse rappresentiamo uno dei cicli di dottorato più bello e coeso che si sia visto al Poliba negli ultimi anni.

E concludo, non per ordine di importanza, ma perchè sento che sia giusto così, ringraziando Giovanni e Guido, che durante questo lungo e tortuoso percorso mi hanno ogni “santissimo giorno” supportata e sopportata. E’ impossibile non ringraziarli; nonostante le tematiche di ricerca e i caratteri profondamente diversi, loro hanno contribuito a questo mio risultato, sia scientifico che umano, con dei modi tutti loro, che odio, ma che ricorderò a vita. Grazie per aver condiviso la disperazione delle 3 di notte nel nuovo “Open Space” e per aver reso quel posto stranissimo chiamato Japigia “casa mia” e per avermi spronata, anche a distanza. Per l’infinita pazienza e per il tempo trascorso assieme, nonostante il mio pessimo italiano e il non “ingless”, scritto non a caso così. Non so dove le nostre strade ci porteranno, ma sò per certo che ovunque andrò, porterò con me un pò di voi.

Qualcuno forse sarà rimasto col dubbio del “DOVE”, “QUANDO” e “QUANTO”...in realtà si capisce abbastanza bene a chi mi stavo riferendo, ma, d’altronde, non importa poi tanto, perchè lui sa.

Auspicandomi di non aver disatteso le aspettative di nessuno, soprattutto dei miei genitori.

Ester.

